Low pressure CVD of polycrystalline silicon : reaction kinetics and reactor modelling

Citation for published version (APA):
Weerts, W. L. M. (1995). *Low pressure CVD of polycrystalline silicon : reaction kinetics and reactor modelling*. [Phd Thesis 1 (Research TU/e / Graduation TU/e), Chemical Engineering and Chemistry]. Technische Universiteit Eindhoven. https://doi.org/10.6100/IR450953

DOI:
10.6100/IR450953

Document status and date:
Published: 01/01/1995

Document Version:
Publisher's PDF, also known as Version of Record (includes final page, issue and volume numbers)

Please check the document version of this publication:

• A submitted manuscript is the version of the article upon submission and before peer-review. There can be important differences between the submitted version and the official published version of record. People interested in the research are advised to contact the author for the final version of the publication, or visit the DOI to the publisher's website.
• The final author version and the galley proof are versions of the publication after peer review.
• The final published version features the final layout of the paper including the volume, issue and page numbers.

Link to publication

General rights
Copyright and moral rights for the publications made accessible in the public portal are retained by the authors and/or other copyright owners and it is a condition of accessing publications that users recognise and abide by the legal requirements associated with these rights.

- Users may download and print one copy of any publication from the public portal for the purpose of private study or research.
- You may not further distribute the material or use it for any profit-making activity or commercial gain
- You may freely distribute the URL identifying the publication in the public portal.

If the publication is distributed under the terms of Article 25fa of the Dutch Copyright Act, indicated by the "Taverne" license above, please follow below link for the End User Agreement:

www.tue.nl/taverne

Take down policy
If you believe that this document breaches copyright please contact us at:

openaccess@tue.nl

providing details and we will investigate your claim.

Download date: 16. Nov. 2023

Low Pressure CVD of Polycrystalline Silicon: Reaction Kinetics and Reactor Modelling

Proefschrift

ter verkrijging van de graad van doctor aan de Technische Universiteit Eindhoven, op gezag van de Rector Magnificus, prof.dr. J.H. van Lint, voor een commissie aangewezen door het College van Dekanen in het openbaar te verdedigen op donderdag 14 december 1995 om 14.00 uur

door

Wilhelmina Louisa Maria Weerts

geboren te Maastricht

Dit proefschrift is goedgekeurd door de promotoren:

prof.dr.ir. G.B. Marin
prof.dr. L.J. Giling

copromotor:

dr. M.H.J.M. de Croon

CIP-DATA KONINKLIJKE BIBLIOTHEEK, DEN HAAG

Weerts, Wilhelmina Lousia Maria

Low pressure CVD of polycrystalline silicon: reaction
kinetics and reactor modelling / Wilhelmina Louisa Maria
Weerts. - Eindhoven : Eindhoven University of Technology
Thesis Technische Universiteit Eindhoven. - With ref. -
With summary in Dutch.
ISBN 90-386-0506-4
Subject headings: polycrystalline silicon.

SUMMARY

To gain insights in the complex interplay between gas phase and surface reactions during the low pressure chemical vapour deposition (LPCVD) of polycrystalline silicon, the latter was subjected to a comprehensive kinetic investigation. Emphasis was put on the development of intrinsic kinetic models which allow a quantitative description of the experimental observations both in the absence and in the presence of gas phase reactions. Besides classical steady state experiments, also transient response experiments were performed. The developed kinetic model was then used for the design and analysis of an industrial-scale hot-wall multiwafer LPCVD reactor.

A continuous flow laboratory reactor was designed, based on the principle of gas jet-agitated reactors. Computational fluid dynamics calculations showed that the penetration of the laminar jets is confined to a small region close to the inlet nozzles, meaning that convective mass transport is insignificant. At the low pressures employed, however, mixing on reactor scale is almost completely determined by fast molecular diffusion. Micromixing effects on the gas phase reactions are absent, because first order and pseudo-first order reactions dominate the gas phase chemistry. The effectiveness of both heat transport on reactor scale and heat transfer between deposition surface and gas phase is large enough to consider temperature uniformity over the complete reactor. Due to the high surface reaction probability of the gas phase intermediates formed during the pyrolysis of silane, significant mass transfer resistances develop for these species. The shape of the corresponding concentration profiles is a complex function of the Damköhler-II number based on the surface kinetics, and a Thiele modulus based on the gas phase kinetics. Depending on the values of these numbers, the concentration gradients of the gas phase intermediates are located within a few millimeter from the growing silicon layer or throughout the complete reactor: the lower the Damköhler-II number and the higher

the Thiele modulus, the larger the fraction of the gas phase reaction volume with a uniform concentration. As these irreducible concentration gradients have to be accounted for during the regression of the experimental data in order to obtain intrinsic kinetic information from the experiments, a one-dimensional reactor model was developed explicitly accounting for these gradients by considering molecular diffusion with simultaneous gas phase reactions.

Steady state kinetic experiments were performed at total pressures between 25 and 125 Pa, temperatures between 863 and 963 K, and inlet hydrogen-to-silane ratios between 0 and 2. Differential operation with respect to silane conversion and silicon deposition is satisfied up to roughly 912 K and 50 Pa in case pure silane is fed. Cofeeding hydrogen expands the differential operating regime towards higher total pressures and higher temperatures, probably as a result of lowering the silane partial pressure. In addition, it also inhibits the silicon growth as vacant surface sites are covered by hydrogen adatoms and, as a result, silane adsorption is hampered. Partial reaction orders of silane typically range from 0.28 and 0.44, depending on silane space time and feed composition. The apparent activation energy of the deposition process amounts to 155.5 kJ mol^{-1}, indicating that the experiments were conducted in a kinetic regime where hydrogen desorption in particular is important. Departure from differential operation at higher pressures and temperatures can be attributed to the occurrence of gas phase reactions. At total pressures higher than 50 Pa, a maximum is attained in the normalized Si_2H_x concentration versus silane space time. The space time at which the maximum is reached is independent of pressure, whereas the heigth of the maximum increases quadratically with pressure. In addition, with increasing temperature the maximum shifts to shorter space times while increasing in heigth. These trends can be explained qualitatively on the basis of a perfectly stirred tank reactor model and a parallel-consecutive kinetic scheme accounting for silicon deposition from silane and disilane produced during pyrolysis of the former.

The reaction kinetics in the absence of gas phase reactions can be adequately described with a six-step elementary reaction mechanism as determined by modelling of the kinetic experiments in this region. Heterogeneous decomposition of silane occurs via dual-site dissociative adsorption forming a surface trihydride species and a hydrogen adatom, followed by potentially fast decomposition of this trihydride species through dihydride and monohydride species towards solid silicon and three hydrogen adatoms. Regeneration of the partially hydrogenated silicon surface takes place by first order recombinative desorption of molecular hydrogen through excitation of a covalently bound hydrogen adatom from a localized surface Si-H bond to a two-dimensional delocalized state followed by recombination of this excited hydrogen atom with a second localized hydrogen adatom. The only kinetically significant reactions involve the dual-site dissociative adsorption of silane and the first order recombinative

desorption of hydrogen. The involved kinetic and thermodynamic parameters were estimated by means of single-response nonlinear regression.

A four-step elementary gas phase reaction network coupled to a ten-step elementary surface reaction network, the latter based on the above mentioned six-step mechanism, allows to describe the experimental observations in the presence of gas phase reactions as well. The gas phase reactions involve dissociation of silane into silylene and hydrogen, formation of disilane from silane and silylene, subsequent decomposition of disilane into silylsilylene and hydrogen, and isomerization of silylsilylene towards disilene. Rice-Ramsperger-Kassel-Marcus (RRKM) calculations showed that none of these reversible reactions is in its high-pressure limit and that pressure fall-off effects have to be accounted for explicitly. The surface reactions involve dual-site adsorption of silane, silylsilylene and disilene, single-site adsorption of silylene and disilane, subsequent decomposition of the formed surface silicon hydride species, and adsorption/ desorption of hydrogen. The kinetic parameters of the most important reactions, as identified by sensitivity analysis, were estimated by means of multi-response nonlinear regression.

Deposition path analyses performed for the laboratory reactor in the complete range of experimental conditions considered revealed that silylene and disilane are by far the most important gas phase intermediates, with a contribution to the silicon growth rate up to roughly 40% depending on space time and total pressure applied. Silylene is almost completely formed through gas phase decomposition of silane. Formation of silylene through gas phase decomposition of disilane is in general less important. Consumption of silylene takes place through surface decomposition into solid silicon and molecular hydrogen, and via insertion into silane. The latter reaction fully accounts for the production of disilane. Consumption of disilane on the other hand takes place via surface decomposition into solid silicon, molecular hydrogen and silane, and to a lesser extent via gas phase decomposition into silylsilylene and hydrogen. The relative importance of gas phase intermediates for the silicon deposition process decreases with increasing silane space time and decreasing total pressure, and is independent of temperature.

The developed kinetic model allows to simulate silicon growth rate data obtained in a conventional hot-wall multiwafer LPCVD reactor without adjustment of any kinetic parameter. The validity of both a one-dimensional two-zone reactor model and a fully two-dimensional reactor model was tested. The former consists of two sets of one-dimensional continuity equations for all gas phase components: one set allows to calculate the concentration profiles along the axial coordinate in the annular zone, while the other set allows to calculate the concentration profiles along the radial coordinate in the interwafer zone. Coupling between both sets is accomplished by the boundary conditions at the wafer edges. The fully two-dimensional reactor model

follows from the straightforward application of the conservation laws of mass, momentum and energy. Calculations with the latter revealed significant concentration gradients for the homogeneously formed gas phase intermediates in both the axial direction of the interwafer zone and the radial direction of the annular zone. Although the one-dimensional two-zone reactor model does not account for these concentration gradients, silicon growth rates calculated using this strongly simplified reactor model do not essentially differ from those calculated on the basis of a fully two-dimensional reactor model. Even under conditions where 20% of the silicon growth originates from reactive gas phase intermediates such as silylene and disilane, a one-dimensional two-zone reactor model is sufficient to adequately describe silicon growth rate data obtained in such a reactor.

Once validated, the one-dimensional two-zone reactor model was used to provide insights in the effects of typical operating conditions such as interwafer spacing and reactor tube radius on the interaction between the chemical reaction kinetics and the mass transport phenomena in an industrial-scale LPCVD reactor. Simulations showed that the radial growth rate non-uniformity across a wafer is completely determined by the radial variations in the growth rates from silylene and disilane. These species are the most important gas phase intermediates with a contribution to the silicon growth rate of typically 1 to 5% at industrially relevant operating conditions. Due to the high reactivity of silylene and disilane on the surface and/or in the gas phase significant concentration gradients for these species develop in the radial direction between successive wafers. With increasing reactor tube radius, i.e. with decreasing surface-to-volume ratio of the annular zone, the radial growth rate non-uniformity increases significantly due to the higher concentrations of silylene and disilane formed in this zone. The effect of interwafer spacing on radial growth rate non-uniformity is less pronounced.

Besides the above mentioned steady state experiments, transient response experiments using the Temporal Analysis of Products (TAP) technique were conducted as well. By quantitative modelling of silane experiments performed on polycrystalline silicon at temperatures roughly coinciding with those applied in the laboratory reactor additional evidence was obtained for the correctness of the six-step mechanism derived for polysilicon deposition in the absence of gas phase reactions.

SAMENVATTING

Om inzicht te verkrijgen in het complexe samenspel van gasfase- en oppervlakreacties tijdens de low-pressure chemical vapour deposition (LPCVD) van polykristallijn silicium, werd dit proces onderworpen aan een uitgebreid kinetisch onderzoek. De nadruk werd hierbij gelegd op de ontwikkeling van intrinsiek kinetische modellen, die een quantitatieve beschrijving van de experimentele waarnemingen mogelijk maken zowel in afwezigheid als in aanwezigheid van gasfasereacties. Behalve klassieke stationaire experimenten werden ook transiënte responsexperimenten uitgevoerd. Het ontwikkelde kinetische model werd vervolgens gebruikt voor het ontwerp en de analyse van een hete-wand multiwafer LPCVD-reactor op industriële schaal.

Een continu doorstroomde laboratoriumreactor werd ontworpen, gebaseerd op het principe van gas jet-geroerde reactoren. Computational fluid dynamics berekeningen lieten zien dat de penetratie van de laminaire jets beperkt blijft tot een klein gebied dichtbij de inlaatnozzles, hetgeen betekent dat convectief massatransport irrelevant is. Echter, bij de toegepaste lage drukken wordt menging op reactorschaal bijna volledig bepaald door snelle moleculaire diffusie. Micromengeffecten op de gasfasereacties zijn afwezig, omdat eerste orde en pseudo-eerste orde reacties de gasfasechemie domineren. De effectiviteit van zowel het warmtetransport op reactorschaal als de warmte-overdracht tussen depositie-oppervlak en gasfase is groot genoeg om temperatuuruniformiteit over de gehele reactor te veronderstellen. Door de hoge oppervlakreactiewaarschijnlijkheid van de gasfase-intermediairen, die gevormd worden tijdens de pyrolyse van silaan, ontstaan significante massa-overdrachtsweerstanden voor deze componenten. De vorm van de bijbehorende concentratieprofielen is een complexe functie van het Damköhler II getal, gebaseerd op de oppervlakkinetiek, en een Thiele modulus, gebaseerd op de gasfasekinetiek. Afhankelijk van de waarden van deze kengetallen zijn de concentratiegradiënten van de gasfase-intermediairen aanwezig over een paar millimeter vanaf de groeiende siliciumlaag of doorheen de gehele reactor: hoe lager het Damköhler II getal en hoe hoger de Thiele modulus, des te groter de fractie van het gasfasereactievolume met een uniforme concentratie. Aangezien deze concentratiegradiënten in rekening moeten worden gebracht tijdens de regressie van de experimentele data om zo intrinsiek kinetische informatie uit de experimenten te kunnen halen, werd een één-dimensionaal reactormodel ontwikkeld, dat expliciet rekening houdt met deze gradiënten door moleculaire diffusie met simultane gasfasereacties te beschouwen.

Stationaire kinetische experimenten werden uitgevoerd bij totaaldrukken van 25 tot 125 Pa, temperaturen tussen 863 en 963 K, en waterstof-silaan inlaatverhoudingen tussen 0 en 2. Aan differentieel bedrijf met betrekking tot silaanconversie en siliciumdepositie wordt voldaan tot ruwweg 912 K en 50 Pa in geval zuiver silaan wordt gevoed. Het toevoegen van waterstof aan de voeding vergroot het regime van differentieel bedrijf richting hogere totaaldrukken en hogere temperaturen, waarschijnlijk als een gevolg van het verlagen van de partiaaldruk van silaan. Daarnaast remt het ook de siliciumgroei, omdat vrije oppervlakplaatsen bedekt worden door waterstofadatomen en dientengevolge de adsorptie van silaan belemmerd wordt. Partiële reactie-ordes van silaan variëren tussen 0.28 en 0.44, afhankelijk van de ruimtetijd van silaan en de voedingssamenstelling. De schijnbare activeringsenergie van het depositieproces bedraagt 155.5 kJ mol^{-1}, hetgeen aangeeft dat de experimenten werden uitgevoerd in een kinetisch regime waar waterstofdesorptie vooral van belang is. Afwijking van differentieel bedrijf bij hogere totaaldrukken en temperaturen kan worden toegeschreven aan het optreden van gasfasereacties. Bij totaaldrukken hoger dan 50 Pa wordt een maximum verkregen in de genormaliseerde Si_2H_x-concentratie versus de ruimtetijd van silaan. De ruimtetijd waarbij het maximum bereikt wordt is onafhankelijk van de druk, terwijl de hoogte van het maximum quadratisch toeneemt met de druk. Verder schuift het maximum met toenemende temperatuur naar kortere ruimtetijden, terwijl het toeneemt in hoogte. Deze trends kunnen qualitatief verklaard worden op basis van een model voor een perfect gemengde reactor en een parallel-consecutief kinetisch schema dat rekening houdt met siliciumdepositie vanuit silaan en vanuit disilaan, gevormd tijdens de pyrolyse van de eerste.

In afwezigheid van gasfasereacties kan de reactiekinetiek goed beschreven worden met een zes-staps elementair reactiemechanisme, zoals bepaald via modellering van de kinetische experimenten in dit gebied. De heterogene ontleding van silaan vindt plaats via dissociatieve adsorptie op twee naburige vrije sites waarbij een trihydride en een waterstofadatoom gevormd worden, gevolgd door potentieel snelle ontleding van dit trihydride via een dihydride en een monohydride naar vast silicium en drie waterstofadatomen. De regeneratie van het gedeeltelijk gehydrogeneerde siliciumoppervlak treedt op via eerste orde recombinatieve desorptie van moleculaire waterstof door excitatie van een covalent gebonden waterstofadatoom vanuit een gelocaliseerde oppervlak Si-H binding naar een twee-dimensionale gedelocaliseerde toestand, gevolgd door recombinatie van dit geëxciteerde waterstofatoom met een tweede gelocaliseerd waterstofadatoom. De enige kinetisch significante reacties betreffen de dissociatieve adsorptie van silaan op twee naburige vrije sites en de eerste orde recombinatieve desorptie van waterstof. De betrokken kinetische en thermodynamische parameters werden geschat middels niet-lineaire enkelvoudige respons regressie.

Een vier-staps elementair gasfasereactienetwerk gekoppeld aan een tien-staps elementair oppervlakreactienetwerk, dit laatste gebaseerd op het bovenvermelde zes-staps mechanisme, maakt het mogelijk ook de experimentele waarnemingen in aanwezigheid van gasfasereacties te beschrijven. De gasfasereacties betreffen de dissociatie van silaan in silyleen en waterstof, de vorming van disilaan uit silaan en silyleen, de daaropvolgende ontleding van disilaan in silylsilyleen en waterstof, en de isomerisatie van silylsilyleen tot disileen. Rice-Ramsperger-Kassel-Marcus (RRKM) berekeningen lieten zien dat geen van deze reversibele reacties zich in de hoge-druk limiet afspeelt en dat drukafhankelijkheidseffecten expliciet dienen te worden meegenomen. De oppervlakreacties betreffen de adsorptie van silaan, silylsilyleen en disileen op twee naburige vrije sites, de adsorptie van silyleen en disilaan op één vrije site, de daaropvolgende ontleding van de op het oppervlak gevormde silicium-hydrides, en de adsorptie/ desorptie van waterstof. De kinetische parameters van de belangrijkste reacties, zoals bepaald via gevoeligheidsanalyses, werden geschat middels niet-lineaire meervoudige respons regressie.

Depositiepadanalyses, uitgevoerd voor de laboratoriumreactor in het gehele bereik van beschouwde experimentele condities, wezen uit dat silyleen en disilaan verreweg de belangrijkste gasfase-intermediairen zijn, met een bijdrage aan de siliciumgroeisnelheid tot ruwweg 40% afhankelijk van de toegepaste ruimtetijd en totaaldruk. Silyleen wordt bijna volledig gevormd door ontleding van silaan in de gasfase. Vorming van silyleen via ontleding van disilaan in de gasfase is in het algemeen van minder belang. Consumptie van silyleen vindt plaats door ontleding in vast silicium en moleculaire waterstof, en via insertie in silaan in de gasfase. Deze laatste reactie neemt volledig de vorming van disilaan voor zijn rekening. Consumptie van disilaan vindt aan de andere kant plaats via ontleding in vast silicium, moleculaire waterstof en silaan, en in mindere mate via ontleding in silylsilyleen en waterstof in de gasfase. Het relatieve belang van gasfase-intermediairen voor het siliciumdepositieproces neemt af met toenemende ruimtetijd van silaan en afnemende totaaldruk, en is onafhankelijk van de temperatuur.

Met het ontwikkelde kinetische model is het mogelijk om siliciumgroeisnelheidsdata, verkregen in een conventionele hete-wand multiwafer LPCVD-reactor, te simuleren zonder aanpassing van enige kinetische parameter. De geldigheid van zowel een één-dimensionaal twee-zone reactormodel als een volledig twee-dimensionaal reactormodel werd getoetst. Het eerste model bestaat uit twee sets één-dimensionale continuïteitsvergelijkingen voor alle gasfasecomponenten: één set laat toe de concentratieprofielen langs de axiale coördinaat in de annulaire zone te berekenen, terwijl de andere set toelaat de concentratieprofielen te berekenen langs de radiale coördinaat in de plakkenzone. Koppeling tussen beide sets wordt tot stand gebracht door de randvoorwaarden op de randen van de plakken. Het volledig tweedimensionale reactormodel volgt uit de rechtstreekse toepassing van de behoudswetten van massa, moment en energie. Berekeningen met het laatste model leverden voor de homogeen gevormde gasfase-intermediairen significante concentratiegradiënten op in zowel de axiale richting van de plakkenzone als de radiale richting van de annulaire zone. Ofschoon het één-dimensionale twee-zone reactormodel geen rekening houdt met deze concentratiegradiënten, zijn de siliciumgroeisnelheden berekend met dit sterk vereenvoudigde reactormodel niet essentieel verschillend van die berekend op basis van het volledig twee-dimensionale reactormodel. Zelfs onder condities waarbij 20% van de siliciumgroei afkomstig is van reactieve gasfase-intermediairen zoals silyleen en disilaan, is een één-dimensionaal twee-zone reactormodel voldoende voor het adequaat kunnen beschrijven van de siliciumgroeisnelheidsdata.

Eenmaal getoetst werd het één-dimensionale twee-zone reactormodel gebruikt om inzicht te verwerven in de effecten van typische bedrijfscondities zoals de afstand tussen de plakken en de straal van de reactorbuis op de interactie tussen de chemische reactiekinetiek en de massatransportverschijnselen in een industriëleschaal LPCVD-reactor. Simulaties lieten zien dat de radiale niet-uniformiteit in de groeisnelheid over een plak volledig bepaald wordt door de radiale variaties in de groeisnelheden van silyleen en disilaan. Deze componenten zijn de belangrijkste gasfase-intermediairen, met een bijdrage aan de siliciumgroeisnelheid van typisch 1 tot 5% onder industrieel relevante bedrijfscondities. Door de hoge reactiviteit van silyleen en disilaan aan het oppervlak en/of in de gasfase ontstaan in de radiale richting tussen opeenvolgende plakken significante concentratiegradiënten voor deze componenten. Met toenemende reactorbuisstraal, d.w.z. met afnemende oppervlak-volume verhouding van de annulaire zone, neemt, als gevolg van de hogere concentraties van silyleen en disilaan in deze zone, de radiale niet-uniformiteit in de groeisnelheid aanzienlijk toe. Het effect van de afstand tussen de plakken op de radiale niet-uniformiteit in de groeisnelheid is veel minder uitgesproken.

Buiten de bovenvermelde stationaire experimenten werden ook transiënte responsexperimenten uitgevoerd, gebruikmakende van de Temporal Analysis of Products (TAP) techniek. Door het quantitatief modelleren van silaanexperimenten, uitgevoerd op polykristallijn silicium bij temperaturen die ruwweg samenvallen met die toegepast in de laboratoriumreactor, werd aanvullend bewijs verkregen voor de juistheid van het zes-staps mechanisme, dat afgeleid werd voor de depositie van polysilicium in afwezigheid van gasfasereacties.

CONTENTS

5 KINETICS IN THE PRESENCE OF GAS PHASE REACTIONS 119

6 LPCVD REACTOR MODELLING AND SIMULATION 177

NOTATION

Roman symbols

a	Whitten-Rabinovitch's correction factor	
a_v	specific surface area	$m_s^2\ m_r^{-3}$
A	pre-exponential factor	reaction dep.
A	affinity	$J\ mol^{-1}$
A	geometric surface area	m^2
A	matrix used during orthogonal collocation	
A_d	total deposition surface area	m^2
A_s	cross section area	m_r^2
b	parameter or parameter estimate	
B	matrix used during orthogonal collocation	
B_1	pressure correction constant for fall-off of unimolecular reaction rate coefficient	
B_2	pressure correction constant for fall-off of unimolecular reaction rate coefficient	$J\ mol^{-1}$
B_3	pressure correction constant for fall-off of unimolecular reaction rate coefficient	$J\ mol^{-1}$
c	collocation point c	
calc	calculated	
c_p	specific heat capacity at constant pressure	$J\ kg^{-1}\ K^{-1}$
C	concentration	$mol\ m^{-3}$ or $mol\ m_g^{-3}$
C	matrix used during orthogonal collocation	
C_i	absolute calibration factor of component i	$mol\ C^{-1}$

d	diameter	m
d	characteristic dimension	m
d	vector used during orthogonal collocation	
D	bond strength	$J\ mol^{-1}$
D	matrix used during orthogonal collocation	
$D_{eff,i}$	effective diffusion coefficient of component i	$m_g^3\ m_r^{-1}\ s^{-1}$
$D_{i,j}$	molecular diffusion coefficient of i in a binary mixture of i and j	$m^2\ s^{-1}$
$D_{i,m}$	effective molecular diffusion coefficient of i in a multicomponent mixture	$m^2\ s^{-1}$
$D^K_{eff,i}$	effective Knudsen diffusion coefficient of component i	$m_g^3\ m_r^{-1}\ s^{-1}$
D^K_i	Knudsen diffusion coefficient of component i	$m_g^2\ s^{-1}$
E	energy	$J\ mol^{-1}$
E	residence time distribution	
E_a	Arrhenius activation energy	$J\ mol^{-1}$
$<\Delta E_J>$	average rotational energy of energized molecule	$J\ mol^{-1}$
E_z	zero-point energy	$J\ mol^{-1}$
E_0	critical energy	$J\ mol^{-1}$
f	vector used in quadrature formula	
$f_1(w/h)$	correction function for Knudsen diffusion coefficient	
$f_2(h/L)$	correction function for Knudsen diffusion coefficient	
F	ratio of the mean regression sum of squares to the mean residual sum of squares	
F	molar flow rate	$mol\ s^{-1}$
F	correction factor for adiabatic rotations	
$\bar{F}$	Laplace transform of the molar flow rate	$mol\ s^{-1}$
F_v	volumetric flow rate	$m^3\ s^{-1}$
g	gravity	$m\ s^{-2}$
G	Gibbs energy	$J\ mol^{-1}$
$G_{i/j}$	relative sensitivity factor of i with respect to j	
G_{Si}	silicon deposition rate or growth rate	$kg\ s^{-1}$
Gr_{Si}	silicon deposition rate or growth rate	$mol\ m^{-2}\ s^{-1}$
h	distance between wafers	$m_r^2\ m_g^{-1}$
h	Planck constant (= $6.6262\ 10^{-34}$)	$J\ s$

H^e	delocalized hydrogen atom	
$\Delta_a H$	adsorption enthalpy	J mol^{-1}
$\Delta_r H$	reaction enthalpy	J mol^{-1}
$\Delta^{\neq} H$	activation enthalpy	J mol^{-1}
I	intensity	arbitrary units
I	electric current	C s^{-1}
I_0	modified Bessel function of first kind and order zero	
j	diffusive mass flux	kg m^{-2} s^{-1}
k	Boltzmann constant (= 1.3807 10^{-23})	J K^{-1}
k	reaction rate coefficient	reaction dep.
k	summation index	
k_a	effective reaction rate coefficient for formation of activated complexes from energized molecules	s^{-1}
k_r	(pseudo-)first order reaction rate coefficient	s^{-1}
K	equilibrium coefficient	reaction dep.
K_0	modified Bessel function of second kind and order zero	
l	length scale	m
$\bar{l}_m$	mean free path length	m
L	surface concentration	mol m^{-2}
L	length	m or m_r
L_t	total surface concentration of active sites available for adsorption or reaction	mol m^{-2} or mol m_s^{-2}
$L^{\neq}$	reaction path degeneracy	
m	reaction order	
m	molecular mass	kg
M	molar mass	kg mol^{-1}
M	collision partner or third body	
M	number of interior collocation points	
n	number of observations	
n	reaction order	
n_i	number of silicon atoms in component i	
ng	number of gas phase reaction steps	
ns	number of surface reaction steps	
N	molar flux with respect to fixed coordinates	mol m^{-2} s^{-1}
N	number of interior collocation points	

N_{av}	constant of Avogadro (= 6.023 10^{23})	mol^{-1}
N_p	inlet pulse size	mol
N(E)	density of quantum states at energies close to E	mol J^{-1}
NG	number of gas phase components	
NRWF	total number of silicon wafers	
NS	number of surface components	
obs	experimentally observed	
p	number of parameters	
p	pressure	Pa
Δp	pressure difference	Pa
$p_{1/2}$	transition pressure	Pa
P(E)	number of quantum states with energy equal to E	
P_m	polynomial with highest power m	
Q	volumetric flow rate at standard conditions	Nml min^{-1}
Q	matrix used during orthogonal collocation	
Q	ratio of TAP signal surface areas with and without reaction	
Q_1	partition function for adiabatic rotations in reactant molecule	
Q_1^+	partition function for adiabatic rotations in activated complex	
Q_2	partition function for all active modes of reactant molecule	
Q_2^*	partition function of energized molecule using ground state of reactant molecule as zero of energy	
r	reaction rate	reaction dep.
r	radial coordinate	m
r	number of active rotational degrees of freedom	
r_v	volumetric reaction rate	mol m^{-3} s^{-1}
r_a	areal reaction rate	mol m^{-2} s^{-1}
R	gas constant (= 8.3144)	J mol^{-1} K^{-1}
R	radius	m
R_{Si}	silicon deposition rate or growth rate	m s^{-1}
RT	thermal molar energy	J mol^{-1}
R_0	inner radius used in reactor model	m

R_1	outer radius used in reactor model	m
s	estimated standard deviation	
s	sticking probability	
s	number of active vibrational degrees of freedom	
s	Laplace transform variable with respect to dimensionless time	
S	entropy	J mol^{-1} K^{-1}
S(b)	objective function	
$S_{i,j}$	selectivity to i with respect to feed j	
$S_{Si_2H_x}$	selectivity towards Si_2H_x	
S_2H_x	all gas phase components containing two silicon atoms	
$\Delta_a S$	adsorption entropy	J mol^{-1} K^{-1}
$\Delta_r S$	reaction entropy	J mol^{-1} K^{-1}
$\Delta^{\neq} S$	activation entropy	J mol^{-1} K^{-1}
t	t-value	
t	time	s
Δt	time interval	s
$t(n\text{-}p,1\text{-}\alpha/2)$	tabulated $\alpha/2$-percentage point of the t-distribution with n-p degrees of freedom	
t_0	delay time	s
T	temperature	K
u	molar average velocity	m s^{-1}
$\mathbf{u}$	mass average velocity	m s^{-1}
u_l	sonic velocity	m s^{-1}
v	number of responses	
V	geometric volume	m^3
V_g	gas phase reaction volume	m^3
w	width of wafer	m_r
$w_{\alpha\alpha}$	weighting factor	
$W_{1/2}$	width at half-height	s
x	energy associated with translational motion along reaction coordinate	J mol^{-1}
x	axial coordinate	m or m_r
Δx	distance between two grid points along axial coordinate	m_r
X_i	conversion of component i	
y	molar fraction	

y	radial coordinate	m
Y	response	
z	coordination number	
z	axial coordinate	m
z	dimensionless axial coordinate	
Z	collision factor	$m^3\ mol^{-1}\ s^{-1}$

Greek symbols

α	heat transfer coefficient	$W\ m^{-2}\ K^{-1}$
α	boat area/tube area	
β	parameter	
γ	reaction probability	
γ	fugacity coefficient	
δ	diffusion layer thickness	m
δ_x	delta-function with respect to axial coordinate	m_r^{-1}
δ_ζ	delta-function with respect to dimensionless axial coordinate	
Δ	interwafer spacing	m
ϵ	power input rate per unit mass of fluid	$W\ kg^{-1}$
ε	porosity	$m_g^3\ m_r^{-3}$
ζ	dimensionless axial coordinate	
θ	angle coordinate	
θ	fractional surface coverage	
$\hat{\theta}$	fraction of vacant surface sites available for adsorption at beginning of experiment	
λ	collisional deactivation efficiency	
λ	Lagrangian multiplier	
λ	thermal conductivity	$W\ m^{-1}\ K^{-1}$
μ	dynamic viscosity	$kg\ m^{-1}\ s^{-1}$
ν	kinematic viscosity	$m^2\ s^{-1}$
ν	stoichiometric coefficient	
ξ	dimensionless radial coordinate	
π	constant (= 3.1415927)	
ρ	density	$kg\ m^{-3}$
σ	stoichiometric number	
σ_{hk}	element of the inverse of the error variance-	

	covariance matrix	
τ	mean residence time	s
τ	characteristic time	s
τ	dimensionless time	
τ	viscous stress	$N\ m^{-2}$
τ	tortuosity	$m_g^2\ m_r^{-2}$
τ_1	pulse width	s
τ_r	repetition time	s
τ_{res}	mean residence time	s
ϕ	Thiele modulus	
ϕ	angle coordinate	
Φ	contribution factor	
Ψ	sensitivity factor	
ω	mass fraction	

Dimensionless groups

Damköhler-I	Da_I	$= k_r\ d\ u^{-1}$
Damköhler-II	Da_{II}	$= k_r\ d^2\ D^{-1}$
Knudsen	Kn	$= \bar{l}_m\ d^{-1}$
Mach	Ma	$= u\ u_l^{-1}$
Nusselt heat transfer	Nu	$= \alpha\ d\ \lambda^{-1}$
Peclet mass transfer	Pe	$= u\ d\ D^{-1}$
Reynolds	Re	$= \rho\ u\ d\ \mu^{-1}$
Thiele modulus	ϕ	$= d\ k_r^{1/2}\ D^{-1/2}$

Superscripts

a	annular region
d	disappearance
f	formation
norm	normalized
SSA	steady state approximation
T	transposed
w	wall
w	interwafer region
—	average

0	centre
0	standard
0	initial
+	activated complex
^	calculated
*	energized molecule
/	reparameterized
$\rightarrow$	forward
$\leftarrow$	backward

Subscripts

a	adsorption
a	adsorbed state
a	areal
ads	adsorption
bim	bimolecular
d	desorption
des	desorption
e	thermal excitation
eff	effective
f	formation
g	gas phase
g	gas phase reaction
gas	gas phase reaction
h	response
i	gas phase component
i	observation
in	inlet
ins	insertion
j	gas phase component
k	gas phase reaction
k	response
k	element
l	surface component
low	lower bound
m	micromixing
m	surface reaction

max	maximum
M	collision partner or third body
n	nozzle
QMS	quadrupole mass spectrometer
r	reaction
r	rotational
r	in the r-direction
reac	reaction
s	stack
s	surface
sam	sample
sur	surface reaction
Si	silicon
t	total
t	reactor tube
uni	unimolecular
up	upper bound
v	vibrational
v	volumetric
vr	vibrational-rotational
w	wafer
z	in the z-direction
0	inlet
0	initial
0	low pressure limit
∞	high pressure limit
*	vacant site

1

INTRODUCTION

Chemical vapour deposition (CVD), the process of synthesizing solid layers from the gaseous phase by chemical reactions, has expanded into a multitude of advanced materials applications, including microelectronics, optoelectronics, protective and optical coatings.

Knowledge of the relation between layer deposition rate, uniformity, composition, conformity and interface abruptness on one hand and reactor geometry and process conditions on the other is a prerequisite for the production of high quality materials. Reactor operation generally relies on semi-empirical correlations and on operating regions selected on the basis of trial and error experimentation. Major drawbacks of such an approach are the lack of flexibility as operating demands change and the limitation of new reactor designs to the proven operating regions of already existing reactors.

Although the development of new CVD processes and reactors is still largely based on the accumulated empirical experience and step-by-step improvement by methods of trial and error, the need for mathematical models, describing the relevant physical and chemical processes in detail, has been recognized. In the last two decades CVD models have evolved from simple analytical models to advanced numerical computer codes, which allow a fully three-dimensional description of the hydrodynamics and the use of multi-step chemical reaction mechanisms. Such models can be used as an aid in reactor design and process optimization, allowing a great saving in the costly and time consuming development and step-by-step improvement of reactor prototypes and process conditions. In addition, these mathematical models can provide fundamental insights in the underlying physical and chemical processes.

Despite the essential role of kinetic rate data in CVD reactor modelling, detailed kinetic studies are very scarce. Reaction data have traditionally been reported in terms of growth rates and their dependence on temperature. Such data are generally disguised by mass transport effects and thus not suitable for reactor design and process optimization. Therefore, detailed mechanistic investigations are recently more and more preferred to the traditional macroscopic deposition studies.

In light of the previous discussion the present thesis is aimed at the development of a comprehensive kinetic model for the low pressure CVD (LPCVD) of polycrystalline silicon and its application in reactor modelling. The deposition occurs from silane at industrially relevant operating conditions, i.e. total pressures around 50 Pa and temperatures close to 900 K. Polycrystalline silicon, commonly referred to as polysilicon, plays a key role in the manufacturing of so-called very large and ultra large scale integration circuits. The most common reactor used for the deposition of polycrystalline silicon is the horizontal hot-wall multiwafer LPCVD reactor. For an extensive overview of the scientific aspects of this CVD process the reader is referred to the literature (Hess *et al.*, 1985; Jensen, 1987; Jasinski *et al.*, 1987; Roenigk, 1987; Kamins, 1988; Hitchman and Jensen, 1993).

The kinetic model is obtained by quantitative modelling of well-defined steady state kinetic experiments performed in a laboratory microbalance reactor, both in the absence and in the presence of gas phase reactions. It provides valuable information on the complex interplay between the gas phase and surface reactions and is used for the design and analysis of an industrial-scale hot-wall multiwafer LPCVD reactor. Besides the above mentioned steady state experiments, transient response kinetic experiments using the Temporal Analysis of Products (TAP) technique (Gleaves *et al.*, 1988; Huinink, 1995) are conducted and evaluated as an alternative approach for investigating the reaction kinetics of the low pressure CVD of polycrystalline silicon. In comparison to steady state experiments extra information is gained due to the time-resolved observations, which allow in principle better discrimination between alternative kinetic models, as well as estimations of the reaction rate coefficients of the individual elementary steps.

Chapter 2 describes the laboratory reactor setup and the mathematical modelling of the experimental data. Furthermore, a thorough examination is performed of the mass and heat transport phenomena inside this reactor, leading to the development of an appropriate reactor model.

Chapter 3 describes the observed effects of the process conditions on the silicon growth rates and gas phase compositions. An important topic concerns the interplay between gas phase and surface reactions as a function of these process conditions.

Chapter 4 reports on the kinetics of silicon deposition in the absence of gas phase reactions.

In Chapter 5 the kinetics of silicon deposition in the presence of gas phase reactions are discussed. The developed kinetic model allows a quantitative description of the observed effects of the process conditions and provides valuable information on the relative importance of gas phase reactions.

Chapter 6 reports on the degree of sophistication needed in the modelling of LPCVD reactors for polysilicon deposition. Therefore, the validity of a one-dimensional two-zone and a fully two-dimensional reactor model is tested by comparing their predictions with experimental growth rate data obtained in such a reactor. Once validated, the developed one-dimensional model is used to provide fundamental insights in the effects of typical operating conditions on the interaction between the chemical reaction kinetics and the mass transport phenomena in an industrial-scale LPCVD reactor.

In Chapter 7 the Temporal Analysis of Products (TAP) technique (Gleaves *et al.*, 1988; Huinink, 1995) is applied to provide direct information about the kinetics of the adsorption and subsequent surface reactions of silane, disilane and trisilane.

References

Gleaves, J.T., Ebner, J.R., Kuechler, T.C., 1988, *Catal. Rev.-Sci. Eng.*, **30**(1), 49.

Hess, D.W., Jensen, K.F., Anderson, T.J., 1985, *Reviews in Chem. Eng.*, **3**(2), 97.

Hitchman, M.L., Jensen, K.F., 1993, Chemical Vapor Deposition, Academic Press, London.

Huinink, J.P., 1995, A Quantitative Analysis of Transient Kinetic Experiments: The Oxidation of CO by O_2/NO on Pt, Thesis TUE, Eindhoven.

Jasinski, J.M., Meyerson, B.S., Scott, B.A., 1987, *Ann. Rev. Phys. Chem.*, **38**, 109.

Jensen, K.F., 1987, *Chem. Eng. Sci.*, **42**(5), 923.

Kamins, T.I., 1988, in Polycrystalline Silicon for Integrated Circuit Applications, Kluwer Academic Publishers, Amsterdam.

Roenigk, K.F., 1987, Analysis of Low Pressure Chemical Vapor Deposition Processes, Thesis University of Minnesota, Minnesota.

2

MICROBALANCE REACTOR SETUP

2.1 Introduction

In order to investigate the kinetics of the low pressure CVD of polycrystalline silicon, a laboratory reactor setup has been designed, suitable for a direct measurement of the silicon growth rate combined with an on-line analysis of the corresponding gas phase composition during continuous flow experiments. The total pressures and temperatures applied are similar to those of conventional hot-wall multiwafer LPCVD reactors, i.e. 10-100 Pa and 850-950 K. Although the applied volumetric flow rates, ranging from 3 to 30 Nml min^{-1}, are much smaller than those usually considered in conventional LPCVD reactors, both reactors operate at about the same mean residence times, i.e. 0.1-1 s.

In this laboratory setup, tube reactor configurations cannot provide for plug flow conditions. The mass Peclet number is typically in the range 0.1-10. Owing to fast molecular diffusion at the low pressures employed, starting from ideal mixing is considered more promising. In order to achieve ideal mixing, the principle of gas jet-agitated reactors was chosen. Gas jet-agitated reactors have been extensively used for the study of both homogeneous and heterogeneous gas-solid reactions (Longwell and Weiss, 1955; Kistiakowsky and Volpi, 1957; Lede and Villermaux, 1977; David and Villermaux, 1973; Patel and Smith, 1975). Temperatures and pressures applied in these kinetic studies cover ranges from 295 to 2000 K and from 2 10^{2} to 10^{5} Pa, while mean residence times vary between 0.1 and 10 s.

In the present chapter the laboratory reactor setup, referred to as the microbalance reactor setup, is treated in detail. Attention is paid to the mathematical modelling of the experimental data. Furthermore, a thorough examination of the mass and heat transport phenomena inside the gas agitated reactor is performed. Absence of concentration and temperature gradients forms an important objective in obtaining intrinsic kinetic rate data, i.e. kinetic rate data not influenced by transport and/or transfer limitations. However, in case such limitations are irreducible, i.e. cannot be eliminated altogether by altering the reactor geometry and/or the operating conditions, they need to be accounted for explicitly during the reactor simulations by the use of an appropriate reactor model. In order to account for the irreducible mass transfer resistances existing for the gas phase intermediates formed during the pyrolysis of silane a reactor model has been developed, which is treated in detail in this chapter as well.

2.2 Equipment and procedures

The microbalance reactor setup, depicted schematically in Appendix 2A, comprises a feed section, a reactor section and an analysis section.

Feed section

In the feed section the gas mixture fed to the reactor is prepared. Silane (ultra-pure quality, Air Products) or disilane (quality 4.0, Air Products) is the main reactant gas. Both gases need to be handled with special care due to pyrophoric behaviour. For this reason an Air Products gas cabinet, especially designed for safely handling silane (disilane), was incorporated in this section. On the flow panel inside this cabinet an excess flow valve and an emergency shut-off valve were mounted. Both valves are able to shut-off the silane flow, the former when a certain preset value (500 Nml min^{-1}) is exceeded, and the latter in case of a signal from the PLC (programmable logical control unit). Other reactant gases are hydrogen and argon. Argon (quality 6.0, Air Products) is used as an inert diluent gas whereas hydrogen (quality 6.0, Air Products) is fed to study inhibition effects on the gas phase and surface kinetics. Argon also serves as internal standard for quantitative analysis of the gas phase composition. Nitrogen (quality 6.0, Air Products) is used as purge gas to protect the electronic part of the microbalance. The flow rates of the process gases (SiH_4, H_2 and Ar) are established with thermal mass flow controllers (Sierra 840D). Typical flow rates are in the range 3-30 Nml min^{-1}.

Reactor section

The reactor section consists of a quartz spherical continuous flow reactor as outlined in Figure 2.1. Spherical geometry was chosen because it favours mixing and uniformity of heat transfer. After premixing, the feed mixture is preheated to overcome intrareactor temperature gradients and injected through the four nozzles of a cross-shaped injector, located in the middle of the reactor. The nozzles are located midway between the centre of the reactor and the wall, in two orthogonal planes. To ensure good mixing, the inner diameters of the reactor, 6.0 10^{-2} m, and the nozzles, 9.0 10^{-4} m, were chosen on the basis of fluid dynamic relations for axial symmetric jets as proposed by David and Matras (1975). The inner diameter of the reactor outlet is 2.2 10^{-2} m. The above reactor configuration permits mean residence times between 0.1 and 1 s at typical LPCVD conditions. In the middle of the reactor, just above the cross-shaped injector, a 10x15 mm^2 sized silicon sample is suspended from a microbalance (Cahn D-200). The silicon sample is cleaved from double-side polished (100) p-type wafer with a resistivity of ~ 0.035 Ω cm and an average thickness of 410 μm. Prior to each series of experiments the silicon sample and reactor wall are precoated with polycrystalline silicon at 50 Pa and 900 K during 30 minutes, after pretreatment with hydrogen at 900 K during 10 minutes.

Both reactor temperature and pressure are regulated to fulfil the need of isothermic and isobaric operating conditions. The reactor is heated using an electrical resistance oven with a heating capacity of 700 W. Temperature regulation is performed on the basis of a chromel-alumel (K-type) thermocouple located between the oven and the reactor wall using a PID controller (Eurotherm 906D). The reaction temperature is measured with a second chromel-alumel thermocouple inside a thermowell located nearby the silicon sample in the centre of the reactor. Substrate temperatures up to 1100 K can be reached in this configuration. Vacuum is maintained by a dual-stage rotary-vane mechanical pump (Leybold D25/BCS). The reactor pressure is regulated via exhaust rate of effluent gases independent of upstream gas flow rates. This is accomplished with the so called gas ballast or gas bypass technique, which involves the injection of nitrogen into the pump throat, thereby forcing the total pressure to the required value (setpoint value). The pressure regulation method comprises an absolute pressure transducer (MKS Baratron 128A), a pressure indicator/controller (MKS PR2000/250C), and a bypass valve (MKS 248A). Pressure setpoint values between 10 and 1 10^3 Pa can be established.

Extensive pumping, while simultaneously outgassing the reactor section by heating the reactor and connected lines, ultimately leads to a pressure increase of 2 10^{-3} Pa min^{-1}, which corresponds to a leak rate of 4 10^{-3} Pa l min^{-1} in the reactor-plus-microbalance volume of roughly 2 l. This leakage produces an impurity flow rate of 4 10^{-5} Nml min^{-1}.

The claimed purity of the feed gases (SiH_4, Ar, H_2, and N_2) implies maximum impurity concentrations - including oxygen and water - of 1 ppm. At typical operating conditions, with total flow rates ranging from 10 to 50 Nml min^{-1}, including the purge gas for the microbalance, these levels give rise to impurity flow rates of 1 10^{-5} to 5 10^{-5} Nml min^{-1}. Hence, the amount of impurities supplied by the feed gases entering the reactor is comparable to that due to leaks.

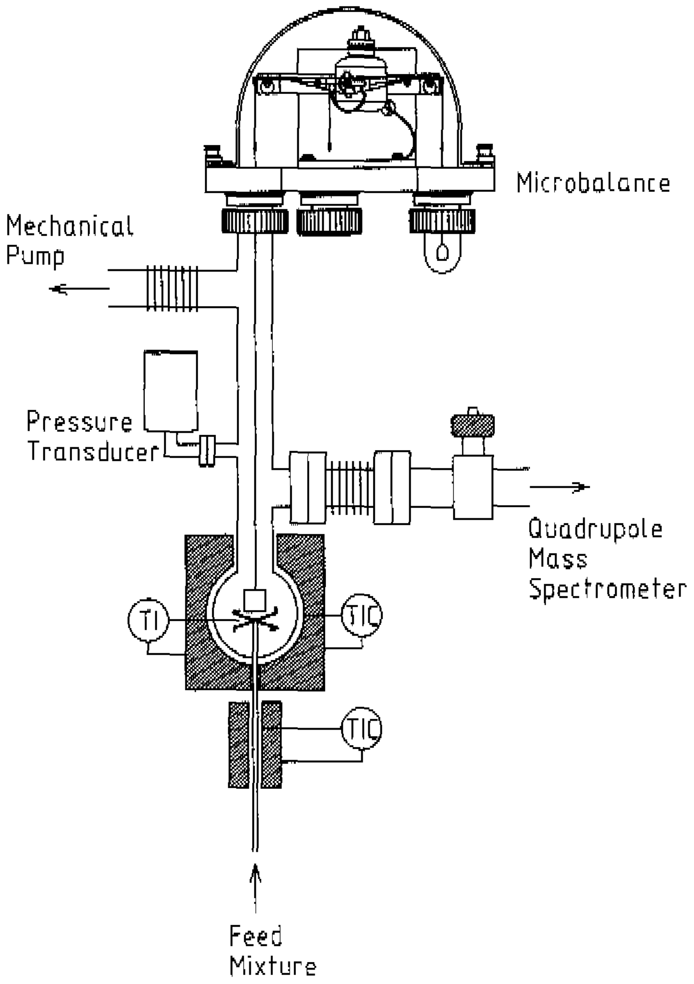

Figure 2.1: Laboratory reactor.

Analysis section

The weight increase due to silicon deposition on the 10x15 mm^2 sized sample in the middle of the reactor is measured with a microbalance (Cahn D-200). The microbalance is operated in the weight range from 0 to 2 mg with a resolution of 0.1 microgram under ideal circumstances. Calibration is performed prior to each series of experiments.

The analysis of the gas mixture is performed with a differentially pumped quadrupole mass spectrometer (Fisons SXP Elite 300H) with a cross beam ion source and a 90° off axis electron multiplier. The detection limit is about 1 ppm. The mass resolution, defined as the full width at halve heigth, amounts to 0.5 AMU. The ionisation energy is kept constant at 70 eV. The high-vacuum inside the analysis chamber is maintained by a turbomolecular pump (Balzers TPU 180H), backed by a diaphragm vacuum pump. The analyser housing allows bake-out to $1\ 10^{-6}$ Pa pressure. Most of the reactor effluent gases are pumped off by the dual-stage rotary-vane mechanical pump (Leybold D25/BCS), and a small fraction reaches the quadrupole mass spectrometer (QMS) through an orifice inlet. All-metal orifices of 20 μm and 10 μm diameter are used.

The quadrupole mass spectrometer is used for the quantitative analysis of silane and Si_2H_x, the latter denoting the total of disilane (Si_2H_6), silylsilylene (H_3SiSiH) and disilene (H_2SiSiH_2). Separate quantitative analysis of these silicon dimers is not possible, because silylsilylene and disilene cannot be calibrated in pure form due to their high reactivity. In addition, the fragmentation patterns of silylsilylene and disilene probably completely overlap with each other and with that of disilane, making a discrimination between these silicon dimers very difficult. Quantitative analysis of hydrogen was considered not accurate enough due to the rather low pumping efficiency for this component.

During the calibration prior to each series of experiments, the relative sensitivity factors of silane and Si_2H_x are determined with respect to the internal standard argon. For this purpose an SiH_4-Si_2H_6-Ar mixture is used. In this way it is implicitly assumed that silylsilylene and disilene possess the same QMS sensitivity as disilane. This assumption is supported by the fact that silylsilylene and disilene are both primary QMS fragmentation products of disilane. It has to be noted that deviations of the QMS sensitivities of silylsilylene and disilene from the QMS sensitivity of disilane probably have no large effect on the final results. From kinetic/reactor modelling studies reported in literature it is known that during silicon deposition at low total pressures silylsilylene and disilene are present in the gas phase in only small amounts compared to disilane (Kleijn, 1991; Becerra and Walsh, 1992).

Figure 2.2 shows the mass spectra of silane and disilane, the latter considered here to be representative for Si_2H_x based on the foregoing points. The silane fragmentation pattern involves one single key fragment, located around the main fragmentation peak at AMU 30, see Figure 2.2a. The disilane fragmentation pattern, which is in good agreement with that published by Simon *et al.* (1992), shows two key fragments, one around AMU 30 and one around the main peak positioned at AMU 60, see Figure 2.2b. The ratio of the intensities around AMU 30 is different from that observed in the silane spectrum. The most important masses of silane are respectively AMU 30 (SiH_2^+), AMU 31 (SiH_3^+), AMU 28 (Si^+) and AMU 29 (SiH^+). The disilane fragmentation pattern shows important peaks in the same region at respectively AMU 29, AMU 31, AMU 28 and AMU 30.

Measurement of the intensities during the calibration as well as during the kinetic experiments takes place at the main peak positions of the species involved. Argon is monitored at AMU 40, silane at AMU 30, and disilane c.q. Si_2H_x at AMU 60. The analysis, however, is complicated by the overlap of the fragmentation patterns of silane and disilane c.q. Si_2H_x at AMU 30. For this reason disilane c.q. Si_2H_x is monitored at AMU 30 as well. The net silane intensity at AMU 30 is now obtained by correcting the overall AMU 30 intensity for the AMU 30 contribution from disilane c.q. Si_2H_x. The latter is obtained by multiplying the measured disilane c.q. Si_2H_x intensity at AMU 60 with the AMU 30/AMU 60 intensity ratio of disilane c.q. Si_2H_x obtained through calibration:

$$(I_{SiH_4})_{30} = (I_t)_{30} - (I_{Si_2H_x})_{60} \left(\frac{(I_{Si_2H_x})_{30}}{(I_{Si_2H_x})_{60}} \right)_{cal} \tag{2.1}$$

with I_i the intensity of component i.

Another complicating factor in the determination of the outlet molar flow rates is the dependency of the QMS sensitivity on the reactor total pressure p_t. In order to account for this pressure dependent behaviour, the intensities of silane, disilane c.q. Si_2H_x and argon are measured as a function of reactor total pressure using the SiH_4-Si_2H_6-Ar calibration mixture. Effects of varying quadrupole settings are eliminated by calibrating the components simultaneously. Influences of the gas phase composition are eliminated by normalizing the intensities to 100% pure component:

$$I_i^{norm} = \frac{p_t}{p_i} I_i \tag{2.2}$$

with I_i^{norm} the normalized intensity of component i. Relative sensitivity factors for silane and disilane c.q. Si_2H_x with respect to the internal standard argon, $G_{i/Ar}$, are then obtained from:

$$G_{i/Ar} = \frac{I_i^{norm}}{I_{Ar}^{norm}} = \frac{a_i + b_i p_t}{a_{Ar} + b_{Ar} p_t} \cong a + b p_t \qquad (2.3)$$

with the parameters a and b obtained by means of linear regression.

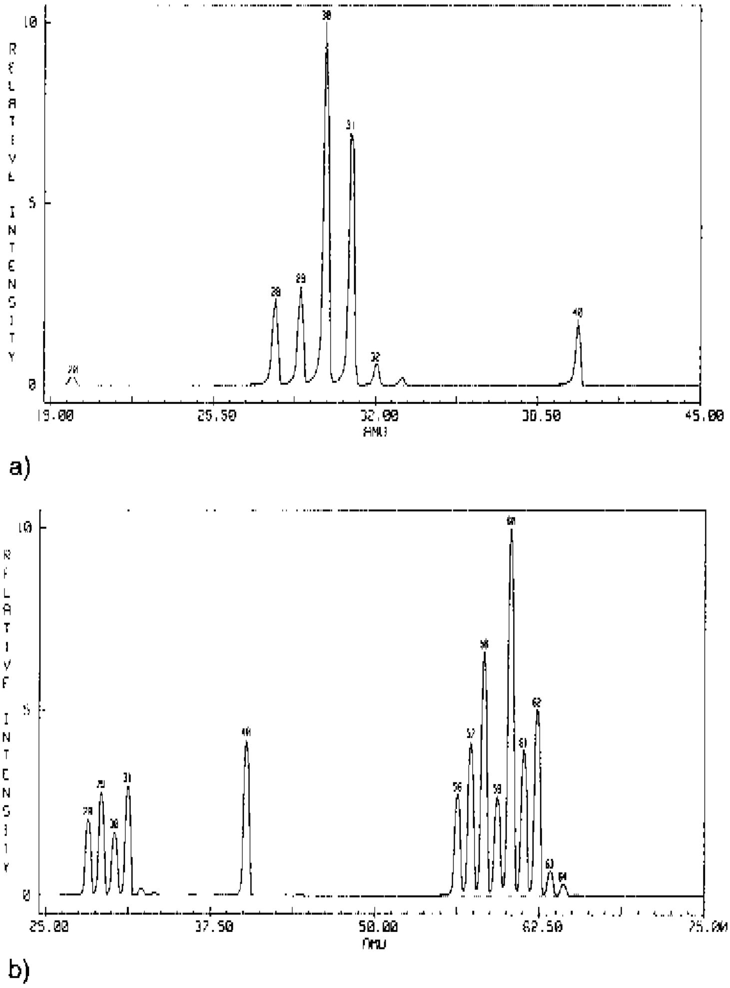

Figure 2.2: *Mass spectra of SiH_4/Ar (a) and Si_2H_6/Ar (b) mixtures (10% Ar) measured at an ionisation energy of 70 eV.*

2.3 Data analysis

The quantitative data analysis is started as soon as steady state conditions are established. At typical operating conditions, steady state conditions are reached after roughly one minute.

Growth rate

The silicon growth rate is determined by linear regression of the measured mass versus time curve. The slope directly yields the growth rate in units kg s^{-1}, G_{Si}. Conversion into units m s^{-1} proceeds through:

$$R_{Si} = \frac{G_{Si}}{\rho_{Si}\, A_{sam}} \tag{2.4}$$

with A_{sam} the geometric surface area of the sample and ρ_{Si} the density of solid silicon, i.e. 2.33 10^3 kg m^{-3}.

Outlet molar flow rates

The outlet molar flow rates of silane and Si_2H_x are calculated according to:

$$F_i = F_{Ar} \frac{1}{G_{i/Ar}} \frac{I_i}{I_{Ar}} \tag{2.5}$$

with F_{Ar} the molar flow rate of the internal standard argon as measured with the thermal mass flow controller of the feed section. The outlet molar flow rate of hydrogen follows from a hydrogen mass balance over the reactor, see paragraph 4.3.1.

Silicon mass balance

The quality of the experimental data is verified by means of a silicon balance between reactor inlet stream and reactor outlet stream plus growth rate:

$$Si\text{-}balance\% = \frac{\frac{\rho_{Si}}{M_{Si}} R_{Si} A_t + \sum n_i F_i}{\sum n_i F_{i,0}}\, 100\% \tag{2.6}$$

with R_{Si} the silicon growth rate in m s^{-1}; A_t the total geometric deposition surface area; M_{Si} the molar mass of solid silicon, i.e. 28.086 10^{-3} kg mol^{-1}; n_i the number of silicon atoms in component i. The inlet molar flow rates are measured with the mass flow controllers. The outlet molar flow rates and silicon growth rate are derived from the mass spectrometric data and microbalance data, respectively. The total geometric deposition surface area is calculated from the geometric surface areas of both silicon sample and reactor wall, and amounts typically to 1.45 10^{-2} m^2. Experiments with a silicon mass balance which deviated more than 5% are rejected.

Space time, conversion and selectivity

The space time of component i is defined as the ratio of the geometric reactor volume to the inlet molar flow rate of component i:

$$\text{Space time}_i = \frac{V}{F_{i,0}} \tag{2.7}$$

The fractional conversion of component i is defined as the ratio of the number of moles of i converted to the number of moles of i fed to the reactor:

$$X_i = \frac{F_{i,0} - F_i}{F_{i,0}} \tag{2.8}$$

The selectivity towards product j is defined as the ratio of the number of moles of silicon atoms in component j formed to the total number of moles of silicon atoms in component i converted:

$$S_{j,i} = \frac{n_j (F_j - F_{j,0})}{n_i (F_{i,0} - F_i)} \tag{2.9}$$

with n_i the number of silicon atoms in reactant i and n_j the number of silicon atoms in product j.

2.4 Mixing performance

In order to carry out reliable kinetic experiments and to clearly delineate the effects of process conditions on the silicon deposition process, it is necessary to obtain the silicon growth rate and the gas phase composition unaffected by transport effects.

2.4.1 Concentration uniformity

With respect to the concentration uniformity inside the laboratory reactor it is necessary to examine the effectiveness of mixing on reactor scale, of micromixing and of gas/solid mass transfer.

Mixing on reactor scale

The analysis which follows provides a description of the extent of reactor scale mixing introduced by the jet motion inside the applied laboratory reactor, see Figure 2.1. In order to reduce the computational complexity from 3D to 2D, two simplifications are made. First, the laboratory reactor is assumed to comprise four equally important regions, each of them encompassing the flow region of a single jet. Second, this model jet is considered straight and spreading out symmetrically about the direction of the inlet nozzles into a cylinder with a diameter equal to the radius of the reactor. With these assumptions the computational problem reduces to the modelling of one single jet in two dimensions. Figure 2.3 illustrates the simplified situation. Pure silane is supplied at pressure $p_{t,0}$ and temperature T_0 through a small tube (d_n= 9 10^{-4} m) at the centre of a larger pipe (d= 3.0 10^{-2} m, L= 4.7 10^{-2} m) open at both ends to silane at operating conditions p_t and T. The length of the pipe is equal to the jet path length. The cylinder walls are considered adiabatic.

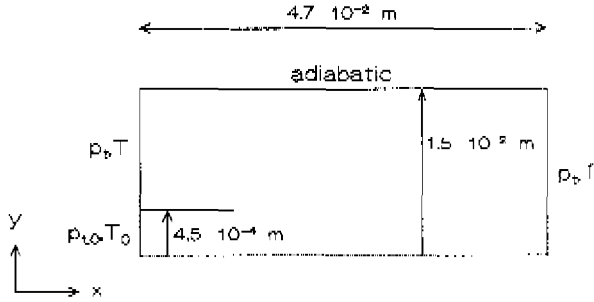

Figure 2.3: Simplified configuration in which the development of a silane jet is simulated.

Based on this configuration, velocity contours were calculated for the operating conditions T= 900 K and p_t= 100 Pa, and mean residence times of 1 s and 0.1 s, corresponding to inlet velocities, u_0, of 44 and 440 m s^{-1}, respectively. Due to the low operating pressure, laminar flow predominates in both situations (Re= 0.5-5).

Moreover, the flow characteristics at the high inlet velocity need to encompass compressibility effects. A generally accepted guideline states that compressibility effects need to be taken into account in case the Mach number (Ma= u_0/u_l) exceeds 0.3. At 900 K and 100 Pa the sonic velocity, u_l, of silane amounts to 509 m s^{-1}. Compressibility effects are therefore important at the inlet velocity of 440 m s^{-1}.

The calculations were performed with a general purpose computer program currently available under the name FLUENT. A detailed description of the theoretical background can be found in the FLUENT User's Manual (1990). The governing partial differential equations expressing the conservation of mass, momentum and energy were integrated together with the appropriate boundary conditions in 2D axisymmetric form using the control volume based finite difference method (Patankar, 1980).

Figure 2.4 shows the axial velocity contours for the underlying situations. At already short distances from the inlet nozzle the axial velocities have decreased drastically compared to the inlet velocities. This considerably reduces the effects normally associated with jets. Since penetration of the jets is confined to a small region close to the inlet nozzle, recirculation of the reactor content is not promoted. In other words, the laminar jets hardly contribute to the mixing on reactor scale.

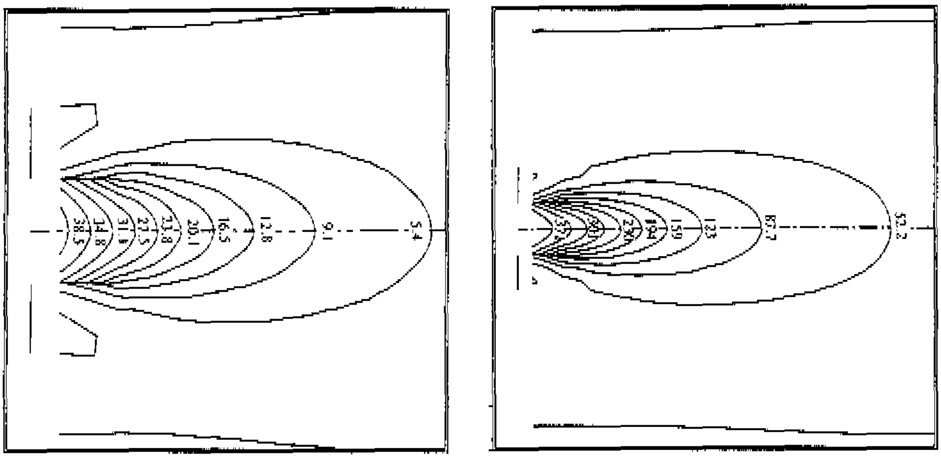

Figure 2.4: Axial velocity contours (m s^{-1}) of silane jet emerging into stagnant medium: a) u_0= 44 m s^{-1} (incompressible), full length in x-direction: 1.5 mm, b) u_0= 440 m s^{-1} (compressible), full length in x-direction: 3 mm. p_r= 100 Pa, T= 900 K.

The above results show that the extent of reactor scale mixing is not significantly effected by convective mass transport. At the low pressures employed, however, molecular diffusion coefficients are roughly three orders of magnitude larger than at atmospheric pressure and reactor scale mixing may thus be accomplished by fast molecular diffusion as well.

Consider a spherical reactor with diameter d= 6 10^{-2} m filled with inert gas A. At time t=0 a tracer gas B is introduced at the reactor wall. Assuming molecular diffusion to be the predominant mode of gas transport, the degree of concentration uniformity reached within time t can be calculated according to (Carslaw and Jaeger, 1959):

$$\frac{C_B^w - \overline{C_B}}{C_B^w - C_B^0} = \frac{6}{\pi^2} \exp\left(-4\pi^2 \frac{D_{A,B}\, t}{d^2} \right) \tag{2.10}$$

with C_B^w the tracer concentration at the reactor wall; C_B^0 the initial tracer concentration in the reactor; $\overline{C_B}$ the mean tracer concentration at time t; d the reactor diameter; $D_{A,B}$ the molecular diffusion coefficient, equal to 0.396 m^2 s^{-1}. The latter value applies to a SiH_4-H_2 mixture and was calculated using the Chapman-Enskog relations (Reid *et al.*, 1987). Concentration uniformity within 1% of the mean is achieved after 1 10^{-3} s at 100 Pa and 900 K, implying that reactor scale mixing by molecular diffusion is fast compared to the mean residence time (0.1-1 s).

Reactor scale mixing could not be verified experimentally using the classical residence time distribution measurements. The measured residence time distribution was almost completely determined by the gas transport through the inlet tube as a result of the relatively high pressure existing there. Instead, spatial concentration measurements were performed using the modified reactor configuration illustrated in Figure 2.5.

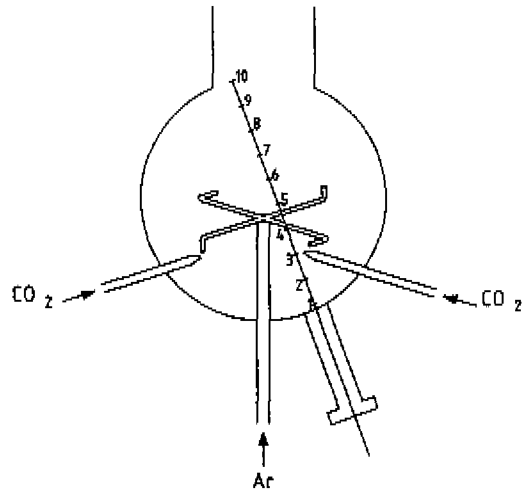

Figure 2.5: *Schematic of the reactor configuration used to verify spatial concentration uniformity.*

A continuous flow of inert gas, Ar, is fed to the reactor through the nozzles of the cross-shaped injector. Simultaneously, a continuous flow of tracer gas, CO_2, is introduced through two inlets. These are placed at right angles with the flow fields of two argon jets emerging in different orthogonal planes. During the experiments the volumetric flow rate of CO_2 was kept small compared to that of Ar, in order to prevent interference with the flow fields of the jets. Mean residence times of 0.1 and 1 s were established by varying the volumetric flow rate of Ar and the total pressure at room temperature. Higher temperatures could not be established, since external heating was impossible due to the outside geometry of the modified reactor. Spatial uniformity of the tracer concentration was determined by mass spectrometric analysis of the sample gas extracted at fixed points inside the reactor using a capillary with an inside diameter of $3.2\ 10^{-4}$ m.

Figure 2.6 shows the deviation from the mean tracer concentration at the various sampling points for 0.1 and 1 s mean residence time. Concentration uniformity to within 5% of the mean is achieved within 0.1 s. At temperatures close to 900 K the deviations will even be smaller owing to the positive temperature dependence of the molecular diffusion coefficients. A calculation analogous to that based on equation (2.10) indicates that a mixing time of $6\ 10^{-4}$ s should be sufficient for reaching a similar degree of concentration uniformity at room temperature. The discrepancy beteen theory and experiment probably results from interference of the concentration fields inside the reactor (d= $6.0\ 10^{-2}$ m) by the rather large outlet of the reactor (d= $2.2\ 10^{-2}$ m).

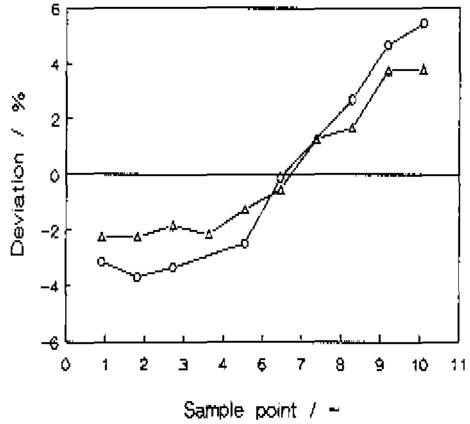

Figure 2.6: Deviation from mean tracer concentration at the various sampling points shown in Figure 2.5 for mean residence times of 0.1 s (o) and 1 s (△).

Based on the measured concentration uniformity, it can be assumed that the residence time distribution (RTD) of the laboratory reactor closely approximates the Poisson distribution of a single perfect macromixer:

$$E(t) = \frac{1}{\tau}\exp\left(-\frac{t}{\tau}\right) \tag{2.11}$$

with E(t) the residence time distribution; τ the mean residence time; t the residence time.

Micromixing

The analysis which follows attempts to provide a description of the extent of micromixing and to evaluate the maximum influence of micromixing effects on reactor performance. Both aspects were studied by considering two elementary gas phase reactions which are likely to play an important role in the gas phase chemistry of the silicon deposition process, i.e. the decomposition of silane and subsequent insertion of silylene into silane to form disilane:

$$SiH_4 \underset{k_{-1}}{\overset{k_1}{\rightleftharpoons}} SiH_2 + H_2 \tag{2.12}$$

$$SiH_4 + SiH_2 \underset{k_{-2}}{\overset{k_2}{\rightleftharpoons}} Si_2H_6 \tag{2.13}$$

The reaction rate coefficients k_1 and k_2 were taken from Kleijn (1991) and amount to 8.7 10^{-3} s^{-1} and 15.7 s^{-1} at 100 Pa and 900 K. The reaction rate coefficients for the opposite elementary steps were calculated from the chemical reaction equilibrium constants, and amount to 1523 m^3 mol^{-1} s^{-1} and 1.05 10^6 m^3 mol^{-1} s^{-1} at the same conditions. The thermodynamic data for the gas phase species involved were taken from Coltrin *et al.* (1986,1989).

For a given state of reactor scale mixing, the level of micromixing can be comprised between two extremes: complete segregation and ideal micromixing. The actual state of micromixing can be estimated by comparing the micromixing time (t_m) with the characteristic time of reaction (t_r) and the mean residence time (τ) as illustrated in Table 2.1.

For first-order gas phase reactions, the conversions calculated for the extreme situations of ideal micromixing and complete segregation coincide (Westerterp *et al.*, 1990). Consequently, micromixing effects will be absent for the unimolecular dissociation reactions of silane and disilane, as long as pressure fall-off effects can be neglected. Silylene insertion into silane or molecular hydrogen is very fast (Inoue and Suzuki, 1985). Due to the high reactivity of silylene, micromixing effects may be expected with respect to the bimolecular reactions given by equations (2.12) and (2.13). To verify the presence of such effects the micromixing time was compared to both the mean residence time and the characteristic times for silylene insertion in case 1.51 10^{-6} mol s^{-1} silane is fed to the reactor at operating conditions of 100 Pa and 900 K, corresponding to a mean residence time of 0.1 s.

Table 2.1: *Influence of the micromixing time, mean residence time and characteristic time of reaction on the state of mixing in a continuous flow reactor (David and Villermaux, 1978).*

	$t_m << t_r$	$t_m \approx t_r$	$t_m >> t_r$
$t_m << \tau$	MM	PS	S
$t_m = \tau$	PS	PS	S
$t_m >> \tau$	S	S	S

MM = ideal micromixing, PS = partial segregation, S = complete segregation

The micromixing time is given by (Westerterp *et al.*, 1990):

$$t_m = \frac{l^2}{12 D_{i,m}} \qquad (2.14)$$

In this expression molecular diffusion is retained as the controlling mechanism with respect to micromixing. Moreover, $D_{i,m}$ is the effective molecular diffusion coefficient of component i in a multicomponent mixture. The smallest length scale in the final stage of mixing is in general taken as the Kolmogoroff scale (Westerterp *et al.*, 1990):

$$l = \left(\frac{\nu^3}{\varepsilon}\right)^{1/4} \qquad (2.15)$$

with ν the kinematic viscosity and ε the power input rate per unit mass of fluid in the reactor. The jet development calculations of the preceding section revealed that energy dissipation is mainly confined to the region close to the inlet nozzle, outside this region energy dissipation is not important. This highly nonuniform distribution of energy dissipation causes the length scale as calculated from equation (2.15) to be a strong function of the position inside the reactor. The length scale is smallest in the regions close to the inlet nozzles and strongly increases along the corresponding jet paths. For this reason, the length scale l is given an upper limit equal to the dimension of the reactor, 6 10^{-2} m. The effective molecular diffusion coefficient of silylene was calculated according to Wilke's approximation (Bird *et al.*, 1960) and amounts to 9.874 10^{-2} m^2 s^{-1}. Substituting the above values into equation (2.14) results in a micromixing time equal to 3 10^{-3} s at 900 K and 100 Pa. Note that this micromixing time is similar to the earlier mentioned reactor scale mixing time, as expected since both characteristic times are now based on the same length scale.

The characteristic reaction time for an n*th* order reaction is given by:

$$t_r = \frac{1}{k\,C_A^{n-1}} \tag{2.16}$$

The gas phase concentrations in the denominator can be obtained by solving the continuity equations for a perfectly stirred tank reactor:

$$F_{i,0} - F_i + V \sum_{k=1}^{ng} \nu_{k,i}\, r_{v,k} = 0 \tag{2.17}$$

using the gas phase chemistry reflected by equations (2.12) and (2.13). In this equation $F_{i,0}$ and F_i are the inlet and outlet molar flow rates of component i; V the reactor volume; ng the number of gas phase steps; $\nu_{k,i}$ the stoichiometric coefficient of component i in gas phase step k; $r_{v,k}$ the rate of gas phase step k. Substitution of the calculated concentrations together with the reaction rate coefficients into equation (2.16) results in the characteristic times for silylene insertion as listed in Table 2.2. Silylene insertion into silane proceeds on a time scale smaller than the micromixing time. Consequently, the reactor behaves as completely segregated with respect to silylene, see Table 2.1.

Table 2.2: *Characteristic times for silylene insertion, micromixing time and mean residence time.* p_t= *100 Pa,* T= *900 K,* $F_{SiH_4,0}$= *1.51 10^{-5} mol s^{-1}.*

reaction	t_r / s	t_m / s	τ / s
$SiH_2 + H_2 \rightarrow SiH_4$	5.7 10^{1}	1 10^{-3}	0.1
$SiH_4 + SiH_2 \rightarrow Si_2H_6$	7.2 10^{-5}		

The gas phase composition calculated according to equation (2.17) prevails in the situation of ideal micromixing, i.e. of complete mixing on molecular scale. In order to quantify the effect of complete segregation with respect to silylene, the gas phase composition is calculated for the extreme situation of complete segregation as well. In case of complete segregation aggregates travel through the reactor in discrete noninteracting packets. Each aggregate can be modelled as a batch reactor with a reaction time equal to its residence time. The average concentration at the outlet of a completely segregated continuous flow reactor is then:

$$\overline{C_i} = \int_0^\infty C_i^{Batch}(t)\, E(t)\, dt \tag{2.18}$$

with E(t) the residence time distribution, given by equation (2.11). The concentration of component i in a batch reactor with residence time t, $C_i^{Batch}(t)$, can be calculated by solving:

$$\frac{dC_i^{Batch}}{dt} = \sum_{k=1}^{ng} \nu_{k,i}\, r_{v,k} \tag{2.19}$$

with initial condition $C_i^{Batch} = C_{i,0}$ at t=0.

The gas phase composition calculated for complete segregation entirely resembles that calculated for ideal micromixing, indicating that micromixing effects are absent. Although silylene reacts with silane at a time scale much smaller than the micromixing time, effects on reactor performance are not found. As micromixing effects become important in case of non-(pseudo-)first order reactions having reaction times comparable to or smaller than the micromixing time, it can be concluded that first and pseudo-first order reactions dominate the gas phase chemistry. Because silane is present in large amounts and exhibits spatial uniformity, silylene insertion into silane is indeed pseudo-first order and thus insensitive to micromixing.

Gas/solid mass transfer

The analysis which follows provides a description of the importance of irreducible concentration gradients inside the laboratory reactor as a result of potentially fast surface reactions. For simplification, the surface reactions are considered to occur on the reactor wall only, i.e. deposition on the silicon sample in the centre of the reactor is neglected.

In case molecular diffusion is the only mode of mass transport, mass transport limitation needs to be accounted for in case the reaction probability is much larger than the ratio of the mean free path length and the characteristic reactor dimension (Boudart, 1968):

$$\gamma_i > \frac{\lambda_m}{d} \tag{2.20}$$

It has to be noted that this condition can easily be transformed into a dimensionless number closely related to the general Damköhler-II number.

The characteristic dimension of the reactor is 6 10^{-2} m, whereas a typical value for the mean free path length at 100 Pa and 900 K is 1 10^{4} m. Literature values for the reaction probability of silane range from 3 10^{-5} (Gates *et al.*, 1990a,b) to 1 10^{-3} (Buss *et al.*, 1988). Comparing this range of values to the ratio obtained from equation (2.20), i.e. 2 10^{-3}, it can be concluded that no mass transport limitation occurs for silane. Since the rate of hydrogen production at the surface is approximately twice the rate of silane disappearance, mass transport limitation will be absent for hydrogen also. Silylene and disilane exhibit much higher surface reaction probabilities than silane. Reaction probabilities for disilane vary between 4 10^{-2} (Buss *et al.*, 1988) and 0.5 (Scott *et al.*, 1989; Gates, 1988), whereas silylene is generally assumed to react with unit probability upon collision with the surface (Coltrin *et al.*, 1984,1986,1989; Kleijn, 1991). According to the criterion postulated by Boudart (1968), mass transport will affect the rates of disappearance of silylene and disilane at the surface and, hence, the gas phase composition and the silicon growth rate. Production of disilane induces production of other silicon containing species like disilene and silylsilylene, which are believed to have the same high surface reaction probabilities as silylene and disilane (Coltrin *et al.*, 1984,1986,1989).

In order to characterize the irreducible mass transport limitations an analytical expression is derived, which is applicable to each intermediate gas phase species formed during the pyrolysis of silane. Using silylene as model component the following simplified kinetic model is considered. Gas phase production of silylene is assumed to occur via unimolecular decomposition of silane:

$$SiH_4 \rightarrow SiH_2 + H_2 \tag{2.21}$$

at a uniform rate r_v^1 equal to the product of the unimolecular reaction rate coefficient and the uniform silane concentration. Gas phase consumption of silylene is considered to proceed via insertion into silane:

$$SiH_2 + SiH_4 \rightarrow Si_2H_6 \tag{2.22}$$

characterized by a pseudo-first order reaction rate coefficient equal to the product of the bimolecular reaction rate coefficient and again the uniform concentration of silane.

Silylene consumption via insertion into hydrogen is not considered. The large positive affinity of reaction (2.21) indicates the insignificance of the backward step. Silylene production via unimolecular decomposition of disilane is not taken into account either. Due to the high surface reactivity of disilane, inclusion of this backward step would require the disilane concentration profile to be solved as well. For the purpose of the present evaluation both simplifications are justified. The surface reaction of silylene is considered to proceed according to:

$$SiH_2 \rightarrow Si(s) + H_2 \qquad (2.23)$$

following first order kinetics with a reaction rate coefficient k_s estimated from kinetic gas theory:

$$k_s = \gamma^0_{SiH_2}\frac{1}{4}\sqrt{\frac{8RT}{\pi M_{SiH_2}}} \qquad (2.24)$$

with $\gamma^0_{SiH_2}$ and M_{SiH_2} the reaction probability at zero coverage and the molar mass of silylene.

In order to reduce the computational complexity from 3D to 1D, the following two assumptions were made. First, the transport phenomena and gas phase as well as surface reaction phenomena are considered independent of angle coordinates θ and ϕ. Second, the outlet of the reactor is considered spreading out over the entire gas phase reaction volume. The latter assumption is treated in paragraph 2.5.1 in more detail. Because convective mass transport is confined to a small region close to the inlet nozzle, see this paragraph, molecular diffusion is assumed to be the only mode of gas transport. Furthermore, gas phase production is considered to be uniform with a rate r_v^1, whereas gas phase consumption is assumed to depend on the local gas phase composition and to follow first order kinetics with a volumetric reaction rate coefficient k_v.

The above considerations lead to the following continuity equation for silylene:

$$-\frac{D_{SiH_2,m}}{r^2}\frac{d}{dr}\left(r^2\frac{dC_{SiH_2}}{dr}\right) = r_v^I - k_v C_{SiH_2} - \frac{F_v}{V}C_{SiH_2} \qquad (2.25)$$

with $D_{SiH_2,m}$ denoting the effective molecular diffusion coeffcient of silylene in a multicomponent mixture. The last term on the right-hand side of this equation represents the outlet molar flow rate divided by the gas phase volume. Symmetry in the centre of the reactor is expressed by the boundary condition:

$$r=0 \qquad \frac{dC_{SiH_2}}{dr} = 0 \tag{2.26}$$

The first order surface reaction enters solely through the boundary condition at the reactor wall:

$$r=R \qquad -D_{SiH_2,m}\frac{dC_{SiH_2}}{dr} = k_s\,C_{SiH_2} \tag{2.27}$$

Integration of the second order differential equation with corresponding boundary conditions, given by equations (2.25) to (2.27), results in the following expression for the silylene concentration as a function of radial coordinate r, see Appendix 2B:

$$C_{SiH_2} = \frac{r_v^f}{\frac{F_v}{V}+k_v}\left(1 - \frac{\frac{R}{r}\sinh((R\sqrt{\alpha})\,\frac{r}{R})}{(1-\frac{D_{SiH_2,m}}{k_s R})\sinh(R\sqrt{\alpha}) + \frac{D_{SiH_2,m}}{k_s R}R\sqrt{\alpha}\cosh(R\sqrt{\alpha})}\right) \tag{2.28}$$

The term in front of the brackets denotes the concentration obtained by applying the steady state approximation for silylene if no reactivity towards the surface exists (k_s= 0):

$$C_{SiH_2}^{SSA} = \frac{r_v^f}{\frac{F_v}{V}+k_v} \tag{2.29}$$

This concentration is determined by the balance between gas phase production on one hand and gas phase consumption and renewal on the other hand. In case surface reaction occurs, the concentration profile can be described in terms of two dimensionless numbers relating the time scale of diffusion to the time scale of surface reaction and of homogeneous reaction and renewal, i.e. the Damköhler-II number given by:

$$Da_{II} = \frac{k_s R}{D_{SiH_2,m}} \tag{2.30}$$

and a modified Thiele modulus defined as:

$$\phi = R\sqrt{\alpha} = R\sqrt{\frac{F_v}{V D_{SiH_2,m}} + \frac{k_v}{D_{SiH_2,m}}} \tag{2.31}$$

Mass transport limitations were calculated for the situation that 3.02 10^{-6} mol s^{-1} silane is fed to the reactor at 100 Pa and 900 K, corresponding to a total volumetric flow rate of 2.26 10^{-4} m^3 s^{-1}. The gas phase composition was calculated by solving the continuity equations given by equation (2.17) with the gas phase chemistry reflected by equations (2.21) and (2.22). The inlet volumetric flow rate was chosen such that the silane conversion is small (1%), and volume changes as a result of reaction stoichiometry can be neglected. Hence, the outlet volumetric flow rate can be equated to the inlet volumetric flow rate. The effective molecular diffusion coefficient of silylene was calculated according to Wilke's approximation (Bird *et al.*, 1960) and amounts to 9.874 10^{-2} m^2 s^{-1}. The uniform production rate of silylene, r_v', amounts to 1.15 10^{-4} mol m^{-3} s^{-1}, and was obtained from the product of the unimolecular reaction rate coefficient for silane decomposition equal to 8.7 10^{-3} m^3 mol^{-1} s^{-1} and the uniform silane concentration equal to 1.325 10^{-2} mol m^{-3}. The pseudo-first order volumetric reaction rate coefficient k_v amounts to 1.39 10^4 s^{-1}. This value was obtained from the product of the bimolecular reaction rate coefficient for silylene insertion into silane equal to 1.05 10^6 m^3 mol^{-1} s^{-1} and the above mentioned silane concentration. The first order surface reaction rate coefficient k_s was estimated from kinetic gas theory according to equation (2.24) assuming a reaction probability at zero coverage of 1, and amounts to 198.91 m s^{-1}.

The above values lead to Da_{II}= 60.4 and ϕ= 11.2. Figure 2.7 shows the corresponding silylene concentration profile calculated according to equation (2.28). The silylene concentration decreases from 8.3 10^{-9} mol m^{-3} in the centre to 1.2 10^{-9} mol m^{-3} at the wall. This substantial drop in concentration is caused by the high value of the Damköhler-II number.

The shape of such a concentration profile can be rationalized in terms of relative time scales of gas phase and surface reactions.

Figure 2.8 shows the silylene concentration profile for different values of the Damköhler-II number and a fixed value of the Thiele modulus. In the limit of $Da_{II} \to 0$, a flat concentration profile appears, the level of which is determined solely by the balance between gas phase production on one hand and gas phase consumption and renewal on the other hand. With increasing Da_{II} number the concentration at the wall decreases and eventually falls to zero in the limit of $Da_{II} \to \infty$. Changes in the Da_{II} number appear to have no effect on the concentration level in the centre of the reactor. This can be understood by analysing equation (2.28) at radial coordinate r=0 for the limits of $Da_{II} \to 0$ and $Da_{II} \to \infty$. In the limit of $Da_{II} \to 0$, the concentration at r=0,

$C_{SiH_2}|_{r=0}$, is always equal to $C_{SiH_2}^{SSA}$ given by equation (2.29). In the limit of $Da_{II} \rightarrow \infty$, however, equation (2.28) reduces to:

$$C_{SiH_2}|_{r=0} = \frac{r_v^f}{\frac{F_v}{V} + k_v}\left(1 - \frac{R\sqrt{\alpha}}{\sinh(R\sqrt{\alpha})}\right) \qquad (2.32)$$

with $R\sqrt{\alpha}$ the earlier defined Thiele modulus. In case of a Thiele modulus larger than roughly 10, the right term inside the brackets is much smaller than unity and equation (2.32) reduces to equation (2.29) as well. Hence, the silylene concentration in the centre of the reactor is independent of the value of the Damköhler-II number and equal to the steady state concentration of silylene belonging to the uniform concentration of silane.

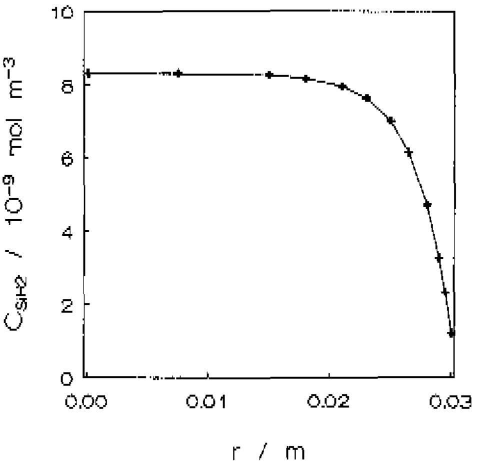

Figure 2.7: Silylene concentration profile calculated with equation (2.28). p_t= 100 Pa, T= 900 K, F_v= 2.26 10^{-4} m^3 s^{-1}, $C_{SiH_2}^{SSA}$= 8.3 10^{-9} mol m^{-3}, Da_{II}= 60.4, ϕ= 11.2.

Figure 2.9 shows the silylene concentration profile for different values of the Thiele modulus and a fixed value of the Damköhler-II number. The lower limit of the Thiele modulus corresponds to k_v= 0. The small value of the Thiele modulus left results from the contribution of the reactor outlet stream to the total disappearance of silylene in the gas phase, see equation (2.31). The upper limit of the Thiele modulus, not shown here, naturally corresponds to $k_v \rightarrow \infty$, leading to a uniform silylene concentration equal to zero. With increasing Thiele modulus the concentration gradient becomes less pronounced in the major part of the reactor and the thickness of the diffusion layer decreases. The higher the Thiele modulus the less important becomes the influence of the surface reaction and the better the silylene concentration is approximated by equation (2.29). The expression relating the diffusion layer thickness to the Thiele modulus is given by, see Appendix 2B:

$$\delta = R \frac{\sinh(R\sqrt{\alpha}) - R\sqrt{\alpha}}{R\sqrt{\alpha}\cosh(R\sqrt{\alpha}) - \sinh(R\sqrt{\alpha})} \tag{2.33}$$

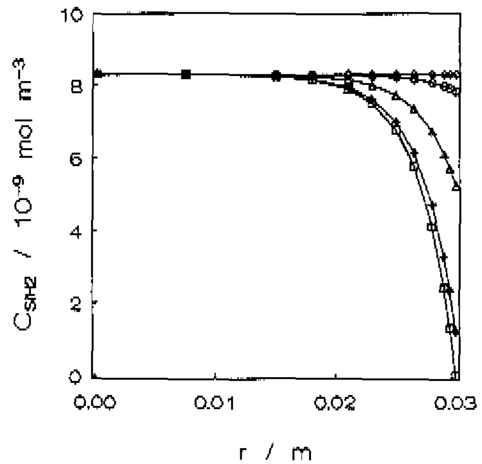

Figure 2.8: *Effect of Damköhler-II number on silylene concentration profile. p_t= 100 Pa, T= 900 K, F_v= 2.26 10^{-4} m^3 s^{-1}, $C_{SiH_2}^{SSA}$ = 8.3 10^{-9} mol m^{-3}, ϕ= 11.2, ◇ $Da_{II} \to 0$, ○ Da_{II}= 0.6, ▲ Da_{II}= 6, + Da_{II}= 60, □ $Da_{II} \to \infty$.*

For a Thiele modulus larger than roughly 10, this equation simplifies to:

$$\delta = \frac{1}{\sqrt{\alpha}} = \frac{1}{\sqrt{\dfrac{F_v}{V D_{SiH_2,m}} + \dfrac{k_v}{D_{SiH_2,m}}}} \tag{2.34}$$

Due to the high gas phase reactivity of silylene, the right term under the square root sign is much larger than the left term and equation (2.34) further reduces to:

$$\delta = \sqrt{\frac{D_{SiH_2,m}}{k_v}} \tag{2.35}$$

with δ usually referred to as the diffusion length (Moffat and Jensen, 1988; de Croon and Giling, 1990), being the mean distance over which a molecule can diffuse prior to reaction in the gas phase. In other words, the diffusion length is the mean distance from the deposition surface up to where surface reactions can significantly influence the gas phase concentrations. Substituting the appropriate values for k_v and $D_{SiH_2,m}$ into equation (2.35) results in a diffusion length for silylene equal to 2.7 10^{-3} m. This value is in close agreement with the value resulting from the calculated concentration profile given in Figure 2.7, i.e. ~3 10^{-3} m.

For a Thiele modulus larger than 10, Figure 2.9 shows a flat profile in the centre of the reactor with a well-defined diffusion layer adjacent to the deposition surface. For a Thiele modulus smaller than 10, however, no sharp interface between bulk of gas phase and diffusion layer exists. In fact, the concentration gradient stretches out over the entire gas phase. The non-uniform profile in the centre of the reactor is caused by the far-reaching effect of the surface reaction on the gas phase composition.

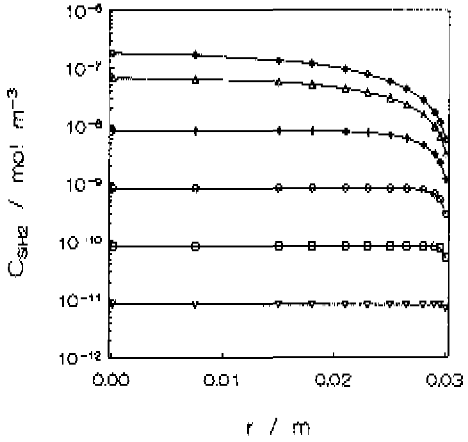

Figure 2.9: *Effect of Thiele modulus on silylene concentration profile. p_t= 100 Pa, T= 900 K, F_v= 2.26 10^{-4} m^3 s^{-1}, $C_{SiH_2}^{SSA}$= 8.3 10^{-9} mol m^{-3}, Da_{II}= 60.4, ◇ ϕ= 0.14, △ ϕ= 3.56, + ϕ= 11.2, o ϕ= 35.6, □ ϕ= 112, ▽ ϕ= 356.*

Disilane (Si_2H_6) has a significantly lower gas phase reactivity than silylene and, hence, will exhibit a concentration gradient stretching out over the entire gas phase. Disilene (H_2SiSiH_2) and silylsilylene (H_3SiSiH) possess high gas phase and surface reactivities resulting in flat concentration profiles throughout the major part of the reactor with a thin well-defined diffusion layer adjacent to the deposition surface.

2.4.2 Temperature uniformity

With respect to the temperature uniformity inside the laboratory reactor it is necessary to examine the effectiveness of both heat transport on reactor scale, i.e. intrareactor uniformity, and heat transfer between deposition surface and gas phase, i.e. interphase uniformity.

Intrareactor

Azay and Côme (1979) showed that a continuous spherical gas jet-agitated reactor, having a residence time distribution corresponding to that of a single perfect mixer, can present important radial temperature gradients. Preheating of the reactants or carrier gas was recommended in order to eliminate temperature gradients.

To quantify the effect of preheating on the extent of temperature uniformity inside the reactor, jet development calculations were conducted in the same way as outlined in the section about reactor scale mixing. The inlet temperature was varied up to 850 K at operating conditions of 100 Pa and 900 K and a mean residence time of 0.1 s. The value of 850 K at the inlet was considered an upper limit, imposed by a maximum allowable value of 2% for the reactant conversion level inside the preheater compared to that inside the reactor. These calculations revealed a significant reduction in temperature nonuniformity with increasing inlet temperature. Figure 2.10a shows the temperature contours when pure silane is entering the reactor at a temperature of 850 K. Due to adiabatic expansion a temperature drop of at least 50 K is observed in the region close to the nozzle, where the Mach number is highest, see Figure 2.10b. Temperature uniformity is reached within a distance of approximately 6 10^{-3} m from this region.

Spatial temperature uniformity was verified experimentally through thermocouple measurements at fixed positions inside the spherical reactor. These measurements showed that in the temperature range considered, i.e. 800-1000 K, radial temperature gradients can be neglected. The maximum spherically averaged temperature difference between reactor centre and reactor wall occurs at 1000 K and amounts to 3 K.

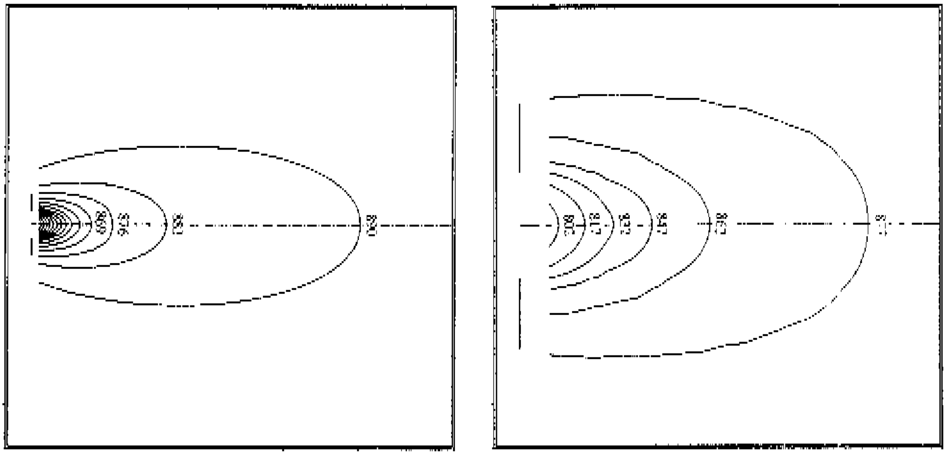

Figure 2.10: *Temperature contours (K) for an inlet temperature of 850 K: a) jet, full length in x-direction: 6 mm, b) region close to inlet nozzle, full length in x-direction: 1.5 mm.* p_t*= 100 Pa, T= 900 K,* τ*=0.1 s.*

Interphase

In order to assess heat transfer resistances, the criterion derived by Mears (1971) for heat transfer limitation in the external film adjacent to a catalyst pellet is applied. The criterion is based on a maximum allowable change of 5% in the silicon growth rate due to a temperature gradient:

$$\frac{|\Delta H_r^0|\; Gr_{Si}}{\alpha\; T} < 0.05\; \frac{R\; T}{E_a} \qquad (2.36)$$

with ΔH_r^0 the standard reaction enthalpy; E_a the activation energy; α the heat transfer coefficient; Gr_{Si} the silicon growth rate in mol m^{-2} s^{-1}.

At typical LPCVD conditions, silicon growth is dominated by heterogeneous silane decomposition via:

$$SiH_4 \rightarrow Si(s) + 2H_2 \qquad (2.37)$$

with a standard reaction enthalpy of -23.8 kJ mol^{-1}. The corresponding growth rate can be calculated according to (Roenigk, 1987):

$$Gr_{Si} = \frac{k_S\, p_{SiH_4}}{1 + K_A\, p_{SiH_4} + K_H \sqrt{p_{H_2}}} \qquad (2.38)$$

At high silane partial pressures, this expression can be rewritten as the ratio of the reaction rate coefficient k_S with an activation energy of 153.8 kJ mol^{-1} and the equilibrium constant K_A possessing no temperature dependence. At 900 K k_S amounts to 1.89 10^{-5} mol m^{-2} s^{-1} Pa^{-1}, which combined with a value of 0.7 Pa^{-1} for K_A results in a growth rate equal to 2.7 10^{-5} mol m^{-2} s^{-1}. A rough estimation for the value of the heat transfer coefficient α is 6 W m^{-2} K^{-1}. This value is based on a Nusselt number equal to 3.66 and a thermal conductivity of 9.9 10^{-2} W m^{-1} K^{-1} (Kleijn, 1991). Substituting the above values into equation (2.36) yields a value of 2.4 10^{-3} for the right term of the criterion, which exceeds the value of 1.2 10^{-4} for the left term. Consequently, heat transfer resistance is not significant.

2.5 Reactor model

2.5.1 Equations

Due to the high surface reaction probability of the gas phase intermediates formed during the pyrolysis of silane, it is necessary to account for the mass transfer resistances of these species during the simulation of the kinetic experiments performed in the microbalance reactor setup, see paragraph 2.4.1. The shape of the concentration profiles was shown to be a complex function of two dimensionless numbers, i.e. the Damköhler-II number based on the surface reaction kinetics and a modified Thiele modulus based on the gas phase reaction kinetics. Depending on the values of these numbers, the concentration gradients of the gas phase intermediates are located within a few millimeter from the growing silicon layer or throughout the complete reactor. Hence, it is impossible to describe the mass transfer between gas phase and deposition surface in terms of a film model. Following such model the resistance to mass transfer would be located in a fictitious layer adjacent to the deposition surface and the rate of mass transfer would be determined by a mass transfer coefficient calculated from empirical correlations. The requirement of empirical correlations for mass transfer coefficients forms another drawback of the film model. For the transport characteristics inside the laboratory reactor no appropriate correlations are found in literature.

Based on the above considerations a reactor model was developed in which the mass transfer between gas phase and deposition surface is accounted for by considering molecular diffusion with simultaneous gas phase reactions. The assumption of molecular diffusion being the only mode of mass transport is in line with the results presented in paragraph 2.4.1. Figure 2.11 shows a schematic representation of the reactor model. In order to reduce the computational complexity from 3D to 1D, the following assumptions were made. First, the transport phenomena and gas phase as well as surface reaction phenomena are considered independent of angle coordinates θ and ϕ. Second, the inlet and outlet of the reactor are considered spreading out over the entire gas phase reaction volume, being confined to a spherical shell of thickness R_1-R_0. This assumption will be treated in detail below. Deposition is considered to occur on the surfaces at $r= R_0$ and $r= R_1$ enclosing this shell. The radial positions R_0 (1.396 10^{-2} m) and R_1 (3.097 10^{-2} m) were derived from the values of the total deposition surface area, i.e. A_d= 1.45 10^{-2} m^2, and gas phase reaction volume, i.e. V_g= 1.13 10^{-4} m^3, during a typical kinetic experiment.

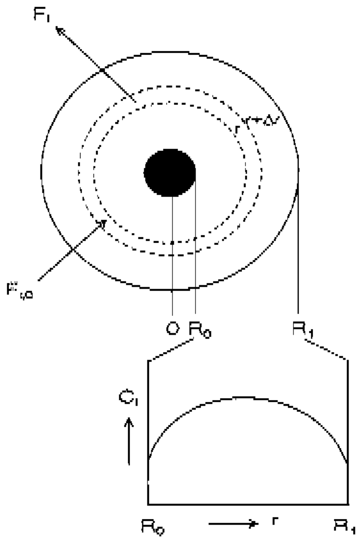

Figure 2.11: Schematic representation of reactor model.

Gas phase

The insignificance of temperature gradients on reactor scale, demonstrated in paragraph 2.4.2, alleviates the need to solve the energy equation. The jet development calculations of paragraph 2.4.1 revealed that convection does not have a significant contribution to the mass transport inside the laboratory reactor, hence making a treatment of the flow field redundant. Furthermore, the laboratory reactor is operated isobarically. Based on these points, the Navier-Stokes or momentum conservation equations need not to be solved as well. Consequently, the gas phase model equations reduce to the continuity equations for all gas phase components considered. Based on the low total pressures ideal gas behaviour is assumed. The inlet and outlet molar flow rates of each component are treated as source terms in the corresponding continuity equations.

The inlet molar flow rates are considered uniform throughout the gas phase reaction volume. This is justified on the following grounds. In paragraph 2.4.1 it was shown that non-reacting components fed through the nozzles of the laboratory reactor easily reach uniform concentrations throughout the gas phase before leaving the reactor. Reacting components such as silane and hydrogen, however, need to satisfy an additional constraint to be uniform in concentration. Both their gas phase consumption and their surface consumption need to proceed slowly compared to the mixing process on reactor scale. If this is the case a fast concentration uniformization makes the location of the inlet arbitrarily. The position of the inlet will thus have no effect on the calculated reactor performance provided reactive components are not fed.

The outlet molar flow rates are spread out over the gas phase volume and coupled to the molar fractions locally existing. This corresponds to the assumption that fluidum elements have no measurable interaction with each other on their way to the outlet, which is an approximation. The correctness of the assumption will depend on the shape of the concentration profiles. Errors are negligible for silane, hydrogen and inert and also for components possessing high gas phase and low surface reactivities and correspondingly high Thiele moduli and low Damköhler-II numbers. Significant effects are only expected for species with low gas phase and high surface reactivities. With respect to most of the silicon containing gas phase species in polysilicon deposition no severe errors are expected.

Based on the foregoing considerations, the continuity equation for gas phase component i becomes:

$$\frac{1}{r^2}\frac{d}{dr}\left(r^2 N_i\right) = \sum_{k=1}^{ng} \nu_{k,i} r_{v,k} + (F_{i,0} - y_i F)/V_g \qquad (2.39)$$

with N_i the molar flux of component i; $F_{i,0}$ the inlet molar flow rate of component i; y_i the molar fraction of component i; F the total molar flow rate at the outlet of the reactor; V_g the gas phase reaction volume and r the radial coordinate. The first term on the right-hand side of this equation denotes the homogeneous net production rate of component i with ng the number of gas phase steps, $\nu_{k,i}$ the stoichiometric coefficient of component i in gas phase step k and $r_{v,k}$ the rate of gas phase step k. Since the kinetic experiments typically involve reaction mixtures containing more than two abundant components and the deposition is associated with significant volume changes, multicomponent diffusion effects need to be accounted for. Therefore, the Stefan-Maxwell equations (Bird *et al.*, 1960) are applied:

$$\frac{dy_i}{dr} = \sum_{j \neq i} \frac{y_i N_j - y_j N_i}{C D_{i,j}} \tag{2.40}$$

relating the molar fluxes of all species in the mixture to all concentration gradients. In these equations, C is the total gas phase concentration (= p_t/RT) and $D_{i,j}$ the molecular diffusion coefficient of gas phase species i in a binary mixture of i and j. The molecular diffusion coefficients are calculated using the Chapman-Enskog relations (Reid *et al.*, 1987). Deposition is accounted for through the boundary conditions at r= R_1 and r= R_0:

$$r = R_0 \qquad N_i = \sum_{m=1}^{ns} v_{m,i} r_{s,m} \tag{2.41}$$

$$r = R_1 \qquad N_i = -\sum_{m=1}^{ns} v_{m,i} r_{s,m} \tag{2.42}$$

The term on the right-hand side of these equations denotes the heterogeneous net production rate of gas phase component i with ns the number of surface steps, $v_{m,i}$ the stoichiometric coefficient of gas phase species i in surface step m and $r_{s,m}$ the rate of surface step m. These boundary conditions state that the molar flux of each gas phase species to the surface is balanced by the net surface production rate of that species.
For an ideal gas mixture containing NG components a set of (2NG-1) independent first-order ordinary differential equations can be defined with molar fraction y_i and molar flux N_i as dependent variables. In this way (NG-1) molar fractions and NG molar fluxes are solved. The molar fraction of the NG*th* species follows from:

$$\sum_{i=1}^{NG} y_i = 1 \tag{2.43}$$

Deposition surface

At steady state, the continuity equation for surface component l is given by:

$$\sum_{m=1}^{ns} v_{m,l} r_{s,m} = 0 \tag{2.44}$$

with $v_{m,l}$ the stoichiometric coefficient of surface component l in surface step m.
For NS surface components, including vacant surface sites, (NS-1) independent nonlinear algebraic equations can be defined with surface concentration L_l as

dependent variable. In this way (NS-1) surface concentrations are solved. The NS*th* surface concentration follows from the condition that the total surface concentration equals the total concentration of active sites, L_t:

$$\sum_{l=1}^{NS} L_l = L_t \tag{2.45}$$

Growth rate and outlet molar flow rates

After solving the set of equations, given by (2.39) to (2.45), the growth rate and the outlet molar flow rates can be calculated. The silicon growth rate is obtained from the following continuity equation for solid silicon, Si(s):

$$R_{Si} = \frac{M_{Si}}{\rho_{Si}} \sum_{m=1}^{ns} \nu_{m,Si} \, r_{s,m} \Big|_{r=R_0} \tag{2.46}$$

with M_{Si}, the molar mass of solid silicon; ρ_{Si}, the density of solid silicon; $\nu_{m,Si}$, the stoichiometric coefficient of solid silicon in surface step m. As the observed growth rate corresponds to the growth rate in the centre of the reactor, the above calculation is performed based on the conditions prevailing at $r = R_0$. The outlet molar flow rate of component i, F_i, is obtained by integrating equation (2.39) over the gas phase reaction volume:

$$F_i = F_{i,0} - \iiint_{V_g} \nabla \cdot N_i \, dV + \iiint_{V_g} \sum_{k=1}^{ng} \nu_{k,i} r_{v,k} \, dV \tag{2.47}$$

The third term on the right-hand side of this equation denotes the volume integrated homogeneous net production rate of gas phase component i. The second term on the other hand represents the surface integrated heterogeneous net production rate of component i, as will be shown in the next paragraph.

2.5.2 Solution procedure

The problem thus involves a set of (2NG-1) independent first order ordinary differential equations coupled through the boundary conditions at $r = R_0$ and $r = R_1$ to two sets of (NS-1) independent nonlinear algebraic equations.

The set of differential equations given by (2.39) and (2.40) subjected to the boundary conditions given by (2.41) and (2.42) is integrated applying the method of orthogonal collocation (Finlayson, 1972). Orthogonal collocation belongs to the methods of weighted residuals, involving expansion of the unknown solution in a set of trial functions. In the method of orthogonal collocation the trial functions are chosen to be sets of orthogonal polynomials satisfying the boundary conditions. The polynomials are easily rewritten for problems involving planar, cylindrical, or spherical geometry. The solution is derived in terms of the value of the solution at the collocation points, which are determined from the roots to the orthogonal polynomials of highest order. In this way the whole problem reduces to a set of algebraic equations. Quadrature formulas can be applied in case the primary information desired from the solution is some integrated property.

For an easy application of the method of orthogonal collocation, the set of differential equations and boundary conditions is made dimensionless by replacing r with ξR_0:

$$\frac{1}{\xi^2}\frac{d}{d\xi}\left(\xi^2 N_i\right) = R_0\sum_{k=1}^{ng} \nu_{k,i} r_{v,k} + R_0(F_{i,0} - y_i F)/V_g \tag{2.48}$$

$$\frac{dy_i}{d\xi} = R_0\sum_{j\neq i} \frac{y_i N_j - y_j N_i}{CD_{i,j}} \tag{2.49}$$

$$\xi = 1 \qquad N_i = \sum_{m=1}^{ns} \nu_{m,i} r_{a,m} \tag{2.50}$$

$$\xi = R_1/R_0 \qquad N_i = -\sum_{m=1}^{ns} \nu_{m,i} r_{a,m} \tag{2.51}$$

The derivatives of the molar flux and the molar fraction are expressed as linear combinations of the values of the solutions at the (M+2) collocation points in the ξ-direction, M being the number of interior collocation points (M= 6). The above set of model equations then becomes, see Appendix 2C:

$$\sum_{cc=1}^{M+2} A_{c,cc} N_{i,cc} = R_0\sum_{k=1}^{ng} \nu_{k,i} r_{v,k} + R_0(F_{i,0} - y_i F)/V_g \qquad c = 2...M+1 \tag{2.52}$$

$$\sum_{cc=1}^{M+2} B_{c,cc} y_{i,cc} = R_0\sum_{j\neq i} \frac{y_i N_j - y_j N_i}{CD_{i,j}} \qquad c = 1...M+2 \tag{2.53}$$

$$N_i = \sum_{m=1}^{ns} \nu_{m,i} r_{a,m} \qquad c = 1 \tag{2.54}$$

$$N_i = -\sum_{m=1}^{ns} \nu_{m,i} r_{a,m} \qquad c = M+2 \tag{2.55}$$

with $A_{c,cc}$ and $B_{c,cc}$ elements of the (M+2)x(M+2) square matrices A and B as shown in Appendix 2C. The total molar flow rate at the outlet of the reactor, F, is derived by summing equation (2.47) over all gas phase components, see Appendix 2D.

Application of the method of orthogonal collocation thus converts the set of (2NG-1) independent first order ordinary differential equations plus boundary conditions, given by (2.48) to (2.51), into a set of (2NG-1)(M+2) independent nonlinear algebraic equations, (2.52) to (2.55). The condition that the total molar fraction equals one, given by equation (2.43), needs to be fulfilled at each collocation point giving rise to an additional set of (M+2) linear algebraic equations.

Combination of the equations for gas phase and deposition surface finally results in a set of (2NG(M+2)+2NS) algebraic equations, which are solved simultaneously using a modified Newton-Raphson method in the standard NAG-library routine C05NBF (NAG, 1991).

2.6 Conclusions

A laboratory reactor setup has been designed for the investigation of the kinetics of the low pressure CVD of polycrystalline silicon. A thorough examination of the mass and heat transport phenomena inside the laboratory reactor showed that mixing on reactor scale is accomplished by fast molecular diffusion. Since penetration of the laminar jets is confined to a small region close to the inlet nozzles, recirculation of the reactor content by means of convective mass transport is practically absent. Micromixing effects can be neglected, because the gas phase reaction network does not comprise non-(pseudo-)first order reactions with characteristic times comparable to or smaller than the micromixing time. The effectiveness of both heat transport on reactor scale and heat transfer between deposition surface and gas phase is large enough to consider temperature uniformity over the complete reactor. Whereas no mass transfer resistances exist for silane and hydrogen, irreducible mass transfer resistances are present for the gas phase intermediates formed during the pyrolysis of silane, e.g. silylene and disilane. These resistances are caused by the very high surface consumption rates of these intermediates compared to their transport rate by molecular diffusion. The shape of their concentration profiles is a complex function of two dimensionless numbers, i.e. the Damköhler-II number based on their surface reaction kinetics and a modified Thiele modulus based on their gas phase reaction kinetics. Since these concentration gradients need to be considered during the simulation of the kinetic experiments, a one-dimensional reactor model has been developed explicitly accounting for these gradients by considering molecular diffusion with simultaneous gas phase reactions.

References

Azay, P., Côme, G.-M., 1979, *Ind. Eng. Chem. Process Des.*, **18**(4), 754.

Beek, J., Miller, R.S., 1959, *Chem. Eng. Prog. Symp. Ser.*, **55**, 33.

Becerra, R., Walsh, R., 1992, *J. Phys. Chem.*, **96**, 10856.

Bird, R.B., Stewart, W.E., Lightfoot, E.N., 1960, Transport Phenomena, Wiley, New York.

Boudart, M., 1968, Kinetics of Chemical Processes, Prentice-Hall, Inc., New Jersey.

Buss, R.J., Ho, P., Breiland, W.G., Coltrin, M.E., 1988, *J. Appl. Phys.*, **63**(8), 2808.

Carslaw, H.S., Jaeger, J.C., 1959, Conduction of Heat in Solids, Oxford University Press, Ely House, London.

Coltrin, M.E., Kee, R.J., Evans, G.H., 1989, *J. Electrochem. Soc.*, **136**, 819.

Coltrin, M.E., Kee, R.J., Miller, J.A., 1984, *J. Electrochem. Soc.*, **131**, 425.

Coltrin, M.E., Kee, R.J., Miller, J.A., 1986, *J. Electrochem. Soc.*, **133**, 1206.

Croon, M.H.J.M. de, Giling, L.J., 1990, *J. Electrochem. Soc.*, **137**(11), 3606.

David, R., Matras, D., 1975, *Can. J. Chem. Eng*, **53**, 297.

David, R., Villermaux, J., 1973, *Can. J. Chem. Eng.*, **51**, 630.

David, R., Villermaux, J., 1978, *J. de Chimie Physique*, **75**, 656.

Finlayson, B.A., 1972, The Method of Weighted Residuals and Variational Principles, Academic Press, New York.

Fluent version 3.02, 1990, User Manual, Flow Simulation International Limited, Sheffield.

Gates, S.M., 1988, *Surf. Sci.*, **195**, 307.

Gates, S.M., Greenlief, C.M., Beach, D.B., Holbert, P.A., 1990a, *J. Chem. Phys.*, **92**(5), 3144.

Gates, S.M., Greenlief, C.M., Kulkarni, S.K., Sawin, H.H., 1990b, *J. Vac. Sci. Technol. A*, **8**(3), 2965.

Inoue, G., Suzuki, M., 1985, *Chem. Phys. Lett.*, **122**, 361.

Kistiakowky, G.B., Volpi, G.G., 1957, *J. Chem. Phys.*, **27**, 1141.

Kleijn, C.R., 1991, Transport Phenomena in Chemical Vapor Deposition Reactors, Ph.D. Thesis TUD, Delft.

Lede, J., Villermaux, J., 1977, *J. Chim. Phys.*, **74**, 468.

Longwell, J.P., Weiss, M.A., 1955, *Ind. Eng. Chem.*, **47**, 1634.

Mears, D.E., 1971, *Journal of Catalysis,* **20**, 127.

Moffat, H.K., Jensen, K.F., 1988, *J. Electrochem. Soc.,* **135**(2), 459.

NAG, Fortran Library Manual, 1991, Mark 15, NAG Ltd, Wilkinson House, Oxford.

Patankar, S.V., 1980, Numerical Heat Transfer and Fluid Flow, Hemisphere Publishing, New York.

Patel, K., Smith, J.M., 1975, *J. Cat.*, **40**, 383.

Reid, R.C., Prausnitz, J.M., Poling, B.E., 1987, The Properties of Gases and Liquids, 4*th* edition, McGraw-Hill, New York.

Roenigk, K.F., 1987, Analysis of Low Pressure Chemical Vapor Deposition Processes, Ph.D. Thesis University of Minnesota, Minnesota.

Scott, B.A., Gates, S.M., Greenlief, C.M., Estes, R.D., in: Mechanisms of Reactions of organometallic Compounds with Surfaces, Eds., D.J. Cole-Hamilton and J.O. Williams, Plenum Press, New York, 1989, 97.

Simon, J., Feurer, R., Reynes, A., Morancho, R., 1992, *Journal of Analytical and Applied Pyrolysis*, **24**, 51.

Westerterp, K.R., Swaay, W.P.M. van, Beenackers, A.A.C.M., 1990, Chemical Reactor Design and Operation, Wiley, New York.

Appendix 2A: Schematic representation of microbalance reactor setup

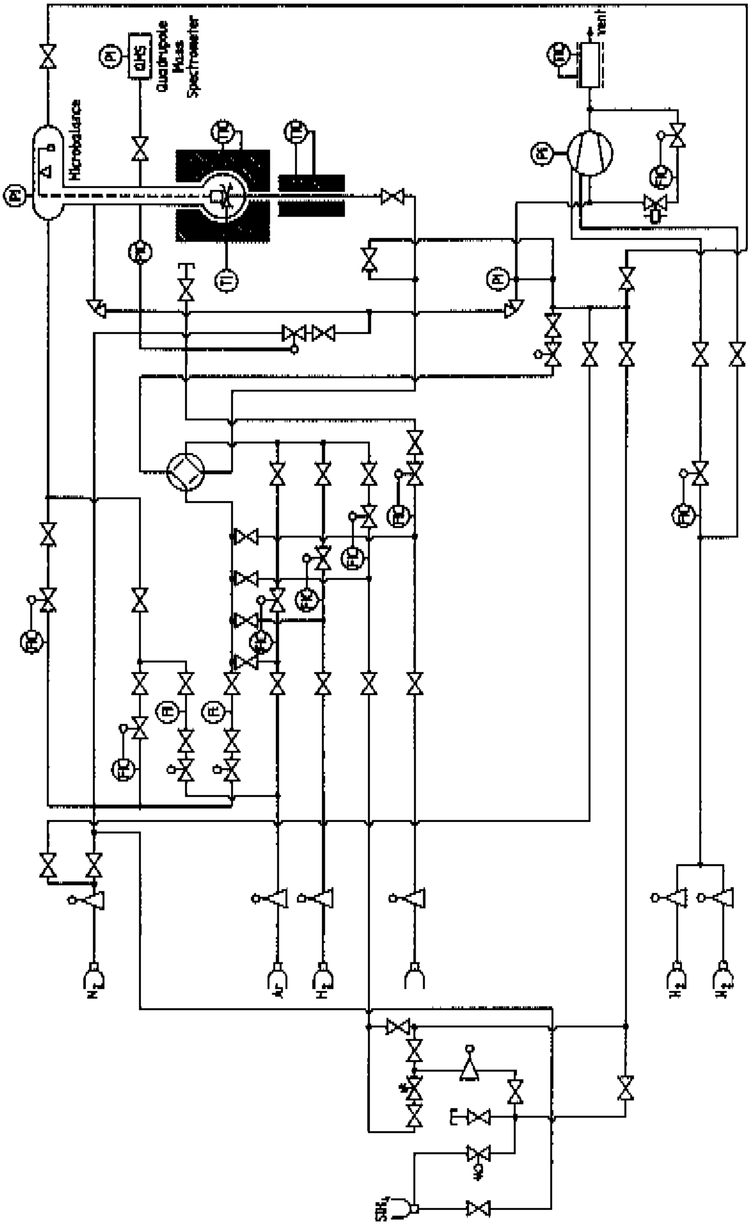


Pressure regulator


Valve


Dosing valve


Emergency shut-off valve


Excess flow shut-off valve


Pneumatic valve


4-way valve

Thermal mass flow controller

Temperature indicator/controller

Pressure indicator/controller

Flow indicator

Pressure indicator

Temperature indicator

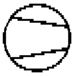
Dual-stage rotary vane
mechanical pump

Appendix 2B Analytical expressions for silylene concentration profile and corresponding diffusion layer thickness

In this Appendix expressions are derived for the concentration profile of silylene and the thickness of the corresponding diffusion layer.

Concentration profile

The continuity equation is given by:

$$-\frac{D_{SiH_2,m}}{r^2}\frac{d}{dr}\left(r^2\frac{dC_{SiH_2}}{dr}\right) = r_v' - k_v C_{SiH_2} - \frac{F_v}{V} C_{SiH_2} \qquad (2B.1)$$

with as boundary conditions:

$$r=0 \qquad \frac{dC_{SiH_2}}{dr} = 0 \qquad (2B.2)$$

$$r=R \qquad -D_{SiH_2,m}\frac{dC_{SiH_2}}{dr} = k_s C_{SiH_2} \qquad (2B.3)$$

In order to integrate the second order differential equation with corresponding boundary conditions, the concentration is rewritten as:

$$C_{SiH_2} = \frac{r_v'}{\frac{F_v}{V} + k_v} + f \qquad (2B.4)$$

Substitution into equation (2B.1) results in:

$$\frac{1}{r^2}\frac{d}{dr}\left(r^2\frac{df}{dr}\right) = \alpha f \qquad (2B.5)$$

with:

$$\alpha = \frac{F_v}{V D_{SiH_2,m}} + \frac{k_v}{D_{SiH_2,m}} \qquad (2B.6)$$

The general solution to equation (2B.5) is given by:

$$f = c_1 \frac{\sinh(\sqrt{\alpha}\, r)}{r} + c_2 \frac{\cosh(\sqrt{\alpha}\, r)}{r} \tag{2B.7}$$

The boundary condition at r=0, given by equation (2B.2), leads to a value of zero for the coefficient c_2. Hence, equation (2B.7) reduces to:

$$f = c_1 \frac{\sinh(\sqrt{\alpha}\, r)}{r} \tag{2B.8}$$

The coefficient c_1 is obtained by applying the boundary condition at r=R, given by equation (2B.3). The right-hand side of this equation is evaluated by substituting equation (2B.4) combined with equation (2B.8):

$$k_s C_{SiH_2} = \beta + k_s c_1 \frac{\sinh(R\sqrt{\alpha})}{R} \tag{2B.9}$$

with:

$$\beta = k_s \frac{r_v'}{\frac{F_v}{V} + k_v} \tag{2B.10}$$

The term on the left-hand side of equation (2B.3) is evaluated by taking the first derivative of equation (2B.8) at the boundary r=R:

$$-D_{SiH_2,m} \frac{df}{dr}\Big|_{r=R} = c_1 D_{SiH_2,m} \left(\frac{\sinh(R\sqrt{\alpha})}{R^2} - \frac{\sqrt{\alpha}\cosh(R\sqrt{\alpha})}{R} \right) \tag{2B.11}$$

Substituting equations (2B.9) and (2B.11) into equation (2B.3) results in:

$$c_1 = \frac{\beta}{\left(\frac{D_{SiH_2,m}}{R^2} - \frac{k_s}{R}\right)\sinh(R\sqrt{\alpha}) - \frac{D_{SiH_2,m}\sqrt{\alpha}}{R}\cosh(R\sqrt{\alpha})} \tag{2B.12}$$

Substituting equation (2B.12) into equation (2B.8) and the resulting expression into equation (2B.4) finally gives:

$$C_{SiH_2} = \frac{r_v'}{\frac{F_v}{V} + k_v} \left(1 - \frac{\frac{R}{r}\sinh((R\sqrt{\alpha})\frac{r}{R})}{(1 - \frac{D_{SiH_2,m}}{k_s R})\sinh(R\sqrt{\alpha}) + \frac{D_{SiH_2,m}}{k_s R} R\sqrt{\alpha}\cosh(R\sqrt{\alpha})} \right) \tag{2B.13}$$

with α given by equation (2B.6).

Diffusion layer thickness

The diffusion layer is defined as a fictitious layer in which no reaction would occur and over which there would exist a concentration gradient yielding a molar flux at the deposition surface identical to that in the presence of reaction in the gas phase. The thickness of the diffusion layer, δ, can be obtained from:

$$-D_{SiH_2,m} \frac{dC_{SiH_2}}{dr}\Big|_{r=R} = -D_{SiH_2,m} \frac{C_{SiH_2}|_{r=R} - C_{SiH_2}|_{r=0}}{\delta} \tag{2B.14}$$

Expressions for the concentrations at r=0 and r=R as well as for the first derivative of the concentration at r=R are obtained from equation (2B.13). Substitution into equation (2B.14) results in the following expression for the thickness of the diffusion layer:

$$\delta = R \frac{\sinh(R\sqrt{\alpha}) - R\sqrt{\alpha}}{R\sqrt{\alpha}\cosh(R\sqrt{\alpha}) - \sinh(R\sqrt{\alpha})} \tag{2B.15}$$

Appendix 2C Solution procedure for model equations

The method of orthogonal collocation is outlined for the differential equations with corresponding boundary conditions, given by equations (2.39) to (2.42). These are rewritten by replacing r by ξR_0:

$$\frac{1}{\xi^2}\frac{d}{d\xi}\left(\xi^2 N_i\right) = R_0 \sum_{k=1}^{ng} \nu_{k,i} r_{v,k} + R_0 (F_{i,0} - y_i F)/V_g \tag{2C.1}$$

$$\frac{dy_i}{d\xi} = R_0 \sum_{j \neq i} \frac{y_i N_j - y_j N_i}{C D_{i,j}} \tag{2C.2}$$

$$\xi = 1 \qquad N_i = \sum_{m=1}^{ns} \nu_{m,i} r_{s,m} \tag{2C.3}$$

$$\xi = R_1/R_0 \qquad N_i = -\sum_{m=1}^{ns} \nu_{m,i} r_{s,m} \tag{2C.4}$$

On the domain $1 \leq \xi \leq R_1/R_0$, the solution of the molar fraction is required to be symmetric about $\xi = 1$, whereas at the same time the solution of the molar flux needs to be antisymmetric about $\xi = 1$. Therefore, a polynomial is defined as a linear combination of both even and odd powers of ξ with the highest power being m:

$$P_m(\xi) = \sum_{c=0}^{m} c_c \xi^c \tag{2C.5}$$

The coefficients c_c are defined in such a way that the successive polynomials are orthogonal to all polynomials of order less than m, with some weighting function $w(\xi)$:

$$\int_a^b w(\xi)\, P_n(\xi)\, P_l(\xi)\, \xi^2\, d\xi = 0 \qquad \text{with } n \neq l \text{ and } n,l = 0,1,\ldots,m \tag{2C.6}$$

This orthogonality condition applies to spherical geometry and completely specifies the polynomials, once choices have been made concerning weigthing function and interval of integration. For the present computations, the weighting function $w(\xi)$ is set to one, while the integration interval is considered to range from a= 1.0 to $b=R_1/R_0= 2.218271$, see paragraph 2.5.1. The first polynomial $P_0(\xi)$ is set to one as well, thereby fixing the coefficients of all higher polynomials. The roots of the polynomial $P_m(\xi)$ in the interval $a \leq \xi \leq b$ are choosen as interior collocation points. A choice is made for *6th* order orthogonal collocation (m=6). Table 2C.1 lists the interior collocation points, calculated as the roots of the polynomial $P_6(\xi)$ by solving equation (2C.6).

Table 2C.1: *Roots of 6th order orthogonal polynomial with weighting function equal to one and range from 1.0 to 2.218271.*

ξ_2 = 1.047653159

ξ_3 = 1.231387361

ξ_4 = 1.500051149

ξ_5 = 1.786313363

ξ_6 = 2.029143622

ξ_7 = 2.180918767

Based on the above polynomials the following trial functions are defined as approximation for the solution of the molar flux and the molar fraction:

$$N(\xi) = b^n + d^n\xi + (1 - \xi)\left(\frac{R_1}{R_0} - \xi\right)\sum_{cc=1}^{M} a^n_{cc} P_{cc-1}(\xi) \qquad (2C.7)$$

$$y(\xi) = b^y + d^y\xi + (1 - \xi)\left(\frac{R_1}{R_0} - \xi\right)\sum_{cc=1}^{M} a^y_{cc} P_{cc-1}(\xi) \qquad (2C.8)$$

Each trial function features (M+2) coefficients, resulting from (M+2) conditions. For both the molar flux and the molar fraction M conditions are provided by the residuals evaluated at the M interior collocation points. In case of the molar flux two additional conditions are povided by the boundary conditions at ξ= 1 and ξ= R_1/R_0, whereas in case of the molar fraction two additional conditions are provided by the residuals evaluated at extra collocation points defined at the above boundaries. The trial functions are polynomials of degree (M+1) in ξ. These are rewritten as:

$$N(\xi) = \sum_{cc=1}^{M+2} d^n_{cc}\xi^{cc-1} \qquad (2C.9)$$

$$y(\xi) = \sum_{cc=1}^{M+2} d_{cc}^{y} \xi^{cc-1} \qquad (2C.10)$$

or in matrix notation as:

$$N = Q\, d^{n} \qquad y = Q\, d^{y} \qquad (2C.11)$$

with N, y, d^n and d^y vectors of length (M+2) and Q an (M+2)x(M+2) matrix. The operators for the molar flux and molar fraction in equations (2C.1) and (2C.2) are now replaced by the matrix operations:

$$\frac{1}{\xi^2}\frac{d}{d\xi}\left(\xi^2 N\right) = C\, Q^{-1} N = A\, N \qquad (2C.12)$$

$$\frac{dy}{d\xi} = D\, Q^{-1} y = B\, y \qquad (2C.13)$$

with the elements of the (M+2)x(M+2) square matrices defined as:

$$Q_{c,cc} = \xi_c^{cc-1} \qquad C_{c,cc} = (cc+1)\,\xi_c^{cc-2} \qquad D_{c,cc} = (cc-1)\,\xi_c^{cc-2} \qquad (2C.14)$$

The derivatives are thus expressed as a linear combination of the values of the solution of the molar flux or molar fraction at the collocation points. Substitution into equations (2C.1) to (2C.4) yields the following set of collocation equations:

$$\sum_{cc=1}^{M+2} A_{c,cc} N_{i,cc} = R_0 \sum_{k=1}^{ng} \nu_{k,i} r_{v,k} + R_0 \left(F_{i,0} - y_i F\right)/V_g \qquad c = 2 \ldots M+1 \qquad (2C.15)$$

$$\sum_{cc=1}^{M+2} B_{c,cc} y_{i,cc} = R_0 \sum_{j \neq i} \frac{y_i N_j - y_j N_i}{C D_{i,j}} \qquad c = 1 \ldots M+2 \qquad (2C.16)$$

$$N_i = \sum_{m=1}^{ns} \nu_{m,i} r_{s,m} \qquad c = 1 \qquad (2C.17)$$

$$N_i = -\sum_{m=1}^{ns} \nu_{m,i} r_{s,m} \qquad c = M+2 \qquad (2C.18)$$

In this way a set of (2NG-1)(M+2) independent nonlinear algebraic equations results with, at each collocation point, (NG-1) molar fractions and NG molar fluxes as unknowns.

Appendix 2D Expression for total molar flow rate at outlet of reactor

The total molar flow rate at the outlet of the reactor, F, is derived by summing equation (2.47) over all gas phase components considered:

$$F = F_0 - \sum_{i=1}^{NG} \iiint_{V_g} \nabla \cdot N_i \, dV + \sum_{i=1}^{NG} \iiint_{V_g} \sum_{k=1}^{ng} \nu_{k,i} r_{v,k} \, dV \tag{2D.1}$$

with F_0 the total molar flow rate at the inlet of the reactor. The second term on the right-hand side of this equation is evaluated using the divergence theorem of Gauss:

$$\iiint_{V_g} \nabla \cdot N_i \, dV = \iint_{A_g} N_i \cdot dA \tag{2D.2}$$

with the right term evaluated from the boundary conditions given by equations (2.41) and (2.42). The third term of equation (2D.1) is determined by means of the quadrature formula:

$$\int_1^{R_1/R_0} f(\xi)\, \xi^2 \, d\xi = \sum_{cc=1}^{M+2} w_{cc} f(\xi) \tag{2D.3}$$

with w_{cc} denoting the weighting factors. The final expression for the total molar flow rate at the outlet of the reactor now becomes:

$$\begin{aligned} F = F_0 &+ 4\pi R_1^2 \sum_{i=1}^{NG} \sum_{m=1}^{ns} \nu_{m,i} r_{a,m} \Big|_{\xi=R_1/R_0} + 4\pi R_0^2 \sum_{i=1}^{NG} \sum_{m=1}^{ns} \nu_{m,i} r_{a,m} \Big|_{\xi=1} \\ &+ 4\pi R_0^3 \sum_{i=1}^{NG} \sum_{cc=1}^{M+2} w_{cc} \sum_{k=1}^{ng} \nu_{k,i} r_{v,k} (\xi_{cc}) \end{aligned} \tag{2D.4}$$

In order to determine the weighting factors, w_{cc}, the integral in equation (2D.3) is evaluated for $f(\xi) = \xi^{cc-1}$:

$$\sum_{cc=1}^{M+2} w_{cc} f(\xi) = \frac{1}{cc+2} \xi^{cc+2} \Big|_1^{R_1/R_0} = f_{cc} \tag{2D.5}$$

and the resulting f vector, consisting of (M+2) elements f_{cc}, is multiplied with the inverse of the (M+2)x(M+2) Q matrix (Finlayson, 1972):

$$w^T = f^T Q^{-1} \tag{2D.6}$$

The resulting weighting factors are listed in Table 2D.1.

Table 2D.1: *Weighting factors*

$w_1 = 0$

$w_2 = 0.13147323$

$w_3 = 0.36005369$

$w_4 = 0.64903533$

$w_5 = 0.87369525$

$w_6 = 0.83918942$

$w_7 = 0.45172118$

$w_8 = 0$

3

EFFECTS OF PROCESS CONDITIONS

3.1 Introduction

The kinetics of the low pressure CVD of polycrystalline silicon has been the subject of a number of experimental studies carried out in conventional hot-wall multiwafer LPCVD reactors (Van den Brekel and Bollen, 1981; Claassen *et al.*, 1982; Jensen and Graves, 1983; Roenigk and Jensen, 1985; Holleman, 1993). Although the general trends observed in this type of reactors may be correlated with the chemistry and kinetics, the interpretation of these investigations is not straightforward because the growth rate is determined by both transport phenomena and intrinsic kinetics. Another shortcoming is that the growth rates are only determined at the end of a run and are quantitatively linked with the process conditions such as inlet composition and flow rates without taking into account the actual gas phase composition at the position where deposition occurs.

The present investigation reports on steady state experiments performed in the microbalance reactor setup, described in Chapter 2. This reactor allows a direct measurement of the growth rate combined with an on-line analysis of the corresponding gas phase composition. Surface characterization techniques are used to investigate the structure and quality of silicon layers deposited at typical LPCVD conditions. In order to assess the effects of the process variables, silicon growth rates as well as silane and Si_2H_x outlet molar flow rates have been measured over a wide range of total pressures, temperatures and feed compositions. An important topic concerns the isolation of regions in which the contribution of gas phase reactions can be neglected. Furthermore, the interplay between gas phase and surface reactions as a function of the process variables is investigated in the region where gas phase reactions contribute significantly to the silicon growth process.

3.2 Experimental conditions

A total of 300 kinetic experiments were performed over the range of experimental conditions listed in Table 3.1. This range coincides with the industrially relevant operation conditions for the deposition of polycrystalline silicon from silane in a conventional hot-wall multiwafer LPCVD reactor.

Table 3.1: *Range of experimental conditions investigated for the deposition of Si(s) from SiH_4.*

p_t	25 - 125	Pa
T	863 - 963	K
$V/F_{SiH_4,0}$	8.5 - 91	$m^3\ s\ mol^{-1}$
X_{SiH_4}	0.4 - 64	%
$H_2/SiH_4\|_0$	0 - 2	-
$SiH_4/Ar\|_0$	0.7 - 9	-

3.3 Characterization of deposited layers

The structure of the deposited layers was studied using Scanning Electron Microscopy (SEM) and Atomic Force Microscopy (AFM), the latter applied in the constant force mode (Binnig and Quate, 1986). The cross-sectional SEM micrograph in Figure 3.1 shows silicon layers deposited at different experimental conditions on top of each other. A columnar structure typical of polycrystalline silicon is visible. The AFM micrographs in Figure 3.2 illustrate the randomly distributed growth centra at the deposition surface. The grain size is approximately 0.1 μm.

The level of impurity elements in the deposited layers was determined using Auger Electron Spectroscopy (AES). The differentiated AES spectrum in Figure 3.3 shows the presence of carbon and oxygen at the surface. Other contaminants were not detected. The distribution of oxygen and carbon throughout the deposited layer was obtained from AES depth profiling by alternating cycles of argon-ion sputtering at a beam voltage of 5 keV, and measurement of the carbon, oxygen, and silicon contents.

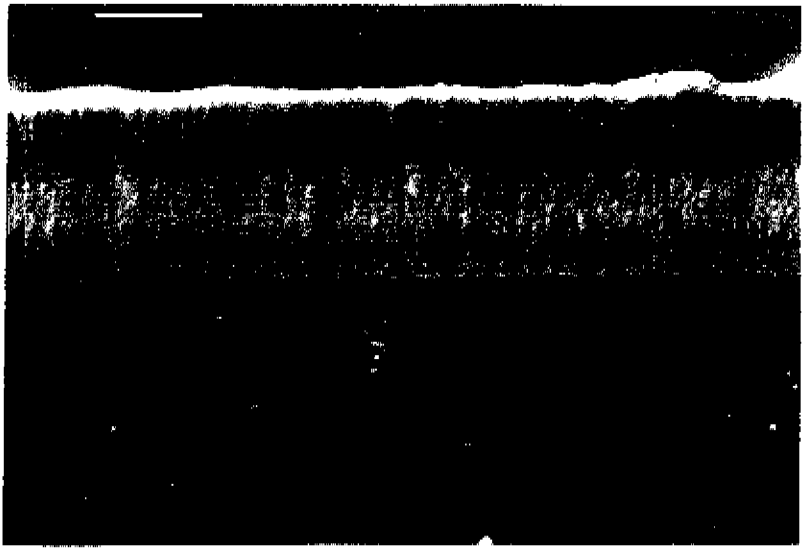

***Figure 3.1:** Scanning electron micrograph of cross section of silicon layers deposited at different experimental conditions on top of each other. Magnification: 1500X.*

Figure 3.4 shows an Auger depth profile of a polycrystalline silicon layer deposited in the microbalance reactor setup. The peak intensities of silicon (SI1: elemental silicon, SI2: both elemental silicon and silicon dioxide) and carbon (C1) are shown in relation to the peak intensity of oxygen (O1) before sputtering as a function of sputter time. A rough estimate of the sputter rate is 4±2 10^{-9} m min^{-1}. Within a distance of 2 10^{-9} m from the surface, corresponding to approximately five atomic layers, the oxygen and carbon impurities reach a level below the detection limit. The signal of elemental silicon (SI1) concurrently increases to a high and constant level. The SI2 signal does not change since its intensity is independent of the extent of oxygen adsorption. During the total sputter time of 60 min (2.4 10^{-7} m) the intensities remained unchanged. Thus, only the topmost layers encompass oxygen and carbon impurities. These impurities probably result from long exposure to the vacuum inside the microbalance reactor setup after deposition was completed. Carbon contamination is generally attributed to the use of an oil-based vacuum pump in low pressure CVD systems.

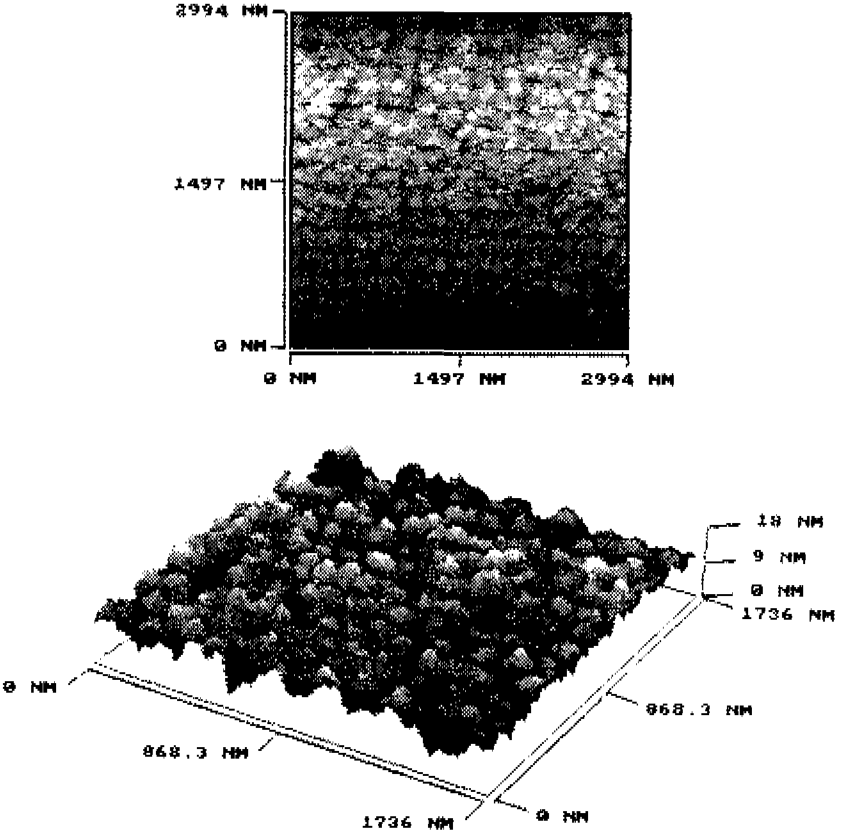

Figure 3.2: *2-D atomic force micrograph (a) with 3-D magnification (b) of surface of silicon layer. Deposition conditions:* $T = 913$ *K,* $p_t = 50$ *Pa,* $SiH_4/Ar|_0 = 4.0$*,* $F_{SiH_4,0} = 8.6$ 10^6 *mol* s^{-1}.

3.4 Space time

3.4.1 Delimitation of differential operating regime

A reactor is operated differentially when effects of reactant conversion on the production rates can be neglected:

$$0.95 < \frac{R(X_i)}{R(X_i + \Delta X_i)} < 1.05 \tag{3.1}$$

with X_i the conversion of reactant i and R the net production rate.

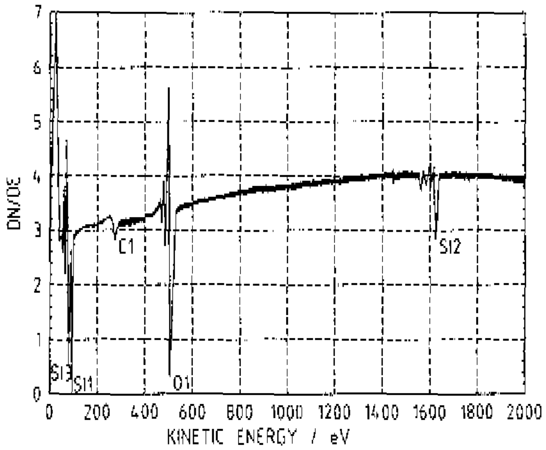

Figure 3.3: Differentiated Auger spectrum of silicon layer. Deposition conditions: $T= 909$ K, $p_t= 25$ Pa, $SiH_4/Ar|_0= 4.0$, $F_{SiH_4,0}= 2.1\ 10^{-6}$ mol s^{-1}. SI1: elemental silicon, SI2: elemental silicon and silicon dioxide, SI3: silicon dioxide, C1: carbon, O1: oxygen.

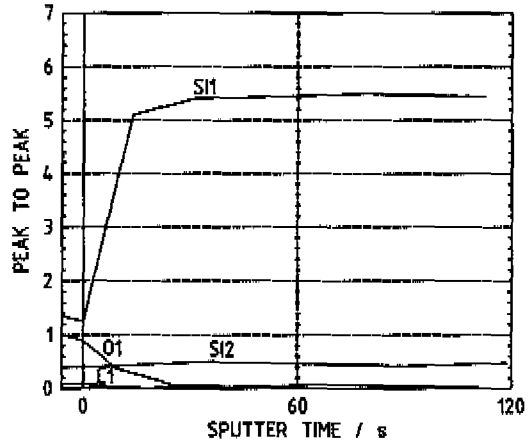

Figure 3.4: Auger depth profile of silicon layer. Deposition conditions: $T= 909$ K, $p_t= 25$ Pa, $SiH_4/Ar|_0= 4.0$, $F_{SiH_4,0}= 2.1\ 10^{-6}$ mol s^{-1}. SI1: elemental silicon, SI2: elemental silicon and silicon dioxide, C1: carbon, O1: oxygen.

At differential operating conditions the production rate is determined by the feed composition only. Flow patterns in the reactor become irrelevant, and the measured conversions can be used directly to determine the net production rates. In the present experimental study differential operating regimes with respect to silane conversion and silicon deposition are distinguished.

In order to assess the regime of differential operation with respect to silane conversion, complete sets of conversion versus space time data were obtained at different temperatures, total pressures and feed compositions. Differential operation with respect to reactant conversion is in general satisfied in case the conversion versus space time curves are straight lines through the origin. Without feeding hydrogen the differential regime appears to be delimited by 912 K at 50 Pa. The transition temperature between differential and non-differential operation is observed to gradually decrease with increasing total pressure and amounts to 863 K at 100 Pa. Cofeeding hydrogen appears to expand the differential regime towards 125 Pa at 912 K. With increasing temperature the upper bound of the differential regime moves to lower total pressures. At 963 K the differential regime is delimited by 50 Pa.

On the other hand, delimitation of the regime of differential operation with respect to silicon deposition requires comparison of complete sets of growth rate versus conversion data at different total pressures, temperatures and feed compositions. Figure 3.5 shows the silicon growth rate as a function of silane conversion at 912 K and different total pressures without feeding hydrogen. At pressures above 50 Pa the growth rate is significantly effected by a small change in conversion, indicating that differential operating conditions with respect to silicon deposition are not satisfied at higher pressures. Addition of hydrogen expands the range of differential conditions towards 100 Pa, see Figure 3.6, probably as a result of lowering the silane partial pressure. Figure 3.7 shows the effect of temperature on the growth rate versus conversion data at 25 Pa without feeding hydrogen. Up to 912 K the reactor is operated differentially. Similar sets of growth rate versus conversion data at higher pressures reveal that the differential operating regime is delimited by 912 K and 50 Pa in case no hydrogen is fed. Cofeeding hydrogen expands the differential regime towards 963 K at 25 Pa, see Figure 3.8. For both type of experiments the transition temperature between differential and non-differential operation gradually decreases with increasing pressure. In case no hydrogen is fed, transition occurs around 863 K at 100 Pa. Feeding hydrogen extends the differential regime to 912 K at the same pressure.

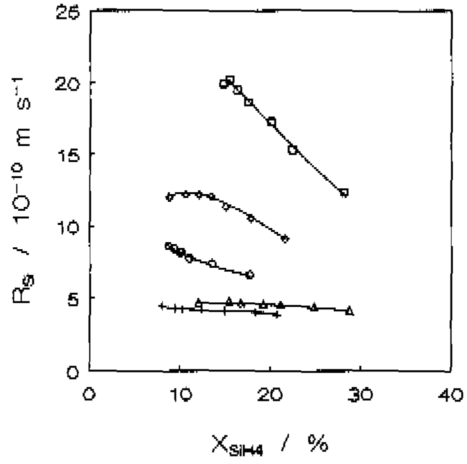

Figure 3.5: *Silicon growth rate versus silane conversion. $SiH_4/Ar|_0$= 4.0, T= 912 K. + p_t= 25 Pa, △ p_t= 50 Pa, o p_t= 80 Pa, ◇ p_t= 100 Pa, □ p_t= 125 Pa.*

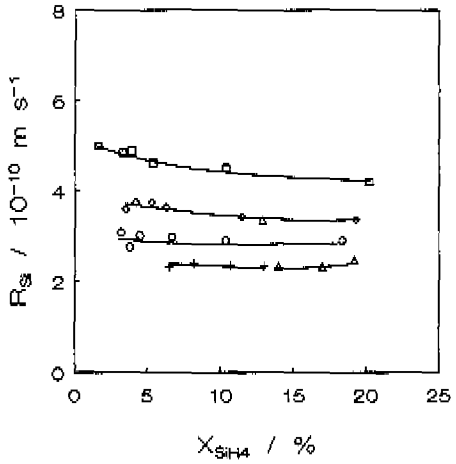

Figure 3.6: *Silicon growth rate versus silane conversion. $SiH_4/H_2|_0$= 1.0, SiH_4/Ar= 4.5, T= 912 K. + p_t= 25 Pa, △ p_t= 50 Pa, o p_t= 80 Pa, ◇ p_t= 100 Pa, □ p_t= 125 Pa.*

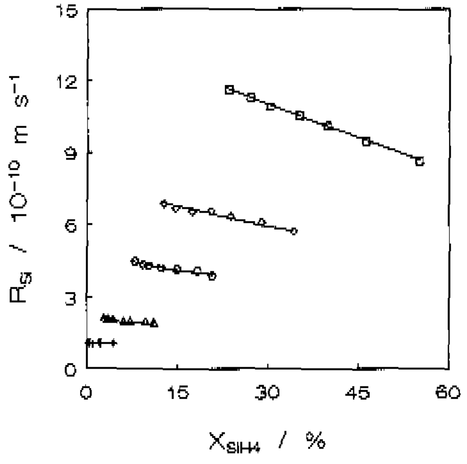

Figure 3.7: *Silicon growth rate versus silane conversion. $SiH_4/Ar|_0$= 4.0, p_t= 25 Pa. + T= 863 K, △ T= 887 K, T= 912 K, ◇ T= 937 K, □ T= 963 K.*

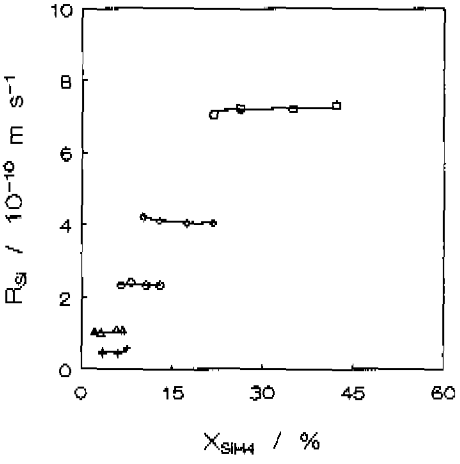

Figure 3.8: *Silicon growth rate versus silane conversion. $SiH_4/H_2|_0$= 1.0, $SiH_4/Ar|_0$= 4.5, p_t= 25 Pa. + T= 863 K, o △ T= 887 K, o T= 912 K, ◇ T= 937 K, □ T= 963 K.*

3.4.2 Contribution of gas phase reactions

The deviation from differential operation is probably due to the onset of gas phase reactions. Evidence for the participation of larger silicon hydride species in the deposition process exists even at the silane pressures employed in the LPCVD regime (Scott *et al.*, 1988; Holleman, 1993).

Figure 3.9 shows the effect of silane space time on the normalized Si_2H_x concentration at 912 K and different total pressures. This concentration refers to the outlet of the laboratory reactor. It has been calculated based on the measured outlet molar flow rates of argon, silane and Si_2H_x and the hydrogen outlet molar flow rate obtained from a simple hydrogen mass balance over the reactor, see paragraph 4.3.1. Except for 50 Pa, a maximum in normalized Si_2H_x concentration is observed at each pressure. The maxima are attained at short space times. With increasing pressure the maximum Si_2H_x concentration increases without changing the corresponding space time. The height of the maximum changes proportionally to the second power of the total pressure.

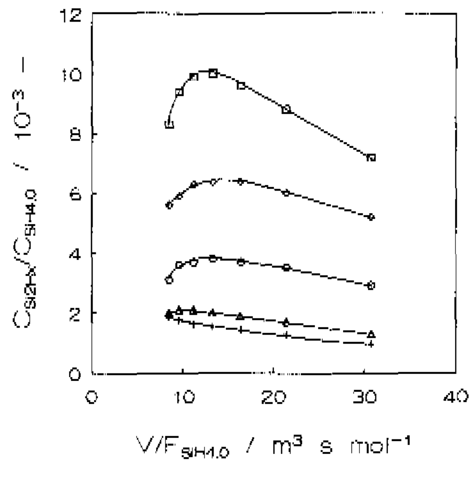

Figure 3.9: *Normalized Si_2H_x concentration versus silane space time. $SiH_4/Ar|_0$= 4.0, T= 912 K. + p_t= 50 Pa, △ p_t= 60 Pa, ○ p_t= 80 Pa, ◇ p_t= 100 Pa, □ p_t= 125 Pa.*

Figure 3.10 shows the effect of space time on the normalized Si_2H_x concentration at the reactor outlet at 100 Pa and different temperatures. With increasing temperature the maximum Si_2H_x concentration increases while shifting to shorter space times.

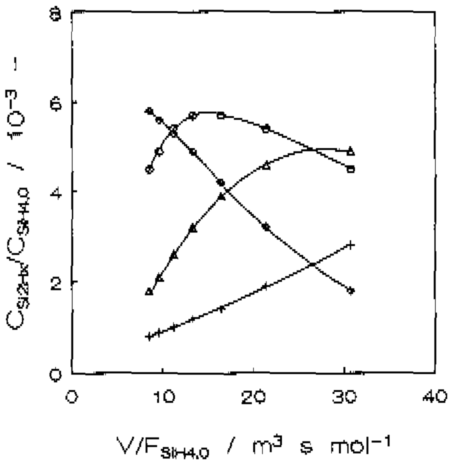

***Figure 3.10:** Normalized Si_2H_x concentration versus silane space time. $SiH_4/Ar|_0 = 4.0$, $p_t = 100$ Pa. + T= 863 K, △ T= 887 K, o T= 912 K, ◇ T= 937 K.*

The trends depicted in Figures 3.9 and 3.10 can be qualitatively explained on the basis of a perfectly stirred tank reactor and the parallel-consecutive kinetic scheme shown in Figure 3.11. The following simplifications were made. The gas/solid mass transfer resistances in general existing for all homogeneously formed gas phase intermediates, see paragraph 2.4.1, are neglected. Hence, the gas phase composition governing the growth rate is identical to the gas phase composition obtained at the outlet of the reactor. Furthermore, it is assumed that the contribution from the isomers H_3SiSiH and H_2SiSiH_2 to the Si_2H_x response measured at the outlet of the reactor can be neglected and hence that the Si_2H_x concentrations depicted in Figures 3.9 and 3.10 merely reflect Si_2H_6 concentrations.

According to the kinetic scheme of Figure 3.11 silicon is deposited either via a direct reaction of silane with the surface or from disilane produced during pyrolysis of silane. The concentration curves shown in Figures 3.9 and 3.10 suggest strongly that upon extrapolation to zero space time, the concentration goes to zero indicating that disilane is not a primary product in silane pyrolysis. There is currently widespread agreement that the route to disilane involves unimolecular dissociation of silane to silylene, SiH_2, and molecular hydrogen and subsequent insertion of silylene into silane (Burgess and Zachariah, 1990; Becerra and Walsh, 1992; Ring and O'Neal, 1992). It is known that the production of disilane is determined by the kinetics of the initial silane decomposition reaction. At typical LPCVD conditions, this unimolecular reaction lies in its low-pressure limit and the corresponding reaction rate coefficient can be written as the product of a second order reaction rate coefficient and the concentration of third bodies, see paragraph 5.3.1. Since hydrogen is an inefficient collider, the latter concentration is taken equal to the actual concentration of silane, giving rise to second-order kinetics with respect to silane. The rate expression for gas phase production of disilane thus becomes:

$$r_2 = k_2\, C_{SiH_4}^2 \tag{3.2}$$

The silicon deposition reactions are considered to be first order in silane or disilane and inversely proportional to the total concentration or inlet concentration of silane to the power m:

$$r_1 = k_1\, C_{SiH_4,0}^{-m}\, C_{SiH_4} \tag{3.3}$$

$$r_3 = k_3\, C_{SiH_4,0}^{-m}\, C_{Si_2H_6} \tag{3.4}$$

The dependence on the inlet concentration of silane to the power -m is qualitatively in accordance with results from H_2 Temperature Programmed Desorption (TPD) (Gates *et al.*, 1990; Imbihl *et al.*, 1989). The relative sticking probabilities (s/s_0) of silane and disilane were found to decrease with increasing exposure or reactant pressure as a result of increasing hydrogen surface coverage, see Figure 4.1 and Figure 5.2.

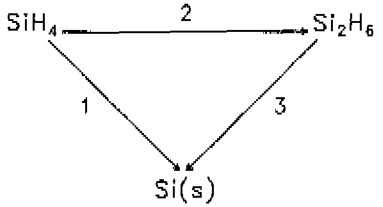

Figure 3.11: *Parallel-consecutive kinetic scheme for deposition of silicon from silane.*

For the above kinetics the continuity equations for silane and disilane for a perfectly stirred tank reactor now become:

$$F_v\, C_{SiH_4,0} - F_v\, C_{SiH_4} - k_1\, C_{SiH_4,0}^{-m}\, C_{SiH_4}\, V - 2\, k_2\, C_{SiH_4}^2\, V = 0 \tag{3.5}$$

$$- F_v\, C_{Si_2H_6} + k_2\, C_{SiH_4}^2\, V - k_3\, C_{SiH_4,0}^{-m}\, C_{Si_2H_6}\, V = 0 \tag{3.6}$$

These continuity equations are based on a constant volumetric flow rate, i.e. volume changes as a result of reaction stoichiometry are not taken into account. Using the hypothesis that the characteristic time for gas phase production of disilane, $(k_2 C_{SiH_4,0})^{-1}$, is much larger than the mean residence time, V/F_v, the following expressions can be derived for the concentrations of silane and disilane:

$$C_{SiH_4} = \frac{C_{SiH_4,0}}{1 + k_1\, C_{SiH_4,0}^{-m}\, V/F_v} \tag{3.7}$$

$$C_{Si_2H_6} = \frac{k_2\, C_{SiH_4,0}^{2}\, V/F_v}{(1 + k_1\, C_{SiH_4,0}^{-m}\, V/F_v)^2\,(1 + k_3\, C_{SiH_4,0}^{-m}\, V/F_v)} \tag{3.8}$$

Dividing equation (3.8) by the inlet concentration of silane and substituting the mean residence time by $C_{SiH_4,0} V/F_{SiH_4,0}$ gives the following expression for the normalized disilane concentration:

$$\frac{C_{Si_2H_6}}{C_{SiH_4,0}} = \frac{k_2\, C_{SiH_4,0}^{2}\, V/F_{SiH_4,0}}{(1 + k_1\, C_{SiH_4,0}^{1-m}\, V/F_{SiH_4,0})^2\,(1 + k_3\, C_{SiH_4,0}^{1-m}\, V/F_{SiH_4,0})} \tag{3.9}$$

with $V/F_{SiH_4,0}$ denoting the silane space time. The maximum value of the normalized disilane concentration, which is obtained by equating the first derivative with respect to silane space time of equation (3.9) to zero, is given by:

$$\frac{C_{Si_2H_6}}{C_{SiH_4,0}}\Big|_{max} = \frac{k_2\, C_{SiH_4,0}^{1+m}}{4\, k_3\, (1 + \frac{k_1}{4\, k_3}\, \alpha)^2\, (1 + \frac{1}{4}\, \alpha)} \tag{3.10}$$

with:

$$\alpha = \sqrt{1 + \frac{8\, k_3}{k_1}} - 1 \tag{3.11}$$

and occurs at a space time given by:

$$V/F_{SiH_4,0}\Big|_{max} = \frac{\alpha}{4\, k_3\, C_{SiH_4,0}^{1-m}} \tag{3.12}$$

As noted earlier total pressure does not effect the position of the maximum, but changes its height according to a second power dependence, see Figure 3.9. The relations given by equations (3.10) to (3.12) correctly describe these experimental trends for m equal to 1. In addition, with increasing temperature the maximum shifts to shorter space times while increasing in heigth, see Figure 3.10. Assuming that both deposition reactions possess the same temperature dependence, the effect of temperature on position and heigth of the maximum is, according to equations (3.10) to (3.12), contained in the factors $k_2C_{SiH_4,0}^2/k_3$ and $1/k_3$, respectively. In the small range of temperatures applied, the inlet concentration of silane is hardly effected by a change in temperature. Hence, agreement with the experimental trends depicted in Figure 3.10 is obtained if silicon deposition from disilane and consequently from silane is activated, with an activation energy smaller than that corresponding to the gas phase production of disilane.

For sufficiently short space times, the normalized disilane concentration increases linearly with space time according to:

$$\lim_{V/F_{SiH_4,0} \to 0} \left(\frac{C_{Si_2H_6}}{C_{SiH_4,0}} \right) = k_2\, C_{SiH_4,0}^2\, V/F_{SiH_4,0} \qquad (3.13)$$

It should be noted that this result is independent of the type of rate equations used for the deposition of silicon from silane and disilane. The initial slopes of the curves shown in Figures 3.9 and 3.10 are determined by the value of $k_2C_{SiH_4,0}^2$ i.e. by the gas phase production rate of disilane in the limit of small silane conversion. As a result of the pressure dependence of the inlet concentration of silane, the initial slope at given range of space times should increase quadratically with increasing total pressure. Although the number of experimental points at short space time is small, see Figure 3.9, extrapolation of the curves to zero space time indeed results in a positive correlation between the initial slope and the total pressure squared. According to equation (3.10) temperature should also effect the slope provided the second order reaction rate coefficient k_2 is temperature dependent. The results depicted in Figure 3.10 indicate a clear positive correlation between temperature and initial slope, corresponding to an activated gas phase production of disilane. Comparison of the initial slopes in the temperature range from 863 to 912 K results in an activation energy of 233 kJ mol^{-1}. This value is in good agreement with the range of activation energies found in literature for the initial reaction in silane pyrolysis, i.e. unimolecular decomposition of silane into silylene and hydrogen. Purnell and Walsh (1966) experimentally obtained a value of 234 kJ mol^{-1} in the temperature range 650-700 K and at pressures ranging from 5 to 30 kPa, whereas Newman *et al.* (1979) found a value of 221 kJ mol^{-1} at 530 kPa in the temperature range between 1035 and 1184 K.

A rough estimate for the relative contributions to silicon deposition from disilane and silane is obtained from:

$$S = \frac{2\,k_3\,C_{Si_2H_6}}{k_1\,C_{SiH_4}} \tag{3.14}$$

The factor two in the numerator accounts for the incorporation of two silicon atoms per disilane molecule reacting at the surface. Substituting the expressions for the silane and disilane concentration, given by equations (3.7) and (3.8), for m equal to 1 gives:

$$S = \frac{2\,k_2\,k_3\,C^2_{SiH_4,0}\;V/F_{SiH_4,0}}{k_1\,(1+k_1\,V/F_{SiH_4,0})\,(1+k_3\,V/F_{SiH_4,0})} \tag{3.15}$$

For sufficiently short space times, equation (3.15) reduces to:

$$\lim_{V/F_{SiH_4,0}\to 0} S = \frac{2\,k_2\,k_3}{k_1}\,C^2_{SiH_4,0}\;V/F_{SiH_4,0} \tag{3.16}$$

At sufficiently small silane conversions, the relative contribution of disilane to the silicon deposition process increases proportionally with increasing space time and quadratically with increasing inlet concentration of silane, i.e. with increasing total pressure. Furthermore, it exhibits the same positive temperature dependence as the initial reaction in silane pyrolysis provided k_1 and k_3 have similar temperature dependences.

3.5 Pressure

The laboratory reactor is operated differentially with respect to silicon deposition up to total pressures of 50 Pa and temperatures of 912 K when no hydrogen is fed. Deviation from differential operation at higher total pressures is probably due to the onset of gas phase reactions. This is in line with the results of Holleman and Verweij (1993) who studied the kinetics of silicon deposition in a conventional hot-wall multiwafer LPCVD reactor. The measured silicon growth rates appeared to be independent of interwafer spacing up to total pressures of 60 Pa while feeding pure silane at 900 K, indicating the insignificance of gas phase reactions up to this pressure.

In order to rule out interference of gas phase reactions with the deposition process, a discrimination is made between total pressures in the ranges from 25 to 50 Pa and from 50 to 125 Pa. The total pressure rather than the inlet partial pressure of silane is chosen as independent variable, because it more uniquely reflects the importance of gas phase reactions.

3.5.1 Pressure range from 25 to 50 Pa

The experimental data reveal an increasing silicon growth rate with increasing inlet partial pressure of silane. Partial reaction orders between 0.28 and 0.44 are obtained at 912 K, depending on silane space time and feed composition.

Different reports concerning the dependence of the silicon growth rate on silane partial pressure are found in literature. At typical LPCVD conditions Claassen *et al.* (1982) and Hitchman *et al.* (1979) report growth rates that are linear in silane pressure, whereas the data of Van den Brekel and Bollen (1981) reveal a less than linear dependence. Holleman and Aarnink (1981) report growth rates that are proportional to the square root of the silane partial pressure. Except LPCVD studies, numerous high temperature (1023-1373 K) studies of the direct reaction of silane with a silicon surface have been reported. Notable among these studies is the early work of Farrow (1974). Farrow observed a linear dependence of the silicon growth rate on silane partial pressure over a temperature range from 293 to 1473 K and silane pressures ranging from 1 10^{-3} to 133 Pa. This dependence is supported by later work of Henderson and Helm (1972), Duchemin *et al.* (1978) and Farnaam and Olander (1984).

3.5.2 Pressure range from 50 to 125 Pa

Figure 3.12 shows the effect of total pressure on silicon growth rate and silane conversion at 912 K and different silane space times. Compared to the pressure effect on the growth rate in the differential regime, i.e. at pressures up to 50 Pa, a more pronounced effect is observed here. In particular at short space time, the silicon growth rate increases drastically with increasing pressure.

The Si_2H_x selectivity generally decreases with increasing silane conversion, see Figure 3.13. The effects of process conditions on the experimentally observed selectivities can thus be disguised by simultaneous changes in conversion. Therefore, an unambiguous determination of the effect of total pressure on the selectivity requires the comparison of complete sets of selectivity versus conversion data at different total pressures, as shown in Figure 3.13 as well. At a given silane conversion the Si_2H_x selectivity increases more than linearly with increasing pressure, indicating the occurrence of gas phase reactions towards Si_2H_x components. The amount of Si_2H_x

components in the gas phase varies between 0.1 and 1 mol%. Due to the high surface reactivity of the Si_2H_x components, but also of silylene being a key intermediate in the formation of these components, a significant increase in silicon growth rate takes place as shown in Figure 3.12a. Van den Brekel and Bollen (1981) measured a typical ratio of 10^5:10^2:1 between monosilane, disilane and trisilane at the outlet of a conventional LPCVD reactor. Although the observed Si_2H_x molar fractions are in good agreement with the ratio found by these authors, Si_3H_x components were not detected in the laboratory reactor. The amounts of these components were obviously too small to fall within the detection limit of the quadrupole mass spectrometer (1 ppm).

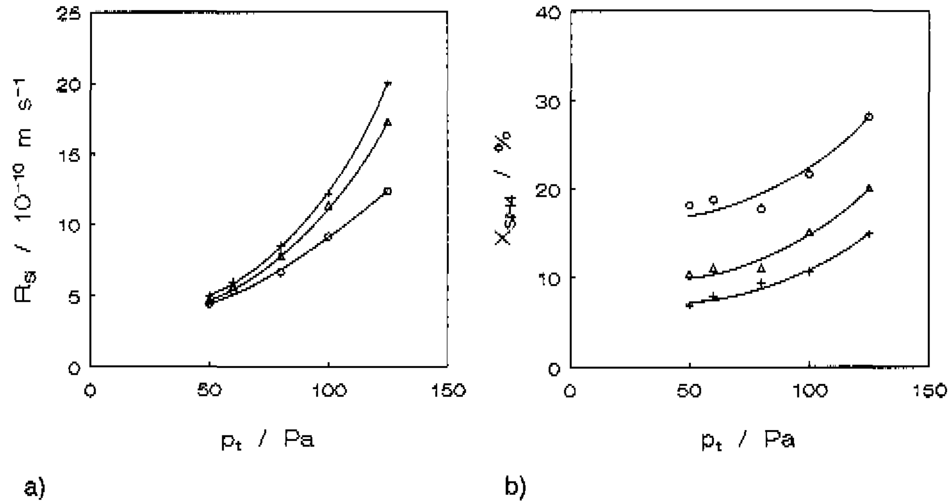

Figure 3.12: Silicon growth rate (a) and silane conversion (b) versus total pressure. $SiH_4/Ar|_0$= 4.0, T= 912 K. + $V/F_{SiH_4,0}$= 9.6 m^3 s mol^{-1}, ▵ $V/F_{SiH_4,0}$= 16.4 m^3 s mol^{-1}, o $V/F_{SiH_4,0}$= 30.7 m^3 s mol^{-1}.

3.6 Inlet hydrogen-to-silane ratio

The effect of the inlet hydrogen-to-silane ratio on the silicon growth rate at 912 K and total pressures of 25 and 50 Pa is shown in Figure 3.14. The use of the inlet hydrogen-to-silane ratio instead of the actual prevailing one is justified, because the laboratory reactor is operated differentially at the conditions considered here, see paragraph 3.4.1. Changing a 1:2 H_2/SiH_4 into a 5:4 H_2/SiH_4 feed ratio reduces the silicon growth rate by approximately 15%. Due to hydrogen adsorption vacant surface sites are blocked and silane adsorption becomes more difficult. As a result the silicon growth rate drops. At 25 Pa hydrogen inhibition is slightly more pronounced than at 50 Pa.

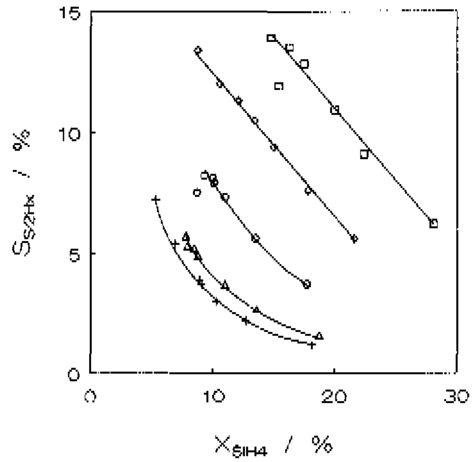

Figure 3.13: *Si_2H_x selectivity versus silane conversion. $SiH_4/Ar|_0$= 4.0, T= 912 K. + p_t= 50 Pa, ▵ p_t= 60 Pa, o p_t= 80 Pa, ◇ p_t= 100 Pa, □ p_t= 125 Pa.*

Apparently conflicting reports concerning the existence of a hydrogen effect are found in the literature. Henderson and Helm (1972), van den Brekel and Bollen (1981), Buss *et al.* (1988), Robbins and Young (1987) and Foster *et al.* (1986) report no evidence for hydrogen inhibition. However, Claassen *et al.* (1982) observed that the growth rate is inversely proportional to the hydrogen pressure for silane partial pressures less than 10 Pa in a hydrogen ambient at 898 K and 66 Pa total pressure. The same authors, however, detected no variation in growth rate in either hydrogen or nitrogen ambients at silane partial pressures higher than 10 Pa. According to Van den Brekel and Bollen (1981) these observations may be explained in terms of incomplete gas heat up in the case of nitrogen ambients. In accordance with the results of Claassen *et al.* (1982), Holleman and Aarnink (1981) and Holleman (1993) report growth rates that are inversely proportional to the hydrogen partial pressure at 898 K. According to these authors the hydrogen inhibiting effect becomes weaker at higher temperatures and turns into an inverse square root dependence at 973 K. Hottier and Cadoret (1981) observed different hydrogen pressure dependences on monocrystalline and polycrystalline silicon layers. On single-crystalline silicon, the growth rate exhibited an inverse square root dependence, whereas on polycrystalline silicon the inhibiting effect was described by an inverse proportional dependence. Experiments of Duchemin *et al.* (1978) with silane partial pressures up to 26 Pa and temperatures up to 1263 K are in support of the inverse square root dependence on hydrogen pressure. These authors attributed this effect to dissociative adsorption of molecular hydrogen. It should be noted that when a hydrogen effect is reported large excesses of hydrogen have been used. Absence of inhibiting effects is in general reported in those cases where only small excesses of hydrogen have been used.

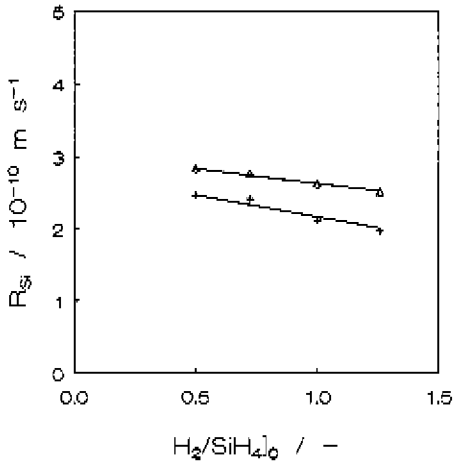

Figure 3.14: *Silicon growth rate versus inlet hydrogen-to-silane ratio. T= 912 K, $F_{SiH_4,0}$= 2.6 10^{-6} mol s^{-1}, F_0= 6.3 10^{-6} mol s^{-1}, argon as balance. + p_t= 25 Pa, △ p_t= 50 Pa.*

3.7 Temperature

Figure 3.15 shows the silicon growth rate, silane conversion and Si_2H_x selectivity as a function of temperature at two different silane space times. With increasing temperature the silicon growth rate and the silane conversion increase. The Si_2H_x selectivity shows a maximum which moves to lower temperatures with increasing space time. Concurrently, the heigth of the maximum decreases slightly.

Figure 3.16 shows the silicon growth rate versus reciprocal temperature in the temperature range from 863 to 963 K at 50 Pa total pressure. A comprehensive UHV study of Buss *et al.* (1988) reports a change in rate-determining step between 900 and

1100 K depending on the silane fluxes, i.e. the silane partial pressures, used. Below this transition temperature, the silicon surface is nearly fully covered with hydrogen and hydrogen desorption completely determines the silicon growth rate. According to Buss *et al.* (1988), this regime is characterized by an apparent activation energy in the range 230-250 kJ mol^{-1}. As temperature increases, the surface coverage of hydrogen starts to decrease and silane adsorption gradually takes over as rate-determining step. As a result, the apparent activation energy decreases and finally reaches a value close to zero.

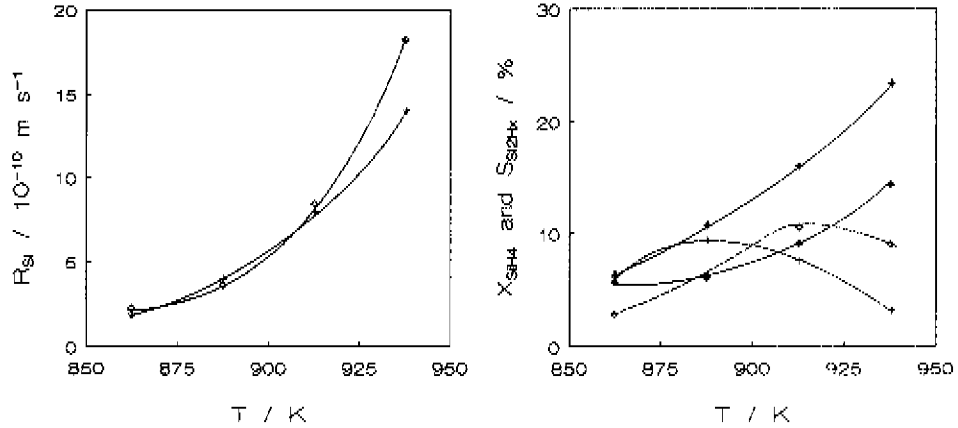

Figure 3.15: Silicon growth rate (a), silane conversion (   ) and Si_2H_x selectivity (-----) (b) versus temperature. $SiH_4/Ar|_0$= 4.0, p_t= 100 Pa. ◊ ♦ $V/F_{SiH_4,0}$= 8.5 m^3 s mol^{-1}, + + $V/F_{SiH_4,0}$= 21.4 m^3 s mol^{-1}.

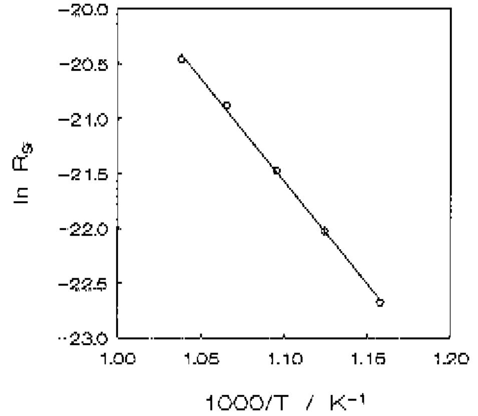

Figure 3.16: Silicon growth rate versus reciprocal temperature. p_t= 50 Pa, $SiH_4/Ar|_0$= 4.0, $V/F_{SiH_4,0}$= 21.9 m^3 s mol^{-1}.

A change in rate-determining step is not reflected by the experimental results depicted in Figure 3.16. The apparent activation energy obtained from the least-mean-squares slope amounts to 155.5 kJ mol^{-1}. This value indicates that the experiments were conducted in a kinetic regime where hydrogen desorption is particularly important. Apparent activation energies for silicon deposition at LPCVD conditions range from 130 kJ mol^{-1} to 180 kJ mol^{-1} (Rosler, 1977; Hottier and Cadoret, 1981; Van den Brekel and Bollen, 1981; Beers and Bloem, 1982; Claassen *et al.*, 1982; Holleman, 1993).

3.8 Conclusions

The laboratory reactor satisfies differential operation with respect to silane conversion and silicon deposition up to roughly 912 K and 50 Pa in case pure silane is fed. Cofeeding hydrogen expands the regime of differential operation towards higher total pressures and higher temperatures, probably as a result of lowering the silane partial pressure.

In the differential operating regime partial reaction orders of silane typically range from 0.28 to 0.44, depending on silane space time and feed composition. The apparent activation energy of the silicon deposition process amounts to 155.5 kJ mol^{-1}, indicating that the kinetic experiments were conducted in a kinetic regime where hydrogen desorption is particularly important. Cofeeding hydrogen inhibits the silicon growth. Due to the adsorption of hydrogen vacant surface sites are blocked and, as a result, silane adsorption is hampered.

Departure from differential operating conditions at higher pressures and temperatures can be attributed to the occurrence of gas phase reactions. At total pressures higher than 50 Pa, a maximum is attained in the normalized Si_2H_x concentration, $C_{Si_2H_x}/C_{SiH_4,0}$, versus silane space time. The position of the maximum is independent of pressure. Its height, however, increases quadratically with pressure. In addition, with increasing temperature the maximum shifts to shorter space times while increasing in heigth. These trends can be qualitatively explained on the basis of a perfectly stirred tank reactor model and a parallel-consecutive kinetic scheme accounting for silicon deposition from silane and from disilane produced during pyrolysis of silane. In this strongly simplified model gas phase production of disilane follows second order kinetics with respect to silane, whereas the silicon deposition reactions are considered first order in silane or disilane and inversely proportional to the total concentration or the inlet concentration of silane. In case the latter reactions are activated in roughly the same way, gas phase production of disilane is found to be more activated. It has the same positive temperature dependence as the initial reaction in silane pyrolysis, i.e. unimolecular dissociation of silane into silylene and hydrogen. The obtained activation energy amounts to 233 kJ mol^{-1}. At sufficiently small silane conversions, a similar dependence on the total pressure and the temperature is found for the relative contribution of disilane to the silicon deposition process and, hence, for the relative importance of gas phase reactions.

References

Becerra, R., Walsh, R., 1992, *J. Phys. Chem.*, **96**, 10856.

Beers, A.M., Bloem, J., 1982, *Appl. Phys. Lett.*, **41**, 153.

Binnig, G., Quate, C.F., 1986, *Phys. Rev. Lett.*, **56**(9).

Brekel, C.H.J. van den, Bollen, L.J.M., 1981, *J. Cryst. Growth*, **54**, 310.

Burgess, D., Zachariah, M.R., 1990, *Mat. Res. Soc. Symp. Proc.*, **168**, 31.

Buss, R.J., Ho, P., Breiland, W.G., Coltrin, M.E., 1988, *J. Appl. Phys.*, **63**(8), 2808.

Claassen, W.A.P., Bloem, J., Valkenburg, W.G.J.N., van den Brekel, C.H.J., 1982, *J. Cryst. Growth*, **57**, 259.

Duchemin, M.J., Bonnet, M.M., Koelsch, M.F., 1978, *J. Electrochem. Soc.*, **125**, 637.

Farnaam, M.K., Olander, D.R., 1984, *Surf. Sci.*, **145**, 390.

Farrow, R.F.C., 1974, *J. Electrochem. Soc.*, **121**, 899.

Foster, D.W., Learn, A.J., Kamins, T.I., 1986, *J. Vac. Sci. Technol. B*, **4**, 1182.

Gates, S.M., Greenlief, C.M., Kulkarni, S.K., Sawin, H.H., 1990, *J. Vac. Sci. Technol. A*, **8**(3), 2965.

Henderson, R.C., Helm, R.F., 1972, *Surf. Sci.*, **30**, 310.

Hitchman, M.L., Kane, J., Widmer, A.E., 1979, *Thin Solid Films*, **59**, 231.

Holleman, J., 1993, Kinetics of Polycrystalline Tungsten and Silicon CVD, Ph.D. Thesis, Twente University of Technology.

Holleman, J., Aarnink, T., in *Proceedings of the Eight International Conference on CVD, 1981*, edited by J.M. Blocher, Jr., G.E. Vuillard, and G. Wahl (The Electrochemical Society, Pennington, NJ, 1981), 307.

Hottier, F., Cadoret, R., 1981, *J. Cryst. Growth*, **52**, 199.

Imbihl, R., Demuth, J.E., Gates, S.M., Scott, B.A., 1989, *Physical Review B*, **39**(8), 5222.

Jensen, K.F., Graves, D.B., 1983, *J. Electrochem. Soc.*, **130**(9), 1950.

Newman, C.G., O'Neal, H.E., Ring, M.A., Leska, F., Shipley, N., 1979, *Int. J. Chem. Kinet.*, **11**, 1167.

Purnell, J.H., Walsh, R., 1966, *Proc. R. Soc. London A.*, **293**, 543.

Ring, M.A., O'Neal, H.E., 1992, *J. Phys. Chem.*, **96**, 10848.

Robbins, D.J., Young, I.M., 1987, *Appl. Phys. Lett.*, **50**, 1575.

Roenigk, K.F., Jensen, K.F., 1985, *J. Electrochem. Soc.*, **132**(2), 448.

Rosler, R.S., 1977, *Solid State Technol.*, **20**, 63.

Scott, B.A., Estes, R.D., Jasinski, J.M., 1988, *J. Chem. Phys.*, **89**(4), 2544.

4

KINETICS IN THE ABSENCE OF GAS PHASE REACTIONS

4.1 Introduction

The chemisorption of silane and subsequent surface steps towards solid silicon have been investigated recently using ultra-high vacuum (UHV) techniques such as temperature programmed desorption (TPD) combined with static secondary ion mass spectrometry (SSIMS) (Gates, 1988; Greenlief *et al.*, 1989; Gates *et al.*, 1990a,b,c), laser-induced thermal desorption (LITD) (Sinniah *et al.*, 1989; Sinniah *et al.*, 1990), scanning tunneling microscopy (STM) (Boland, 1991,1992) and modulated molecular beam scattering (MMBS) (Farnaam and Olander, 1984). These mechanistic studies were performed on well-defined single-crystalline silicon surfaces such as Si(100)-(2x1) and Si(111)-(7x7), which have been considered extensively in literature (Chadi, 1979; Takayanagi *et al.*, 1985; Hamers *et al.*, 1986; Roberts and Needs, 1990).
The mechanistic information provided by these studies has been used as a basis of several surface chemical kinetic models for very low pressure silicon growth from silane on Si(100) (Gates *et al.*, 1990c; Greve and Racanelli, 1991; Gates and Kulkarni, 1991). Greve and Racanelli (1991) derived an expression for the silicon growth rate based on a four-step mechanism and regressed this expression on experimental growth rate data obtained by ultra-high vacuum chemical vapor deposition (UHVCVD) at total pressures around 0.1 Pa. Gates and Kulkarni (1991) applied a similar mechanism for the simulation of literature data for both silicon growth rate and hydrogen surface coverage measured as a function of temperature.

Recently, Holleman and Verweij (1993) reported on a comprehensive kinetic study of the decomposition of silane in a conventional hot-wall multiwafer LPCVD reactor at total pressures between 10 and 1000 Pa. Heterogeneous and homogeneous decomposition of silane were separated by varying the amount of wafer area per unit volume and the silane partial pressure as well as the total pressure. In order to simulate the silicon growth rates obtained in the region where gas phase reactions could be omitted, a five-step mechanism was developed including the most important mechanistic aspects of the above mentioned UHV studies. The silicon growth rate could be described adequately in terms of the reaction rate coefficients of silane adsorption and hydrogen desorption only. An important drawback of this investigation is that the growth rates were determined at the end of a run and quantitatively linked with the inlet composition, total pressure and flow rates without taking into account the actual gas phase composition at the position where deposition occurred.

The present work reports on the development of a six-step elementary reaction mechanism valid in the region of process conditions where the contribution of gas phase reactions can be omitted. This mechanism is derived by modelling of the kinetic experiments lying mainly in the differential operating regime derived in paragraph 3.4.1 and is based on the above mentioned mechanistic and kinetic studies. It should be noted that direct translation of results obtained under UHV conditions to a reaction mechanism applicable under LPCVD conditions is not obvious. Under LPCVD conditions the surface reactions occur on polycrystalline silicon, incorporating many crystallographic orientations with specific chemical features. Moreover, even when the order of reaction and hence the kinetic parameters for an elementary reaction are clear under controlled UHV conditions, the situation may be different under LPCVD conditions, where kinetics may be coverage dependent.

In order to simulate the experimentally obtained growth rates, model equations are derived coupling the silicon growth rate to the governing gas phase composition inside the reactor. The kinetic and thermodynamic parameters present in the modelling equations are estimated using a single-response nonlinear minimization routine (Marquardt, 1963). Discrimination among rival models is based on statistical testing, whenever it is not possible by direct process observation or physico-chemical laws. The purpose of the developed kinetic model is to provide a statistically sound and a physically reasonable description of the experimental data.

4.2 Construction of reaction network

The basis for the reaction network used in the present work is given by the elementary reactions (1-6) listed in Table 4.1. This way of presenting a reaction network was developed by Temkin (1971) and allows a straightforward calculation of the net production rates of the components involved in the surface reactions. Reaction (1) concerns dissociative adsorption of silane. Depending on the crystallographic orientation of the silicon surface used, two distinct adsorption mechanisms have been identified in the literature. On Si(100)-(2x1) silane was found to adsorb dissociatively forming a surface trihydride species, SiH_3^*, and a hydrogen adatom, H^*, as shown in Table 4.1 (Gates *et al.*, 1990a,b,c). The symbol * denotes a dangling bond on a vacant silicon surface atom. The number density of dangling bonds on Si(100)-(2x1) amounts to 6.8 10^{18} m^{-2} (Feldman *et al.*, 1980). The two dangling bonds required for silane adsorption could originate from the silicon surface atoms of one Si-Si dimer or from the surface atoms of two adjacent Si-Si dimers (Gates *et al.*, 1990b). On Si(111)-(7x7), possessing a number density of dangling bonds equal to 3.0 10^{18} m^{-2} (Takayanagi *et al.*, 1985; Avouris and Wolkow, 1989), formation of a surface dihydride species, SiH_2^*, was observed with simultaneous release of molecular hydrogen (Farnaam and Olander, 1984; Gates *et al.*, 1990b,c):

$$SiH_4 + * \rightarrow SiH_2* + H_2 \tag{4.1}$$

Table 4.1: *Elementary reactions considered on the silicon surface (1-6) and global reactions (α,β).*

	σ_α	σ_β	
$SiH_4 + 2^* \rightarrow SiH_3^* + H^*$	1		(1)
$SiH_3^* + {}^* \rightarrow SiH_2^* + H^*$	1		(2)
$SiH_2^* + {}^* \rightarrow SiH^* + H^*$	1		(3)
$SiH^* \rightarrow Si(s) + H^*$	1		(4)
+			
$SiH_4 + 4^* \rightarrow Si(s) + 4H^*$		1	(α)
$H^* \rightleftharpoons H^\theta + {}^*$		2	(5)
$H^* + H^\theta \rightleftharpoons H_2 + {}^*$		2	(6)
+			
$SiH_4 \rightarrow Si(s) + 2H_2$			(β)

Gates *et al.* (1990b) ascribed the difference in adsorption mechanism to the difference in distance between adjacent dangling bonds on Si(111)-(7x7), i.e. 0.7 nm (Takayanagi *et al.*, 1985), and dangling bonds on the dimers on Si(100)-(2x1), i.e. 0.24 nm (Ciraci and Batra, 1986). Reported activation energies, however, show no disparity, regardless of crystallographic orientation. Gates *et al.* (1989) found a value of 13 kJ mol^{-1} for the Si(111)-(7x7) surface. In a later paper, Gates and Kulkarni (1991) postulated the same value as a good approximation for the Si(100)-(2x1) surface. Buss *et al.* (1988) obtained values ranging from 0 to 17 kJ mol^{-1} for adsorption on polycrystalline silicon.

An appropriate measure for the surface reactivity of a gas phase species is denoted by the sticking probability, s, which is defined as the net rate of adsorption divided by the rate of collision with the surface (Boudart and Djéga-Mariadassou, 1984). Scott *et al.* (1989) measured a sticking probability $\leq 1\ 10^{-5}$ for silane towards Si(111)-(7x7) at room temperature. The sticking probability decreased strongly with hydrogen coverage, approaching $5\ 10^{-7}$ at 0.5 monolayer of adsorbed hydrogen. Gates *et al.* (1990b,c) obtained sticking probabilities on clean surfaces, s_0, of $3\ 10^{-5}$ and $2\ 10^{-5}$ for silane adsorption at 673 K on Si(100)-(2x1) and Si(111)-(7x7), respectively. Plots of the relative sticking probability, s/s_0, versus hydrogen surface coverage, θ_H, at this temperature are shown in Figure 4.1.

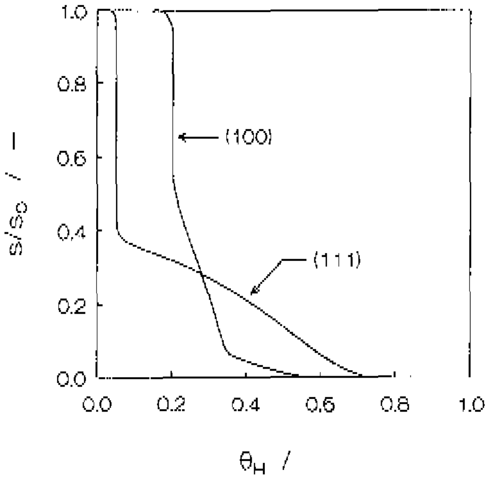

Figure 4.1: Relative sticking probability of SiH_4 versus the hydrogen surface coverage for Si(100)-(2x1) and Si(111)-(7x7). T_s= 673 K (Gates et al., 1990c).

A sharp drop by a factor of roughly 2 occurs at low θ_H. This abrupt decrease in s/s_0 was attributed to filling of reactive defect sites. At high θ_H the Si(100)-(2x1) and Si(111)-(7x7) surfaces clearly exhibit different saturation behaviour towards silane. On Si(100)-(2x1) saturation occurred when ~1 10^{18} SiH_4 m^{-2} were adsorbed, corresponding to 4 10^{18} H m^{-2} or θ_H= 0.6 H/Si, which is well below one monolayer. According to Gates *et al.* (1990b,c) saturation resulted from the requirement of two adjacent dangling bonds for adsorption via reaction (1) of Table 4.1. On Si(111)-(7x7), however, no saturation occurred up to exposures of 10^{25} SiH_4 m^{-2}. The corresponding θ_H approached 1 H/Si, despite the fact that the density of dangling bonds on the Si(111)-(7x7) surface is 0.39 dangling bond per surface silicon atom (Avouris and Wolkow, 1989). Obviously, silane adsorption on a hydrogen covered Si(111) surface is not restricted to the dangling bonds as required for the adsorption reaction given by equation (4.1). Gates *et al.* (1990b) proposed a mechanism involving insertion of surface H or SiH_x fragments into strained surface Si-Si bonds with an activation energy in the range 4-21 kJ mol^{-1}.

In the present work silane adsorption is considered to proceed through reaction (1) of Table 4.1, which is in line with the work of Holleman and Verweij (1993). The inclusion of the adsorption reaction given by equation (4.1) did not further improve the modelling results. Evidence for the irreversible adsorption of silane is provided by the TAP (Temporal Analysis of Products) alternating pulse experiments with silane and deuterium presented in paragraph 7.3.1, revealing no desorption of deuterated silicon containing gas phase species. Reaction (1) is treated here as an elementary reaction obeying third order kinetics, but will undoubtedly comprise a number of lower order elementary reactions in reality.

Trihydride decomposition is assumed to occur through interaction with a vacant surface site without direct release of molecular hydrogen into the gas phase, reaction (2) of Table 4.1, which is completely in line with the results of Greenlief *et al.* (1989) and Gates *et al.* (1990a). The stability of the surface trihydride species is controlled by the number of dangling bonds or vacant surface sites. This effect was manifested in a slight decrease of the pseudo-first order pre-exponentional factor of trihydride decomposition on Si(100)-(2x1) as the number of dangling bonds decreased (Gates *et al.*, 1990a).

Dihydride decomposition is known to proceed via at least two mechanisms. Gates *et al.* (1990a) postulated that a surface dihydride species decomposes via interaction with a vacant surface site, see reaction (3) of Table 4.1. An additional reaction observed for dihydride decomposition involves direct release of molecular hydrogen into the gas phase (Gupta *et al.*, 1988; Greenlief, 1989; Gates *et al.*, 1990a):

$$2SiH_2* \rightarrow 2SiH* + H_2 \qquad (4.2)$$

As indicated in paragraph 3.7, silicon growth is controlled predominantly by the rate of hydrogen desorption in the complete range of process conditions investigated, see Table 3.1. Consequently, hydrogen adatoms are the only kinetically significant surface species and the surface concentrations of the silicon hydride species are negligible. Due to the abundance of vacant surface sites compared to sites occupied by dihydride species, reaction (3) of Table 4.1 is more likely to occur than the reaction given by equation (4.2). Moreover, the use of the second order dihydride decomposition reaction does not lead to essentially different model equations than those treated in paragraph 4.3.2, indicating the insensitivity of the deposition kinetics for the kinetics of dihydride decomposition.

In the present work monohydride species, SiH*, and hydrogen adatoms, H*, are treated as separate surface species, although experimentally not distinguishable. The basic difference between these species is that the hydrogen atom in SiH* is bonded to a silicon adatom, whereas H* denotes a hydrogen atom bonded to a silicon surface atom. Monohydride decomposition is considered to proceed via reaction (4) of Table 4.1. In most mechanistic and kinetic modelling studies, monohydride decomposition is taken into account through global reaction (γ) of Table 4.2 assuming first order kinetics with respect to the hydrogen surface coverage (Gates *et al.*, 1990b,c; Gates and Kulkarni, 1991; Greve and Racanelli, 1991; Holleman and Verweij, 1993). Besides the assumption of first order hydrogen desorption kinetics, no further specifications are made with regard to the underlying mechanism. In the present work, however, global reaction (γ) is thought to consist of the elementary reactions (4-6), describing the formation of solid silicon and the subsequent recombinative desorption of hydrogen.

Table 4.2: *Elementary reactions (4-6) considered in monohydride decomposition via global reaction (γ).*

	σ_{γ}	
$SiH^{*} \rightarrow Si(s) + H^{*}$	2	(4)
$H^{*} \rightleftharpoons H^{\theta} + {}^{*}$	1	(5)
$H^{*} + H^{\theta} \rightleftharpoons H_2 + {}^{*}$	1	(6)
+ ------------------------------------		
$2SiH^{*} \rightarrow 2Si(s) + H_2 + 2^{*}$		(γ)

In the usual picture of recombinative hydrogen desorption, the hydrogen adatoms diffuse from site to site, occasionally undergoing a collision leading to reaction and desorption:

$$2H* \rightarrow 2* + H_2 \tag{4.3}$$

Such mechanism, which is frequently observed for recombinative hydrogen desorption from metal surfaces, yields a desorption rate varying quadratically with the hydrogen surface coverage. Neglecting the role of the surface bonding during the desorption process, the standard enthalpy of hydrogen desorption is equal to $2D^0$(Si-H)-D^0(H-H), where D^0 is the bond strength. Substituting a H-H bond strength equal to 439 kJ mol^{-1} and assuming an Si-H bond strength of 376 kJ mol^{-1} (Walsh *et al.*, 1981) the standard hydrogen desorption enthalpy amounts to 314 kJ mol^{-1}. Studies of hydrogen desorption from Si(111)-(7x7) indeed report second order kinetics with respect to the hydrogen surface coverage, described in terms of the above mentioned mechanism with activation energies around 254 kJ mol^{-1} (Schulze and Henzler, 1983; Koehler *et al.*, 1988; Wise *et al.*, 1991). Reider *et al.* (1991A) observed an intermediate desorption order of 1.56 for the same surface.

For Si(100)-(2x1), however, studies of hydrogen desorption report first order kinetics with respect to the hydrogen surface coverage with activation energies ranging from 188 to 243 kJ mol^{-1} (Wise *et al.* 1991; Sinniah *et al.*, 1989,1990; Höfer, 1992). The origin of this unusual first order desorption kinetics is still a matter of debate. Wise *et al.* (1991) measured first order kinetics with an activation energy of 243±8 kJ mol^{-1}. These authors proposed that surface dimerization, present on the (2x1) reconstructed surface and absent on the (7x7) surface, is responsible for the unusual first order kinetics. The transformation of the two singly occupied dangling bonds on a Si-Si dimer into a π-bond lowers the total energy of the Si-Si dimer by 21-75 kJ mol^{-1} (Nachtigall *et al.*, 1991; Boland, 1991,1992). Adsorption of a hydrogen atom, on the other hand, breaks this π-bond to form a Si-H bond on one side and a true dangling bond on the other side of the dimer. Therefore a partially hydrogen covered surface can lower the total energy by the pairing of the hydrogen adatoms on dimers, resulting in Si-Si dimers with either no hydrogen or two hydrogen adatoms bonded to them. Pairwise occupation of the dimers becomes thus energetically favorable relative to singly occupied dimers. Assuming the π-bond energy is totally regained through pairwise desorption, the standard enthalpy of hydrogen desorption lies in the range 239-293 kJ mol^{-1}. In case hydrogen adsorption is considered to be non-activated, the range of activation energies for hydrogen desorption is the same and thus in good agreement with the value found by Wise *et al.* (1991). Such a preferential pairing was indeed observed in recent scanning tunneling microscopy (STM) studies of annealed H/Si(100)-(2x1) surfaces by Boland (1991,1992). Initially at room temperature, hydrogen adatoms singly occupied the Si dimer units while at higher temperatures, ~630 K, these adatoms tended to pair up. Furthermore, at low coverages hydrogen adsorption was observed to be random and subsequent annealing to 630 K was observed to promote the hydrogen pairing. Based on these results Boland concluded that hydrogen adsorption is random, and thermally activated diffusion is necessary to generate the thermodynamically favored hydrogen pairing. However, TPD measurements of Widdra and Weinberg (1994) showed that hydrogen pairing occurred even at temperatures as low as 150 K without annealing to higher temperatures. Because of the high activation energies for hydrogen diffusion on silicon surfaces, e.g. 145 kJ mol^{-1} (Reider *et al.*, 1991B), these authors rejected the possibility that diffusion of adsorbed hydrogen is responsible for pairing.

A second mechanism frequently encountered for hydrogen desorption from Si(100)-(2x1) is that of Sinniah *et al.* (1989,1990), who measured first-order desorption kinetics with an apparent activation energy of 188±8 kJ mol^{-1}. In case of non-activated hydrogen adsorption, the standard enthalpy of hydrogen desorption is 188±8 kJ mol^{-1} as well and thus significantly lower than the above mentioned range, 239-293 kJ mol^{-1}. Sinniah *et al.* (1989) postulated a two-step mechanistic model, which incorporates the rather low apparent activation energy and the first order dependence on the hydrogen surface coverage. The mechanistic model is illustrated by reactions (5) and (6) of Table 4.1. The activated H_2 desorption reaction proceeds via excitation of a covalently bound hydrogen adatom from a localized Si-H bond to a two-dimensional delocalized state H^e. The H^e state is bound to the surface by 188 kJ mol^{-1}, i.e. 188 kJ mol^{-1} higher in energy than the original Si-H bond possessing a bond strength of 376 kJ mol^{-1}. The final elementary step in the recombinative desorption mechanism is the reaction of the excited delocalized hydrogen atom H^e with a localized hydrogen adatom leading to H_2 desorption, reaction (6). This reaction is considered to proceed potentially fast compared to excitation of a hydrogen adatom, reaction (5), giving rise to the first order desorption kinetics. Furthermore, the formation of a localized hydrogen adatom via interaction of a delocalized hydrogen atom with a vacant surface site is considered very slow. For any appreciable coverage of localized hydrogen adatoms the diffusion length of a H^e atom necessary to find such localized hydrogen adatom is not very large making recombination with another localized hydrogen adatom, reaction (6), much more likely to occur than interaction with a vacant surface site, the reverse of reaction (5). Based on isotope mixing experiments, Sinniah *et al.* (1990) rejected the possibility that desorption occurs via a pairing mechanism as described above. The authors dosed a clean Si(100)-(2x1) surface with 0.25 monolayers of deuterium and annealed to 650 K to promote pairing. The surface was then cooled to 120 K and exposed to an equivalent dose of hydrogen atoms. The measured thermal desorption yield revealed complete isotope mixing, i.e. H_2:HD:D_2~1:2:1, arguing against first order desorption kinetics due to recombination of prepaired hydrogen adatoms.

In the present work hydrogen desorption is accounted for via first order kinetics, which is in line with the work reported by Holleman and Verweij (1993). These authors found good agreement between calculated and measured growth rates assuming first order hydrogen desorption kinetics. From the above given considerations it is clear that the literature is not able to uniquely identify the mechanism of first order hydrogen desorption. Reported observations place severe constraints on both proposed mechanisms. In the present work a choice is made for the band model of Sinniah *et al.* (1989,1990). In order to take into account the hydrogen inhibition effects shown in paragraph 3.6, dissociative adsorption of molecular hydrogen was taken into account by considering reaction (6) of Table 4.1 reversible.

Gobal reaction (α) of Table 4.1 describes the decomposition of silane into solid silicon and four hydrogen adatoms through elementary steps (1-4). The decomposition reactions of the surface trihydride, dihydride and monohydride species are considered to be potentially fast compared to the adsorption reaction of silane. The rate of global reaction (α) is therefore given by the rate of silane adsorption via reaction (1). Concurrently, silane adsorption is considered to be potentially fast compared to hydrogen desorption, i.e. excitation of a covalently bound hydrogen adatom given by reaction (5) of Table 4.1. The latter step thus proceeds potentially slow compared to all the other steps of the reaction mechanism. However, it is not truly a rate-determining step in the classical use of the term (Boudart, 1968), since the steps leading to hydrogen adatom formation are not equilibrated.

The kinetic insignificance of the surface trihydride and dihydride species in the range of experimental conditions considered is consistent with the stabilities of these species measured recently by combining SSIMS and TPD (Greenlief *et al.*, 1989; Gates *et al.*, 1990a; Jasinski and Gates, 1991). Trihydride appeared to be the least stable and decomposed at temperatures beneath roughly 650 K. A region of intermediate temperature spanned from 650 to 750 K involving dihydride decomposition. The monohydride species were the most stable and decomposed at temperatures above roughly 750 K. This high monohydride stability seems in contradiction with the kinetic insignificance of these surface species invoked by the above treated mechanism. However, it is important to realize that the above mentioned experimental techniques are not able to distinguish between hydrogen desorption from silicon adatoms and hydrogen desorption from silicon surface atoms as a result of complete experimental resemblance between SiH^* and H^* (Gates *et al.*, 1990c).

4.3 Kinetic parameter determination

4.3.1 Experimental

Most of the experiments used during the kinetic modelling covered the differential operating regime determined in paragraph 3.4.1. The corresponding range of experimental conditions is shown in Table 4.3.

Table 4.3: *Range of experimental conditions where gas phase reactions can be neglected.*

p_t	25 - 50	Pa
T	863 - 963	K
$V/F_{SiH_4,0}$	22 - 91	$m^3\ s\ mol^{-1}$
X_{SiH_4}	0.4 - 64	%
$H_2/SiH_4\|_0$	0 - 2	-
$SiH_4/Ar\|_0$	0.7 - 9	-

As shown in paragraph 3.4.2, the contribution of gas phase reactions to the deposition can be neglected in the above range of experimental conditions. Silane, hydrogen and argon consequently form the only abundant gas phase components. In paragraph 2.4.1 it was shown that silicon deposition from silane is not accompanied with gas/solid mass transfer resistances. Hence, the gas phase composition governing the deposition rate is identical to the gas phase composition measured at the outlet of the reactor. Due to the low pumping efficiency for hydrogen, the outlet molar flow rate of this component was not measured quantitatively, see paragraph 2.2. Instead, the hydrogen outlet molar flow rate can be calculated from a simple hydrogen mass balance according to:

$$F_{H_2} = F_{H_2,0} + 2(F_{SiH_4,0} - F_{SiH_4}) \tag{4.4}$$

with $F_{i,0}$ and F_i the molar flow rates of component i at the inlet and outlet of the reactor. The actual gas phase composition inside the reactor is then calculated from:

$$C_i = \left(\frac{F_i}{F_{SiH_4} + F_{H_2} + F_{Ar}} \right) C \tag{4.5}$$

with C_i the concentration of component i and C the total gas phase concentration.

4.3.2 Model equations

The modelling equations are derived on the basis of a Langmuir surface, satisfying the following assumptions:

1] Adsorption is confined to one monolayer

2] Each adspecies is localized on an active site

3] The surface is uniform in the sense that all active sites are thermodynamically and kinetically identical

4] The thermodynamic and kinetic properties of adspecies are not influenced by the surface coverage, i.e. repulsive interactions from neighbouring adspecies are not taken into account.

As noted in paragraph 4.2, hydrogen adatoms form the only kinetically significant surface species at the experimental conditions applied. Starting from the mechanism shown in Table 4.1 with global reaction (α) and elementary reactions (5) and (6) as kinetically significant reactions, the steady state mass balance for hydrogen adatoms becomes:

$$4k_1 C_{SiH_4}\frac{L_*^2}{L_t} - k_5 L_{H*} + k_{-5} L_{H\theta} L_* - k_6 L_{H*} L_{H\theta} + k_{-6} C_{H_2} L_* = 0 \qquad (4.6)$$

Here, L_l is the surface concentration of component I and L_t the total surface concentration of active sites available for adsorption or reaction. The first term at the left-hand side represents the rate of hydrogen adatom production via global reaction (α), which is equal to four times the rate of silane adsorption via reaction (1). Each silane molecule converted to solid silicon produces four hydrogen adatoms, see global reaction (α). Silane adsorption is considered to proceed on nearest neighbour vacant surface sites. The rate of adsorption is therefore proportional to the concentration of pairs of adjacent vacant surface sites, i.e. to the concentration of dual adsorption sites. If the arrangement of vacant surface sites is such that each is surrounded by z equidistant sites, the concentration of dual adsorption sites is then one-half the product of the concentration of vacant surface sites, L_*, and the average number of adjacent vacant surface sites, $z\theta_*$ or $zL_*L_t^{-1}$ (Hougen and Watson, 1947). The factor of one half results from the fact that, in the summation represented by the product of the concentration of vacant surface sites and fraction of vacant surface sites, each pair of vacant surface sites is counted twice. Substituting $\theta_* = L_*L_t^{-1}$ results in an adsorption rate that is proportional to L_t and not to L_t^2 as it might appear prima facie. This is in line with the results of a more sophisticated treatment of a dual-site adsorption mechanism by Boudart and Djéga-Mariadassou (1984). In the present work the factor of ½z, denoting the number of kinetically equivalent adsorption possibilities, is accounted for through reaction rate coefficient k_1. The four terms left at the left-hand side represent the hydrogen adatom formation and disappearance rates corresponding to the elementary steps of reactions (5) and (6) and written in a straightforward way following the law of mass action.

An additional expression relating the concentration of hydrogen adatoms with that of vacant surface sites is obtained by equating the summed concentrations with the total concentration of active surface sites per square meter, L_t:

$$L_t = L_* + L_{H*} \tag{4.7}$$

The concentration of excited hydrogen atoms, $L_{H@}$, has been omitted from this equation, because these species are not bonded to the surface in the usual localized way. In the present work, L_t is taken equal to 1.13 10^{-5} mol m^{-2}, corresponding to the number density of dangling bonds on Si(100), 6.8 10^{18} m^{-2} (Feldman *et al.*, 1980). It should be noted that the reaction model makes no assumptions about the details of the surface structure.

It has been pointed out that desorption of molecular hydrogen via reaction of a delocalized hydrogen atom with a localized hydrogen adatom, reaction (6) of Table 4.1, is potentially very fast compared to formation of a delocalized hydrogen atom, reaction (5) of Table 4.1. An expression for the concentration of delocalized hydrogen atoms consequently is obtained by applying the steady state approximation for this species:

$$L_{H@} = \frac{k_5 L_{H*} + k_{-6} C_{H_2} L_*}{k_{-5} L_* + k_6 L_{H*}} \tag{4.8}$$

Substituting this expression into equation (4.6) and assuming that the recombination of a localized hydrogen adatom with a delocalized hydrogen atom is potentially very fast compared to the interaction of a delocalized hydrogen atom with a vacant surface site (Sinniah *et al.*, 1989,1990), i.e.:

$$k_{-5} L_* \ll k_6 L_{H*} \tag{4.9}$$

finally results in the following mass balance for hydrogen adatoms:

$$4 k_1 C_{SiH_4} \frac{L_*^2}{L_t} - 2 k_5 L_{H*} + \frac{2 k_5 K_H C_{H_2} L_*^2}{L_{H*}} = 0 \tag{4.10}$$

In this expression, K_H is the equilibrium coefficient of molecular hydrogen adsorption, defined as:

$$K_H = \frac{k_{-5}k_{-6}}{k_5 k_6} \tag{4.11}$$

The surface concentrations of hydrogen adatoms and vacant surface sites are obtained by solving the set of algebraic equations given by (4.7) and (4.10) with a modified Newton-Raphson method in the standard NAG-library routine C05NBF (NAG, 1991). Assuming that each silane molecule reacting at the surface leads to incorporation of a silicon atom into the growing layer, the silicon growth rate in units m s^{-1}, R_{Si}, can now be calculated by equating the growth rate in units mol m^{-2} s^{-1}, Gr_{Si}, with the silane adsorption rate and subsequently multiplying with the molar volume of solid silicon:

$$R_{Si} = Gr_{Si}\frac{M_{Si}}{\rho_{Si}} = k_1 C_{SiH_4}\frac{L_t^2}{L_t}\frac{M_{Si}}{\rho_{Si}} \tag{4.12}$$

with M_{Si} the molar mass of solid silicon, i.e. 28.086 10^{-3} kg mol^{-1}, and ρ_{Si} the density of solid silicon, i.e. 2.33 10^3 kg m^{-3}. The silicon growth rate is of course proportional to L_t as well.

4.3.3 Regression analysis

The model equations given by (4.7), (4.10) and (4.12) feature details of silane adsorption and hydrogen desorption only. The rate coefficient corresponding to the dual-site dissociative adsorption of silane, k_1 (m^3 mol^{-1} s^{-1}), is expressed according to the transition state theory (Laidler, 1973) in terms of a standard activation entropy, $\Delta^{\neq}S^0_1$, and a standard activation enthalpy, $\Delta^{\neq}H^0_1$, i.e.:

$$k_1 = \frac{z}{2}\frac{kT}{h}\exp\left(\frac{\Delta^{\neq}S_1^0}{R}\right)\exp\left(-\frac{\Delta^{\neq}H_1^0}{RT}\right) \tag{4.13}$$

in which k is the Boltzmann constant, h the Planck constant and z the number of nearest neighbours of an active surface site, taken equal to 4. The rate coefficient of the excitation of a hydrogen adatom into a delocalized state, k_5 (s^{-1}), is also expressed according to the transition state theory in terms of a standard activation entropy, $\Delta^{\neq}S^0_5$, and a standard activation enthalpy, $\Delta^{\neq}H^0_5$, i.e.:

$$k_5 = \frac{kT}{h}\exp\left(\frac{\Delta^{\neq}S_5^0}{R}\right)\exp\left(-\frac{\Delta^{\neq}H_5^0}{RT}\right) \tag{4.14}$$

The equilibrium coefficient corresponding to the dissociative adsorption of molecular hydrogen, K_H (m^3 mol^{-1}), is expressed in Van 't Hoff form in terms of a standard adsorption entropy, $\Delta_a S^0_H$, and a standard adsorption enthalpy, $\Delta_a H^0_H$, i.e.:

$$K_H = \exp\left(\frac{\Delta_a S_H^0}{R}\right)\exp\left(-\frac{\Delta_a H_H^0}{RT}\right) \tag{4.15}$$

Note that the standard activation and standard adsorption enthalpies used in the above equations correspond to the usual definition of standard activation and standard adsorption energies (Benson, 1968).

In the literature it is generally agreed that silane adsorption is not or only slightly activated. Reported activation energies range between 0 and 17 kJ mol^{-1} (Gates *et al.*, 1989; Gates and Kulkarni, 1991; Buss *et al.*, 1988). Hence, the standard activation enthalpy of silane adsorption, $\Delta^{\neq}H_1$, was kept fixed at zero during the regression. The remaining kinetic and thermodynamic parameters were determined as outlined by Froment and Hosten (1981). Maximum likelihood parameter estimates, b, were obtained by minimization of the least square criterion applied on the observed and calculated silicon growth rates, i.e. by minimizing the residual sum of squares:

$$S(b) = \sum_{i=1}^{n} [R_{Si,i} - \hat{R}_{Si,i}]^2 \quad \rightarrow \quad MIN \tag{4.16}$$

with n the number of observations; $R_{Si,i}$ the observed growth rate; $\hat{R}_{Si,i}$ the calculated growth rate. The minimization of S(b) was performed using a single-response nonlinear minimization routine (Marquardt, 1963). Model discrimination was based on statistical testing of the global regression and of the significance of the kinetic and thermodynamic parameter estimates. The significance of the global regression was expressed by means of the ratio of the mean regression sum of squares to the mean residual sum of squares, which is distributed according to F (Draper and Smith, 1966):

$$F\text{-}ratio = \frac{(n-p)\sum_{i=1}^{n} \hat{R}_{Si,i}^2}{p\sum_{i=1}^{n} [R_{Si,i} - \hat{R}_{Si,i}]^2} \tag{4.17}$$

in which p is the number of parameters. A high value of the F-ratio corresponds to a high significance of the global regression, i.e. the model equations describe the experimental growth rates satisfactorily. The parameter estimates were tested for significance by means of their approximate individual t-values, which are defined as the ratio of the parameter estimate b_i and the estimated standard error of the parameter estimate s(b$_i$):

$$t_i = \frac{b_i}{s(b_i)} \tag{4.18}$$

The approximate individual t-values were used to determine the (1-α) confidence intervals according to:

$$b_i - t(n-p, 1-0.5\alpha)s(b_i) \leq \beta_i \leq b_i + t(n-p, 1-0.5\alpha)s(b_i) \tag{4.19}$$

with (n-p) denoting the number of degrees of freedom. A parameter estimate is different from zero with a probability of 95% when its t-value exceeds the corresponding tabulated value. The tabulated t-value corresponding to a probability level of 95% and 100 degrees of freedom amounts to 2.0.

In order to facilitate the simultaneous estimation of the standard activation entropy and enthalpy corresponding to k_5, and the standard adsorption entropy and enthalpy corresponding to K_H, reparameterization was applied (Kittrell, 1970):

$$k_5 = \frac{kT}{h}\exp\left(\frac{\Delta^{\neq}S_5^0}{R} - \frac{\Delta^{\neq}H_5^0}{RT_m}\right)\exp\left(-\frac{\Delta^{\neq}H_5^0}{R}\left(\frac{1}{T} - \frac{1}{T_m}\right)\right) \tag{4.20}$$

$$K_H = \exp\left(\frac{\Delta_a S_H^0}{R} - \frac{\Delta_a H_H^0}{RT_m}\right)\exp\left(-\frac{\Delta_a H_H^0}{R}\left(\frac{1}{T} - \frac{1}{T_m}\right)\right) \tag{4.21}$$

with T_m the average temperature of the experiments, in this work 915.5 K.

In total, the silicon growth rates from 150 experiments, covering the range of experimental conditions summarized in Table 4.3, were used as responses during the regression. The gas phase concentrations of silane and hydrogen, needed to solve the set of model equations, were obtained from the measured flow rates according to equations (4.4) and (4.5).

The final kinetic and thermodynamic parameter estimates with their corresponding 95%-confidence intervals are shown in Table 4.4. The F-value of the regression amounted to 3200. The t-values of the parameter estimates ranged between 15 and 750, indicating the statistical significance of these estimates. The largest value for the binary correlation coefficient between two parameter estimates occurred for the standard activation entropy of silane adsorption and the reparameterized standard entropy change of hydrogen adsorption and amounted to 0.90. Figure 4.2 shows a parity diagram of the calculated versus the observed growth rates. The absence of systematic deviations reflects the adequacy of the model equations used. The calculated and observed growth rates usually deviated by less than 15%.

Table 4.4: *Kinetic and thermodynamic parameter estimates with their approximate individual 95%-confidence intervals obtained from a regression analysis of 150 experiments in the range of experimental conditions listed in Table 4.3. The model equations (4.7), (4.10) and (4.12), which are based on the reaction network shown in Table 4.1, were applied during the simulations. Standard state: 1 mol m*$^{-3}$ *and* θ*= 0.5.*

Parameter	Estimate with 95%-confidence interval
$\Delta^{\neq}S^0_1$ / J mol^{-1} K^{-1}	-172±3
$\Delta^{\neq}H^0_1$ / kJ mol^{-1}	0*
$\Delta^{\neq}S^0_5$ / J mol^{-1} K^{-1}	-33±16
$\Delta^{\neq}H^0_5$ / kJ mol^{-1}	186±14
$\Delta_a S^0_H$ / J mol^{-1} K^{-1}	-336±55
$\Delta_a H^0_H$ / kJ mol^{-1}	-369±50

* fixed

4.4 Assessment of parameter estimates

Examination of the individual kinetic and thermodynamic parameter estimates as given in Table 4.4 can provide insight into the validity of the proposed reaction model of Table 4.1.

The small 95%-confidence interval of the estimated standard activation entropy of silane adsorption, $\Delta^{\neq}S^0_1$, arises from keeping the value of the standard activation enthalpy of silane adsorption fixed during the regression. An upper limit for the standard activation entropy loss can be calculated by assuming that the transition state possesses neither translational nor external rotational degrees of freedom. On the basis of statistical thermodynamics (McClelland, 1973) a value of 239 J mol^{-1} K^{-1} can be calculated for the summed contributions of translational and external rotational entropy of silane in the gas phase at one atmosphere and 900 K. Transformation of the estimated value of Table 4.4 from standard states of 1 mol m^{-3} to standard states of 1 atmosphere, yields a value of -150 J mol^{-1} K^{-1}. The entropy loss is indeed smaller than 239 J mol^{-1} K^{-1}. Another way to assess the physical meaning of the estimated standard activation entropy involves calculation of the initial sticking probability, s_0. For the present situation, the sticking probability at a given value of surface coverage, s, is given by:

$$s = \frac{k_1 C_{SiH_4} \dfrac{L_*^2}{L_t}}{\dfrac{1}{4}\sqrt{\dfrac{8RT}{\pi M_{SiH_4}}}\, C_{SiH_4}} \tag{4.22}$$

with M_{SiH_4} denoting the molar mass of silane, i.e. 32.118 10^{-3} kg mol^{-1}. Following Tompkins treatment of dissociative adsorption involving pairs of adjacent vacant surface sites (Tompkins, 1978), the sticking probabilty at given hydrogen surface coverage can be related to the initial sticking probability according to:

$$s = s_0 (1-\theta_{H*})^2 \tag{4.23}$$

Substituting this expression into equation (4.22) and using $L_* L_t^{-1}=\theta_*$ and $(1-\theta_{H*})=\theta_*$ gives for the initial sticking probability:

$$s_0 = \frac{k_1 L_t}{\dfrac{1}{4}\sqrt{\dfrac{8RT}{\pi M_{SiH_4}}}} \tag{4.24}$$

Substituting equation (4.13) together with the estimates listed in Table 4.4 into equation (4.24) yields an initial sticking probability equal to 2.3 10^{-3} at 900 K. It is important to realize that the same value applies to the reaction probability at zero coverage, γ^0. The reaction probability at a given value of surface coverage is defined as the ratio of the net rate of silicon growth divided by the rate of collision with the surface (Buss *et al.*, 1988; Gates and Kulkarni, 1991). Because desorption of surface dihydride and monohydride species does not occur, the net rate of silicon growth is equal to the net rate of adsorption, see equation (4.12), and the values of reaction and sticking probability consequently coincide. Literature values for initial sticking and reaction probabilities range between 1 10^{-5} and 1 10^{-3} (Buss *et al.*, 1988; Scott *et al.*, 1989; Gates *et al.*, 1990b,c; Holleman and Verweij, 1993). The calculated value of 2.3 10^{-3} is in good agreement with the values found by Buss *et al.* (1988), 1 10^{-3}, and Holleman and Verweij (1993), 8 10^{-4}.

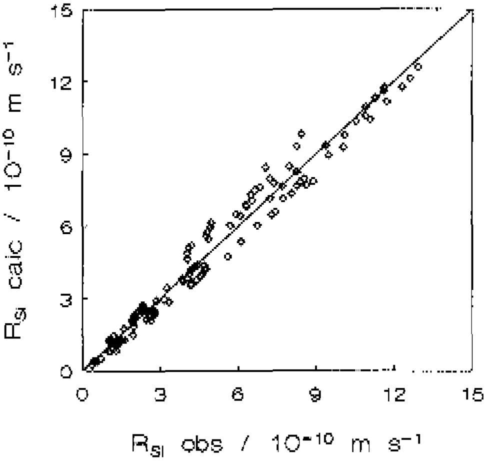

Figure 4.2: Calculated versus experimentally observed silicon growth rates in the range of experimental conditions summarized in Table 4.3. Calculated growth rates were obtained from equation (4.12) after solving equations (4.7) and (4.10) with the set of parameters given in Table 4.4.

For the excitation of a hydrogen adatom into a delocalized state, Arrhenius parameters equal to A_5= 9.6 10^{11} s^{-1} and $E_{a,5}$= 194 kJ mol^{-1} are obtained by combining equation (4.14) with the corresponding estimated values of the standard activation entropy and enthalpy at 900 K. These values are in good agreement with the results of Sinniah *et al.* (1990), who experimentally obtained a pre-exponential factor equal to 2.2 10^{11} s^{-1} and an apparent activation energy of 188 kJ mol^{-1} for hydrogen desorption from Si(100).

Within its 95%-confidence interval, the estimated standard reaction enthalpy of dissociative hydrogen adsorption, $\Delta_a H^0_H$, is in good agreement with the standard enthalpy change estimated according to D^0(H-H)-2D^0(Si-H), i.e. -314 kJ mol^{-1}. It should be kept in mind that the latter value represents an upper limit as it is based on an upper limit for the Si-H bond strength equal to 376 kJ mol^{-1} (Walsh *et al.*, 1981).

Following Everett's treatment (Everett, 1950a) the standard entropy change of Langmuir adsorption is given by:

$$\Delta_a S^0 = S^0_a - S^0_g \qquad (4.25)$$

where S^0_g is the entropy in the gas phase taken at one atmosphere and S^0_a is the entropy in the adsorbed state at a degree of coverage of half a monolayer. It should be noted that at half monolayer coverage the configurational entropy of localized adsorption vanishes. Vannice *et al.* (1979) showed that values obtained for $\Delta_a S^0$ must conform to certain rules and guidelines in order to have any physical meaning and thereby support the proposed reaction model. These rules and guidelines, originally postulated by Boudart *et al.* (1967), can be summarized as follows:

$$0 < -\Delta_a S^0 < S^0_g \tag{4.26}$$

$$42 < -\Delta_a S^0 \leq 51 - 0.0014\,\Delta_a H^0 \tag{4.27}$$

The lower limit of equation (4.26) follows directly from the necessary loss of entropy when a molecule is transferred without dissociation from a three-dimensional to a two-dimensional phase. The upper limit expresses the fact that a molecule cannot loose more entropy than it possesses. The lower limit of equation (4.27) follows by calculating the entropy change which occurs when a gas condenses to a liquid at the critical state. The equality sign in this equation corresponds to physical adsorption of a wide variety of compounds on charcoal in less than a monolayer at 298 K (Everett, 1950b). Transformation of the estimated standard reaction entropy of dissociative hydrogen adsorption from standard states of 1 mol m^{-3} to standard states of 1 atmosphere, yields a value of -314 J mol^{-1} K^{-1}. This value fulfils the strict rule reflected by the lower limit of equation (4.26) as well as the less stringent guidelines represented by equation (4.27). However, the strict rule reflected by the upper limit of equation (4.26) is not satisfied. Using statistical thermodynamics (McClelland, 1973), a value of 163 J mol^{-1} K^{-1} is calculated for the entropy of molecular hydrogen in the gas phase at one atmosphere and 900 K, which is significantly below 314 J mol^{-1} K^{-1}.

4.5 Conclusions

The reaction kinetics of the deposition of polycrystalline silicon from silane in the absence of gas phase reactions can be adequately described using a six-step elementary reaction mechanism. The only kinetically significant reactions involve dual-site dissociative adsorption of silane and first order recombinative desorption of hydrogen, which is considered to take place in two steps following the band model of Sinniah *et al.* (1989,1990). The involved kinetic and thermodynamic parameter estimates exhibit good statistical significance. In addition, both the standard activation entropy of silane adsorption and the standard activation entropy and enthalpy associated with the excitation of a hydrogen adatom into a delocalized state were found to be physically reasonable as well. Examination of the equilibrium coefficient of hydrogen adsorption, however, showed that the change in standard entropy is much too large in absolute sense, despite the physically meaningful value found for the corresponding change in standard enthalpy.

References

Avouris, P., Wolkow, R., 1989, *Phys. Rev. B.*, **39**, 5091.

Benson, S.W., 1968, Thermochemical Kinetics, Wiley, New York.

Boland, J.J., 1991, *Phys. rev. Lett.*, **67**(12), 1539.

Boland, J.J., 1992, *J. Vac. Sci. Technol. A*, **10**(4), 2458.

Boudart, M., 1968, Kinetics of Chemical Processes, Prentice-Hall, Englewood Cliffs, New Jersey.

Boudart, M., Djéga-Mariadassou, G., 1984, Kinetics of Heterogeneous Catalytic Reactions, Princeton University Press, Princeton, New Jersey.

Boudart, M., Mears, D.E., Vannice, M.A., 1967, *Ind. Chim. Belge*, **32**, 281.

Buss, R.J., Ho, P., Breiland, W.G., Coltrin, M.E., 1988, *J. Appl. Phys.*, **63**(8), 2808.

Chadi, F.J., 1979, *Phys. Rev. Lett.*, **43**, 43.

Ciraci, S., Batra, I.P., 1986, *Surf. Sci.*, **178**, 80.

Draper, N.R., Smith, H., 1966, Applied Regression Analysis, Wiley, New York.

Everett, D.H., 1950a, *Trans. Faraday Soc.*, **46**, 942.

Everett, D.H., 1950b, *Trans. Faraday Soc.*, **46**, 957.

Farnaam, M.K., Olander, D.R., 1984, *Surf. Sci.*, **145**, 390.

Feldman, L.C., Silverman, P.J., Stensgaard, I., 1980, *Nucl. Instrum. Meth.*, **168**, 589.

Froment, G.F., Hosten, L.H., in "Catalysis Science and Technology", Eds. Anderson, J.R., Boudart, M., Springer Verlag, Berlin, 1981, 98.

Gates, S.M., 1988, *Surf. Sci.*, **195**, 307.

Gates, S.M., Greenlief, C.M., Beach, D.B., 1990a, *J. Chem. Phys.*, **93**(10), 7493.

Gates, S.M., Greenlief, C.M., Beach, D.B., Holbert, P.A., 1990b, *J. Chem. Phys.*, **92**(5), 3144.

Gates, S.M., Greenlief, C.M., Beach, D.B., Kunz, R.R., 1989, *Chem. Phys. Lett.*, **154**, 505.

Gates, S.M., Greenlief, C.M., Kulkarni, S.K., Sawin, H.H., 1990c, *J. Vac. Sci. Technol. A*, **8**(3), 2965.

Gates, S.M., Kulkarni, S.K., 1991, *Appl. Phys. Lett.*, **58**(25), 2963.

Greenlief, C.M., Gates, S.M., Holbert, P.A., 1989, *J. Vac. Sci. Technol. A*, **7**(3), 1845.

Greve, D.W., Racanelli, M., 1991, *J. Electrochem. Soc.*, **138**(6), 1744.

Gupta, P., Colvin, V.L., George, S.M., 1988, *Phys. Rev. B,* **37**(14), 8234.

Hamers, R.J., Tromp, R.M., Demuth, 1986, *Phys. Rev. Lett.*, **56**, 1972.

Höfer, U., Leping, L., Heinz, T.F., 1992, *Phys. Rev. B.*, **45**(16), 9485.

Holleman, J., Verweij, J.F., 1993, *J. Electrochem. Soc.*, **140**(7), 2089.

Hougen, O.A., Watson, K.M., 1947, Chemical Process Principles, Part Three, Kinetics and Catalysis, Wiley, New York.

Jasinski, J.M., Gates, S.M., 1991, *Acc. Chem. Res.,* **24**, 9.

Kittrell, J.R., 1970, *Adv. Chem. Eng.,* **8**, 97.

Koehler, B.G., Mak, C.H., Arthur, D.A., Coon, P.A., George, S.M., 1988, *J. Chem. Phys.*, **89**, 1709.

Laidler, K.J., 1973, Chemical Kinetics, McGraw-Hill, New York.

Marquardt, D.W., 1963, *J. Soc. Indust. Appl. Math.,* **11**, 431.

McClelland, B.J., 1973, Statistical thermodynamics, Chapman and Hall & Science paperbacks, London.

Nachtigall, P., Jordan, K.D., Janda, K.C., 1991, *J. Chem. Phys.*, **95**(11), 8652.

NAG, Fortran Library Manual, 1991, Mark 15, NAG Ltd, Wilkinson House, Oxford.

Reider, G.A., Höfer, U., Heinz, T.F., 1991A, *J. Chem. Phys.*, **94**(5), 4080.

Reider, G.A., Höfer, U., Heinz, T.F., 1991B, *Phys. Rev. Lett.*, **66**, 1994.

Roberts, N., Needs, R.J., 1990, *Surf. Sci.*, **236**, 112.

Schulze, G., Henzler, M., 1983, *Surf. Sci.,* **124**, 336.

Scott, B.A., Gates, S.M., Greenlief, C.M., Estes, R.D., in: Mechanisms of Reactions of Organometallic Compounds with Surfaces, Eds., D.J. Cole-Hamilton and J.O. Williams, Plenum Press, New York, 1989, 97.

Sinniah, K., Sherman, M.G., Lewis, L.B., Weinberg, W.H., Yates, J.T., Janda, K.C., 1989, *Phys. Rev. Lett.,* **62**(5), 567.

Sinniah, K., Sherman, M.G., Lewis, L.B., Weinberg, W.H., Yates, J.T., Janda, K.C., 1990, *J. Chem. Phys.,* **92**(9), 5700-5711.

Takayanagi, K., Tanishiro, Y., Takahashi, M., 1985, *J. Vac. Sci. Technol. A.,* **3**, 1502.

Temkin, M.I., 1971, *Int. Chem. Eng.,* **11**(4), 709.

Tompkins, F.C., 1978, Chemisorption of Gases on Metals, Academic Press, London.

Vannice, M.A., Hyun, S.H., Kalpakci, B., Liauh, W.C., 1979, *J. Catal.*, **56**, 358.

Walsh, R., 1981, *Acc. Chem. Res.,* **14**, 246.

Widdra, W., Weinberg, W.H., in: Gas-Phase and Surface Chemistry in Electronic Materials Processing, Eds., T.J. Mountziaris, G.R. Paz-Pujalt, F.T.J. Smith, P.R. Westmoreland, Materials Research Society, Pittsburgh, Pennsylvania, 1994, 69.

Wise, M.L., Koehler, B.G., Gupta, P., Coon, P.A., George, S.M., 1991, *Surf. Sci.*, **258**, 166.

5

KINETICS IN THE PRESENCE OF GAS PHASE REACTIONS

5.1 Introduction

The deposition of silicon from silane at conditions where gas phase reactions play an important role too has been investigated by several groups (Coltrin *et al.*, 1984, 1986,1989; Breiland *et al.*, 1986a,b; Becerra and Walsh, 1992; Ring and O'Neal, 1992; Holleman and Verweij, 1993). Modelling work of Coltrin *et al.* (1984,1986,1989) in combination with experimental research by Breiland *et al.* (1986a,b) demonstrated that under atmospheric pressure conditions silicon growth may be almost completely determined by reactive intermediates formed in the gas phase and that a full treatment of the gas phase kinetics can involve as much as 20 different reactive intermediates and the same number of gas phase reactions. H_2SiSiH_2, Si_2H_2 and Si_2 were shown to be the most important gas phase species with respect to silicon deposition in the temperature range from 900 to 1300 K. Recently, a lot of effort has been put in the modelling of the product-time evolution curves of H_2, Si_2H_6, Si_3H_8, solid silicon and incorporated molecular hydrogen obtained by Purnell and Walsh (1966) via silane pyrolysis batch experiments in the pressure and temperature ranges of 51 to 205 Pa and 652 to 703 K. Becerra and Walsh (1992) used a mechanism involving 15 gas phase elementary steps together with five alternative silicon deposition processes. Although the observed kinetic behaviour could be simulated quite well for three of these deposition processes, the values of the adjusted kinetic parameters featuring in these deposition processes were not physically reasonable. Ring and O'Neal (1992) modelled the above data using an even more complex mechanism including 25 elementary gas phase steps together with three termination mechanisms, one of which involving termination by gas phase polymerization. Holleman and Verweij (1993) reported on a comprehensive kinetic study of silicon deposition from silane in a conventional hot-wall multiwafer LPCVD reactor in the total pressure range from 10 to 1000 Pa at 900 K. By varying the amount of wafer area per unit volume and the silane partial pressure as well as the total pressure, insights in the relative importance of gas phase reactions were gained. In order to adequately describe the silicon growth in the region where gas phase reactions were important, gas phase production and subsequent surface decomposition of SiH_2, Si_2H_6 and Si_3H_8 were accounted for.

The present work reports on the development of a kinetic model valid over a wide range of experimental conditions including the range where the contribution of gas phase reactions needs to be taken into account. The kinetic model consists of four elementary gas phase reactions coupled to ten elementary reactions taking place on the silicon surface. The gas phase reaction network is constructed as a closed subsystem among species that are thermodynamically favoured, and consists of reactions that are unimolecular in at least one direction. In order to describe the effects of pressure adequately, the fall-off behaviour of each of the unimolecular rate coefficients is quantified using the Rice-Ramsperger-Kassel-Marcus (RRKM) theory (Robinson and Holbrook, 1972). The surface reaction network is based on the six-step elementary reaction mechanism proposed in Chapter 4 for the deposition of silicon from silane, supplemented with elementary adsorption reactions for the silicon containing species formed through the gas phase reactions.

For the simulation of the experimental data the reactor model equations presented in Chapter 2 are used, which take into account the gas/solid mass transfer resistances for the reactive gas phase species. The kinetic and thermodynamic parameters of the most sensitive reactions are estimated using a multi-response nonlinear minimization algorithm (Marquardt, 1963; Froment and Hosten, 1981). Initial values are taken from the RRKM calculations and the results presented in Chapter 4. Discrimination among rival models is based on statistical testing, whenever it is not possible by direct process observation or physico-chemical laws. The purpose of the kinetic model is to provide a statistically sound and a physically reasonable description of the experimental data.

The developed kinetic model provides insights in the relative importance of the gas phase reactions in the silicon deposition process. It can also be used to predict the influence of various process variables on the performance of an industrial hot-wall multiwafer LPCVD reactor as will be shown in Chapter 6.

5.2 Construction of reaction network

5.2.1 Thermodynamic evaluation of gas phase composition

The equilibrium calculations presented here refer to isothermic and isobaric conditions, and were conducted with SAGE (Solgasmix-based Advanced Gibbs-Energy Minimizer), a computer program originally developed by Eriksson (1975) and based on minimization of the total Gibbs energy, see Appendix 5A.

The following set of silicon containing gas phase species was considered: Si, SiH, SiH_2, SiH_3, SiH_4, Si_2, Si_2H_2, Si_2H_3, H_2SiSiH_2, H_3SiSiH, Si_2H_5, Si_2H_6, Si_3, and Si_3H_8. This selection is primarily based on the species present in the reaction network proposed by Coltrin *et al.* (1984,1986,1989) for atmospheric pressure conditions and a temperature range from 850 to 1450 K. To meet the conditions of low pressure chemical vapor deposition of polycrystalline silicon, pure silane was used at total pressures between 10 and 1000 Pa and temperatures between 600 and 1200 K. The thermodynamic data for the gaseous species were taken from Coltrin *et al.* (1986), who fitted the temperature dependence of the data obtained by Ho *et al.* (1985,1986) from ab initio electronic structure calculations. In a later paper Coltrin *et al.* (1989) included some corrections attributed to the standard formation enthalpy of several species. The thermodynamic data for solid silicon were taken from Barin and Knacke (1974).

Two extreme situations were considered, i.e., homogeneous and heterogeneous equilibrium. In case of homogeneous equilibrium the formation of solid silicon is omitted. The gas phase is equilibrated internally and the supersaturation is maximal. Clearly, gas phase reactions have a major impact on the final equilibrium composition. In the heterogeneous equilibrium situation, the formation of solid silicon is taken into account and equilibrium is established between gas phase and solid silicon. Only temperature and pressure effect the gas phase composition. The supersaturation of the gas phase is essentially zero.

Homogeneous equilibrium

Figure 5.1a shows the variation of the gas phase composition as a function of temperature at 100 Pa total pressure. Silane partly reacts to disilane, trisilane and hydrogen already at temperatures as low as 600 K. Above 750 K silane starts to exhibit greater thermodynamic instability and reacts mainly to H_2 and Si_3. Concurrently, the molar fractions of disilane and trisilane sharply decrease. At 900 K a ratio between monosilane, disilane, and trisilane of 10^5:10^2:1 is observed, which is also reported by van den Brekel and Bollen (1981) for typical LPCVD experiments. The temperature regime above 800 K is best characterized by the global reaction:

$$3\,SiH_4 \rightleftharpoons Si_3 + 6\,H_2 \tag{5.1}$$

mechanistically taking place through a number of elementary reactions. The formation of Si_3, the largest silicon cluster considered, is a direct sign of the onset of gas phase particle nucleation. It should be noted that a larger silicon cluster like Si_4 or Si_5, if included, would replace Si_3 as most abundant silicon containing species. Lack of structural and thermodynamic data, however, makes inclusion of such larger cluster impossible.

Recently, Tao and Hunt (1992) performed thermodynamic calculations for the homogeneous equilibrium situation for typical CVD conditions. The gas phase composition calculated by these authors for 100 Pa and pure silane feed as a function of temperature shows good agreement with the results presented here. Gardeniers (1990) performed thermodynamic calculations for atmospheric pressure and a feed composition of 1% SiH_4 in H_2. A detailed comparison with this work is difficult due to the reduced pressure and pure silane feed used in the present study. Nevertheless, comparison shows that already at low temperatures the pure silane feed gives rise to the onset of gas phase reactions, shifting the curves of the silicon containing gas phase species, especially those of the saturated ones, to higher molar fractions and lower temperatures.

Figure 5.1b shows the variation of the gas phase composition as a function of total pressure at 900 K. Over the total range of pressures considered, the global reaction given by equation (5.1) remains valid. Concurrently with a slight decrease in the molar fractions of H_2 and Si_3, an increase in the molar fraction of SiH_4 takes place, which is in accordance with Le Chatelier's principle, i.e. the equilibrium of reaction (5.1) will shift to the left with increasing total pressure.

Heterogeneous equilibrium

In case formation of solid silicon is not omitted, the existence of silicon containing gas phase species becomes physically irrelevant. The molar fractions are about ten decades lower compared to those prevailing in the homogeneous equilibrium situation. This provides direct evidence for the thermodynamic instability of the silicon containing gas phase species with respect to elemental silicon at the temperatures under consideration.

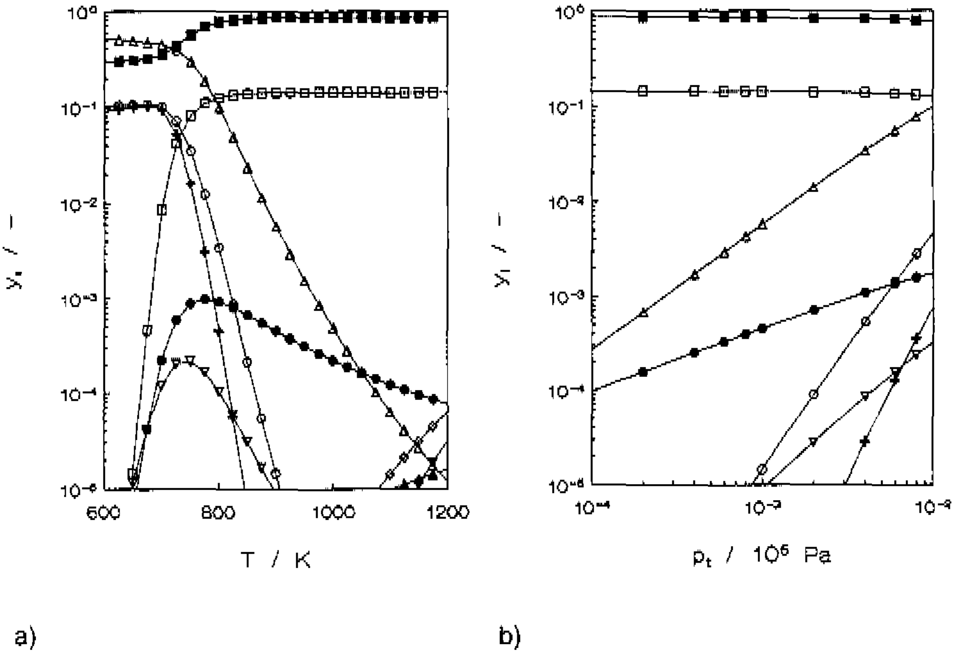

Figure 5.1: *Calculated gas phase composition in the homogeneous equilibrium situation: a) molar fractions versus temperature, p_t= 100 Pa, pure silane feed; b) molar fractions versus total pressure, T= 900 K, pure silane feed. Gas phase species:* ▵ *SiH_4,* ▴ *SiH_2,* ▾ *Si,* o *Si_2H_6,* ▿ *H_2SiSiH_2,* ● *Si_2H_2,* ◊ *Si_2,* + *Si_3H_8,* □ *Si_3 and* ■ *H_2.*

5.2.2 Gas phase reactions

The thermodynamic analysis performed in the preceding paragraph is useful in identifying the gas phase species required in the gas phase reaction network. In the range of experimental conditions covered during the kinetic experiments, i.e. temperatures between 862 and 962 K and total pressures between 25 and 100 Pa, totally 7 gas phase species have a molar fraction larger than 1 10^{-5}, i.e. SiH_4, Si_2H_6, H_2SiSiH_2, Si_2H_2, Si_3H_8, Si_3 and H_2, see Figure 5.1. The lower limit of 1 10^{-5} reflects a minimum contribution to the silicon deposition rate of 1% compared to that of silane, assuming unit reaction probabilities for the homogeneously formed silicon containing species and a value of 2 10^{-3} for silane, see Chapter 4.

Although Si_3 is an important species from a thermodynamic viewpoint, its formation rate is very slow and hence its kinetic significance can be neglected. In addition, the absence of trisilane and other Si_3H_x species in the reaction mixture, see paragraph 3.5.2, provides direct evidence for the insignificance of chemical routes towards these species at the experimental conditions applied. Although SiH_2 is not important in a thermodynamic sense, it plays a key role in the overall gas phase chemistry. It is formed in the initial silane decomposition reaction (Purnell and Walsh, 1966; White *et al.*, 1985) and easily inserts into silane to form disilane (Inoue and Suzuki, 1985; Jasinski, 1986). Because H_2SiSiH_2 is formed by isomerization of H_3SiSiH (Gaspar *et al.*, 1987; Becerra and Walsh, 1987), one of the products of disilane decomposition (Dzarnoski *et al.*, 1982), this species needs to be taken into account as well in order to form a closed subsystem. The inclusion of Si_2H_2, which in turn is formed from H_2SiSiH_2 (Coltrin *et al.*, 1989; Burgess and Zachariah, 1990), will not basically change the growth rate contribution along the homogeneous path as both species are assumed to have unit reaction probabilities (Coltrin *et al.*, 1986,1989). Hence, Si_2H_2 is omitted from the gas phase kinetic scheme.

Based on the above considerations the following set of silicon containing species was considered in the gas phase reaction network: SiH_4, SiH_2, Si_2H_6, H_3SiSiH and H_2SiSiH_2, the latter two species being two Si_2H_4 isomers called silylsilylene and disilene. The corresponding elementary gas phase reactions used to simulate the kinetic experiments are given in Table 5.1.

Table 5.1: *Elementary reactions considered in the gas phase (1-4).*

$SiH_4 \rightleftharpoons SiH_2 + H_2$	(1)
$SiH_4 + SiH_2 \rightleftharpoons Si_2H_6$	(2)
$Si_2H_6 \rightleftharpoons H_3SiSiH + H_2$	(3)
$H_3SiSiH \rightleftharpoons H_2SiSiH_2$	(4)

It is interesting to note that only silicon hydride species containing an even number of hydrogen atoms are involved in the gas phase kinetic scheme. The fact that the gas phase chemistry of silane is merely determined by this kind of species is consistent with the gas phase reaction networks recently published to describe the silicon deposition process at similar temperatures and total pressures ranging from 50 Pa to atmospheric pressure (Coltrin *et al.*, 1984,1986,1989; White *et al.*, 1985; Breiland *et al.*, 1986a,b; Burgess and Zachariah, 1990; Becerra and Walsh, 1992; Ring and O'Neal, 1992; Kleijn, 1991b; Holleman and Verweij, 1993).

5.2.3 Surface reactions

The basis for the reaction network used for the description of the silicon growth from silane and the homogeneously formed gas phase species is given by the elementary reactions (5-14) listed in Table 5.2. Besides the adsorption of silane, which was treated in detail in paragraph 4.2, the adsorption of all silane pyrolysis products is taken into account, see reactions (6-9).

The interaction of disilane with single-crystalline surfaces is recently as thoroughly investigated as silane decomposition. Mechanistic UHV studies on Si(111)-(7x7) (Imbihl *et al.*, 1989; Kulkarni *et al.*, 1990b; Gates, 1988; Uram and Jansson, 1991) and Si(100)-(2x1) (Gates and Chiang, 1991) report that disilane adsorbs via a molecular precursor state. Using modulated molecular beam spectroscopy (MMBS) Kulkarni *et al.* (1990b) observed a surface residence time of ~50 μs for disilane as an intact molecule on Si(111) at room temperature, and attributed this to a molecular precursor state on a hydrogenated surface. The residence time decreased with increasing surface temperature and could not be measured (< 20 μs) above 525 K.

Depending on the crystallographic orientation of the silicon surface used, several mechanisms for disilane chemisorption have been identified in the literature. Using H_2 TPD, Gates (1988) obtained an apparent activation energy of -10.9 kJ mol^{-1} in the limit of zero coverage and proposed an adsorption reaction involving the formation of two surface trihydride species:

$$Si_2H_6 + 2* \rightarrow 2SiH_3* \tag{5.2}$$

Vibrational spectroscopy (Imbihl *et al.*, 1989; Uram and Jansson, 1989) provided additional evidence for the occurrence of this reaction on Si(111)-(7x7) with apparent activation energies amounting to -7.1 and -7.9 kJ mol^{-1}. The absence of a deuterium kinetic isotope effect (DKIE) in the chemisorption of Si_2H_6 and Si_2D_6 on this surface (Gates, 1988) is consistent with a mechanism where an Si-Si bond scission reaction like (5.2) forms the rate-determining step, but argues against a mechanism involving a Si-H bond breaking reaction as rate-determining step, e.g.:

$$Si_2H_6 + 2* \rightarrow Si_2H_5* + H* \tag{5.3}$$

Kulkarni *et al.* (1990a,b) identified three distinct temperature regions for disilane adsorption on Si(111)-(7x7) using MMBS. At temperatures below 675 K, a fully hydrogenated inert surface resulted from disilane adsorption, and silicon deposition could be neglected. Between 675 and 775 K slight silane evolution was observed. This was attributed to the decomposition of disilane emitting a silane molecule and chemisorbing a dihydride species, see reaction (7) of Table 5.2, followed by fast dissociation of this so formed surface dihydride species. The apparent activation energy amounted to ~13 kJ mol^{-1}. At temperatures above 775 K, disilane adsorption was believed to occur via two competing mechanisms, both producing silane. One mechanism involved the decomposition into silane and chemisorbed dihydride, see reaction (7) of Table 5.2, which was predicted to be the main channel of silicon growth from disilane at temperatures between 773 and 1173 K. The chemisorbed dihydride then rapidly reacts to two hydrogen adatoms, that in turn serve as active sites for the second chemisorption mechanism:

$$Si_2H_6 + 2H* \rightarrow 2SiH_4 + 2* \qquad (5.4)$$

This process appeared to be more active at H removal from the surface than the usual way of recombinative hydrogen desorption.

Kulkarni *et al.* (1990b) observed an increasing sticking probability, s, with increasing surface temperature from 0 at room temperature on a Si(111)-(7x7) surface passivated with SiH_x species to 0.3 at 1125 K. Scott *et al.* (1989) obtained an initial sticking probability, s_0, of 0.5±0.1 at room temperature, decreasing to ~0.1 at 573 K. These values are in good agreement with the one found by Imbihl *et al.* (1989) at room temperature, $s_0=0.3\pm0.1$. Gates (1988) distinguished two regimes for disilane adsorption on Si(111) as a function of disilane exposure at room temperature. In the limit of zero hydrogen coverage a sticking probability of 0.47±0.1 was observed. Departure from precursor kinetics occurred when roughly 3 10^{17} molecules Si_2H_6 m^{-2} were adsorbed, corresponding to about 2 10^{18} or 20% of a monolayer of H atoms. After an exposure of roughly 1 10^{18} m^{-2} the sticking probability dropped dramatically, and continuously decreased with increasing exposure from 1 10^{18} to 1 10^{20} Si_2H_6 m^{-2}. This behaviour is consistent with the results of Imbihl *et al.* (1989), who determined the relative sticking probability, s/s_0, as a function of hydrogen surface coverage, θ_H, at 300 K, see Figure 5.2. The sharp drop in s/s_0 at low θ_H was attributed to filling of reactive defect sites.

In the present work disilane adsorption is considered to proceed through reaction (7) of Table 5.2. This reaction is treated as an elementary reaction, but will undoubtedly comprise a number of elementary reactions in reality, as evidenced by the MMBS experiments of Kulkarni *et al.* (1990a,b) and the negative apparent activation energies generally observed (Gates, 1988; Imbihl *et al.*, 1989; Uram and Jansson, 1989).

The adsorption of silylene, silylsilylene and disilene is taken into account through reactions (6), (8) and (9) of Table 5.2, all of them producing one or more surface dihydride species. It is assumed that the adsorption of these reactive gas phase intermediates takes place without simultaneous evolution of a silicon containing gas phase species or direct release of molecular hydrogen. Since the subsequent surface decomposition reactions are considered to be potentially fast, the type of surface species formed during each of these adsorption reactions becomes completely irrelevant.

The elementary reactions involving SiH_x^* (x= 1,2,3) decomposition, reactions (10-12), together with those reflecting molecular hydrogen desorption, reactions (13) and (14), were already treated in detail in paragraph 4.2.

The global reactions (α-ε), built up from elementary steps and symbolized by the columns with stoichiometric numbers σ_α to σ_ε, describe the decomposition of silane, silylene, disilane, silylsilylene and disilene into solid silicon and hydrogen adatoms. The decomposition reactions of surface trihydride, dihydride and monohydride species are considered to be potentially fast compared to the adsorption reactions of the above gas phase species. The rates of the global reactions (α-ε) are consequently given by the rates of the corresponding adsorption reactions given by (5-9), as follows from the stoichiometric numbers. Together with the elementary reactions (13) and (14) these global reactions take part in the global deposition paths ($\alpha\alpha$-$\varepsilon\varepsilon$), symbolized by the columns with stoichiometric numbers $\sigma_{\alpha\alpha}$ to $\sigma_{\varepsilon\varepsilon}$. In these sequences, the global reactions (α-ε) are now potentially fast compared to the desorption of hydrogen or more specifically the excitation of a covalently bound hydrogen adatom given by reaction (13).

The above way of presenting a complex reaction network was developed by Temkin (1971) and allows a straightforward calculation of the net production rates of the components involved in the surface reactions.

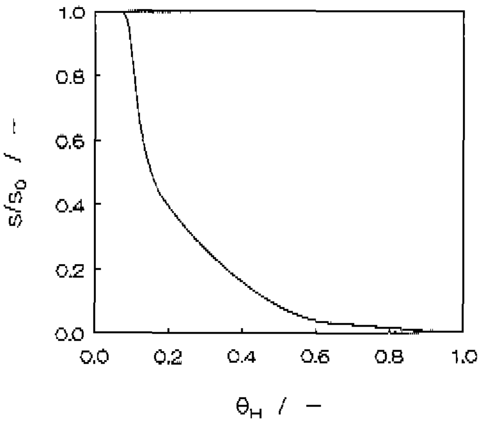

Figure 5.2: Relative sticking probability of Si_2H_6 versus the hydrogen surface coverage for Si(111)-(7x7). T_s= 300 K (Imbihl et al., 1989).

Table 5.2: *Elementary reactions considered on the silicon surface (5-14) with corresponding global adsorption reactions (α-ε) and global deposition paths (αα-εε).*

	σ_α	σ_β	σ_γ	σ_δ	σ_ε	
$SiH_4 + 2^* \rightarrow SiH_3^* + H^*$	1	0	0	0	0	(5)
$SiH_2 + {}^* \rightarrow SiH_2^*$	0	1	0	0	0	(6)
$Si_2H_6 + {}^* \rightarrow SiH_4 + SiH_2^*$	0	0	1	0	0	(7)
$H_3SiSiH + 2^* \rightarrow 2SiH_2^*$	0	0	0	1	0	(8)
$H_2SiSiH_2 + 2^* \rightarrow 2SiH_2^*$	0	0	0	0	1	(9)
$SiH_3^* + {}^* \rightarrow SiH_2^* + H^*$	1	0	0	0	0	(10)
$SiH_2^* + {}^* \rightarrow SiH^* + H^*$	1	1	1	2	2	(11)
$SiH^* \rightarrow Si(s) + H^*$	1	1	1	2	2	(12)
+ --	$\sigma_{\alpha\alpha}$	$\sigma_{\beta\beta}$	$\sigma_{\gamma\gamma}$	$\sigma_{\delta\delta}$	$\sigma_{\varepsilon\varepsilon}$	
$SiH_4 + 4^* \rightarrow Si(s) + 4H^*$	1	0	0	0	0	(α)
$SiH_2 + 2^* \rightarrow Si(s) + 2H^*$	0	1	0	0	0	(β)
$Si_2H_6 + 2^* \rightarrow Si(s) + 2H^* + SiH_4$	0	0	1	0	0	(γ)
$H_3SiSiH + 4^* \rightarrow 2Si(s) + 4H^*$	0	0	0	1	0	(δ)
$H_2SiSiH_2 + 4^* \rightarrow 2Si(s) + 4H^*$	0	0	0	0	1	(ε)
$H^* \rightleftharpoons H^{\circ} + {}^*$	2	1	1	2	2	(13)
$H^* + H^{\circ} \rightleftharpoons H_2 + {}^*$	2	1	1	2	2	(14)
+ --						
$SiH_4 \rightarrow Si(s) + 2H_2$						(αα)
$SiH_2 \rightarrow Si(s) + H_2$						(ββ)
$Si_2H_6 \rightarrow Si(s) + H_2 + SiH_4$						(γγ)
$H_3SiSiH \rightarrow 2Si(s) + 2H_2$						(δδ)
$H_2SiSiH_2 \rightarrow 2Si(s) + 2H_2$						(εε)

5.3 Unimolecular gas phase kinetics

The decline or fall-off in the unimolecular reaction rate coefficients with decreasing pressure is an important phenomenon in CVD chemistry at low or moderate pressures (Jensen, 1987; Hitchman and Jensen, 1993). The present paragraph focusses on the fall-off behaviour of the unimolecular dissociation reactions listed in Table 5.1, supplemented with two unimolecular dissociation reactions of trisilane.

5.3.1 Pressure fall-off

According to the classical Lindemann theory, a unimolecular reaction, A → Products, comprises three steps, i.e., collisional activation, collisional deactivation and unimolecular dissociation or isomerization:

$$A + M \xrightarrow{k_1} A^* + M \tag{5.5}$$

$$A^* + M \xrightarrow{k_2} A + M \tag{5.6}$$

$$A^* \xrightarrow{k_3} \text{Products} \tag{5.7}$$

with M denoting a collision partner for species A, commonly referred to as bath gas. Application of the steady-state approximation to the energized molecules A^* yields the following expression for the reaction rate:

$$r = k_{uni} C_A \tag{5.8}$$

with:

$$k_{uni} = \frac{k_1 C_M}{1 + k_2 C_M / k_3} \tag{5.9}$$

In the high-pressure limit, i.e. when $k_2C_M >> k_3$, k_{uni} is independent of total pressure:

$$k_{uni} = k_\infty = \frac{k_1 k_3}{k_2} \tag{5.10}$$

with k_∞ the high pressure rate coefficient independent of total pressure. The unimolecular reaction is first order in A. In the low-pressure limit, i.e. when $k_2C_M << k_3$, k_{uni} is proportional to the total pressure:

$$k_{uni} = k_0 = k_1\, C_M \tag{5.11}$$

Hence, the total reaction order of the unimolecular reaction is now two. Although the Lindemann theory correctly predicts a transition from first order to second order as the pressure is lowered, it fails when more detailed quantitative aspects of these reactions are investigated.

Among the various unimolecular reaction rate theories elaborated since Lindemann's theory, the Rice-Ramsperger-Kassel-Marcus (RRKM) theory is accepted to be the most accurate practical treatment of unimolecular reactions. The main development in comparison with the simple Lindemann theory consists in taking into account the distribution of the reaction rate coefficients k_1 and k_3 as a function of the energy content of the molecules, as will be shown in the next paragraph.

5.3.2 The Rice-Ramsperger-Kassel-Marcus theory

The nomenclature used in this section is consistent with that of Robinson and Holbrook (1972). Only the essential features of the RRKM (Rice-Ramsperger-Kassel-Marcus) theory are presented here. A complete development of the theory is given in the above reference.

According to the RRKM theory, the reaction scheme for a unimolecular reaction comprises the following steps:

$$A + M \underset{k_2}{\overset{\delta k_{1(E^* \to E^* + \delta E^*)}}{\rightleftharpoons}} A^*_{(E^* \to E^* + \delta E^*)} + M \tag{5.12}$$

$$A^*_{(E^*)} \xrightarrow{k_a(E^*)} A^+ \xrightarrow{k^+} \text{Products} \tag{5.13}$$

The first step involves energization of the molecules A into the small energy range E^* to $E^*+\delta E^*$. During the second step energized molecules with a specific energy E^* are converted to activated complexes A^+, that finally decompose into products.

A potential energy diagram illustrating the terminology used is shown in Figure 5.3. An energized molecule, A^*, contains in its active degrees of freedom a non-fixed energy E^* greater than the critical or threshold energy E_0 below which classical reaction cannot occur. The critical energy E_0 is defined as the difference between the ground-state energies of A^+ and A. The non-fixed energy E^* is the energy content of the energized molecule that is not fixed by any basic principle and is considered to be free to move around the molecule. It comprises both vibrational and rotational non-fixed energy, denoted E_v^* and E_r^*, the sum of these being E^* or E_{vr}^*. The total non-fixed energy of the activated complex, E^+, contains both vibrational and rotational non-fixed energy, denoted E_v^+ and E_r^+, the sum of these being E_{vr}^+. The energy associated with the translation of the activated complex along the reaction coordinate is denoted x.

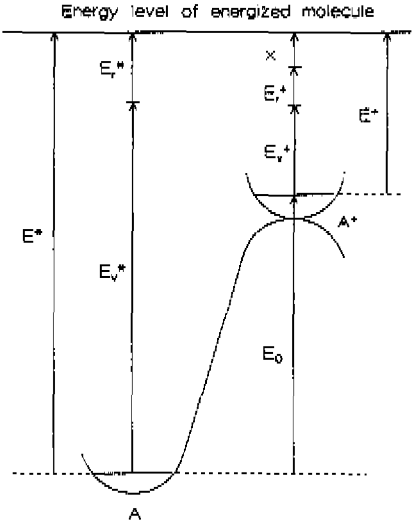

***Figure 5.3:** Potential energy diagram of a unimolecular reaction; adiabatic and inactive degrees of freedom are not included (Robinson and Holbrook, 1972).*

The fundamental RRKM expression for the unimolecular reaction rate coefficient is (Robinson and Holbrook, 1972):

$$k_{uni} = \frac{L^{\ne} Q_1' \exp(-E_0/kT)}{h\, Q_1 Q_2} \int_{E^+=0}^{\infty} \frac{\{ \sum_{E_{vr}^+=0}^{E^+} P(E_{vr}^+) \} \exp(-E^+/kT)\, dE^+}{1 + k_a(E_0+E^+)/F k_2 C_M} \qquad (5.14)$$

with:

$$k_a(E_0+E^+) = \frac{L^{\ne}}{h\, N^*(E_0+E^+)} \sum_{E_{vr}^+=0}^{E^+} P(E_{vr}^+) \qquad (5.15)$$

Q_2 is the ordinary molecular partition function for all active modes of the reactant A, comprising usually all the vibrations and internal rotations of the molecule. Q_1' and Q_1 are the partition functions for the adiabatic rotations in the activated complex and the reactant molecule. $N^*(E_0+E^+)$ is the density of quantum states or the number of quantum states per unit range of energy at energies close to E^*. $P(E_{vr}^+)$ is the number of vibrational-rotational quantum states of the activated complex A' with vibrational-rotational non-fixed energy equal to E_{vr}^+. The summation in equations (5.14) and (5.15) runs over all possible distributions of E^+ between E_{vr}' and x, from $E_{vr}'= 0$ (in which case all the non-fixed energy is translational energy along the reaction coordinate), up to the maximum possible value of E_{vr}' below E^+ (in which case the minimum possible energy along the reaction coordinate prevails). $\Sigma P(E_{vr}')$ is thus the total number of vibrational-rotational quantum states of the activated complex with energies less than or equal to E^+. The straightforward formulation of $k_a(E_0+E^+)$ refers basically to the rate of reaction by a single reaction path from energized molecule with non-fixed energy $E^* = E_0+E^+$ to activated complex. Inclusion of the statistical factor or reaction path degeneracy $L^{\ddagger}$ accounts for the kinetically equivalent reaction paths. By integrating from $E^+= 0$ to ∞ and summing for each value of E^+ the contributions from the different possible divisions of the energy E^+ between E_{vr}' and x, all possible activated complexes are considered.

The de-energization rate coefficient k_2 is considered to be independent of energy and is often equated to the collision factor Z. The basic RRKM theory treats activation and deactivation as single-step processes rather than ladder-climbing processes in which molecules acquire or loose their energy in a series of small steps. The strong-collision assumption is adequate for thermal reactions in the temperature range of conventional kinetic studies unless very small molecules are involved.

The factor F in the denominator of equation (5.14) corrects for the contribution of adiabatic rotations to the non-fixed energy in the transition state. When the moments of inertia of the activated complex are significantly larger than those of the energized molecule, the adiabatic rotations release energy into the other active degrees of freedom of the molecule, thereby increasing the number of available quantum states of the activated complex and hence increasing the specific reaction rate coefficient k_a. Among the various expressions found in literature for the evaluation of the factor F, the one postulated by Waage and Rabinovitch (1970a,b) is considered most accurate:

$$F = \left(1 - \frac{(s-1)<\Delta E_j>}{E_0 + a(E_0)E_z}\right)^{1} \tag{5.16}$$

with $a(E_0)$ is the Whitten-Rabinovitch's correction factor (Whitten and Rabinovitch, 1963) calculated at the critical energy; E_z the zero-point energy of the molecular vibrations; s the number of active vibrational degrees of freedom, which should be replaced by s+r/2 if there are in addition r active rotational degrees of freedom; $<\Delta E_J>$ the average rotational energy of the energized molecules.

The high-pressure limit

In the high-pressure limit k_{uni} equals the genuine pressure-independent first-order rate coefficient k_∞. By letting $C_M \rightarrow \infty$ and reversing the order of summation and integration in equation (5.14) the following expression for k_∞ is obtained:

$$\begin{aligned} k_\infty = \lim_{C_M\to\infty} k_{uni} &= \frac{L^* Q_1^+}{h\, Q_1\, Q_2}\, kT \exp(-E_0/kT) \sum_{E_{vr}^+=0}^{\infty} [P(E_{vr}^+)\exp(E_{vr}^+/kT)] \\ &= L^* \frac{kT}{h} \frac{Q_1^+ Q_2^+}{Q_1 Q_2} \exp(-E_0/kT) \end{aligned} \tag{5.17}$$

in which the contribution of the adiabatic rotations amounts to a factor of Q_1^+/Q_1. Except for the transmission coefficient this result is identical with that obtained from the absolute rate theory for a unimolecular reaction (Laidler, 1973). This is reasonable in view of the similarity of the treatments involved. The absolute rate theory assumes equilibrium between activated complexes and reactant molecules. Although the RRKM theory admits equilibrium between activated complexes and energized molecules, both theories coincide since at high pressures the energized and reactant molecules are in equilibrium as well.

The low-pressure limit

In the limit of very low pressure the first-order rate coefficient from equation (5.14) is proportional to the pressure. The resulting bimolecular rate coefficient k_{bim} is then given by:

$$\begin{aligned} k_{bim} = \lim_{C_M\to 0} \frac{k_{uni}}{C_M} &= \frac{F Q_1^+}{Q_1} \frac{k_2}{Q_2} \int_{E^*=E_0}^{\infty} N^*(E^*) \exp(-E^*/kT)\, dE^* \\ &= \frac{F Q_1^+}{Q_1} \frac{k_2 Q_2^*}{Q_2} \end{aligned} \tag{5.18}$$

in which Q_2^* is the partition function for the energized molecules using the ground state of A for the zero of energy. The factor FQ_1^+/Q_1 accounts for the contribution of the adiabatic rotations. Besides this factor the reaction rate is simply the rate of energization, which indicates that at sufficiently low pressures all energized molecules react.

5.3.3 Unimolecular reaction rate coefficients

RRKM calculations were performed for the set of reactions listed in Table 5.3 using a public domain computer program available from QCPE (Quantum Chemistry Program Exchange) (Hase and Bunker, 1973), which was modified to compute $k_{uni}(T,p_t)$ and $k_a(E^*)$ according to equations (5.14) and (5.15). Consistent sets of frequencies, molecular properties and other important RRKM parameters were taken from literature and are tabulated in Appendix 5B. The collision diameter and reduced mass were taken with respect to silane as bath gas. Overall rotations were assumed to be adiabatic, while all vibrations and internal rotations were considered active. The processes of activation and deactivation were treated as essentially single-step processes, underlying the strong-collision assumption. No correction was made for anharmonicity. The sum of states for the activated complex, $\Sigma(P_{vr}')$, was determined by direct count (Rabinovitch and Setser, 1964), whereas the density of states for the molecule, $N^*(E^*)$, was evaluated by means of the Whitten-Rabinovitch semiclassical method (Whitten and Rabinovitch, 1963; Whitten and Rabinovitch, 1964) in most cases. It should be noted that calculations performed with the program UNIMOL (Gilbert *et al.*, 1993) produced similar results.

Transition pressures

An important fall-off characteristic is the transition pressure $p_{1/2}$, which corresponds to the pressure at which k_{uni}/k_∞ equals 0.5. Table 5.3 lists the $p_{1/2}$-values obtained by interpolating the RRKM based fall-off data for the unimolecular reactions considered. In general, the transition pressure is related to both the number and the frequencies of the internal degrees of freedom of the reactant molecule. Due to the greater number of low-frequency internal degrees of freedom, the disilane and trisilane decomposition reactions possess lower transition pressures than the decomposition reaction of silane. The transition pressure for the isomerization reaction of silylsilylene is not very accurate. A complicating factor in the calculation of the fall-off data of this reaction is the small critical energy in comparison to the zero-point energies of both the reactant and the transition state. The small critical energy makes replacement of the essentially stepwise increase in the number of energy levels of the reactant by a continuous distribution function inadequate. Moreover, in case E_0/kT is less than 10 the RRKM based equilibrium hypothesis concerning the concentrations of energized molecules and activated complexes starts to break down as well (Robinson and Holbrook, 1972). The $p_{1/2}$-values in Table 5.3 indicate that none of the unimolecular reactions is in its high-pressure limit in the pressure range covered during the kinetic experiments.

Table 5.3: *Transition pressures. T= 900 K and silane as bath gas.*

reaction	$p_{1/2}$/100 kPa
$SiH_4 \rightarrow SiH_2 + H_2$	3.77
$H_3SiSiH \rightarrow H_2SiSiH_2$	99.6
$Si_2H_6 \rightarrow SiH_4 + SiH_2$	0.73
$Si_2H_6 \rightarrow H_3SiSiH + H_2$	0.70
$Si_3H_8 \rightarrow Si_2H_6 + SiH_2$	0.019
$Si_3H_8 \rightarrow H_3SiSiH + SiH_4$	0.019

Empirical fall-off relations

In order to describe the effects of total pressure adequately, pressure fall-off effects need to be accounted for during the simulation of the kinetic experiments. It is important to realize that both the pre-exponential factor and the Arrhenius activation energy change as a function of pressure. In the low pressure limit the pressure dependence of the unimolecular reaction rate coefficient is confined to the pre-exponential factor only. Changing pressure in the region close to the high-pressure limit can result in a substantial change in the Arrhenius activation energy as well. As noted earlier, in the low pressure limit all energized molecules react and collisional de-energization is of no significance. However, with increasing pressure competition between reaction and collisional de-energization starts to occur. Energized molecules with energies near the critical energy have relatively long lifetimes compared to rapidly reacting molecules with higher energies, and are thus more likely to be de-energized. The more highly energized molecules thus contribute more heavily to the global rate of reaction, making the activation energy correspondingly higher. In the high-pressure limit the maximum activation energy prevails, being equal to the one obtained from the absolute rate theory.

For easy computer implementation the RRKM based fall-off data were correlated to the following empirical relation:

$$k_{uni} = A\, p_t^{B_1} \exp\left(-\frac{E_a + B_2 \ln p_t + B_3 (\ln p_t)^2}{RT} \right) \tag{5.19}$$

with the constants B_1, B_2 and B_3 serving to describe the pressure dependence of the pre-exponential factor A and the Arrhenius activation energy E_a. Using the nonlinear single response regression technique as outlined in paragraph 4.3.3, the Arrhenius parameters and pressure correction constants were determined for the pressure range from 1 to 1000 Pa and the temperature range from 800 to 1000 K, see Table 5.4.

Table 5.4: *Pre-exponential factor, activation energy and pressure correction constants for unimolecular reaction rate coefficients. Conditions: p_t= 1-1000 Pa, T= 800-1000 K and silane as bath gas.*

reaction	A / s^{-1}	E_a / J mol^{-1}	B_1 / -	B_2 / J mol^{-1}	B_3 / J mol^{-1}
$SiH_4 \rightarrow SiH_2 + H_2$	$3.53\ 10^{8}$	$215.8\ 10^{3}$	1.0013	$-3.55\ 10^{1}$	$1.23\ 10^{1}$
$H_3SiSiH \rightarrow H_2SiSiH_2$	$6.02\ 10^{4}$	$4.2\ 10^{3}$	1.0001	$7.86\ 10^{-2}$	$8.37\ 10^{-2}$
$Si_2H_6 \rightarrow SiH_4 + SiH_2$	$3.53\ 10^{9}$	$163.3\ 10^{3}$	1.0953	$1.21\ 10^{3}$	$1.80\ 10^{2}$
$Si_2H_6 \rightarrow H_3SiSiH + H_2$	$9.68\ 10^{9}$	$180.6\ 10^{3}$	1.1076	$1.97\ 10^{3}$	$1.55\ 10^{2}$
$Si_3H_8 \rightarrow Si_2H_6 + SiH_2$	$3.99\ 10^{10}$	$165.2\ 10^{3}$	1.2143	$4.00\ 10^{3}$	$1.92\ 10^{2}$
$Si_3H_8 \rightarrow H_3SiSiH + SiH_4$	$2.54\ 10^{10}$	$158.1\ 10^{3}$	1.2214	$4.01\ 10^{3}$	$1.94\ 10^{2}$

Table 5.4 shows that the pressure correction constants B_2 and B_3 are irrelevant in case the unimolecular reaction possesses a high transition pressure. This is in agreement with the fact that in the low pressure limit the pressure dependence is confined to the pre-exponential factor. In contrast, the activation energies of the disilane and trisilane dissociation reactions change significantly with pressure. At 100 Pa the relative changes in these activation energies amount to 5-15%.

Collision efficiency

As noted earlier, the basic RRKM theory treats the processes of activation and deactivation as single-step processes in which molecules are assumed to acquire or loose their energy in one single step. The strong collision assumption is realistic for moderate to large molecules. According to Moffat *et al.* (1991) silane molecules have a collision efficiency close to unity. Small molecules like argon and hydrogen, however, possess collision efficiencies much smaller than unity (Robinson and Holbrook, 1972; Robinson, 1975). To correct for limited energy transfer upon collision several methods are applicable, the most sophisticated involving a very detailed mathematical treatment (Robinson and Holbrook, 1972). A good alternative, however, consists in replacing k_2 in equations (5.14) and (5.18) by λk_2 in which λ is a constant collisional deactivation efficiency. The number of collisions required to de-energize an energized molecule to a level below the critical energy is then equal to $1/\lambda$. This is an oversimplification. In fact, the number of collisions needed to de-energize a given energized molecule depends on the excess energy of this molecule, being the energy above the critical energy for reaction.

For the present purposes it is more convenient to replace the total pressure, p_t, in equation (5.19) with an effective total pressure, p_{eff}, defined according to:

$$p_{eff} = \sum_{i=1}^{NG} \lambda_i p_i \tag{5.20}$$

with NG the number of gas phase components and p_i and λ_i the partial pressure and collisional deactivation efficiency of gas phase component i. The effects of gas phase composition on the de-energization rate coefficient k_2 are much smaller and hence have been omitted.

The only abundant gas phase components in the reaction mixture are silane, hydrogen and argon. As mentioned above silane has a collisional deactivation efficiency close to unity. Experimentally obtained values for the collisional deactivation efficiencies for argon and hydrogen are much smaller and range between 0.2 and 0.5 (Robinson, 1975; Robinson and Holbrook, 1972). During the simulation of the kinetic experiments the effective total pressure can be calculated for each set of experimental conditions using equation (5.20). In this way easy allowance is made for varying gas phase composition and hence for varying overall energy transfer with changing process conditions.

5.4 Kinetic parameter determination

5.4.1 Experimental

In total 210 experiments were used during the kinetic modelling, 150 of which covering the range of experimental conditions where gas phase reactions can be neglected, see Table 4.3, and 60 applying to the range of experimental conditions where gas phase reactions need to be considered, see Table 5.5.

Table 5.5: *Range of experimental conditions where gas phase reactions need to be taken into account.*

p_t	50 - 125	Pa
T	887 - 963	K
$V/F_{SiH_4,0}$	11 - 55	$m^3\ s\ mol^{-1}$
X_{SiH_4}	1.6 - 59	%
$H_2/SiH_4\|_0$	1.0	-
$SiH_4/Ar\|_0$	4.5	-

5.4.2 Model equations

During the simulations of the kinetic experiments, the reactor model equations given by (2.39) to (2.45) were applied in order to account for the gas/solid mass transfer resistances of the reactive gas phase species. The kinetic model used consists of the elementary gas phase reactions of Table 5.1 coupled to the global adsorption reactions (α-ε) and the elementary reactions (13) and (14) of the surface reaction network given in Table 5.2. In total six gas phase species are involved, i.e. SiH_4, SiH_2, Si_2H_6, H_3SiSiH, H_2SiSiH_2 and H_2, and besides vacant surface sites only one kinetically significant surface species exists, i.e. hydrogen adatoms denoted by H^*.

Following the law of mass action for the rates of the elementary gas phase steps of Table 5.1, the homogeneous net production rates of the above gas phase species are given by:

$$\sum_{k=1}^{ng} \nu_{k,i} r_{v,k} = \sum_{k=1}^{ng} \left(\nu_{k,i}\, k_k \prod_{i=1}^{NG} C_i^{\nu_{k,i}} \right) \qquad (5.21)$$

with ng the number of gas phase steps; $\nu_{k,i}$ the stoichiometric coefficient of component i in gas phase step k; $r_{v,k}$ the rate of gas phase step k; k_k the rate coefficient of gas phase step k; NG the number of gas phase components; C_i the gas phase concentration of component i.

As noted in paragraph 5.2.3, the rates of the global reactions (α-ε) are determined by the rates of the corresponding elementary adsorption reactions, see reactions (5-9) of Table 5.2. Following the law of mass action for the rates of these adsorption reactions, the heterogeneous net production rates of the silicon containing gas phase species are given by:

$$\sum_{m=1}^{ns} \nu_{m,i} r_{a,m} = \sum_{m=1}^{ns}\left(\nu_{m,i}\, k_m \prod_{i=1}^{NG} C_i^{\nu_{m,i}} \prod_{l=1}^{NS} L_l^{\nu_{m,l}}\right) \tag{5.22}$$

with ns the number of surface steps; $\nu_{m,i}$ the stoichiometric coefficient of gas phase component i in surface step m; $r_{a,m}$ the rate of surface step m; k_m the reaction rate coefficient of surface step m; NS the number of surface components; L_l the concentration of surface component l; $\nu_{m,l}$ the stoichiometric coefficient of surface component l in surface step m. The heterogeneous net production rate of molecular hydrogen is calculated from those of the silicon containing species using the stoichiometry of the global deposition paths (αα-εε) of Table 5.2.

The net production rate of hydrogen adatoms follows from:

$$\begin{aligned}\sum_{m=1}^{ns} \nu_{m,H*} r_{a,m} = {} & 4k_5 C_{SiH_4}\frac{L_*^2}{L_t} + 2k_6 C_{SiH_2} L_* + 2k_7 C_{Si_2H_6} L_* + 4k_8 C_{H_3SiSiH}\frac{L_*^2}{L_t} \\ & + 4k_9 C_{H_2SiSiH_2}\frac{L_*^2}{L_t} - k_{13} L_{H*} + k_{-13} L_{H^e} L_* - k_{14} L_{H*} L_{H^e} + k_{-14} C_{H_2} L_*\end{aligned} \tag{5.23}$$

The first five terms at the right-hand side of the equality sign represent the rates of hydrogen adatom production via the global adsorption reactions (α-ε). In addition to silane, silylsilylene and disilene are considered to adsorb via dual-site mechanisms as well, see paragraph 4.3.2. The four terms left represent the hydrogen adatom formation and disappearance rates corresponding to the elementary reactions (13) and (14) and written in a straightforward way following the law of mass action. The concentration of delocalized hydrogen atoms is obtained by applying the steady state approximation for this species, see paragraph 4.3.2:

$$L_{H^e} = \frac{k_{13} L_{H*} + k_{-14} C_{H_2} L_*}{k_{-13} L_* + k_{14} L_{H*}} \tag{5.24}$$

Together with the assumption that the recombination of a localized hydrogen adatom with a delocalized hydrogen atom proceeds potentially very fast compared to the interaction of a delocalized hydrogen atom with a vacant surface site, see also paragraph 4.3.2:

$$k_{-13} L_* \ll k_{14} L_{H*} \tag{5.25}$$

the net production rate of hydrogen adatoms finally becomes:

$$\sum_{m=1}^{ns} \nu_{m,H*} r_{a,m} = 4\,k_5\,C_{SiH_4}\frac{L_*^2}{L_t} + 2\,k_6\,C_{SiH_2}L_* + 2\,k_7\,C_{Si_2H_6}L_* + 4\,k_8\,C_{H_3SiSiH}\frac{L_*^2}{L_t}$$
$$+ 4\,k_9\,C_{H_2SiSiH_2}\frac{L_*^2}{L_t} - 2\,k_{13}L_{H*} + \frac{2\,k_{13}K_H C_{H_2}L_*^2}{L_{H*}} \tag{5.26}$$

with K_H the equilibrium coefficient of molecular hydrogen adsorption:

$$K_H = \frac{k_{13}k_{14}}{k_{13}k_{14}} \tag{5.27}$$

After solving the reactor model equations (2.39) to (2.45) using the net production rates as defined above, the silicon growth rate and the molar flow rates of the gas phase species at the reactor outlet can be calculated from equations (2.46) and (2.47). More specifically, the silicon growth rate is calculated from:

$$R_{Si} = \frac{M_{Si}}{\rho_{Si}}\sum_{m=1}^{ns} \nu_{m,Si} r_{a,m}\Big|_{\xi=1} = \frac{M_{Si}}{\rho_{Si}}\left(k_5\,C_{SiH_4}\frac{L_*^2}{L_t} + k_6\,C_{SiH_2}L_* + k_7\,C_{Si_2H_6}L_*\right.$$
$$\left. + 2\,k_8\,C_{H_3SiSiH}\frac{L_*^2}{L_t} + 2\,k_9\,C_{H_2SiSiH_2}\frac{L_*^2}{L_t}\right)_{\xi=1} \tag{5.28}$$

and the outlet molar flow rate of species i from:

$$F_i = F_{i,0} + 4\pi R_i^2 \sum_{m=1}^{ns} \nu_{m,i} r_{a,m}\Big|_{\xi=R_i/R_0} + 4\pi R_0^2 \sum_{m=1}^{ns} \nu_{m,i} r_{a,m}\Big|_{\xi=1}$$
$$+ 4\pi R_0^3 \sum_{cc=1}^{M+2} w_{cc} \sum_{k=1}^{ng} \nu_{k,i}\, r_{v,k}\,(\xi_{cc}) \tag{5.29}$$

In these expressions, M_{Si} is the molar mass of solid silicon, i.e. 28.086 10^{-3} kg mol^{-1}; ρ_{Si} the density of solid silicon, i.e. 2.33 10^3 kg m^{-3}; $F_{i,0}$ and F_i the molar flow rates of gas phase species i at the reactor inlet and outlet; R_0 and R_1 the inner and outer radius as defined in reactor model, see Figure 2.11; ξ the dimensionless radial coordinate; M the number of interior collocation points and w_{cc} the weighting factors, see paragraph 2.5.2. The homogeneous and heterogeneous net production rates in equation (5.29) are again calculated according to equations (5.21) and (5.22).

5.4.3 Regression analysis

Since the total number of rate and equilibrium coefficients featuring in the reactor model equations is 15, a set of 30 kinetic and thermodynamic parameters would have to be estimated. This number can however be reduced by the use of thermodynamic and physico-chemical relations and sensitivity analysis. The rate coefficients of the unimolecular gas phase steps, k_1, k_{-2}, k_3 and k_4 (s^{-1}), are calculated using the empirical relation given by equation (5.19) with the total pressure, p_t, replaced by the effective total pressure, p_{eff}, see equation (5.20):

$$k_k = A_k\left(\sum_{i=1}^{NG}\lambda_i p_i\right)^{B_{1,k}} \exp\left(-\frac{E_{a,k}+B_{2,k}\ln\left(\sum_{i=1}^{NG}\lambda_i p_i\right)+B_{3,k}\left(\ln\left(\sum_{i=1}^{NG}\lambda_i p_i\right)\right)^2}{RT}\right) \tag{5.30}$$

Here, A_k and $E_{a,k}$ are the pre-exponential factor and Arrhenius activation energy of gas phase step k. Table 5.4 contains the pressure correction constants $B_{1,k}$, $B_{2,k}$ and $B_{3,k}$ for each of the unimolecular gas phase steps under consideration. The collisional efficiencies, λ_i, were set to 1.0 except for hydrogen and argon. For these small molecules the collisional deactivation efficiency was set equal to 0.3. Through a formal sensitivity analysis, see Appendix 5C, small sensitivities for all gas phase reaction rate coefficients were detected except for that corresponding to the initiation step, reaction (1). For this reason the pre-exponential factors A_{-2}, A_3 and A_4 as well as the activation energies $E_{a,-2}$, $E_{a,3}$ and $E_{a,4}$ were kept fixed at the RRKM based values listed in Table 5.4, whereas the pre-exponential factor of the initial step in silane pyrolysis, A_1, was adjusted during the regression of the kinetic experiments. Due to a strong correlation between the activation energy of the initial step in silane pyrolysis, $E_{a,1}$, and the standard enthalpy change of hydrogen adsorpion, $\Delta_a H^0_H$, the former was not adjusted either but kept fixed at the RRKM value listed in Table 5.4.

The rate coefficients of the reverse gas phase steps, k_{-1}, k_2, k_{-3} ($m^3\ mol^{-1}\ s^{-1}$) and k_{-4} (s^{-1}), are calculated from the equilibrium constants and the forward step rate coefficients according to:

$$k_{-k} = k_k / K_k \tag{5.31}$$

with the equilibrium constant, K_k, calculated at the reaction temperature using the most recent thermodynamic data base of Coltrin *et al.* (1986,1989).

The rate coefficient of silane adsorption is expressed in Arrhenius form according to:

$$k_5 = A_5 \exp\left(-\frac{E_{a,5}}{RT}\right) \tag{5.32}$$

with the pre-exponential factor and the activation energy kept fixed during the regression at the values derived in the region where gas phase reactions can be omitted, see paragraph 4.3.3. Assuming silane adsorption to be non-activated, i.e. $E_{a,5}= 0$, and substituting the estimated standard activation entropy given in Table 4.4 into equation (4.13) yields a pre-exponential factor equal to $3.89\ 10^4\ m^3\ mol^{-1}\ s^{-1}$ at T= 900 K. The rate coefficients corresponding to the other elementary adsorption reactions, k_6 to k_9 ($m^3\ mol^{-1}\ s^{-1}$), are calculated from kinetic gas theory:

$$k_m = A_m \exp\left(-\frac{E_{a,m}}{RT}\right) = s_0 \frac{1}{4}\sqrt{\frac{8RT}{\pi M_i}}\, L_t^{-1} \tag{5.33}$$

where s_0 denotes the initial sticking probability and M_i the molar mass of gas phase species i. This means that the corresponding activation energies $E_{a,6}$ to $E_{a,9}$ were kept fixed at zero during the regression. The pre-exponential factors A_6 to A_9 were kept fixed at the values calculated from equation (5.33) for T= 900 K and an initial sticking probability equal to 0.1 in case of disilane, see paragraph 5.2.3, and 1.0 in case of silylene, silylsilylene and disilene.

The rate coefficient corresponding to the excitation of a hydrogen adatom into a delocalized state, k_{13} (s^{-1}), is expressed in Arrhenius form as well:

$$k_{13} = A_{13} \exp\left(-\frac{E_{a,13}}{RT}\right) \tag{5.34}$$

The equilibrium coefficient corresponding to the dissociative adsorption of molecular hydrogen, K_H ($m^3\ mol^{-1}$), is expressed in Van 't Hoff form:

$$K_H = A_H \exp\left(-\frac{\Delta_a H_H^0}{RT}\right) = \exp\left(\frac{\Delta_a S_H^0}{R}\right) \exp\left(-\frac{\Delta_a H_H^0}{RT}\right) \tag{5.35}$$

By sensitivity analysis large sensitivities for both the rate coefficient corresponding to the excitation of a hydrogen adatom, k_{13}, and the equilibrium coefficient reflecting molecular hydrogen adsorption, K_H, were detected. Therefore, the pre-exponential factors A_{13} and A_H with the corresponding $E_{a,13}$ and $\Delta_a H^0_H$ were adjusted during the regression of the kinetic experiments.

The number of kinetic and thermodynamic parameters to be estimated could thus be reduced to 5, i.e. A_1, A_{13}, A_H, $E_{a,13}$ and $\Delta_a H^0_H$, which were determined using the Marquardt multi-response nonlinear regression algorithm (Marquardt, 1963; Froment and Hosten, 1981). Maximum likelihood parameter estimates, b, were obtained by minimization of the least square criterion applied on the observed, Y, and calculated, $\hat{Y}$, responses:

$$S(b) = \sum_{h=1}^{v} \sum_{k=1}^{v} \sigma_{hk} \sum_{i=1}^{n} (Y_{ih} - \hat{Y}_{ih})(Y_{ik} - \hat{Y}_{ik}) \tag{5.36}$$

where v is the number of responses, n the number of observations and σ_{hk} the (h,k) elements of the inverse of the error variance-covariance matrix. This criterion is based on the assumption that the experimental errors are normally distributed with a zero mean. The elements σ_{hk} of the inverse of the error variance-covariance matrix were obtained from an unweighted preliminary parameter estimation, i.e. from a parameter estimation using a unit error variance-covariance matrix. The silicon growth rates as well as the molar flow rates of silane and Si_2H_x components at the reactor outlet were used as responses. The calculated Si_2H_x response was obtained by summing the individually calculated outlet molar flow rates of H_3SiSiH, H_2SiSiH_2 and Si_2H_6. The observed Si_2H_x response was obtained from the mass spectrometric signal measured at AMU 60, see paragraph 2.2. Statistical testing of the significance of both the global regression and the kinetic and thermodynamic parameter estimates was performed as outlined in paragraph 4.3.3. To facilitate the simultaneous estimation of the pre-exponential factor and Arrhenius activation energy corresponding to k_{13}, and the standard adsorption entropy and enthalpy corresponding to K_H, reparameterization was applied (Kittrell, 1970):

$$k_{13} = A_{13}' \exp\left(-\frac{E_{a,13}}{R}\left(\frac{1}{T} - \frac{1}{T_m}\right)\right) \tag{5.37}$$

$$K_H = A_H' \exp\left(-\frac{\Delta_a H_H^0}{R}\left(\frac{1}{T} - \frac{1}{T_m}\right)\right) \tag{5.38}$$

with T_m the average temperature of the experiments, in the present chapter equal to 914.8 K. The non-reparameterized pre-exponential factors can be deduced from the above reparameterized ones according to:

$$A_{13} = A_{13}' \exp\left(\frac{E_{a,13}}{R T_m}\right) \tag{5.39}$$

$$A_H = A_H' \exp\left(\frac{\Delta_a H_H^0}{R T_m}\right) \tag{5.40}$$

In total 210 experiments, covering the complementary ranges of experimental conditions of Tables 4.3 and 5.5, were used during the regression. Si_2H_x responses from experiments at total pressures lower than 50 Pa were not considered, because gas phase reactions were found to be insignificant at these pressures, see paragraph 3.4. Hence, the total number of experimental Si_2H_x responses considered during the regression amounted to 60. The calculations were performed on a Silicon Graphics Power Challenge Computer. The CPU time required to simulate one experiment amounts to approximately 1 second. During every iteration in the Marquardt algorithm every experiment has to be simulated at least 6 times, i.e. the number of parameters to be estimated plus one. Every iteration in the Marquardt routine thus takes at least 21 minutes CPU time. When good initial parameter estimates are provided approximately 5 iterations are sufficient to reach the minimum of the objective function. As initial estimate for the pre-exponential factor of the homogeneous silane decomposition reaction, A_1, the value calculated from the RRKM theory was applied, see Table 5.4. Initial estimates for the other parameters, i.e. A_{13}, A_H, $E_{a,13}$ and $\Delta_a H^0_H$, were obtained from the modelling results in the absence of gas phase reactions, see Table 4.4.

The final kinetic and thermodynamic parameter estimates with their corresponding 95%-confidence intervals are shown in Table 5.6. The F-value of the regression amounted to 59000. The t-values of the parameter estimates ranged between 17 and 84, indicating the statistical significance of the corresponding estimates. The largest value for the binary correlation coefficient between two parameter estimates occurred for the reparameterized pre-exponential factors corresponding to hydrogen adsorption and to the excitation of a hydrogen adatom into a delocalized state and amounted to 0.83. Figures 5.4 and 5.5 show parity diagrams of the calculated versus the observed silicon growth rates and silane and Si_2H_x outlet molar flow rates. The absence of systematic deviations reflects the adequacy of the model equations used. The calculated and observed growth rates and silane outlet molar flow rates usually deviated by less than 15%. The deviations between the calculated and observed outlet molar flow rates of Si_2H_x components were somewhat larger and typically deviated by less than 20%.

Table 5.6: *Kinetic and thermodynamic parameter estimates with their approximate individual 95%-confidence intervals obtained from a regression analysis of 210 experiments in the complementary ranges of experimental conditions listed in Tables 4.3 and 5.5. The set of model equations given by (2.39) to (2.45), (5.28) and (5.29), and based on the gas phase and surface reaction network shown in Tables 5.1 and 5.2 were applied during the simulations.*

reaction	A or A' estimate with 95%-confidence interval / s^{-1}, $m^3\ mol^{-1}$ or $m^3\ mol^{-1}\ s^{-1}$	E_a or Δ_aH^0 estimate with 95%-confidence interval / kJ mol^{-1}
(1)	$(1.28 \pm 0.03)\ 10^{10}$	215.8
(-2)	$3.53\ 10^9$	163.3
(3)	$9.68\ 10^8$	180.6
(4)	$6.02\ 10^4$	4.2
(5)	$3.89\ 10^4$	0.0
(6)	$1.76\ 10^7$	0.0
(7)	$1.23\ 10^6$	0.0
(8)	$1.25\ 10^7$	0.0
(9)	$1.25\ 10^7$	0.0
(13)	$7.8 \pm 0.4\ '$	188±10
(H)	$(3.5 \pm 0.5)\ 10^3\ '$	-361±23

' reparameterized

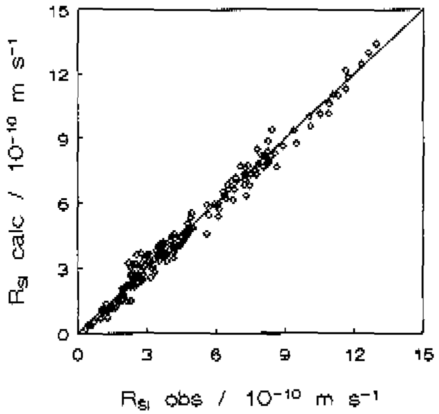

Figure 5.4: *Calculated versus experimentally observed silicon growth rates in the complementary ranges of experimental conditions listed in Tables 4.3 and 5.5. Calculated growth rates were obtained from equation (5.28) after solving equations (2.39) to (2.45) with the set of parameters given in Table 5.6.*

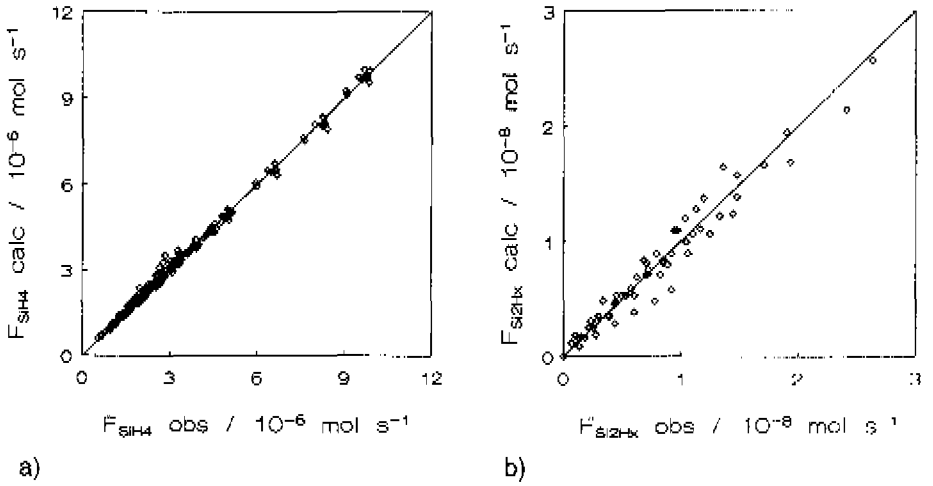

Figure 5.5: Calculated versus experimentally observed silane (a) and Si_2H_x (b) molar flow rates at outlet of reactor in the complementary ranges of experimental conditions listed in Tables 4.3 and 5.5. Calculated molar flow rates were obtained from equation (5.29) after solving equations (2.39) to (2.45) with the set of parameters given in Table 5.6.

5.5 Assessment of parameter estimates

Examination of the individual kinetic and thermodynamic parameter estimates as given in Table 5.6 can provide insight into the validity of the proposed reaction model shown in Tables 5.1 and 5.2.

The estimated value of the pre-exponential factor of the initial reaction in silane pyrolysis, reaction (1) of Table 5.1, deviates by almost a factor of forty from the value obtained from the RRKM analysis, see Table 5.4, giving rise to a similar discrepancy in the corresponding unimolecular rate coefficient, k_1. Applying equation (5.19) with the pressure correction constants and the Arrhenius parameters given in Table 5.4, results in a k_1-value of 1.0 10^{-2} s^{-1} at p_{eff}= 100 Pa and 900 K. In contrast, the estimated pre-exponential factor of Table 5.6 gives rise to a k_1-value of 3.8 10^{-1} s^{-1}. An explanation for this discrepancy is that the former value is derived by means of RRKM analysis of experiments at much higher pressure and/or lower temperature than generally applied in low pressure CVD of polycrystalline silicon. The estimated value is, however, in good agreement with the value of 3.5 10^{-1} s^{-1} obtained by Holleman and Verweij (1993) through fitting of the growth rate data in a conventional LPCVD reactor at 100 Pa total pressure and 898 K. Moreover, the same authors calculated values of 5.2 10^{-1} s^{-1} and

2.9 10^{-1} s^{-1} using Jasinski's (Jasinski and Chu, 1988) and Inoue's (Inoue and Suzuki, 1985) values for the rate coefficient of the reverse step, k_{-1}, combined with the thermodynamic data of Kleijn (1991a). Yeckel *et al.* (1989) fitted the rate coefficient for silane decomposition to growth rate data obtained by Meyerson and Olbricht (1984) for in-situ doped polycrystalline silicon in an LPCVD reactor at 896 K, 13.3 Pa and 100% silane. In case disilane was considered to contribute to the silicon deposition rate as well, a value 3.9 10^{1} m^{3} mol^{-1} s^{-1} was obtained, which can be transformed into a value of 5.2 10^{-1} s^{-1} for 100 Pa total pressure and 100% silane at the same temperature.

In Table 5.7 a comparison is made between the values of the standard activation entropy and enthalpy of hydrogen adatom excitation and the standard entropy and enthalpy of molecular hydrogen adsorption estimated in the region where gas phase reactions can be neglected and those estimated in the complete region considered. For the latter situation, the kinetic and thermodynamic quantities were derived as follows. The standard activation entropy of hydrogen adatom excitation, $\Delta^{\ddagger}S^{0}_{13}$, was calculated according to:

$$\Delta^{\ddagger}S^{0}_{13} = R \ln\left(\frac{A_{13}h}{e\,k\,T_{m}}\right) \tag{5.41}$$

with the non-reparameterized pre-exponential factor, A_{13}, calculated from the reparameterized one, A'_{13}, according to equation (5.39). The standard activation enthalpy of hydrogen adatom excitation, $\Delta^{\ddagger}H^{0}_{13}$, was taken equal to the estimated Arrhenius activation energy, $E_{a,13}$, minus the average thermal molar energy, RT_{m}. The standard entropy of hydrogen adsorption, $\Delta_{a}S^{0}_{H}$, was calculated according to:

$$\Delta_{a}S^{0}_{H} = R \ln(A_{H}) \tag{5.42}$$

with the non-reparameterized pre-exponential factor, A_{H}, calculated from the reparameterized one, A'_{H}, according to equation (5.40). The standard enthalpy of hydrogen adsorption, $\Delta_{a}H^{0}_{H}$, was estimated directly during the regression analysis, see Table 5.6.

Obviously, the deviations between both sets of parameter estimates is very small. Within their 95%-confidence intervals the parameter estimates of the two regions coincide. The assessment of the parameter estimates, see paragraph 4.4, showed that the standard activation entropy and enthalpy associated with the excitation of a hydrogen adatom into a delocalized state are physically reasonable. Examination of the equilibrium coefficient of molecular hydrogen adsorption revealed that the change in standard entropy is much too large in absolute sense, despite the physically meaningful estimate of the corresponding change in standard enthalpy.

Table 5.7: *The standard activation entropy and enthalpy associated with hydrogen adatom excitation and the standard reaction entropy and enthalpy associated with molecular hydrogen adsorption estimated in both the region where gas phase reactions can be neglected, see paragraph 4.3.3, and the same region expanded with the region where gas phase reactions need to be accounted for, see paragraph 5.4.3. Standard state: 1 mol* m^{-3}, *θ= 0.5.*

parameter	region including gas phase reactions**	region without gas phase reactions***
$\Delta^{\ddagger}S^{0}_{13}$ / J mol^{-1} K^{-1}	-40*	-33±16
$\Delta^{\ddagger}H^{0}_{13}$ / kJ mol^{-1}	180±10	186±14
$\Delta_{a}S^{0}_{H}$ / J mol^{-1} K^{-1}	-327*	-336±55
$\Delta_{a}H^{0}_{H}$ / kJ mol^{-1}	-361±23	-369±50

* the corresponding 95%-confidence intervals were not obtained from regression

** in total 210 experiments were conducted in the complementary ranges of experimental conditions listed in Tables 4.3 and 5.5

*** in total 150 experiments were conducted in the range of experimental conditions listed in Table 4.3

5.6 Simulation results

Figure 5.6 shows the conversion of silane as a function of space time at 963 K and total pressures of 25 and 50 Pa. Even at silane conversions as high as 64%, the kinetic model provides a good description of the experimentally obtained conversions. The effect of total pressure is also simulated correctly. The model also describes the dependence of the silane conversion on space time adequately over a broad range of temperatures as can be seen in Figure 5.7. The simulations confirm the existence of a differential operating regime with respect to silane conversion at the lower temperatures considered. At 50 Pa differential operation is delimited at roughly 888 K. At higher temperatures differential operation with respect to silane conversion is no longer satisfied.

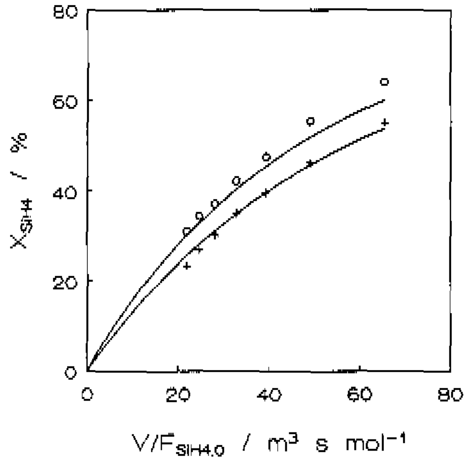

Figure 5.6: *Silane conversion versus silane space time. Lines: calculated with equations (2.39) to (2.45) and the set of parameters given in Table 5.6. Points: experiments. Conditions: $SiH_4/Ar|_0$= 4.0, T= 963 K. + p_t= 25 Pa, o p_t= 50 Pa.*

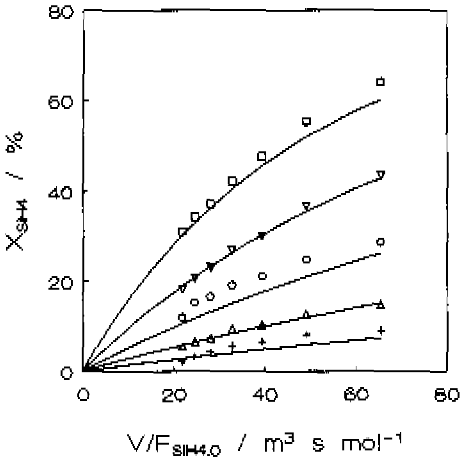

Figure 5.7: *Silane conversion versus silane space time. Lines: calculated with equations (2.39) to (2.45) and the set of parameters given in Table 5.6. Points: experiments. Conditions: $SiH_4/Ar|_0$= 4.0, p_t= 50 Pa. + T= 863 K, ▵ T= 888 K, o T= 912 K, ▿ T= 938 K, □ T=963 K.*

Figure 5.8 shows the silicon growth rate as a function of silane conversion at 50 Pa and different temperatures. The increase in silane conversion was brought about by an increase in space time, see Figure 5.7. Clearly, at each of the considered temperatures the agreement between experimental and calculated growth rates is good. Consequently, the effect of temperature on the dependence between silicon growth rate and silane conversion and hence space time is simulated correctly.

Figure 5.9 shows the experimental and simulated silicon growth rates versus the inlet hydrogen-to-silane ratio at 912 K and total pressures of 25 and 50 Pa. The direct relation between silicon growth rate and inlet hydrogen-to-silane ratio is justified because the experiments were performed in the regime of differential operation with respect to silane conversion and silicon deposition, see paragraph 3.4.1. In this regime gas phase reactions are not important and silicon deposition is predominantly determined by heterogeneous decomposition of silane. Hence, the rate of silicon deposition equals the rate of silane adsorption, given by reaction (5) in Table 5.2, and depends on the concentration of vacant surface sites squared. Due to the enhanced adsorption of molecular hydrogen with increasing inlet hydrogen-to-silane ratio, the fraction of vacant surface sites decreases, see Table 5.8 for calculated values, thereby slowing down the adsorption of silane and hence the deposition of silicon. Increasing the inlet hydrogen-to-silane ratio from 0.5 to 1.25 leads to a relative decrease in the fraction of vacant surface sites of about 11% and to a decrease in deposition rate by a factor of 1.25. The adequate simulation of the observed hydrogen inhibiting effect on the silicon growth rate shows that reactions (5) and (14) of Table 5.2 provide a good way to account for the competitive adsorption of silane and hydrogen.

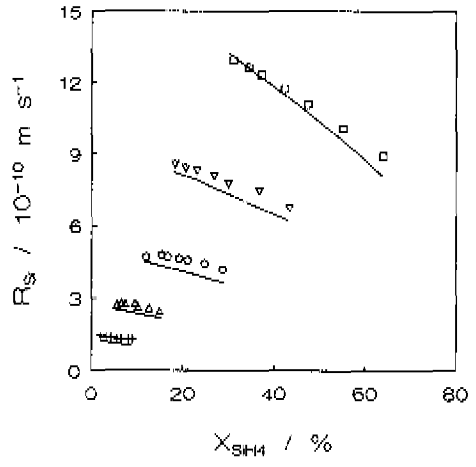

Figure 5.8: *Silicon growth rate versus silane space time. Lines: calculated with equations (2.39) to (2.45) and the set of parameters given in Table 5.6. Points: experiments. Conditions: $SiH_4/Ar|_0$= 4.0, p_t= 50 Pa. + T= 863 K, △ T= 888 K, ○ T= 912 K, ▽ T= 938 K, □ T=963 K.*

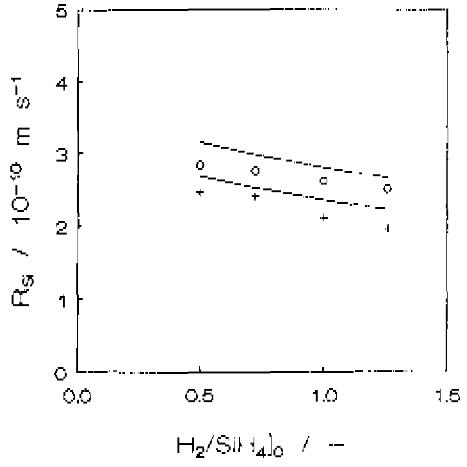

Figure 5.9: *Silicon growth rate versus inlet hydrogen-to-silane ratio. Lines: calculated with equations (2.39) to (2.45) and the set of parameters given in Table 5.6. Points: experiments. Conditions: T= 912 K, $F_{SiH_4,0}$= 2.6 10^{-6} mol s^{-1}, F_0= 6.3 10^{-6} mol s^{-1}, argon as balance. + p_t= 25 Pa, ○ p_t= 50 Pa.*

Figures 5.10 and 5.11 show the silicon growth rate and the silane conversion versus the silane space time at 100 Pa total pressure and different temperatures. Obviously, both the effects of space time and temperature on silicon growth rate and silane conversion are also adequately described by the model at 100 Pa. Even silane conversions as high as 60% and silicon growth rates up to 1.5 10^{-9} m s^{-1} are simulated correctly. At 938 K and 963 K, the experimentally observed growth rates exhibit maximum values at short space time. The occurrence of these maximum growth rates will be explained in paragraph 5.7.1.

Table 5.8: *Fraction of vacant surface sites versus the inlet hydrogen-to-silane ratio at 25 and 50 Pa total pressure. Calculated with equations (2.39) to (2.45) and the set of parameters given in Table 5.6. Conditions: $T = 912$ K, $F_{SiH_4,0} = 2.6\ 10^{-6}$ mol s^{-1}, $F_0 = 6.3\ 10^{-6}$ mol s^{-1}, argon as balance.*

$H_2/SiH_4\|_0$ / -	$\theta.$ / -	
	25 Pa	50 Pa
0.50	0.207	0.154
0.73	0.199	0.149
1.00	0.191	0.143
1.25	0.185	0.138

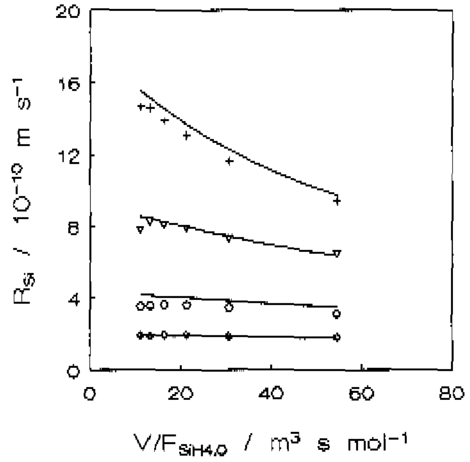

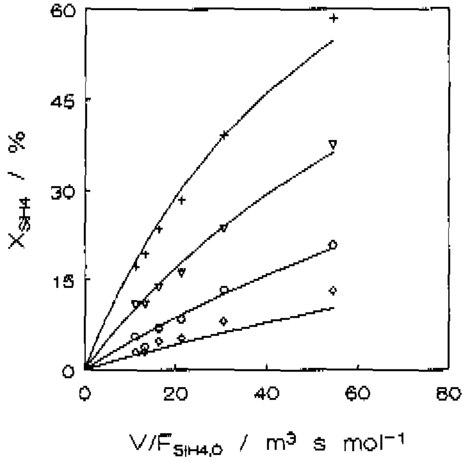

Figure 5.10: *Silicon growth rate versus silane space time. Lines: calculated with equations (2.39) to (2.45) and the set of parameters given in Table 5.6. Points: experiments. Conditions: $SiH_4/Ar|_0 = 4.5$, $SiH_4/H_2|_0 = 1.0$, $p_t = 100$ Pa. ◊ $T = 888$ o 912 K, ▿ $T = 938$ K, + $T = 963$ K.*

Figure 5.11: *Silane conversion versus silane space time. Lines: calculated with equations (2.39) to (2.45) and the set of parameters given in Table 5.6. Points: experiments. Conditions: $SiH_4/Ar|_0 = 4.5$, $SiH_4/H_2|_0 = 1.0$, $p_t = 100$ Pa. ◊ $T = 888$ K, K, o $T = 912$ K, ▿ $T = 938$ K, + $T = 963$ K.*

Figure 5.12 shows the simulations of the Si_2H_x selectivities as a function of space time over a broad range of temperatures at 100 Pa total pressure. Except at 888 K, the calculated Si_2H_x selectivities agree well with the experiments. It should be noted that the deviation between experimental and simulated selectivities at the former temperature is caused mainly by the concurrent deviation between experimental and simulated silane conversions, see Figure 5.11.

The model also adequately describes the effect of pressure as can be seen in Figure 5.13, where the silicon growth rate, silane conversion and Si_2H_x selectivity are plotted versus the space time at 80 Pa total pressure and a temperature of 938 K.

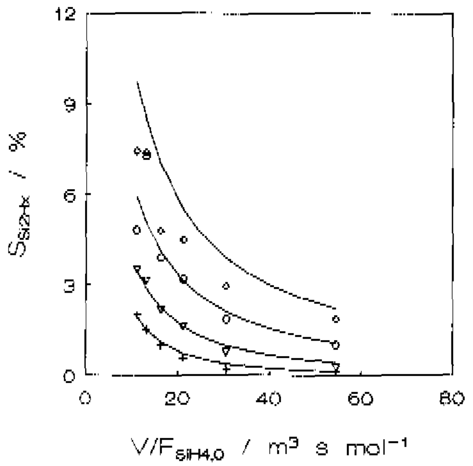

Figure 5.12: *Si_2H_x selectivity versus silane space time. Lines: calculated with equations (2.39) to (2.45) and the set of parameters given in Table 5.6. Points: experiments. Conditions: $SiH_4/Ar|_0$= 4.5, $SiH_4/H_2|_0$= 1.0, p_t= 100 Pa. ◇ T= 888 K, o T=912 K, ▿ T= 938 K, + T= 963 K.*

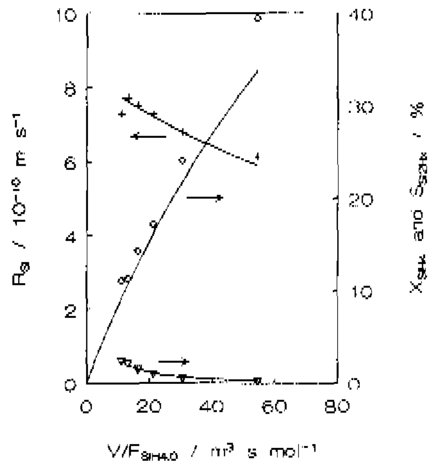

Figure 5.13: *Silicon growth rate (+), silane conversion (◇) and Si_2H_x selectivity (▿) versus silane space time. Lines: calculated with equations (2.39) to (2.45) and the set of parameters given in Table 5.6. Points: experiments. Conditions: $SiH_4/Ar|_0$= 4.5, $SiH_4/H_2|_0$= 1.0, p_t= 80 Pa, T= 938 K.*

Figure 5.14 shows the silicon growth rate, silane conversion and Si_2H_x selectivity as a function of space time at 80 Pa and 913 K. Note that these conditions were not considered during the regression. In contrast to the figures presented before, the feed mixture was not diluted with hydrogen. Hence, over the range of space times considered the actual partial pressure of silane exceeds 50 Pa. The results show that except for the silane conversion, the simulations are not adequate. The Si_2H_x

selectivity as well as the silicon growth rate is simulated typically too low. A possible explanation for these deviations could be the omission of less straightforward reactions such as insertion into surface Si-H bonds. The disilane adsorption reaction denoted by equation (5.4) belongs to that category of reactions.

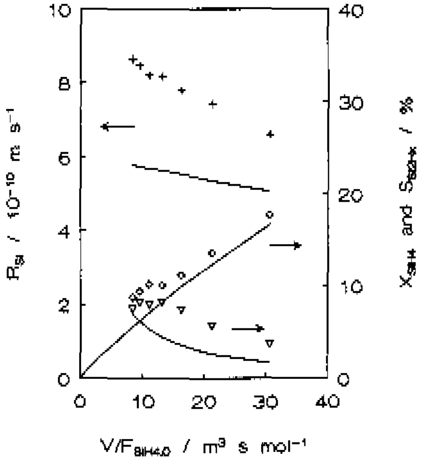

Figure 5.14: *Silicon growth rate (+), silane conversion (◊) and Si_2H_x selectivity (▿) versus silane space time. Lines: calculated with equations (2.39) to (2.45) and the set of parameters given in Table 5.6. Points: experiments. Conditions: $SiH_4/Ar|_0$= 4.0, $SiH_4/H_2|_0$= 0.0, p_t= 80 Pa, T= 913 K. Not considered during regression.*

5.7 Deposition path analysis and relative importance of gas phase reactions

5.7.1 Pressure range from 50 to 125 Pa

Effect of space time

Figure 5.15 shows the silicon growth rate, silane conversion and Si_2H_x selectivity versus the silane space time at 100 Pa and 963 K. The simulations have been extrapolated to zero space time. The silicon growth rate first increases from 12.7 10^{-10} m s^{-1} at zero space time to 17.1 10^{-10} m s^{-1} at 2.3 m^3 s mol^{-1} and then gradually decreases with increasing space time. The Si_2H_x selectivity starts at zero, because SiH_2 needs to be formed first, almost instantaneously reaches a maximum value of 36% and then strongly decreases with increasing space time. Figure 5.16 shows, in addition to the experimental and simulated silicon growth rate, the calculated total silicon growth rate due to gas phase intermediates, i.e. SiH_2, H_3SiSiH, H_2SiSiH_2 and Si_2H_6, and the calculated individual growth rates from the most abundant silicon containing gas phase species versus space time. As the observed growth rates correspond to the centre of the reactor, the growth rates were calculated for the conditions prevailing at $r= R_0$ after solving equations (2.39) to (2.45) with the set of parameters in Table 5.6.

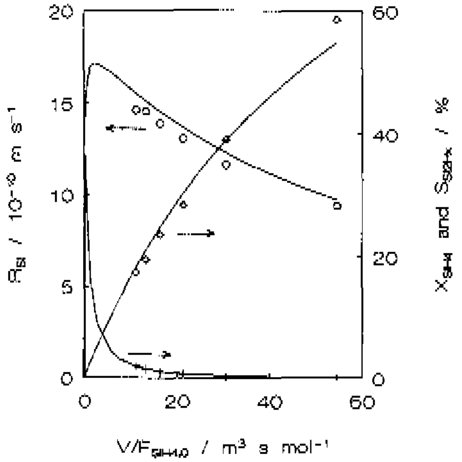

Figure 5.15: Silicon growth rate (o), silane conversion (◊) and Si_2H_x selectivity (+) versus silane space time. Lines: calculated with equations (2.39) to (2.45) and the set of parameters given in Table 5.6. Points: experiments. Conditions: $SiH_4/Ar|_0= 4.5$, $SiH_4/H_2|_0 = 1.0$, $p_t= 100$ Pa, $T= 963$ K.

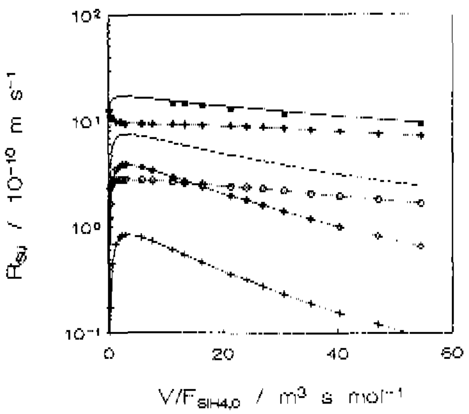

Figure 5.16: Silicon growth rate (——) plus experimental points (■), total silicon growth rate due to the gas phase intermediates (-----) and the individual silicon growth rates from the most abundant silicon containing gas phase species (······). + SiH_4, o SiH_2, ◊ Si_2H_6, + H_2SiSiH_2. Calculated at $r= R_0$ after solving equations (2.39) to (2.45) with the set of parameters given in Table 5.6. Conditions: $SiH_4/Ar|_0= 4.5$, $SiH_4/H_2|_0= 1.0$, $p_t= 100$ Pa, $T= 963$ K.

Figure 5.17 shows the corresponding calculated normalized concentrations of the gas phase intermediates and the calculated fraction of vacant surface sites versus space time. It should be noted that the slopes of the curves at the high conversion sides of Figures 5.16 and 5.17 are not completely determined by chemical kinetics but also slightly effected by changes in the diffusive mass transport as a result of varying gas phase composition, in particular the increasing H_2 concentration, with silane conversion. Silylsilylene, H_3SiSiH, is omitted from the above figures, because its contribution to the silicon growth rate can be neglected.

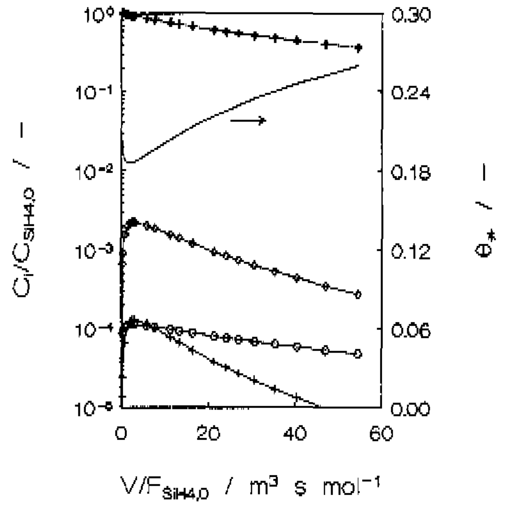

Figure 5.17: *Normalized concentrations of the most abundant silicon containing gas phase species (······) together with the fraction of vacant surface sites (———) versus silane space time. + SiH_4, o SiH_2, ◊ Si_2H_6, + H_2SiSiH_2. Calculated at $r= R_0$ after solving equations (2.39) to (2.45) with the set of parameters given in Table 5.6. Conditions: $SiH_4/Ar|_0= 4.5$, $SiH_4/H_2|_0= 1.0$, $p_t= 100$ Pa, $T= 963$ K.*

At space times close to zero the total silicon growth rate is determined by heterogeneous decomposition of silane and silylene only. The contribution of silylene to the silicon growth rate is practically constant and amounts to roughly 16%. With increasing space time the total growth rate due to the gas phase intermediates starts to increase as a result of the formation of disilane and disilene. The fraction of vacant surface sites is determined by the balance between consumption through adsorption of the various silicon containing gas phase species, reactions (5-9), and production through desorption of molecular hydrogen or more specifically through excitation of hydrogen adatoms, reaction (13). With increasing space time the gas phase concentrations and hence the adsorption rates of disilane and disilene increase. The rate of hydrogen adatom excitation, however, is not directly effected by a change in the space time, and the fraction of vacant surface sites consequently decreases, from 0.207 to 0.186. This decrease clearly effects the growth rate contribution from silane, which decreases by approximately 24% in this stage of the deposition process. At the position where the total growth rate due to the gas phase intermediates has reached its maximum value, the contribution from silane to the total growth rate amounts to 55.8%, whereas the rest percentage is built up of the contributions from silylene, 16.4%, disilane, 22.7% and disilene, 5.0%. Upon further increasing the space time, the total growth rate due to the gas phase intermediates starts to decrease as a result of a decrease in the concentrations of disilane and disilene in particular. The main cause for the decrease in the concentrations of these species is twofold. The most obvious reason is the decreasing silane concentration with increasing space time. A second, less obvious reason, is the increasing of hydrogen concentration with increasing silane conversion, which reduces the overall collision efficiency of the reaction mixture and hence the unimolecular reaction rate coefficients, see paragraph 5.3.3, thereby slowing down the gas phase reactions. Concurrently with the decrease in the concentrations of disilane, disilene and silane, an increase in the fraction of vacant surface sites takes place as a result of a decrease in the adsorption rates of these species without a direct change in the rate of hydrogen adatom excitation.

In order to investigate the interplay between gas phase and surface reactions at the point where the growth rate due to the gas phase intermediates is maximal, a contribution analysis was performed for the corresponding space time of 2.8 m^3 s mol^{-1}, giving rise to a silane conversion of 5.5%. A general description of the contribution analysis is given in Appendix 5C. Important to realize is that due to the occurrence of surface as well as gas phase reactions, the contribution analysis inevitably encloses a reactor specific geometrical factor, viz. the ratio of the deposition surface area to the gas phase reaction volume. This ratio, denoted here by A_d/V_g, amounts to 128.3 m^{-1} for the present reactor configuration, see paragraph 2.5.1.

At the point where the growth rate due to gas phase intermediates is maximal, silane consumption occurs for 31% through homogeneous dissociation, see reaction (1), for 28% through insertion of silylene, see reaction (2), and for 41% via heterogeneous decomposition according to global reaction (α). Production of silane occurs for 34% via homogeneous decomposition of disilane, see reaction (-2), and for 66% via heterogeneous decomposition of disilane according to global reaction (γ). Formation of silylene is determined for 80% by homogeneous decomposition of silane and for

20% by homogeneous decomposition of disilane according to reaction (-2). Silylene consumption takes place for 73% via insertion into silane and for 27% via heterogeneous decomposition according to global reaction (β). Insertion of silylene into molecular hydrogen, reaction (-1), has no important contribution to the total disappearance of silylene at the conditions considered. This is consistent with the rather high value of 6.37 for the dimensionless affinity of this reaction, see Table 5.9, indicating that the reverse step is not important. Dilution with large amounts of hydrogen obviously does not force the equilibrium of the initial silane pyrolysis reaction to the left. Except through reduction of the unimolecular gas phase rate coefficients as a consequence of a lower collision efficiency, see paragraph 5.3.3, hydrogen will have no further quenching effect on the gas phase chemistry. Disilane consumption is for 31% accounted for by homogeneous decomposition into silane and silylene, for 8% by homogeneous decomposition into silylsilylene and hydrogen and for 61% by heterogeneous decomposition. Insertion of silylene into silane accounts for 100% to the disilane production. Disilane formation via insertion of silylsilylene into hydrogen has no significant contribution, which also follows from the rather high value of 4.55 for the dimensionless affinity of this reaction, see Table 5.9. The paths to and from H_3SiSiH are not discussed, because its contribution to the silicon growth rate is too low. Disilene disappearance occurs for 96% through isomerization towards silylsilylene, see reaction (-4), and for 4% through heterogeneous decomposition. Production of disilene is fully accounted for by isomerization of silylsilylene. The dimensionless affinity of this isomerization reaction, reaction (4), amounts to 0.04, indicating that its forward and backward steps proceed at the same rate and hence are equilibrated.

Table 5.9: *Dimensionless affinities as defined in Appendix 5C and rates of the forward steps of the considered elementary gas phase reactions. Calculated after solving equations (2.39) to (2.45) with the set of parameters given in Table 5.6. Conditions:* $SiH_4/Ar|_0 = 4.5$, $SiH_4/H_2|_0 = 1.0$, $V/F_{SiH_4,0} = 2.8\ m^3\ s\ mol^{-1}$, $p_t = 100$ *Pa,* $T = 963$ *K, corresponding to* $X_{SiH_4} = 5.5$ *%.*

gas phase reaction	A/RT / -	$\overrightarrow{r}$ / mol m^{-3} s^{-1}
$SiH_4 \rightleftharpoons SiH_2 + H_2$	6.37	7.78 10^{-3}
$SiH_2 + SiH_4 \rightleftharpoons Si_2H_6$	1.28	7.08 10^{-3}
$Si_2H_6 \rightleftharpoons H_3SiSiH + H_2$	4.55	4.71 10^{-4}
$H_3SiSiH \rightleftharpoons H_2SiSiH_2$	0.04	1.06 10^{-2}

A summary of the above contribution analysis is shown in the left part of Table 5.10. Instead of the contribution percentages of the individual reaction steps, the contribution percentages obtained after summation over all gas phase steps and over all surface steps are given. Production contribution percentages for the gas phase intermediates are omitted, because formation of these species is a matter of gas phase kinetics only. In order to investigate the effect of silane space time and hence of silane conversion on the interplay between surface and gas phase reactions, similar contribution percentages were calculated for a space time of 40.4 m^3 s mol^{-1} corresponding to a silane conversion of 46.3%, see right part of Table 5.10. Comparison shows that the relative importance of the gas phase reactions with respect to the consumption of the gas phase species reduces with increasing silane conversion.

Table 5.10: *Contribution analyses with respect to the consumption of the most important gas phase species at silane space times of 2.8 and 40.4* m^3 *s* mol^{-1}*, performed as described in Appendix 5C after solving equations (2.39) to (2.45) with the set of parameters given in Table 5.6. Conditions:* $SiH_4/Ar|_0 = 4.5$, $SiH_4/H_2|_0 = 1.0$, $p_t = 100$ *Pa,* $T = 963$ *K.* $A_d/V_g = 128.3$ m^{-1}*.*

$V/F_{SiH_4,0}$ / m^3 s mol^{-1}	2.8		40.4	
X_{SiH_4} / %	5.5		46.3	
	surface / %	gas phase / %	surface / %	gas phase / %
SiH_4				
consumption	41	59	67	33
production	66	34	76	24
SiH_2				
consumption	27	73	55	45
Si_2H_6				
consumption	61	39	72	28
H_2SiSiH_2				
consumption	4	96	8	92

It is possible to make a semi-quantitative prediction of the concentration level of silylene with respect to that of silane by applying the pseudo-steady-state approximation for this species. Herefore, a contribution analysis was performed at $r = R_0$. Contrary to the integral contribution analysis described in Appendix 5C, this local contribution analysis is based on the gas phase and surface concentrations locally existing. Moreover, it has to account for the inlet and outlet molar flow rates contributing to the total formation and disappearance of the gas phase components as well.

In the range of space times considered, i.e. at space times between 2.8 and 40.4 m^3 s mol^{-1}, the major part of silylene is formed through homogeneous decomposition of silane, reaction (1). Because silylene is not fed, the inlet of the reactor is irrelevant with respect to the formation of this species. Silylene consumption, on the other hand, is accounted for by insertion into silane, reaction (2), and by heterogeneous decomposition, global reaction (β). The contribution of the outlet molar flow rate to the total silylene consumption is typically less than 0.1% and can therefore be omitted. The absolute concentration level of silylene is determined by the balance between production through reaction (1) having a first order rate coefficient k_1 and consumption through reactions (2) and (β) with pseudo-first order rate coefficients $k_2C_{SiH_4}$ and $k_6L.A_d/V_g$. Because these pseudo-first order rate coefficients vary with space time as a result of varying gas phase and surface composition, the present calculations are performed at one single space time. At $V/F_{SiH_4,0}$= 2.8 m^3 s mol^{-1}, k_1 is equal to 1.5 s^{-1}, whereas $k_2C_{SiH_4}$ and $k_6L.A_d/V_g$ amount to 8.8 10^3 s^{-1} and 4.8 10^3 s^{-1}, respectively. Comparison shows that the silylene disappearance reactions possess rate coefficients that are much larger than the silylene formation reaction, showing that silylene is a very reactive intermediate. The time required for silylene to reach its maximum concentration is indeed vanishingly small, see Figure 5.17. Moreover, the silylene concentration has no explicit dependence on space time but is determined implicitly by the concentration of silane. On the above grounds, the ratio between the absolute concentration levels of silylene and silane can be calculated according to $k_1/(k_2C_{SiH_4}+k_6L.A_d/V_g)$ (Boudart, 1968). Substitution of the above mentioned values for the (pseudo-)first order rate coefficients results in a ratio of 1.1 10^{-4}, which is very close to the simulated value of 1.2 10^{-4}.

Effect of temperature

Table 5.11 gives a global picture of the effect of temperature on the relative contribution from gas phase intermediates to the silicon deposition rate at 100 Pa. The calculations were performed for the conditions at r= R_0 after solving the reactor model equations (2.39) to (2.45) with the set of parameters given in Table 5.6. The space times were adapted such that the silane conversions at the different temperatures were all equal to 30%. In the small range of temperatures considered, the concentration of silane is hardly effected by a change in temperature and amounts to roughly 3.6 10^{-3} mol m^{-3}. The relative contribution from H_3SiSiH to the total growth rate due to gas phase intermediates is typically less than 1 10^{-3} and is consequently completely irrelevant. The relative contribution from H_2SiSiH_2 is in the order of a few percent.

Table 5.11: *Fraction of vacant surface sites, growth rate, total contribution from all intermediates to the growth rate, individual contributions from the most important intermediates to the total growth rate due to intermediates, and ratio between the growth rates from silylene and disilane versus temperature. Calculated at r= R_0 after solving equations (2.39) to (2.45) with the set of parameters given in Table 5.6. Conditions:* $SiH_4/Ar|_0$= *4.5,* $SiH_4/H_2|_0$= *1.0,* p_t= *100 Pa and* X_{SiH_4}= *30%.*

T / K	θ_* / -	R_{Si} / 10^{-10} m s^{-1}	$\Phi_{int/tot}$ / -	$\Phi_{SiH_2/int}$ / -	$\Phi_{Si_2H_6/int}$ / -	$R_{Si,SiH_2}/R_{Si,Si_2H_6}$ / -
888	0.063	1.26	0.379	0.169	0.775	0.218
912	0.101	3.03	0.341	0.272	0.665	0.409
938	0.156	6.90	0.332	0.394	0.535	0.736
963	0.221	13.71	0.348	0.505	0.418	1.208

As mentioned earlier, the fraction of vacant surface sites is determined by the balance between consumption through adsorption of the various silicon containing gas phase species, reactions (5-9), and production through desorption of molecular hydrogen or more specifically through excitation of hydrogen adatoms, reaction (13). Since hydrogen adatom excitation is activated, $E_{a,13}$= 188 kJ mol^{-1}, and adsorption of silicon hydride species is non-activated, higher temperatures lead to higher fractions of vacant surface sites and hence to higher silicon deposition rates, see equation (5.28). A higher θ_* results in higher individual growth rates from the various silicon containing gas phase species. Since SiH_4, H_3SiSiH and H_2SiSiH_2 adsorb via dual-site adsorption mechanisms, the effect of increasing θ_* is more pronounced for these species than for SiH_2 and Si_2H_6, occupying only one vacant site upon adsorption. The effects of higher concentrations of the gas phase intermediates with increasing temperature are not considered in the above discussion. Naturally, these effects will positively influence the adsorption rates and hence the growth rates from the intermediates, thereby slightly decreasing the fraction of vacant surface sites.

The growth rate contribution from all gas phase intermediates, $\Phi_{int/tot}$, is independent of temperature and is almost completely determined by the growth rate contributions from silylene and disilane. This independency of temperature can be attributed in first approximation to the roughly equal activation energies of the gas phase decomposition of silane and the first order desorption of hydrogen. Interestingly to see is that with varying temperature a change in most contributing gas phase intermediate takes place. At 888 K disilane contributes for 78% and silylene for 17% to the growth rate due to gas phase intermediates, whereas at 963 K these percentages amount to 42% and 51%, respectively. Since the adsorption reactions of silylene and disilane are kinetically equivalent in the sense that both are non-activated and require the same number of vacant surface sites, the above effect of temperature has to be explained by the ratio between the gas phase concentrations of silylene and disilane. An expression for this ratio can be derived from a pseudo-steady-state mass balance for disilane:

$$\begin{aligned} & k_2\, C_{SiH_4}\, C_{SiH_2} + k_{-3}\, C_{H_3SiSiH}\, C_{H_2} - k_{-2}\, C_{Si_2H_6} - \\ & k_3\, C_{Si_2H_8} - k_7\, C_{Si_2H_6}\, L_{*} \frac{A_d}{V_g} - C_{Si_2H_8} \frac{F_v}{V_g} = 0 \end{aligned} \tag{5.43}$$

in which the last term on the left-hand side denotes the molar flow rate of disilane at the reactor outlet in units mol m^{-3} s^{-1}, see model equation (2.39). A contribution analysis at r= R_0 showed that production of disilane is completely accounted for by silylene insertion into silane, reaction (2). Disilane disappearance, on the other hand, takes place through homogeneous decomposition into silane and silylene, reaction (-2), through heterogeneous decomposition according to global reaction (γ), and to a lesser extent via homogeneous decomposition into silylsilylene and hydrogen, see reaction (3). The contribution of the outlet molar flow rate to the total disappearance of disilane is typically less than 2% and is therefore skipped from the mass balance given by equation (5.43). Rearrangement of the terms left at the left-hand side of equation (5.43) results in the following expression for the ratio between the silylene and disilane concentration:

$$\frac{C_{SiH_2}}{C_{Si_2H_6}} = \frac{k_{-2} + k_3 + k_7\, L_{*} \frac{A_d}{V_g}}{k_2\, C_{SiH_4}} \tag{5.44}$$

The denominator is almost independent on temperature, since both the second order rate coefficient k_2 and the silane concentration C_{SiH_4} hardly change with temperature. On the other hand, all individual terms of the numerator increase with increasing temperature. The first order rate coefficients k_{-2} and k_3 have activation energies of at least 163.3 and 180.6 kJ mol^{-1}, see Table 5.6. The actual activation energies are even higher due to their dependence on effective pressure, see paragraph 5.3.3. The term left in the numerator increases due to the increase in the fraction of vacant surface sites with temperature, see Table 5.11. In this way it is shown that with rising temperature the ratio of silylene concentration to disilane concentration increases and hence the relative contribution of silylene to the silicon growth rate.

Effect of pressure

Table 5.12 gives a global picture of the effect of total pressure on the relative contribution from gas phase intermediates to the silicon deposition rate at 963 K. The calculations were again performed for the conditions at r= R_0 after solving the reactor model equations (2.39) to (2.45) with the set of parameters given in Table 5.6. The space times were adapted such that the silane conversions at the different pressures were all equal to 30%. The lumped contribution from H_3SiSiH and H_2SiSiH_2 to the total growth rate due to gas phase intermediates is typically in the order of a few percent. Hence these species are not considered.

Table 5.12: *Fraction of vacant surface sites, growth rate, total contribution from all intermediates to the growth rate, individual contributions from the most important intermediates to the total growth rate due to intermediates, and ratio between the growth rates from silylene and disilane versus total pressure. Calculated at r= R_0 after solving equations (2.39) to (2.45) with the set of parameters given in Table 5.6. Conditions: $SiH_4/Ar|_0$= 4.5, $SiH_4/H_2|_0$= 1.0, T= 963 K and X_{SiH_4}= 30%.*

p_t / Pa	θ_* / -	R_{Si} / 10^{-10} m s^{-1}	$\Phi_{int/tot}$ / -	$\Phi_{SiH_2/int}$ / -	$\Phi_{Si_2H_6/int}$ / -	$R_{Si,SiH_2}/R_{Si,Si_2H_6}$ / -
50	0.309	9.99	0.123	0.832	0.156	5.333
80	0.249	12.17	0.253	0.629	0.326	1.929
100	0.221	13.71	0.348	0.505	0.418	1.208

As mentioned earlier, the fraction of vacant surface sites is determined by the balance between consumption through adsorption of the various silicon containing gas phase species, reactions (5-9), and production through desorption of molecular hydrogen or more specific through excitation of hydrogen adatoms, reaction (13). Since the gas phase concentrations and hence the adsorption rates of all silicon hydride species increase with increasing pressure and the rate of hydrogen adatom excitation is not directly effected by a change in pressure, higher pressures lead to lower fractions of vacant surface sites.

The growth rate contribution from all gas phase intermediates, $\Phi_{int/tot}$, rises with total pressure and is almost completely determined by the growth rate contributions from silylene and disilane. As for the situation of varying temperature, a shift in the relative contribution of the gas phase intermediates occurs with varying total pressure. At 50 Pa silylene contributes for 83% and disilane for 16% to the growth rate due to gas phase intermediates, whereas at 100 Pa these percentages amount to 51% and 42%, respectively. Since the adsorption reactions of silylene and disilane are kinetically equivalent, the above effect of pressure has again to be explained by the ratio between the gas phase concentrations of silylene and disilane. This can be verified with the help of equation (5.44), which relates the above ratio to the (pseudo-)first order rate coefficients of the most important formation and disappearance reactions of disilane. Since the effect of pressure cannot be visualized prima facie, the various (pseudo-)first order rate coefficients have been calculated at the different pressures applied, see Table 5.13. This table also lists the silylene to disilane concentration ratio calculated on the basis of these (pseudo-)first order rate coeffcients. The denominator, $k_2C_{SiH_4}$, increases with pressure since both k_2 and C_{SiH_4} increase with increasing pressure. The increase in the unimolecular rate coefficient k_2 is a consequence of its pressure fall-off behaviour, see paragraph 5.3.3. The rate coefficient of the reverse reaction, k_{-2}, naturally increases in the same way as k_2 with pressure. Also k_3 increases with pressure but in a slightly different way than k_2 and k_{-2}. Contrary to the homogeneous terms k_{-2} and k_3, the heterogeneous term $k_7L.A_d/V_g$ decreases with pressure. This is a direct result of the decrease in the fraction of vacant surface sites, see Table 5.12. Because the heterogeneous term is significantly larger than the sum of the homogeneous terms, the decrease in the former obviously exceeds the increase in the latter, thereby effectively lowering the numerator with pressure. In this way it is shown that with rising pressure the ratio of silylene concentration to disilane concentration decreases and hence the relative contribution of silylene to the silicon growth rate.

Table 5.13: *Individual terms of the numerator and denominator of equation (5.44) and the ratio between silylene and disilane concentration versus total pressure. Calculated at* $r= R_0$ *after solving equations (2.39) to (2.45) with the set of parameters given in Table 5.6. Conditions:* $SiH_4/Ar|_0= 4.5$, $SiH_4/H_2|_0= 1.0$, $T= 963$ *K and* $X_{SiH_4}= 30\%$.

p_t / Pa	$k_2C_{SiH_4}$ / s^{-1}	k_{-2} / s^{-1}	k_3 / s^{-1}	$k_7L.A_d/V_g$ / s^{-1}	$C_{SiH_2}/C_{Si_2H_6}$ / -
50	1.48 10^3	7.99 10^1	2.01 10^1	5.49 10^2	0.44
80	3.43 10^3	1.16 10^2	2.83 10^1	4.42 10^2	0.17
100	5.11 10^3	1.38 10^2	3.33 10^1	3.91 10^2	0.11

5.7.2 Pressure range from 25 to 50 Pa

Figure 5.18 shows the silicon growth rate, the growth rate due to gas phase intermediates and the ratio between the individual growth rates from silylene and disilane versus temperature for the total pressures of 25 and 50 Pa using pure silane as feed. The space times were adapted such that the silane conversions were all equal to 30%.

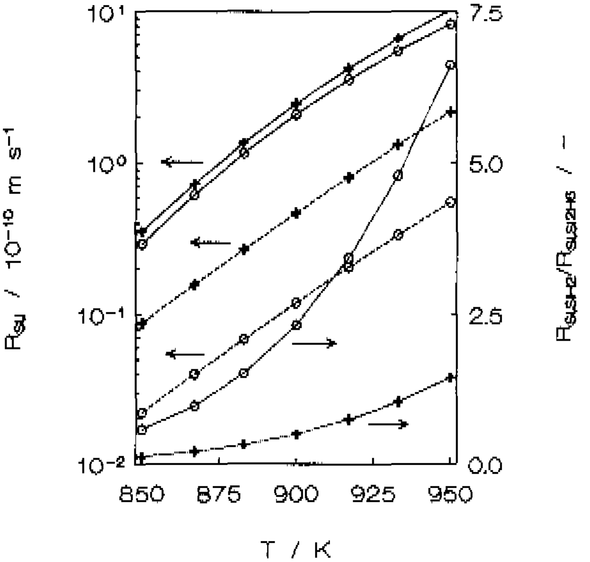

Figure 5.18: Silicon growth rate (———), growth rate due to gas phase intermediates (------) and ratio between growth rates from silylene and disilane (·······) versus temperature. Calculated at r= R_0 after solving equations (2.39) to (2.45) with the set of parameters given in Table 5.6. Conditions: 100% SiH_4 feed, X_{SiH_4}= 30%. o p_t= 25 Pa, + p_t= 50 Pa.

The depicted trends are in line with the results discussed in paragraph 5.7.1 for the high-pressure regime. In the above range of experimental conditions, which includes the industrially relevant operating conditions for the deposition of polycrystalline silicon from silane as discussed in Chapter 6, silicon growth is largely determined by heterogeneous decomposition of silane. At 25 Pa and 900 K adsorption of silane accounts for 94% to the silicon growth rate, whereas 6% is due to adsorption of gas phase intermediates. At 50 Pa and 900 K the same percentages amount to 81% and

19%, respectively. Temperature, however, has no significant effect on these growth rate contributions. The total growth rate due to gas phase intermediates is built up almost completely of the growth rates from silylene and disilane. The Si_2H_4 isomers are insignificant with respect to the total growth rate due to intermediates, as follows from their lumped contribution of typically less than 4%. The ratio between the silylene and disilane growth rate, $R_{Si,SiH_2}/R_{Si,Si_2H_6}$, increases with temperature and decreases with total pressure, see also paragraph 5.7.1. At 25 Pa and 950 K silicon growth due to gas phase intermediates occurs for 13% through adsorption of disilane and for 86% through adsorption of silylene, resulting in an upper value of 6.6 for the above ratio. The lower value prevails at 50 Pa and 850 K, where a value of 0.123 is calulated, based on growth rate contributions from silylene and disilane of 11% and 87%, respectively.

The above discussion applies to one conversion level only. The effect of space time and hence of silane conversion is qualitatively similar to that presented in Figure 5.16. The trends depicted therein reveal a negative effect of the silane conversion on the growth rate contribution from gas phase intermediates and a positive effect on the ratio between the growth rates from silylene and disilane.

5.8 Conclusions

A four-step elementary gas phase reaction network coupled to a ten-step elementary surface reaction network provides an adequate description of the polysilicon deposition process, at least for silane partial pressures up to 50 Pa. In case of higher partial pressures of silane, simulated Si_2H_x selectivities and silicon growth rates are typically too low, probably due to the omission of less straightforward reactions such as insertion into surface Si-H bonds.

The gas phase reaction network considers dissociation of silane into silylene and hydrogen, formation of disilane from silane and silylene, subsequent decomposition of disilane into silylsilylene and hydrogen, and isomerization of silylsilylene towards disilene. RRKM calculations showed that none of these reactions is in its high-pressure limit and that pressure fall-off effects need to be accounted for explicitly. The surface reaction network, on the other hand, considers dual-site adsorption of silane, silylsilylene and disilene, single-site adsorption of silylene and disilane, subsequent decomposition of the surface hydride species, and adsorption/ desorption of molecular hydrogen.

In the range of silane conversions applied, the relative importance of gas phase intermediates for silicon deposition decreases with increasing conversion and decreasing total pressure, and is independent of temperature. Silylene and disilane are by far the most contributing gas phase intermediates. Silylene is formed through homogeneous decomposition of both silane and disilane and is consumed via insertion into silane and via heterogeneous decomposition into solid silicon and molecular hydrogen. Production of disilane is completely accounted for by insertion of silylene into silane. Disilane consumption on the other hand takes place through homogeneous decomposition into silane and silylene, through heterogeneous decomposition into solid silicon, molecular hydrogen and silane, and to a lesser extent via homogeneous decomposition into silylsilylene and hydrogen. The total contribution of these species to the silicon growth rate amounts typically to 20% at the experimental conditions covered. Moreover, the ratio between the growth rates from silylene and disilane is affected by a change in either of the process variables considered, i.e. space time, total pressure and temperature. It increases with increasing temperature and space time, or conversion, and with decreasing total pressure.

The above conclusions could be reached using quantitative modelling of the kinetic experiments. Herefore, a kinetic model describing the experimental data in the absence of gas phase reactions was developed first. This model was then coupled to a set of gas phase reactions and additional surface reactions and applied in the reactor model equations taking explicitly into account the significant concentration gradients of the gas phase intermediates. This allowed an adequate description of the experimental data in the presence of gas phase reactions.

References

Barin, I., Knacke, O., Thermochemical properties of inorganic substances, Springer, Berlin, 1974.

Becerra, R., Walsh, R., 1987, *J. Phys. Chem.*, **91**, 5765.

Becerra, R., Walsh, R., 1992, *J. Phys. Chem.*, **96**, 10856.

Boudart, M., 1968, Kinetics of Chemical Processes, Prentice-Hall, Englewood Cliffs, New Jersey.

Breiland, W.G., Coltrin, M.E., Ho, P., 1986a, *J. Appl. Phys.*, **59**(9), 3267.

Breiland, W.G., Ho, P., Coltrin, M.E., 1986b, *J. Appl. Phys.*, **60**, 1505.

Brekel, C.H.J. van den, Bollen, L.J.M., 1981, *J. Crystal Growth*, **54**, 310.

Burgess, D., Zachariah, M.R., 1990, *Mat. Res. Soc. Symp. Proc.*, **168**, 31.

Coltrin, M.E., Kee, R.J., Miller, J.A., 1984, *J. Electrochem. Soc.*, **131**(2), 425.

Coltrin, M.E., Kee, R.J., Miller, J.A., 1986, *J. Electrochem. Soc.*, **133**(6), 1206.

Coltrin, M.E., Kee, R.J., Evans, G.H., 1989, *J. Electrochem. Soc.*, **136**(3), 819.

Dzarnoski, J., Rickborn, S.F., O'Neal, H.E., Ring, M.A., 1982, *Organometallics*, **1**, 1217.

Eriksson, G., 1975, *Chem. Scr.*, **8**, 100.

Froment, G.F., Hosten, L.H., in "Catalysis Science and Technology", Eds. Anderson, J.R., Boudart, M., Springer Verlag, Berlin, 1981, 98.

Gardeniers, J.G.R., 1990, Crystal habit of CVD-grown silicon in relation to adsorption processes, Ph.D. Thesis, Nijmegen.

Gaspar, P.P., Boo, B-H., Svoboda, D.L., 1987, *J. Phys. Chem.*, **91**. 5011.

Gates, S.M., 1988, *Surf. Sci.*, **195**, 307.

Gates, S.M., Chiang, C.M., 1991, *Chem. Phys. Lett.*, **184**(5,6), 448.

Gilbert, R.G., Smith, S.C., Jordan, M.J.T., 1993, UNIMOL program suite (calculation of fall-off curves for unimolecular and recombination reactions), School of Chemistry, Sydney University, Australia.

Hase, W.L., Bunker, D.L., 1973, QCPE **11**, 234.

Hitchman, M.L., Jensen, K.F., 1993, Chemical Vapor Deposition, Academic Press, London.

Ho, P., Coltrin, M.E., Binkley, J.S., Melius, C.F., 1985, *J. Phys. Chem.*, **89**(21), 4647.

Ho, P., Coltrin, M.E., Binkley, J.S., Melius, C.F., 1986, *J. Phys. Chem.*, **90**, 3399.

Holleman, J., Verweij, J.F., 1993, *J. Electrochem. Soc.*, **140**(7), 2089.

Imbihl, R., Demuth, J.E., Gates, S.M., Scott, B.A., 1989, *Phys. Rev. B*, **39**(8), 5222.

Inoue, G., Suzuki, M., 1985, *Chem. Phys. Lett.*, **122**, 361.

Jasinski, J.M., 1986, *J. Phys. Chem.*, **90**, 555.

Jasinski, J.M., Chu, J.O., 1988, *J. Chem. Phys.*, **88**, 1678.

Jensen, K.F., 1987, *Chem. Eng. Sci.*, **42**, 923.

Kittrell, J.R., 1970, *Adv. Chem. Eng.*, **8**, 97.

Kleijn, C.R., 1991a, *J. Electrochem. Soc.*, **138**, 2190.

Kleijn, C.R., 1991b, Transport Phenomena in Chemical Vapor Deposition Reactors, Ph.D. Thesis TUD, Delft.

Kulkarni, S.K., Gates, S.M., Greenlief, C.M., Sawin, H.H., 1990a, *Surf. Sci.*, **239**, 26.

Kulkarni, S.K., Gates, S.M., Scott, B.A., Sawin, H.H., 1990b, *Surf. Sci.*, **239**, 13.

Laidler, K.J., 1973, Chemical Kinetics, McGraw-Hill, New York.

Marquardt, D.W., 1963, *J. Soc. Indust. Appl. Math.*, **11**, 431.

Meyerson, B.S., Olbricht, W., 1984, *J. Electrochem. Soc.*, **131**, 2361.

Moffat, H.K., Jensen, K.F., Carr, R.W., 1991, *J. Phys. Chem.*, **95**, 145.

Moffat, H.K., Jensen, K.F., Carr, R.W., 1992, *J. Phys. Chem.*, **96**, 7695.

Purnell, J.H., Walsh, R., 1966, *Proc. R. Soc. London*, **A 293**, 543.

Rabinovitch, B.S., Setser, D.W., 1964, *Adv. Photochem.*, **3**, 1.

Ring, M.A., O'Neal, H.E., 1992, *J. Phys. Chem.*, **96**, 10848.

Robinson, P.J., in Reaction Kinetics, Volume 1, Specialist Periodical Reports, 1975, edited by P.G. Ashmore (The Chemical Society, Burlington House, London), 93.

Robinson, P.J., Holbrook, K.A., 1972, Unimolecular Reactions, Wiley, New York.

Roenigk, K.F., Jensen, K.F., Carr, R.W., 1987, *J. Phys. Chem.*, **91**, 5732.

Scott, B.A., Gates, S.M., Greenlief, C.M., Estes, R.D., in: Mechanisms of Reactions of Organometallic Compounds with Surfaces, Eds., D.J. Cole-Hamilton and J.O. Williams, Plenum Press, New York, 1989, 97.

Tao, M., Hunt, L.P., 1992, *J. Electrochem. Soc.*, **139**(3), 806.

Temkin, M.I., 1971, *Int. Chem. Eng.*, **11**(**4**), 709.

Uram, K.J., Jansson, U., 1991, *Surf. Sci.*, **249**, 105.

Waage, E.V., Rabinovitch, B.S., 1970a, *J. Chem. Phys.*, **52**, 5581.

Waage, E.V., Rabinovitch, B.S., 1970b, *J. Chem. Phys.*, **53**, 3389.

White, R.T., Espino-Rios, R.L., Rogers, D.S., Ring, M.A., O'Neal, H.E., 1985, *Int. J. Chem. Kinet.*, **17**, 1029.

Whitten, G.Z., Rabinovitch, B.S., 1963, *J. Chem. Phys.*, **38**, 2466.

Whitten, G.Z., Rabinovitch, B.S., 1964, *J. Chem. Phys.*, **41**, 1883.

Yeckel, A., Middleman, S., Hochberg, A.K., 1989, *J. Electrochem. Soc.*, **136**(7), 2038

Appendix 5A Computational method used for minimization of total Gibbs energy

Minimization of the total Gibb's energy is accomplished by means of the Lagrangian-multiplier technique. For a mixture of n species, the total Gibb's energy of a system at temperature T and total pressure p_t can be represented by:

$$G_{T,p_t} = f(n_1, n_2, .., n_n) \tag{5A.1}$$

with n_i the number of moles of component i. The thermodynamic equilibrium calculation involves n equilibrium equations, one for each species, and m material balance equations as constraints, one for each element:

$$\Delta_f G_i^o + RT\ln(\gamma_i y_i p_t) + \sum_k \lambda_k a_{i,k} = 0 \qquad (i=1,2,....,n) \tag{5A.2}$$

$$\sum_i n_i a_{i,k} - A_k = 0 \qquad (k=1,2,....,m) \tag{5A.3}$$

with $\Delta_f G_i^o$ the standard Gibb's energy of formation of component i; λ_k the Lagrangian multiplier of element k; A_k the total number of moles of element k present in the system; $a_{i,k}$ the total number of atoms of element k present in species i. The Lagrangian multipliers serve to restrict the size of the corrections made to the numbers of moles during the iteration process. Large corrections could lead to divergence. The term inside the brackets in equation (5A.2) represents the fugacity of component i with γ_i and y_i denoting the fugacity coefficient and molar fraction of component i. In case of low total pressure, ideal gas behaviour can be assumed and the fugacity coefficients can be set to unity.

In the above way n equilibrium equations and m material balance equations are specified in order to solve the same number of unknowns, i.e. n molar fractions, n_i, and m Lagrangian multipliers, λ_k. Solving this set of equations permits the determination of the equilibrium composition for a thermodynamic state specified by an assigned temperature T and total pressure p_t. Beside temperature and pressure, the standard Gibb's energy of formation as a function of temperature is needed for all species. If these data are not available, it is possible to use both the standard enthalpy of formation and standard entropy at 298 K combined with the specific heat at constant pressure as a function of temperature.

Appendix 5B Input data for RRKM calculations

In this Appendix the frequencies with corresponding degeneracies, molecular properties and RRKM parameters for reactant and transition state are listed for each of the unimolecular gas phase reactions under consideration.

***Table 5B.1**: Frequencies with corresponding degeneracies in parentheses, molecular properties and RRKM parameters of silane and corresponding transition state in the decomposition of silane into silylene and molecular hydrogen (Roenigk et al., 1987).*

vibrational frequencies (cm^{-1})				
- silane	2187	2183 (3)	978 (2)	910 (3)
- transition state	2108	2103	1328	993
	839 (2)	523 (2)		
product of moments of inertia (10^{-50} amu^3 m^6)				
- silane	1.806			
- transition state	2.012			
critical energy ($kJ\ mol^{-1}$)	230.1			
reaction path degeneracy (-)	6			
collision diameter (10^{-10} m)	4.084			
reduced mass (10^{-3} $kg\ mol^{-1}$)	16.059			

***Table 5B.2**: Frequencies with corresponding degeneracies in parentheses, molecular properties and RRKM parameters of silylsilylene and corresponding transition state in the isomerization of silylsilylene to disilene (Coltrin et al., 1989).*

vibrational frequencies (cm^{-1})					
- silylsilylene	2056 (4)	923 (2)	874	711	426
	381 (2)	121			
- transition state	2056 (4)	931 (3)	874	711	381 (2)
moments of inertia (10^{-20} amu m^2)					
- silylsilylene	7.994	93.878	96.050		
- transition state	7.080	83.409	86.724		
critical energy ($kJ\ mol^{-1}$)	22.2				
reaction path degeneracy (-)	3				
collision diameter (10^{-10} m)	4.343				
reduced mass (10^{-3} $kg\ mol^{-1}$)	20.944				

Table 5B.3: *Frequencies with corresponding degeneracies in parentheses, molecular properties and RRKM parameters of disilane and corresponding transition state in the decomposition of disilane into silane and silylene (Roenigk et al., 1987).*

vibrational frequencies (cm^{-1})					
- disilane	2164 (6)	936 (5)	844	628 (2)	432
	379 (2)				
- transition state	2142 (5)	1585	955 (2)	926 (4)	243 (2)
	147 (2)	128			
internal rotation disilane					
- reduced moment of inertia (10^{-20} amu m^2)	3.184				
- barrier (kJ mol^{-1})	4,2				
- symmetry number	3				
product of moments of inertia (10^{-65} amu^3 m^6)					
- disilane	1,098				
- transition state	1.186				
critical energy (kJ mol^{-1})	205.9				
reaction path degeneracy (-)	18				
collision diameter (10^{-10} m)	4,456				
reduced mass (10^{-3} kg mol^{-1})	21.183				

Table 5B.4: *Frequencies with corresponding degeneracies in parentheses, molecular properties and RRKM parameters of disilane and corresponding transition state in the decomposition of disilane into silylsilylene and molecular hydrogen (Moffat et al., 1992).*

vibrational frequencies (cm^{-1})					
- disilane	2164 (6)	936 (5)	844	628 (2)	432
	379 (2)	128 (1)			
- transition state	2150 (4)	1328	874 (4)	456 (3)	322 (2)
	170	112 (2)			
critical energy (kJ mol^{-1})	223.0				
reaction path degeneracy (-)	6				
collision diameter (10^{-10} m)	4.456				
reduced mass (10^{-3} kg mol^{-1})	21,183				

Table 5B.5: *Frequencies with corresponding degeneracies in parentheses, molecular properties and RRKM parameters of trisilane and corresponding transition state in the decomposition of trisilane into disilane and silylene (Moffat et al., 1992).*

vibrational frequencies (cm^{-1})					
- trisilane	2150 (8)	920 (7)	654 (3)	413 (3)	370 (3)
	135	121 (2)			
- transition state	2150 (7)	958 (6)	630 (4)	393 (3)	219
	120 (4)	61			
critical energy (kJ mol^{-1})	216.3				
reaction path degeneracy (-)	6				
collision diameter (10^{-10} m)	4.823				
reduced mass (10^{-3} kg mol^{-1})	23.828				

Table 5B.6: *Frequencies with corresponding degeneracies in parentheses, molecular properties and RRKM parameters of trisilane and corresponding transition state in the decomposition of trisilane into silylsilylene and silane (Moffat et al., 1992).*

vibrational frequencies (cm^{-1})					
- trisilane	2150 (8)	920 (7)	654 (3)	413 (3)	370 (3)
	135	121 (2)			
- transition state	2150 (7)	958 (6)	612 (4)	349 (4)	141 (2)
	121 (2)	69			
critical energy (kJ mol^{-1})	209.2				
reaction path degeneracy (-)	6				
collision diameter (10^{-10} m)	4.823				
reduced mass (10^{-3} kg mol^{-1})	23.828				

Appendix 5C Techniques used for identification of most important reactions

Sensitivity analysis

The sensitivity analysis discloses the changes of a response brought about by the perturbation of the kinetic parameters, thus connecting the prediction of the model with the rate coefficients of the reactions in the model. By definition, a linear sensitivity factor of respons Y in experiment n with respect to parameter l, Ψ_{nl}, is calculated according to:

$$\Psi_{nl} = \frac{\partial \ln Y_n}{\partial \ln b_l} \tag{5C.1}$$

with b_l the *lth* parameter.

In the present work sensitivity factors of the silicon growth rate and of the silane and disilane molar flow rates at the reactor outlet are calculated after solving the complete set of reactor model equations given by (2.39) to (2.45). The parameters considered are the pre-exponential factors of the individual elementary steps.

Contribution analysis

The contribution analysis is a powerful tool for reaction pathway analysis. It determines the relative importance of an elementary step with respect to the total formation or disappearance rate of a species. The disappearance contribution factor of step k towards the disappearance of component i in experiment n is calculated as the ratio of the rate of disappearance of i resulting from step k, r_{kin}^d, to the total rate of disappearance of i:

$$\Phi_{kin}^d = \frac{r_{kin}^d}{\sum_k r_{kin}^d} \tag{5C.2}$$

Here, r_{kin}^d, is equal to $\alpha_{ki}\overrightarrow{r}_k$ when i appears on the left side of a reaction and to $\alpha_{-ki}\overleftarrow{r}_k$ when i appears on the right. In a similar way, the formation contribution factor is calculated by using the rates of steps in which component i is formed:

$$\Phi_{kin}^f = \frac{r_{kin}^f}{\sum_k r_{kin}^f} \tag{5C.3}$$

with r_{kin}^f is equal to $\alpha_{-ki}\overrightarrow{r}_k$ when i appears on the right side of a reaction and to $\alpha_{ki}\overleftarrow{r}_k$ when i appears on the left.

The disappearance and formation contribution factors are considered with respect to all steps of the complete reaction network. The summations in equations (5C.2) and (5C.3) therefore run over all gas phase and surface steps. The reaction rates of the contributing steps, r_{kin} in mol s^{-1}, are calculated after solving the complete set of reactor model equations given by (2.39) to (2.45). In case of a gas phase step, the corresponding volumetric reaction rate, $r_{v,kin}$ in mol m^{-3} s^{-1}, is integrated over the gas phase reaction volume by means of quadrature according to:

$$r_{kin} = \iiint_{V_g} r_{v,kin} \, dV = 4 \pi R_0^3 \sum_{cc=1}^{M+2} w_{cc} \, r_{v,kin}(\xi_{cc}) \tag{5C.4}$$

In case of a surface step, the areal reaction rate, $r_{a,kin}$ in mol m^{-2} s^{-1}, is integrated over the total deposition surface area according to:

$$r_{kin} = \iint_{A_d} r_{a,kin} \, dA = 4 \pi R_0^2 \, r_{a,kin}\big|_{\xi=1} + 4 \pi R_1^2 \, r_{a,kin}\big|_{\xi=R_1/R_0} \tag{5C.5}$$

It should be noted that due to the occurrence of both surface and gas phase reactions, the contribution analysis as described above inevitably encloses the ratio of deposition surface area to gas phase reaction volume, A_d/V_g, amounting to 128.3 m^{-1} for the present reactor configuration.

Affinity

The value of the affinity of a reaction, **A**, provides direct information on the direction in which the reaction proceeds and its approach to equilibrium. It is defined as the Gibbs energy difference of the reaction with a minus sign. For elementary reactions the following relation holds:

$$\mathbf{A} = R T \ln \frac{\vec{r}}{\overleftarrow{r}} \tag{5C.6}$$

The rates of the forward and backward steps are calculated after solving the complete set of reactor model equations given by (2.39) to (2.45), in the same way as outlined for the contribution analysis. The rate of a reaction and of the backward step can be easily deduced from the affinity and the rate of the forward step according to:

$$\overleftarrow{r} = \vec{r} \exp\left(-\frac{\mathbf{A}}{R T}\right) \tag{5C.7}$$

$$r = \overrightarrow{r} - \overleftarrow{r} = \overrightarrow{r}\left[1 - \exp\left(-\frac{\boldsymbol{A}}{RT}\right)\right] \tag{5C.8}$$

in which **A**/RT is often referred to as the dimensionless affinity.

6

LPCVD REACTOR MODELLING AND SIMULATION

6.1 Introduction

The hot-wall multiwafer low-pressure chemical vapour deposition (LPCVD) reactor, first introduced in the late seventies (Rosler, 1977), is the most common reactor for the deposition of polycrystalline silicon from silane. It realizes a large packing density of silicon wafers perpendicularly to the axis of the tube and an excellent layer thickness uniformity across each wafer as well as from wafer to wafer.

To gain quantitative insights in the interaction of the mass transport phenomena with the chemical reaction kinetics in such a reactor, several mathematical reactor models of different degrees of sophistication have been proposed up to now (Jensen and Graves, 1983; Roenigk and Jensen, 1985,1987; Middleman and Yeckel, 1986; Wilke *et al.*, 1986; Joshi, 1987; Roenigk, 1987; Yeckel and Middleman, 1987; Vinante *et al.*, 1989; Yeckel *et al.*, 1989; Hopfmann *et al.*, 1991; Azzaro *et al.*, 1992,1994; Badgwell *et al.*, 1992a,b; Duverneuil and Couderc, 1992). The majority of these studies is based on the pioneering work of Jensen and Graves (1983). Basically, the model developed by these authors consists of a combination of two sets of one-dimensional, i.e. axial in the annular zone between the reactor wall and the edges of the wafers and radial in the interwafer zone, continuity equations for the species considered, coupled to each other by the boundary conditions at the wafer edges. In a later paper, Roenigk and Jensen (1985) extended the original model concepts to encompass multicomponent effects by implementing the Stefan-Maxwell equations. The extended model also allows an arbitrary number of gas phase and surface reactions. The nonlinear model equations are solved by orthogonal collocation (Finlayson, 1972). Besides such simplified one-dimensional models, more sophisticated two-dimensional models have been developed recently, treating the hydrodynamics and the mass transport with chemical reactions in a more detailed manner. In order to reduce the computational effort the modelling domain is in general confined to a single interwafer space and the corresponding annular space, situated somewhere in the middle of the wafer section to eliminate possible effects from the upstream and downstream ends of the wafer load. Most of the assumptions postulated in the simplified one-dimensional models are relaxed. The most comprehensive work in this field was reported by Azzaro *et al.* (1994). The model developed by these authors consists of the conservation equations of mass and momentum, which are solved using a finite difference method and an implicit Gauss Seidel algorithm.

The present work reports on the degree of sophistication needed in the modelling to adequately describe silicon growth in a commercial LPCVD reactor at operating conditions that are industrially relevant, i.e. total pressures around 50 Pa and temperatures around 900 K. The applied rate equations were obtained by regression of a set of kinetic rate data collected with a microbalance reactor at similar conditions, see Chapter 5. Four elementary gas phase reactions between six gas phase species and ten elementary surface reactions are considered.

A one-dimensional two-zone and a fully two-dimensional reactor model are compared. In the former case the reactor is thought to consist of an annular zone between the wafer edges and the reactor wall and of an interwafer zone. The corresponding model, similar to that developed by Roenigk and Jensen (1985), consists of two sets of one-dimensional continuity equations for all gas phase components. One set allows to calculate the concentration profiles along the axial coordinate in the annular zone, while the other set allows to calculate the concentration profiles along the radial coordinate in the interwafer zone. Coupling between both sets is accomplished by the boundary conditions at the wafer edges. The model equations are solved simultaneously by applying the method of orthogonal collocation. The fully two-dimensional reactor model follows from the straightforward application of the conservation laws of mass, momentum and energy. The corresponding equations are solved by means of the control volume based finite difference method of Patankar and Spalding (Patankar, 1980). Multicomponent diffusion is accounted for by using the Stefan-Maxwell equations in both models.

The validity of these reactor models is tested by comparing their predictions with the experimental growth rate data obtained in a commercial LPCVD reactor. Of course no adjustment of the kinetic parameter values is performed during the reactor model validation. Once validated, the one-dimensional two-zone model is used to provide insights in the effects of typical operating conditions such as interwafer spacing and reactor tube radius on the interaction between the chemical reaction kinetics and the mass transport phenomena in an industrial-scale LPCVD reactor capable of processing 200-mm wafers.

6.2 Experimental

6.2.1 Equipment and procedures

The growth experiments were carried out in a conventional hot-wall multiwafer LPCVD reactor of the TEMPRESS type Junior at TNO-TPD Eindhoven. Figure 6.1 shows the reactor configuration. As illustrated the reactor consists of four distinct sections, from front to back: 1) premixing section, 2) preheating section, 3) wafer section and 4) downstream section. The premixing section is separated from the preheating section by an insulation ring which serves to maintain uniform temperature control in the wafer section and prevents heating of the gas inlets. The preheating and downstream sections are located immediately upstream and downstream of the wafer section. These are empty tube sections with lengths similar to that of the wafer section. Reactant gases enter the reactor, mix in the premixing section, are heated in the preheating section and then flow through the annular passage between the wafer edges and the reactor wall before leaving the reactor.

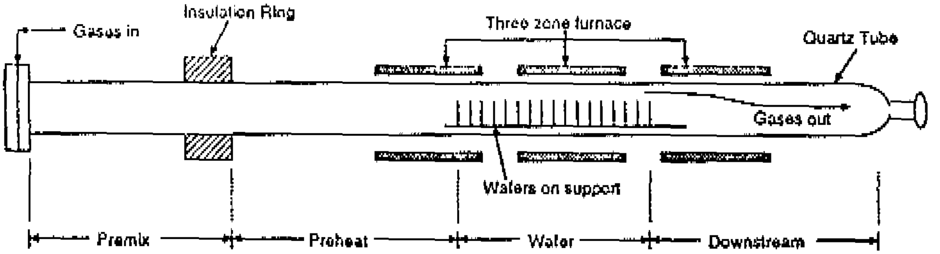

Figure 6.1: Schematic diagram of a conventional hot-wall multiwafer LPCVD reactor (Roenigk, 1987).

Table 6.1 summarizes the important features of the geometry of the TEMPRESS LPCVD reactor. The reactor consists of a 1.5 m long fused quartz reactor tube with an inner diameter of 0.132 m, mounted within a three-zone resistance heating element. Temperature control of the heating zones is performed on the basis of platina/platina(13% rhodium) (R-type) spike thermocouples. Temperature profiling is based on chromel-alumel (K-type) thermocouples which are moved in axial direction through the empty reactor at two radial positions, i.e. in the centre and close to the wall. The three heating zones are tuned so that the entire wafer section exhibits radial as well as axial temperature uniformity within 1 K of the deposition temperature at the pressures and total gas flow rates used during the deposition experiments. Vacuum is maintained by a dual-stage rotary-vane mechanical pump (Leybold D65/BCS). The reactor pressure is measured with an absolute pressure transducer (MKS Baratron 222) and controlled, independent of upstream gas flow rates, via the exhaust rate of effluent gases using a butterfly valve in the pump line. The upstream flow rates of the used gases, i.e. silane (99.99%) and hydrogen (99.999%) both supplied by Air Products, are established with thermal mass flow controllers (Brooks 5850E).

Table 6.1: *Geometrical features of the TEMPRESS LPCVD reactor.*

Reactor length*	L_3	0.94 m
Wafer section length	L	0.29 m
Reactor tube radius	R_t	0.067 m
Wafer radius	R_w	0.05 m
Interwafer spacing	Δ	0.01 m
Boat surface area/tube surface area	α	0.1
First wafer in wafer section**		0.32 m
Last wafer in wafer section**		0.61 m
Number of wafers in wafer section	NRWF	30

* The reactor length as specified here comprises the preheating, the wafer and the downstream section. The premixing section is not included.

** The axial positions of the first and last wafer of the load are important in case the reactor model accounts for the preheating and downstream sections.

A 0.38 m long fused quartz boat containing thirty-eight 0.10 m diameter silicon wafers is mounted coaxially with the furnace axis. Thirty single-side polished (100) p-type silicon wafers are positioned at equal distances of 0.01 m in the wafer section, with the polished sides directed to the downstream end of the reactor tube. These substrates were oxidized ex-situ to a thickness of 100 nm to facilitate post-deposition layer thickness measurement. At the upstream and downstream ends of the boat, just outside the wafer section, four dummy wafers are positioned at equal distances of 0.005 m. These wafers serve to smooth out axial and radial temperature variations over the deposition wafers caused by radiative heat losses to the cooled reactor inlet and outlet doors.

6.2.2 Process conditions

In order to investigate the effects of total pressure and temperature in the range of industrially relevant operating conditions for the deposition of polycrystalline silicon from silane, a set of four deposition runs was performed at the conditions listed in Table 6.2.

Table 6.2: *Operating conditions of the experimental runs performed in the TEMPRESS LPCVD reactor.*

run	p_t / Pa	T / K	Q_{SiH_4}* / Nml min^{-1}
1	25	900	90
2	50	850	90
3	50	900	90
4	50	950	90

* silane volumetric flow rate at inlet of reactor

6.2.3 Characterization of deposited layers

Layer thickness measurements were performed on the polished sides, i.e. the back sides, of at most 7 monitor wafers in the 30 wafer load, i.e. wafer numbers (1), 5, 10, 15, 20, 25, (29), by means of interferometry and ellipsometry. Deviations between these methods were within 5%. In the range of experimental conditions applied, see Table 6.2, the measured radial thickness variations were smaller than the experimental accuracy. Silicon growth rates were calculated by dividing the measured layer thicknesses by the corresponding deposition times. In addition, for each of the monitor wafers a radially averaged growth rate was calculated as the arithmetic mean of all growth rates measured on the wafer.

Figure 6.2 shows a typical scanning electron micrograph of the cross section of a silicon layer deposited at 50 Pa and 900 K. On top of the 100 nm thick silicon dioxide layer the columnar structure typical of polycrystalline silicon is visible.

The differentiated Auger Electron Spectroscopy (AES) spectrum in Figure 6.3 shows the presence of carbon and oxygen at the surface of a silicon layer deposited at 50

Pa and 900 K. Other contaminants were not detected. AES depth profiling by alternating cycles of argon-ion sputtering revealed that the presence of carbon and oxygen impurities is limited to the topmost layers only. Beneath the topmost layers the concentration levels of these elements are below the detection limit.

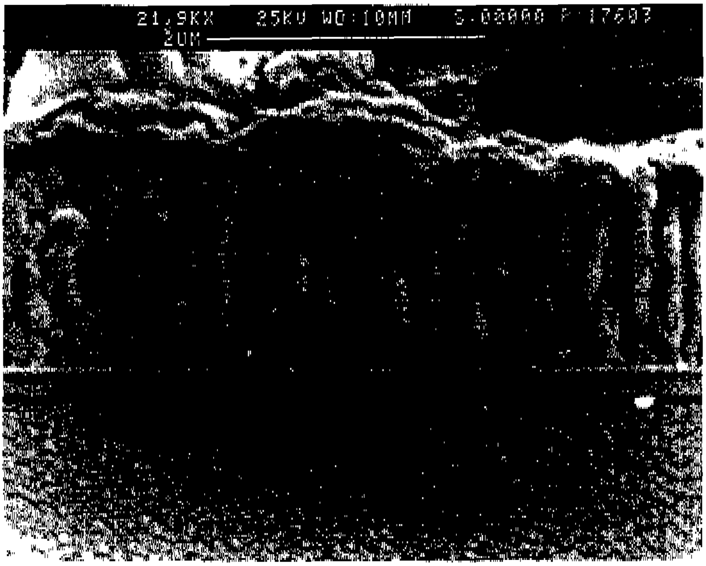

Figure 6.2: *Scanning electron micrograph of cross section of silicon layer. Magnification: 21900X. Deposition conditions: $T = 900$ K, $p_t = 50$ Pa, 100% SiH_4, $Q_{SiH_4} = 90$ Nml min^{-1}.*

6.3 Reactor models

6.3.1 One-dimensional two-zone reactor model

6.3.1.1 Assumptions

The one-dimensional two-zone reactor model is based on several assumptions, which will be discussed in detail below. The dimensionless groups used are calculated based on the geometrical reactor features and process conditions listed in Tables 6.1 and 6.2 and on pseudo-first order surface reaction rate coefficients deduced from the kinetic parameter estimates presented in Table 5.6.

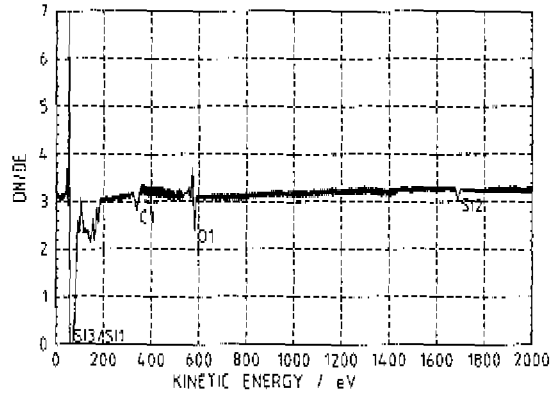

Figure 6.3: *Differentiated Auger spectrum of silicon layer. Deposition conditions: T= 900 K, p_r= 50 Pa, 100% SiH_4, Q_{SiH_4}= 90 Nml min^{-1}. SI1: elemental silicon, SI2: elemental silicon and silicon dioxide, SI3: silicon dioxide, C1: carbon, O1: oxygen.*

Whether or not all the reactor sections are needed in the mathematical model depends primarily on the ongoing chemistry and kinetics. For silicon growth a flattening of the axial deposition rate profile is typically observed towards the downstream end of the wafer section (Hitchman and Jensen, 1993). This behaviour implies negligible reaction taking place in the downstream section relative to the wafer section. It also indicates that the downstream section can be neglected by imposing a zero axial gradient boundary condition on the molar fractions at the end of the wafer section as reflected by the well-known outlet boundary condition put forward by Danckwerts (Danckwerts, 1953). Furthermore, effects of the premixing and preheating sections are omitted as well. As long as no significant gas phase and surface reactions occur prior to the wafer section neglecting both upstream sections is justified (Hitchman and Jensen, 1993). The model development hence reduces to the description of the performance of the wafer section only. Figure 6.4 shows a schematic representation of the reactor configuration considered in the one-dimensional two-zone model. The wafer section consists of an annular zone between the wafer edges and the reactor wall and of an interwafer zone containing the silicon wafers. These zones consist of (NRWF-1) annular and interwafer spaces, respectively.

Depending on the relative magnitude of the mean free path of the gas phase molecules and the characteristic dimension of the reactor as reflected by the Knudsen number, Kn= $\bar{l}_m/d$, the fluid flow can be in the continuum regime, $Kn < 0.1$, in the Knudsen or so-called free-molecular regime, $Kn > 10$, or in the transition regime, $0.1 < Kn < 10$. For the present conditions the mean free path length is at most $7\ 10^{-4}$ m, which implies that even in the interwafer region, with a characteristic dimension of $1\ 10^{-2}$ m, the transport phenomena are in the continuum regime where collisions between gas phase molecules only dominate. Hence, a continuum description is allowed.

Since the time scales of convection and diffusion are short compared to that of silicon growth, the reactor is assumed to operate under steady state conditions, thereby eliminating the need for the accumulation terms in the continuity equations of the gas phase species.

Based on the low total pressures applied ideal gas behaviour is considered.

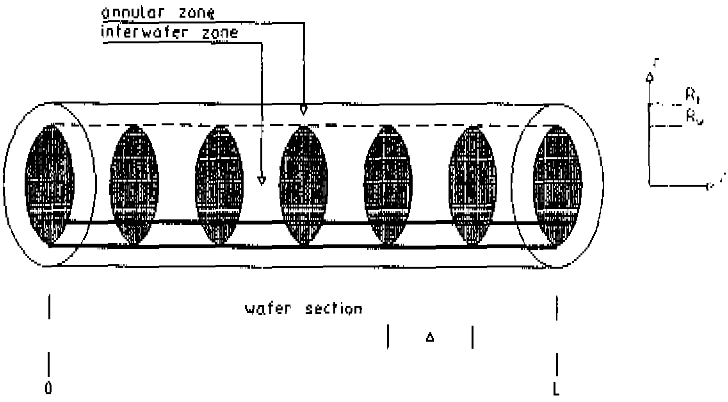

Figure 6.4: Schematic representation of the two zones considered in the one-dimensional two-zone reactor model.

For the relatively low growth rates achieved in LPCVD reactors, the heat of reaction associated with the gas phase and deposition reactions is small in comparison with the furnace heat flux. Moreover, thermal entrance lengths are short relative to reactor lengths (Roenigk, 1987). Hence, the wafer and gas temperatures might be expected to closely follow the tube wall temperatures as determined by the furnace settings, and the wafer section can be considered isothermal. On the above grounds an energy balance is redundant (Roenigk, 1987).

The Reynolds number for the annular zone, given by $Re= \rho u(R_t-R_w)/\mu$, is roughly equal to 0.1, which is well below the value of 2300 reflecting the transition point between laminar and turbulent flow. The gas flow is thus highly laminar. Middleman and Yeckel (1986) showed by simulating the gas flow past the wafer edges in two dimensions that for deposition rates commonly encountered in LPCVD reactors details of the gas flow have no significant impact on predictions of interwafer growth rate and uniformity for Reynolds numbers as large as 25. This is primarily the result of the large diffusion coefficients at the low pressures employed leading to diffusive mass transport dominating over convective mass transport. Moreover, the relatively close wafer spacing combined with the fast diffusion implies that effects from recirculating eddies near the wafer edges are insignificant and that the mass transport between the wafers is governed by multicomponent diffusion only. According to Vinante *et al.* (1989) the hypothesis of a purely axial movement in the annular zone and of a motionless gas in the interwafer zone is not far from the real situation. Since the flow field in the interwafer zone is hardly influenced by the flow field in the annular zone (Middleman and Yeckel, 1986), a flat velocity profile is assumed in the latter. Furthermore, the reactor is considered isobaric, because no significant pressure drop over the reactor is expected at the low pressures employed. Based on the foregoing points the Navier-Stokes or momentum conservation equations do not need to be solved.

The Peclet number, $Pe= uL/D$, for axial mass transport in the annular zone is roughly equal to 1. Because this dimensionless number is a measure for the importance of diffusive mass transport relative to convective mass transport, it is obvious that both convection and diffusion determine the axial mass transport in the annular zone. The axial diffusion reduces the variation in reactant concentration and hence improves the layer thickness uniformity along the reactor.

The Damköhler-II number, given by $Da_{II}= k_r d^2/D$, relates the time scale of diffusional mass transport to the time scale of surface reaction. In this expression k_r denotes a pseudo-first order surface reaction rate coefficient and d some characteristic dimension, being equal to Δ in the interwafer zone and to (R_t-R_w) in the annular zone. With respect to silane no concentration gradients are expected in either the axial direction of the interwafer zone or the radial direction of the annular zone. The Damköhler-II number for silane is much smaller than unity in both zones. It should be noted that the existence of radial concentration gradients in the annular zone not only depends on the magnitude of the Damköhler-II number but also on the magnitude of the Peclet number for radial mass transport. A large value of this mass Peclet number may induce radial gradients despite a small value of the Damköhler-II number. Due to the small Δ/R_w ratios typically used in LPCVD reactors, axial concentration gradients in the interwafer zone are in general insignificant provided the corresponding Damköhler-II number is small. On the basis of the foregoing considerations concentration gradients in the axial direction of the interwafer zone and in the radial direction of the annular zone are not accounted for.

Finally, the gas flow is supposed to be axisymmetric, thereby neglecting possible effects induced by the assymetry of the wafer boat, and the wafers are considered infinitesimally thin.

6.3.1.2 Equations

In the following the one-dimensional model equations for the interwafer and annular zone are described together with the equation used for the calculation of the radially averaged silicon growth rates.

Interwafer zone

The continuity equation for component i has the form:

$$\frac{1}{r}\frac{d}{dr}\left(rN_i^w\right) = \frac{2}{\Delta}\sum_{m=1}^{ns} \nu_{m,i} r_{a,m} + \sum_{k=1}^{ng} \nu_{k,i} r_{v,k} \qquad (6.1)$$

Here Δ is the interwafer spacing; N_i the molar flux of component i; r the radial coordinate; $\nu_{m,i}$ the stoichiometric coefficient of gas phase species i in surface step m; $r_{a,m}$ the rate of surface step m; ns the number of surface steps; $\nu_{k,i}$ the stoichiometric coefficient of component i in gas phase step k; $r_{v,k}$ the rate of gas phase step k; ng the number of gas phase steps. The superscript w denotes the interwafer zone. The first term at the right-hand side includes the heterogeneous net production rates of component i at the wafers. The second term denotes the homogeneous net production rate of component i. Symmetry at the reactor axis and continuity of the molar fractions from the wafer edge to the annular zone are expressed by the boundary conditions:

$$r = 0 \qquad N_i^w = 0 \qquad (6.2)$$

$$r = R_w \qquad y_i^w = y_i^a \qquad (6.3)$$

with R_w the wafer radius; y_i the molar fraction of component i. The superscript a denotes the annular zone. Multicomponent diffusion effects are accounted for by the Stefan-Maxwell equations (Bird *et al.*, 1960):

$$\frac{dy_i^w}{dr} = \sum_{j\neq i} \frac{y_i^w N_j^w - y_j^w N_i^w}{C D_{i,j}} \qquad (6.4)$$

relating the molar fluxes of all components in the mixture to the concentration gradients of all components. Here C is the total gas phase concentration (= p_t/RT) and $D_{i,j}$ the molecular diffusion coefficient of gas phase species i in a binary mixture of i and j. The binary diffusion coefficients are calculated using the Chapman-Enskog relations (Reid *et al.*, 1987). Since the molar fractions must sum up to unity, i.e.:

$$\sum_{i=1}^{NG} y_i^w = 1 \tag{6.5}$$

there are for an ideal gas mixture containing NG components (NG-1) independent Stefan-Maxwell equations.

The model equations for the interwafer zone thus consist of a set of (2NG-1) independent first-order ordinary differential equations and one algebraic equation with the molar fraction y_i^w and the molar flux N_i^w as dependent variables.

Annular zone

The continuity equation for component i has the form:

$$\frac{dN_i^a}{dz} = \frac{2}{R_t^2 - R_w^2}\left(R_t(1+\alpha)\sum_{m=1}^{ns} \nu_{m,i} r_{a,m} + R_w N_i^w|_{r=R_w}\right) + \sum_{k=1}^{ng} \nu_{k,i} r_{v,k} \tag{6.6}$$

Here z is the axial coordinate; R_t the radius of the reactor tube; α the ratio of boat-to-tube surface area. The first term at the right-hand side includes the heterogeneous net production rates of component i at the tube wall and the carrier boat and the molar flux of component i to/from the interwafer zone. The molar flux of component i to/from the interwafer zone, $N_i^w|_{r=R_w}$, is obtained by integrating the continuity equation for the interwafer zone, equation (6.1), over the wafer radius according to:

$$N_i^w|_{r=R_w} = \frac{1}{R_w}\int_0^{R_w}\left(\frac{2}{\Delta}\sum_{m=1}^{ns} \nu_{m,i} r_{a,m} + \sum_{k=1}^{ng} \nu_{k,i} r_{v,k}\right) r\,dr \tag{6.7}$$

Continuity of the molar fluxes across the inlet to the wafer section is expressed by:

$$z = 0 \qquad N_i^a = u_0\, C\, y_{i,0}^a \tag{6.8}$$

with the molar average velocity at z= 0 obtained from:

$$u_0 = 5.66\,10^{6}\,\frac{T}{\pi\,(R_t^2 - R_w^2)\,p_t}\sum_{i=1}^{NG} Q_i \tag{6.9}$$

In case gas phase reactions are involved, the molar fractions of the produced gas phase intermediates at z= 0, $y^a_{i,0}$, are determined by applying the pseudo-steady-state approximation for these intermediate species. Furthermore, it is assumed that no diffusion takes place across the plane at the end of the wafer section:

$$z = L \qquad \frac{dy_i^a}{dz} = 0 \tag{6.10}$$

which implicitly means that negligible reaction occurs downstream of the wafer section. Equations (6.8) and (6.10) are known as the Danckwerts boundary conditions (Danckwerts, 1953) applying to a closed vessel, i.e. plug flow is assumed to be the only mode of mass transport in the connected inlet and outlet tubes. Multicomponent diffusion effects are again accounted for by (NG-1) independent Stefan-Maxwell equations:

$$\frac{dy_i^a}{dr} = \sum_{j \neq i} \frac{y_i^a N_j^a - y_j^a N_i^a}{C D_{i,j}} \tag{6.11}$$

which need to be supplemented with one algebraic equation to sum up the molar fractions to unity:

$$\sum_{i=1}^{NG} y_i^a = 1 \tag{6.12}$$

The model equations for the annular zone thus consist a set of (2NG-1) independent first-order ordinary differential equations and one algebraic equation with the molar fraction y_i^a and the molar flux N_i^a as dependent variables.

Radially averaged silicon growth rate

After solving the complete set of model equations, the radially averaged silicon growth rate is obtained from:

$$\overline{R_{Si}} = \frac{2 \int_0^{R_w} R_{Si}(r)\, r\, dr}{R_w^2} \tag{6.13}$$

with $R_{Si}(r)$ the silicon growth rate on the wafer at radial position r. The integral in this equation is determined using a quadrature formula, as will be shown later.

6.3.1.3 Solution procedure

The mathematical problem is built up of two one-dimensional boundary value problems. It consists of the integration of two sets of (2NG-1) nonlinear first-order ordinary differential equations with corresponding boundary conditions, i.e. equations (6.1) to (6.4) for the interwafer zone and equations (6.6), (6.8), (6.10) and (6.11) for the annular zone. The above sets are coupled through the boundary conditions at the wafer edges, given by equation (6.3), and the molar fluxes to/from the interwafer zone featuring in equation (6.6). To integrate the complete set of 2(2NG-1) differential equations with corresponding boundary conditions, 6*th* order orthogonal collocation (Finlayson, 1972) was applied in both the r-direction of the interwafer zone and the z-direction of the annular zone, see Appendix 6A. In this way a set of (2NG-1)(M+N+4) independent algebraic equations is obtained, M and N being the number of interior collocation points in the r- and z-direction. Together with the (M+N+4) additional conditions stating that the sum of the molar fractions at each collocation point needs to be unity, a total set of 2NG(M+N+4) algebraic equations is obtained, which are solved simultaneously using a modified Newton-Raphson method in the standard NAG-library routine C05NBF (NAG, 1991). A typical reactor simulation requires a CPU-time of 30 minutes on a Silicon Graphics Power Challenge Computer.

6.3.2 Fully two-dimensional reactor model

6.3.2.1 Assumptions

The fully two-dimensional reactor model is based primarily on some general assumptions, which have already been discussed in detail in the context of the one-dimensional reactor model:

- the gas mixture is assumed to behave as a continuum
- the gases are considered to be ideal gases
- the gas flow in the reactor is assumed to be stationary and laminar
- the gas flow is considered to be axisymmetric

Figure 6.5 shows a schematic representation of the reactor configuration considered in the fully two-dimensional model. The effects of the premixing section are lumped into the treatment of the preheating section. The model development thus involves the description of the performance and coupling of the preheating, the wafer and the downstream sections. Compared to the one-dimensional two-zone reactor model the modelling domain is expanded so that the inlet and outlet boundaries are removed from the wafer section. In this way possible effects associated with the idealised inlet and outlet of the simplified one-dimensional model, see equations (6.8) and (6.10), are minimized.

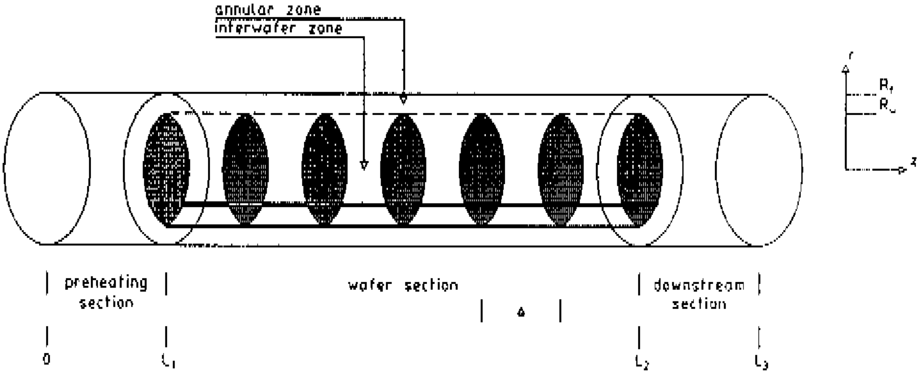

Figure 6.5: Schematic representation of reactor configuration considered in the fully two-dimensional reactor model.

The annular and interwafer zones consist of (NRWF-1) annular and interwafer spaces. Each interwafer space in turn consists of a silicon wafer $5\ 10^{4}$ m thick and the gas phase volume located downstream of it.

6.3.2.2 Equations

In the following the two-dimensional model equations representing the conservation of mass, momentum and energy are given. The general derivation and form of these equations is given in standard references on transport phenomena (Bird *et al.*, 1960; see also Kleijn, 1991).

Continuity equation for the gas mixture

$$\frac{1}{r}\frac{\partial}{\partial r}(r\rho \mathbf{u}_r) + \frac{\partial}{\partial z}(\rho \mathbf{u}_z) = 0 \qquad (6.14)$$

with ρ the density of the gas mixture; $\mathbf{u}_r$ and $\mathbf{u}_z$ the mass average velocity components in radial and axial direction.

Navier-Stokes or momentum balance equations

$$-\frac{1}{r}\frac{\partial}{\partial r}(r\rho\,\boldsymbol{u}_r\boldsymbol{u}_r) - \frac{\partial}{\partial z}(\rho\,\boldsymbol{u}_r\boldsymbol{u}_z) - \frac{1}{r}\frac{\partial}{\partial r}(r\tau_{rr}) - \frac{\partial \tau_{rz}}{\partial z} - \frac{\partial p_t}{\partial r} = 0 \qquad (6.15)$$

$$-\frac{1}{r}\frac{\partial}{\partial r}(r\rho\,\boldsymbol{u}_r\boldsymbol{u}_z) - \frac{\partial}{\partial z}(\rho\,\boldsymbol{u}_z\boldsymbol{u}_z) - \frac{1}{r}\frac{\partial}{\partial r}(r\tau_{rz}) - \frac{\partial \tau_{zz}}{\partial z} - \frac{\partial p_t}{\partial z} = 0 \qquad (6.16)$$

where p_t is the total pressure; τ_{rr}, τ_{zz} and τ_{rz} the normal and tangential (or shear) viscous stress tensor components, for Newtonian fluids defined as:

$$\tau_{rr} = -2\mu\frac{\partial \boldsymbol{u}_r}{\partial r} + \frac{2}{3}\mu\left(\frac{1}{r}\frac{\partial}{\partial r}(r\boldsymbol{u}_r) + \frac{\partial \boldsymbol{u}_z}{\partial z}\right) \qquad (6.17)$$

$$\tau_{zz} = -2\mu\frac{\partial \boldsymbol{u}_z}{\partial z} + \frac{2}{3}\mu\left(\frac{1}{r}\frac{\partial}{\partial r}(r\boldsymbol{u}_r) + \frac{\partial \boldsymbol{u}_z}{\partial z}\right) \qquad (6.18)$$

$$\tau_{rz} = \tau_{zr} = -\mu\left(\frac{\partial \boldsymbol{u}_z}{\partial r} + \frac{\partial \boldsymbol{u}_r}{\partial z}\right) \qquad (6.19)$$

with μ the dynamic viscosity of the gas mixture.

Energy equation

$$-c_p\left(\frac{1}{r}\frac{\partial}{\partial r}(r\rho\,\boldsymbol{u}_r T) + \frac{\partial}{\partial z}(\rho\,\boldsymbol{u}_z T)\right) + \frac{1}{r}\frac{\partial}{\partial r}\left(\lambda r\frac{\partial T}{\partial r}\right) + \frac{\partial}{\partial z}\left(\lambda\frac{\partial T}{\partial z}\right) = 0 \qquad (6.20)$$

with T the absolute temperature; c_p the specific heat capacity at constant pressure of the gas mixture; λ the thermal conductivity of the gas mixture. Heat effects associated with gas phase reactions are neglected.

Continuity equation for gas phase component i

$$-\frac{1}{r}\frac{\partial}{\partial r}(r\rho \boldsymbol{u}_r \omega_i + r j_{i,r}) - \frac{\partial}{\partial z}(\rho \boldsymbol{u}_z \omega_i + j_{i,z}) + M_i \sum_{k=1}^{nq} \nu_{k,i} r_{v,k} = 0 \tag{6.21}$$

where ω_i is the mass fraction of component i; M_i the molar mass of component i; $j_{i,r}$ and $j_{i,z}$ the diffusive mass flux components in radial and axial direction due to concentration gradients. The so-called Soret effect, causing diffusion fluxes as a result of temperature gradients, has been neglected. In an NG component gas mixture there are (NG-1) independent continuity equations of the form of equation (6.21) since the mass fractions must sum up to unity:

$$\sum_{i=1}^{NG} \omega_i = 1 \tag{6.22}$$

In case of ordinary diffusion in a multicomponent gas mixture the diffusive mass fluxes can be calculated from the Stefan-Maxwell equations in terms of mass fractions and mass fluxes (Kleijn, 1991):

$$\frac{\partial \omega_i}{\partial r} + \omega_i \frac{\partial}{\partial r}(\ln M) = \frac{M}{\rho} \sum_{j=1}^{NG} \frac{\omega_i j_{j,r} - \omega_j j_{i,r}}{M_j D_{i,j}} \tag{6.23}$$

$$\frac{\partial \omega_i}{\partial z} + \omega_i \frac{\partial}{\partial z}(\ln M) = \frac{M}{\rho} \sum_{j=1}^{NG} \frac{\omega_i j_{j,z} - \omega_j j_{i,z}}{M_j D_{i,j}} \tag{6.24}$$

with M the average molar mass of the gas mixture. The diffusive mass fluxes must sum up to zero.

Transport properties of gas phase species and mixture

The binary diffusion coefficients as well as the transport properties of the individual gas phase species are calculated from the Chapman-Enskog kinetic theory of gases (Hirschfelder *et al.*, 1967). Semi-empirical mixture rules (Kleijn, 1991) are used to calculate the transport properties of the gas phase mixture as a function of temperature, total pressure and gas phase composition.

Boundary conditions

In order for the above set of equations to have a unique solution, boundary conditions must be specified for the velocity components, the species concentrations and the temperature in the inflow and the outflow of the reactor, on the reactor walls and on the wafer surfaces:

$$z = 0 \quad \wedge \quad 0 < r < R_t \qquad \mathbf{u}_z = 5.66\,10^{-6} \frac{T_0}{\pi R_t^2 p_{t0}} \sum_{i=1}^{NG} Q_i \, , \qquad \mathbf{u}_r = 0 \, , \qquad T = T_0 \, ,$$

$$\lambda \frac{\partial T}{\partial z} = 0 \, , \qquad \omega_i = \frac{M_i Q_i}{\sum_{j=1}^{NG} M_j Q_j} \, , \qquad j_{i,z} = 0 \tag{6.25}$$

$$z = L_3 \quad \wedge \quad 0 < r < R_t \qquad \frac{\partial}{\partial z}(\rho \mathbf{u}_z) = 0 \, , \qquad \mathbf{u}_r = 0 \, , \qquad \lambda \frac{\partial T}{\partial z} = 0 \, , \qquad j_{i,z} = 0 \tag{6.26}$$

$$(\, 0 < z < L_1 \ \vee \ L_2 < z < L_3 \,) \quad \wedge \quad r = R_t \qquad \mathbf{u}_z = 0 \, , \qquad \mathbf{u}_r = \frac{1}{\rho} \sum_{i=1}^{NG} M_i \sum_{m=1}^{ns} \nu_{m,i} r_{a,m} \, ,$$

$$\lambda \frac{\partial T}{\partial r} = 0 \, , \qquad \rho \mathbf{u}_r \omega_i + j_{i,r} = M_i \sum_{m=1}^{ns} \nu_{m,i} r_{a,m} \tag{6.27}$$

$$L_1 < z < L_2 \quad \wedge \quad r = R_t \qquad \mathbf{u}_z = 0 \, , \qquad \mathbf{u}_r = \frac{1}{\rho} \sum_{i=1}^{NG} M_i \sum_{m=1}^{ns} \nu_{m,i} r_{a,m} \, , \qquad T = T_w \, ,$$

$$\rho \mathbf{u}_r \omega_i + j_{i,r} = M_i \sum_{m=1}^{ns} \nu_{m,i} r_{a,m} \tag{6.28}$$

$$z = z_w \quad \wedge \quad 0 < r < R_w \qquad \mathbf{u}_z = \frac{1}{\rho} \sum_{i=1}^{NG} M_i \sum_{m=1}^{ns} \nu_{m,i} r_{a,m} \, , \qquad \mathbf{u}_r = 0 \, , \qquad T = T_w \, ,$$

$$\rho \mathbf{u}_z \omega_i + j_{i,z} = M_i \sum_{m=1}^{ns} \nu_{m,i} r_{a,m} \tag{6.29}$$

The boundary conditions defined on the reactor walls and wafer surfaces need some further explanation. At these solid boundaries, the net total mass flux of species i normal to the surface is balanced by the net mass production rate of species i on the surface:

$$\underline{n}\cdot(\rho\,\underline{u}\,\omega_i + j_i) = M_i \sum_{m=1}^{ns} \nu_{m,i}\, r_{s,m} \tag{6.30}$$

with $\underline{n}$ a unity vector normal to the surface. The total net mass flux normal to the surface is obtained by summing equation (6.30) over all gas phase species. Since all mass fractions sum up to unity and all diffusive mass fluxes to zero, the velocity component normal to the surface becomes:

$$\underline{n}\cdot\underline{u} = \frac{1}{\rho}\sum_{i=1}^{NG} M_i \sum_{m=1}^{ns} \nu_{m,i}\, r_{s,m} \tag{6.31}$$

Furthermore, the usual no-slip boundary conditions are assumed to hold on all solid surfaces. The wall and wafer temperatures inside the wafer section are supposed to be fixed by the furnace setting, whereas the walls outside the wafer section are assumed to be adiabatic. Heat effects associated with surface reactions are neglected. Besides all boundary conditions mentioned above, an additional constraint has to be fulfilled, i.e. the total pressure must be specified at one particular point inside the reactor. Hence, a total pressure equal to p_{t0} is prescribed in the outlet of the reactor.

Radially averaged silicon growth rate

After solving the complete set of model equations, the radially averaged silicon growth rate is obtained from equation (6.13). The integration is carried out by a stepwise summation according to:

$$\overline{R_{Si}} = \frac{\sum_{j} R_{Si,j}\,(r_j^2 - r_{j-1}^2)}{R_w^2} \tag{6.32}$$

with r_j and r_{j-1} the radial positions of the north and south wall of the *jth* control volume, and $R_{Si,j}$ the silicon growth rate in the enclosed grid point.

6.3.2.3 Solution procedure

The governing set of coupled non-linear partial differential equations with corresponding boundary conditions is solved by means of the control volume based finite difference method of Patankar and Spalding (Patankar, 1980) using the Fortran computer code CVDMODEL developed by Kleijn (Kleijn, 1991). For a detailed description of the theoretical background of the implemented numerical techniques, the reader is referred to the above mentioned references. Here, only the essential features relevant for the present calculations are given.

The equations are discretized on a non-uniform, cylindrical grid with 267 grid points in the axial direction and 22 grid points in the radial direction. Near the wafers and the wall, the grid is locally refined in order to accurately capture the concentration gradients of the gas phase intermediates. The resulting matrix equations are solved iteratively using the line-by-line TDMA and two-dimensional plane-TDMA (= Tri-diagonal Matrix Algorithm) methods (Patankar, 1980; Kleijn, 1991). To verify the convergence of the iterative solution procedure, four criteria are used: (i) the error in the global mass balance, <1%; (ii) the error in the global mass balance for each of the gas phase species, <1%; (iii) the residuals of the equations (absolute values, summed over the grid, normalized by a characteristic value for the variable and normalized by the number of grid points), $<10^{-3}$, except for the residuals of the energy equations, $<10^{-5}$ and (iv) the relative changes of the variables from one iteration to the next in a representative monitor point, $<10^{-5}$. The monitor point is located in the annular zone near the outlet of the reactor. More severe convergence criteria than applied did not change the calculated deposition rates significantly. A typical reactor simulation satisfying the above convergence criteria requires approximately 7000 iterations corresponding to a CPU-time of about 10 hours on a Silicon Graphics Power Challenge Computer.

6.4 Kinetic model

The kinetic model used has been developed by modelling of a large set of kinetic experiments performed in the range of industrially relevant operation conditions for the deposition of polycrystalline silicon, see Chapter 5. It consists of four elementary gas phase reactions coupled to ten elementary surface reactions, see Table 6.3.

Surface reactions (10) to (12) are assumed to proceed instantaneously while all other reactions are considered kinetically significant. Hence, besides the gas phase species hydrogen, silane, silylene, disilane, disilene and silylsilylene, hydrogen adatoms form the only kinetically significant surface species.

Following the law of mass action for the rates of the forward and reverse steps of the elementary gas phase reactions (1) to (4), the homogeneous net production rates of the above gas phase components are given by:

$$\sum_{k=1}^{ng} \nu_{k,i}\, r_{v,k} = \sum_{k=1}^{ng} \left(\nu_{k,i}\, k_k \prod_{i=1}^{NG} C_i^{\nu_{k,i}} \right) \tag{6.33}$$

with k_k the rate coefficient of gas phase step k; C_i the gas phase concentration of component i; NG the number of gas phase components. The rate coefficients of the unimolecular steps (1), (-2), (3) and (4) are calculated using the empirical relation given by equation (5.30). The rate coefficients of the reverse steps are calculated from thermodynamics.

The calculation of the heterogeneous net production rates of the above gas phase species is less straightforward. The complexity of the surface reaction network does not allow a straightforward derivation of closed kinetic expressions relating the silicon deposition rates from the individual silicon containing gas phase species to gas phase concentrations only. The dual-site adsorption mechanisms give rise to third order algebraic equations from which no simple analytical expression for the surface concentration of vacant sites can be deduced. Hence, this concentration is obtained numerically. According to the kinetic model presented in Table 6.3 the steady state mass balance for hydrogen adatoms is given by, see also equation (5.26):

$$\begin{aligned} &4 k_5 C_{SiH_4} \frac{L_*^2}{L_t} + 2 k_6 C_{SiH_2} L_* + 2 k_7 C_{Si_2H_6} L_* + 4 k_8 C_{H_3SiSiH} \frac{L_*^2}{L_t} \\ &+ 4 k_9 C_{H_2SiSiH_2} \frac{L_*^2}{L_t} - 2 k_{13} L_{H*} + \frac{2 k_{13} K_H C_{H_2} L_*^2}{L_{H*}} \quad 0 \end{aligned} \tag{6.34}$$

Substitution of the additional expression relating the concentration of hydrogen adatoms with that of vacant surface sites, i.e. $L_{H*} = L_t - L_*$, yields the following third order equation in L_*:

$$a_0 L_*^3 + a_1 L_*^2 + a_2 L_* + a_3 = 0 \tag{6.35}$$

with the coefficients a_0 to a_3 given by:

$$a_0 = -\frac{4 k_5 C_{SiH_4}}{L_t} \quad \frac{4 k_8 C_{H_3SiSiH}}{L_t} - \frac{4 k_9 C_{H_2SiSiH_2}}{L_t} \tag{6.36}$$

$$\begin{aligned} a_1 &= 4 k_5 C_{SiH_4} + 4 k_8 C_{H_3SiSiH} + 4 k_9 C_{H_2SiSiH_2} \\ &\quad 2 k_6 C_{SiH_2} - 2 k_7 C_{Si_2H_6} - 2 k_{13} + 2 k_{13} K_H C_{H_2} \end{aligned} \tag{6.37}$$

$$a_2 = 2k_6 C_{SiH_2} L_t + 2k_7 C_{Si_2H_6} L_t + 4k_{13} L_t \tag{6.38}$$

$$a_3 = -2k_{13} L_t^2 \tag{6.39}$$

This third order equation is solved with the NAG-library routine C02AGF, which uses a variant of Laguerre's method to find the roots of a real polynomial equation. This routine has been linked to both the one-dimensional two-zone and the fully two-dimensional reactor model. The polynomial equation given by (6.35) yields three real solutions for $L_{\cdot}$, only one of them lying between zero and L_t. This value of $L_{\cdot}$ is subsequently used to calculate the heterogeneous net production rates of the silicon containing gas phase species following the law of mass action for the rates of adsorption reactions (5) to (9):

$$\sum_{m=1}^{ns} \nu_{m,i}\, r_{a,m} = \sum_{m=1}^{ns} \left(\nu_{m,i}\, k_m \prod_{i=1}^{NG} C_i^{\nu_{m,i}} \prod_{l=1}^{NS} L_l^{\nu_{m,l}} \right) \tag{6.40}$$

with L_l the concentration of surface component l; NS the number of surface components; $\nu_{m,l}$ the stoichiometric coefficient of surface component l in surface step m; k_m the rate coefficient of surface step m, expressed in Arrhenius form. The heterogeneous net production rate of molecular hydrogen is calculated from those of the silicon containing species using the stoichiometry of the global deposition paths, see Table 5.2.

After solving the complete set of governing equations of either the one-dimensional two-zone or the fully two-dimensional model, the silicon growth rate is calculated from:

$$\begin{aligned} R_{Si} = \frac{M_{Si}}{\rho_{Si}} \sum_{m=1}^{ns} \nu_{m,Si}\, r_{a,m} = \frac{M_{Si}}{\rho_{Si}} \Bigg(& k_5\, C_{SiH_4} \frac{L_{\cdot}^2}{L_t} + k_6\, C_{SiH_2}\, L_{\cdot} + k_7\, C_{Si_2H_6}\, L_{\cdot} \\ & + 2\, k_8\, C_{H_3SiSiH} \frac{L_{\cdot}^2}{L_t} + 2\, k_9\, C_{H_2SiSiH_2} \frac{L_{\cdot}^2}{L_t} \Bigg) \end{aligned} \tag{6.41}$$

with M_{Si} and ρ_{Si} denoting the molar mass and the density of solid silicon, i.e. 28.086 10^{-3} kg mol^{-1} and 2.33 10^3 kg m^{-3}, respectively.

***Table 6.3:** Elementary reactions and corresponding kinetic parameter values considered in the gas phase (1-4) and on the silicon surface (5-14).*

Gas Phase Reactions *	A / s^{-1} or $m^3\ mol^{-1}\ s^{-1}$	E_a / $kJ\ mol^{-1}$	
$SiH_4 \rightleftharpoons SiH_2 + H_2$	$1.28\ 10^{10}$	215.8	(1)
$SiH_4 + SiH_2 \rightleftharpoons Si_2H_6$	$3.53\ 10^{9}$	163.3	(2)
$Si_2H_6 \rightleftharpoons H_3SiSiH + H_2$	$9.68\ 10^{9}$	180.6	(3)
$H_3SiSiH \rightleftharpoons H_2SiSiH_2$	$6.02\ 10^{4}$	4.2	(4)

Surface Reactions	A / s^{-1}, $m^3\ mol^{-1}\ s^{-1}$ or $m^3\ mol^{-1}$	E_a / $kJ\ mol^{-1}$	
$SiH_4 + 2^* \rightarrow SiH_3^* + H^*$	$3.89\ 10^{4}$	0.0	(5)
$SiH_2 + {}^* \rightarrow SiH_2^*$	$1.76\ 10^{7}$	0.0	(6)
$Si_2H_6 + {}^* \rightarrow SiH_4 + SiH_2^*$	$1.23\ 10^{6}$	0.0	(7)
$H_3SiSiH + 2^* \rightarrow 2SiH_2^*$	$1.25\ 10^{7}$	0.0	(8)
$H_2SiSiH_2 + 2^* \rightarrow 2SiH_2^*$	$1.25\ 10^{7}$	0.0	(9)
$SiH_3^* + {}^* \rightarrow SiH_2^* + H^*$	potentially instantaneous		(10)
$SiH_2^* + {}^* \rightarrow SiH^* + H^*$	potentially instantaneous		(11)
$SiH^* \rightarrow Si(s) + H^*$	potentially instantaneous		(12)
$H^* \rightleftharpoons H^0 + {}^*$	$4.47\ 10^{11}$	188.4	(13) **
$H^* + H^0 \rightleftharpoons H_2 + {}^*$	$8.99\ 10^{-18}$	-360.6	(14) ***

---

* The Arrhenius parameters listed apply to the forward steps of reactions (1), (3) and (4) and to the reverse step of reaction (2). The rate coefficients of these reaction steps need to be calculated from equation (5.30) using a collision efficiency equal to 0.3 for hydrogen and 1.0 for the other gas phase species and the pressure correction constants as listed in Table 5.4. The rate coefficients of the reverse steps are calculated from thermodynamics, see equation (5.31).

** The Arrhenius parameters listed apply to hydrogen adatom excitation.

*** The values listed are the pre-exponential factor and the change in standard enthalpy for the dissociative adsorption of molecular hydrogen. The corresponding equilibrium coefficient is expressed in Van 't Hoff form, see equation (5.35).

6.5 Validation and assessment of reactor models

The validity of the one-dimensional two-zone and the fully two-dimensional reactor models is tested by comparing their predictions with the experimental growth rates obtained in the range of operating conditions as listed in Table 6.2. Figure 6.6 shows that both reactor models adequately describe the radially averaged axial growth rate profiles over a broad range of temperatures at 50 Pa. The effect of total pressure is simulated adequately as well. This is shown in Figure 6.7 where the silicon growth rate is plotted versus the axial reactor coordinate at 900 K and pressures of 25 and 50 Pa. Within the complete range of experimental conditions, the calculated radial non-uniformities are smaller than the experimental accuracy of the layer thickness measurements.

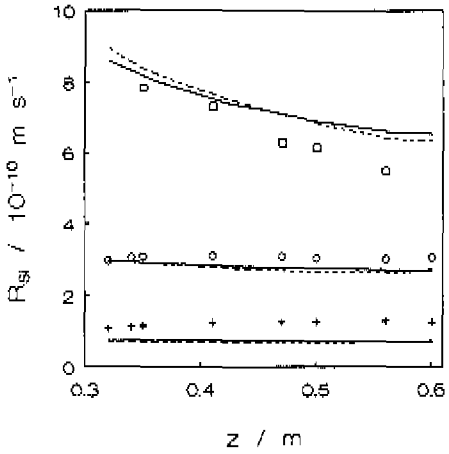

Figure 6.6: Radially averaged silicon growth rate versus the axial reactor coordinate. Dashed lines: fully two-dimensional model. Full lines: one-dimensional two-zone model. Points: experiments. Conditions: Q_{SiH_4}= 90 Nml min^{-1}, 100% SiH_4, p_t= 50 Pa.
+ T= 850 K, o T= 900 K, □ T= 950 K.

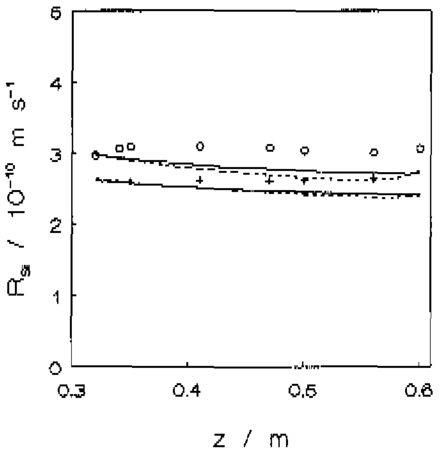

Figure 6.7: Radially averaged silicon growth rate versus the axial reactor coordinate. Dashed lines: fully two-dimensional model. Full lines: one-dimensional two-zone model. Points: experiments. Conditions: Q_{SiH_4}= 90 Nml min^{-1}, 100% SiH_4, T= 900K.
+ p_t= 25 Pa, o p_t= 50 Pa.

Clearly, both the one-dimensional two-zone model and the fully two-dimensional model adequately describe the experimental growth rate data along the axial coordinate. The much higher degree of sophistication applied in the fully two-dimensional model thus seems to be redundant. In the following part the additional simplifications made in the development of the one-dimensional two-zone model will be discussed.

The calculations with the fully two-dimensional model revealed temperature uniformity within 0.2 K in the interwafer zone and a negligible total pressure drop across the reactor. The largest pressure drop relative to the reference pressure prescribed in the outlet of the reactor was calculated for 25 Pa and 900 K and amounted to 1.3 Pa. In general, a small pressure drop takes place across the wafer section, determined largely by the size of the annular zone cross-sectional area (Coronell and Jensen, 1992). The above considerations clearly justify the assumptions concerning isothermal and isobaric operation used in the development of the one-dimensional two-zone model.

Figure 6.8 shows a typical profile of the axial mass average velocity component versus the radial reactor coordinate at 50 Pa and 900 K midway between two successive wafers, i.e. at z= Δ/2. Clearly, the gas mixture is motionless in axial direction between successive wafers. The axial velocity components associated with the so-called Stefan flow, caused by the non-equimolar counter-diffusion, are too small in absolute sense to be captured in this figure. The radial velocity component on the other hand is practically zero everywhere, except at the immediate vicinity of the wafer edges.

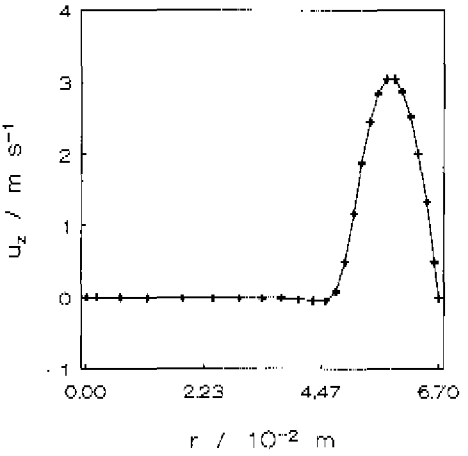

Figure 6.8: *Axial mass average velocity component versus the radial reactor coordinate at z= Δ/2. Calculated with fully two-dimensional model. Conditions:* Q_{SiH_4}= *90 Nml* min^{-1}, *100%* SiH_4, p_r= *50 Pa, T= 900 K.*

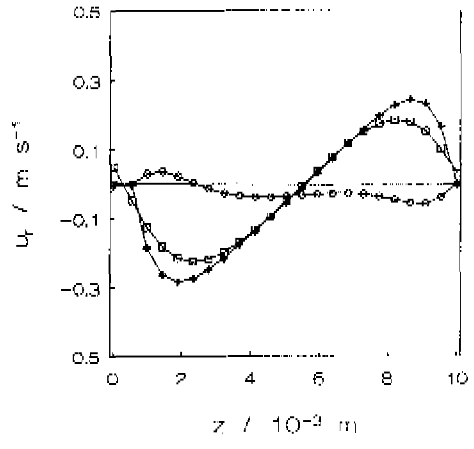

Figure 6.9: *Radial mass average velocity component versus the axial coordinate between two successive wafers at different radial positions. Calculated with fully two-dimensional model. Conditions:* Q_{SiH_4}= *90 Nml* min^{-1}, *100%* SiH_4, p_r= *50 Pa, T= 900 K, o r= 4.83* 10^{2} *m, + r= 5.00* 10^{2} *m, □ r= 5.15* 10^{2} *m.*

In Figure 6.9 the radial mass average velocity component is plotted versus the axial position between two successive wafers at 50 Pa and 900 K for different radial positions. These profiles show a radial gas entrance immediately downstream of the first wafer and the corresponding radial gas exit just upstream of the second wafer. However, the small value of the radial velocity component at $4.83\ 10^{-2}$ indicates that this gas circulation is confined to the outer 2 mm of the interwafer zone only. The above considerations validate the hypothesis of a purely axial gas movement in the annular zone and of a motionless gas in the interwafer zone as postulated in the development of the one-dimensional two-zone model.

Figure 6.10 shows the calculated silane molar fraction profiles versus the axial reactor coordinate at 50 Pa and the three considered temperatures, i.e. 850, 900 and 950 K. The dotted vertical lines reflect the boundaries of the wafer section. Table 6.4 lists the values of the silane conversion at the entrance and exit of the wafer section, as calculated using the one-dimensional two-zone model.

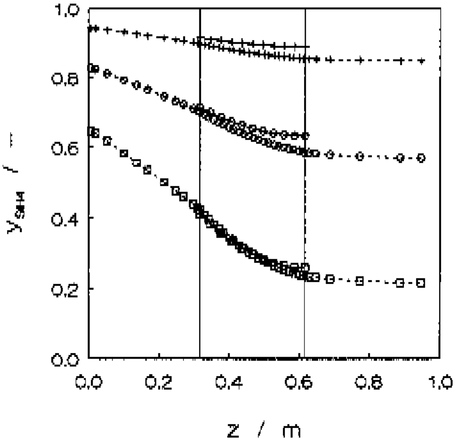

Figure 6.10: Silane molar fraction versus axial reactor coordinate at different temperatures. Dashed lines: fully two-dimensional model. Full lines: one-dimensional two-zone model. Conditions: Q_{SiH_4}= 90 Nml min^{-1}, 100% SiH_4, p_t= 50 Pa. + T= 850 K, o T= 900 K, □ T= 950 K.

Clearly, the agreement between the silane molar fraction profiles calculated using the one-dimensional two-zone model and those obtained with the fully two-dimensional model is satisfactory. This underlines the correctness of omitting the preheating and downstream sections and of using the Danckwerts boundary conditions in the one-dimensional two-zone model. The Danckwerts entrance boundary condition, given by equation (6.8), leads to a significant step change in composition at the wafer section entrance. This concentration discontinuity results from the allowance of diffusion on the downstream side of the boundary but not on the upstream side of the boundary and, hence, confirms the relative importance of axial diffusion in the annular zone. In case convection was the only mode of transport, a silane molar fraction equal to one would have been calculated at the same point. The axial diffusion thus reduces the variation in reactant concentration and, hence, improves the layer thickness uniformity along the wafer section.

Comparison of the results shown in Figures 6.6 and 6.10 reveals that changes in the molar fraction of silane have no large impact on the silicon growth rate. This is consistent with the rather low partial reaction order of silane determined in Chapter 3. Depending on silane space time and feed composition, the partial reaction order varied between 0.28 and 0.44 at 900 K.

Table 6.4: *Silane conversion at the entrance and exit of the wafer section versus temperature. Calculated with the one-dimensional two-zone model. Conditions:* Q_{SiH_4} = *90 Nml min*$^{-1}$*, 100%* SiH_4*,* p_t = *50 Pa.*

T / K	X_{SiH_4} / %	
	entrance	exit
850	8.6	11.2
900	28.7	37.0
950	58.7	74.2

The full lines in Figures 6.11 and 6.12 represent typical molar fraction profiles of silylene and disilane calculated at 50 Pa and 900 K using the fully two-dimensional model. The molar fractions are plotted as a function of the radial reactor coordinate for different axial positions between two successive wafers located in the middle of the wafer section. These results clearly demonstrate the existence of significant variations in the silylene and disilane molar fractions, from high values in the annular zone to much lower values in the interwafer zone. These differences can be linked to the different surface-to-volume ratios of the annular and interwafer zone. Mass transport effects are of minor importance in this context, as will be shown later. Note that silylene and to a lesser extent disilane show significant concentration gradients in both the axial direction of the interwafer zone and the radial direction of the annular zone.

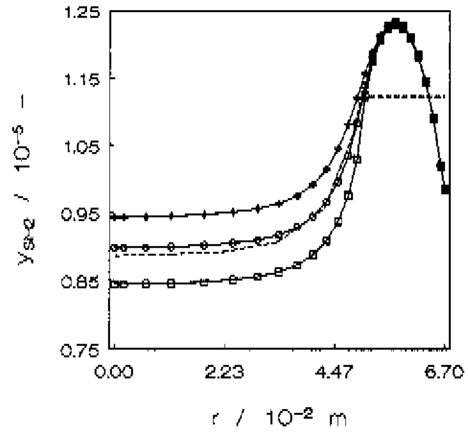

Figure 6.11: *Silylene molar fraction versus the radial reactor coordinate at different axial positions. Full lines: fully two-dimensional model. Dashed lines: one-dimensional two-zone model. Conditions: Q_{SiH_4}= 90 Nml min^{-1}, 100% SiH_4, p_t= 50 Pa, T= 900 K. □ z= 1.0 and 9.5 mm, o z= 2.3 and 8.2 mm, + z= 5.25 mm.*

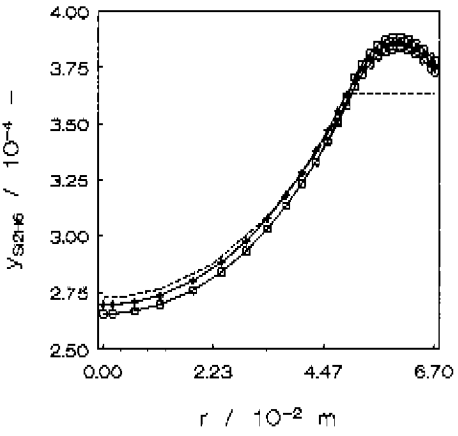

Figure 6.12: *Disilane molar fraction versus the radial reactor coordinate at different axial positions. Full lines: fully two-dimensional model. Dashed lines: one-dimensional two-zone model. Conditions: Q_{SiH_4}= 90 Nml min^{-1}, 100% SiH_4, p_t= 50 Pa, T= 900 K. □ z= 1.0 and 9.5 mm, + z= 5.25 mm.*

The molar fraction profiles of the two Si_2H_4 isomers, not shown, exhibit similar gradients as silylene in both directions. Silane on the other hand, being much less reactive than the above mentioned gas phase intermediates, has completely flat profiles. Although the one-dimensional two-zone model does not account for these concentration gradients of the gas phase intermediates, silicon growth rates calculated using this strongly simplified reactor model do not significantly differ from those calculated using the fully two-dimensional model, see Figures 6.6 and 6.7. This is caused by the relatively small contribution of the reactive intermediates to the silicon growth rate. At 50 Pa and 900 K the average contribution of the most important gas phase intermediates, i.e. silylene and disilane, amounts to roughly 20%. Furthermore, the dashed lines in Figures 6.11 and 6.12 show that the radial molar fraction profiles of silylene and disilane calculated with the one-dimensional two-zone model roughly fall in between those calculated with the fully two-dimensional model at the different axial positions. Hence, the use of the one-dimensional reactor model results in molar fractions at the surface that are only slightly different from those calculated with the two-dimensional reactor model. Consequently, the errors in the calculated wafer growth rates introduced by neglecting the concentration profiles in both the axial direction of the interwafer zone and the radial direction of the annular zone are typically less than one percent only. The difference between the radially averaged growth rates predicted by these models will thus be less than one percent as well. Based on these considerations, it can be concluded that even under conditions where 20% of the silicon growth originates from gas phase intermediates a one-dimensional two-zone model is sufficient.

6.6 Interaction between chemical kinetics and mass transport phenomena in an industrial-scale reactor

Many micro-electronics manufacturers are currently scaling up from 150 mm to 200 mm diameter wafers. In order to meet this tendency towards larger wafers, the performance of an industrial-scale LPCVD reactor capable of processing 200 mm wafers will be discussed. The simulations were performed using the one-dimensional two-zone model as outlined in paragraph 6.3.1. Table 6.5 lists the base-case operating conditions and geometrical reactor features.

Table 6.5: *Base-case geometrical reactor features and operating conditions, used for simulation of industrial-scale LPCVD reactor.*

L	0.75 m
R_t	0.16 m
R_w	0.10 m
Δ	0.00503 m
A_d/V_g *	168.8 m^{-1}
NRWF	150
p_t	25 Pa
T	900 K
Q_{SiH_4}	400 Nml min^{-1}

* The surface-to-volume ratio given here applies to the wafer section.

In the micro-electronics industry generally two approaches are used to counter the silane conversion effects on the axial growth rate uniformity, i.e. temperature profiling and gas injection at the downstream end of the wafer section. It should be noted that the simulations presented below do not account for this, but are intended to provide insights in the effects of typical operating conditions on the interaction between the mass transport phenomena and the chemical reaction kinetics in such a reactor. In this context, the interwafer spacing and the reactor tube radius appear to be the most appropriate parameters to adjust, because changes in either one of them provide additional insights in the interplay between the surface and gas phase reactions. Since temperature profiling and gas injection are not considered, adjustment of the silane volumetric flow rate is less interesting.

Figure 6.13 shows the total silicon growth rate, the growth rate due to the gas phase intermediates and the individual growth rates from silane, silylene and disilane versus the axial reactor coordinate for the conditions listed in Table 6.5. The plotted growth rates concern radially averaged values. The total silicon growth rate decreases from 2.0 10^{-10} m s^{-1} on the first wafer to 1.4 10^{-10} m s^{-1} on the last wafer of the load, corresponding to an axial non-uniformity of roughly 35%. The latter is calculated from the radially averaged silicon growth rates at the entrance and exit of the wafer section according to:

$$\textit{axial non-uniformity} = 2\,\frac{\overline{R}_{Si}\big|_{z=0} - \overline{R}_{Si}\big|_{z=L}}{\overline{R}_{Si}\big|_{z=0} + \overline{R}_{Si}\big|_{z=L}} \tag{6.42}$$

As can be seen in Figure 6.13, the total growth rate is almost completely determined by heterogeneous decomposition of silane. The silane conversion increases from 47.8% at the entrance to 66.3% at the exit of the wafer section. The contribution from all gas phase intermediates to the growth rate is approximately constant over the complete length of the wafer section. It corresponds to the growth rate contributions from SiH_2 and Si_2H_6 and amounts to roughly 3%. The growth rate from silylene is more or less constant over the length of the wafer section, reflecting the high reactivity of this intermediate, see also paragraph 5.7.1. The fact that disilane is less reactive, both in the gas phase and on the surface, is consistent with the decrease in the corresponding growth rate along the axial coordinate of the wafer section. It has to be noted, however, that the corresponding concentration variations are partially levelled off by the axial diffusion in the annular zone. The lumped contribution from H_2SiSiH_2 and H_3SiSiH to the total growth rate due to gas phase intermediates is typically less than 1%. Hence, these species are not considered in the following discussion concerning radial growth rate uniformity.

Figure 6.14 shows similar results versus the radial coordinate in the interwafer space corresponding to a silane conversion of 53.5%. In order to mark the radial variations in silicon growth rate, especially those existing close to the edge of the wafer, a non-uniformity percentage is plotted as well, calculated relative to the growth rate in the centre of the wafer according to:

$$\textit{local radial non-uniformity} = \frac{R_{Si}(r) - R_{Si}|_{r=0}}{R_{Si}|_{r=0}} \tag{6.43}$$

The growth rate non-uniformity sharply increases on the periphery of the wafer and shows a maximum of 6.3% at the edge of the wafer. The wafer edge non-uniformity, which slightly decreases from 7.5 to 5.7% along the length of the wafer section, is caused by radial variations in the growth rates from both silylene and disilane, see Figure 6.14. This is in contrast to the results of Badgwell *et al.* (1992b) who attributed similar radial growth rate non-uniformities to radial temperature variations across the wafers.

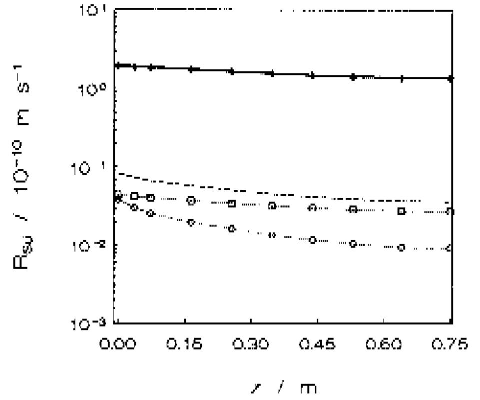

Figure 6.13: *Radially averaged silicon growth rate ( ), total silicon growth rate due to gas phase intermediates (------) and individual silicon growth rates from the most abundant silicon containing gas phase species (·······) versus the axial reactor coordinate. + SiH_4, □ SiH_2, o Si_2H_6. Calculated with one-dimensional two-zone model. Conditions: Q_{SiH_4}= 400 Nml min^{-1}, 100% SiH_4, p_t= 25 Pa, T= 900 K.*

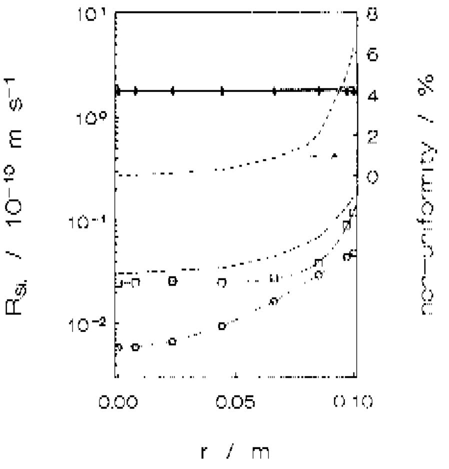

Figure 6.14: *Silicon growth rate ( ), total silicon growth rate due to gas phase intermediates (------), individual silicon growth rates from the most abundant silicon containing gas phase species (·······) and growth rate non-uniformity (- - - -) versus the radial coordinate of the interwafer zone. + SiH_4, □ SiH_2, o Si_2H_6. Calculated with one-dimensional two-zone model. Conditions: Q_{SiH_4}= 400 Nml min^{-1}, 100% SiH_4, p_t= 25 Pa, T= 900 K, X_{SiH_4}= 53.5%.*

The importance of gas phase and surface reactions with respect to the net production of the most important silicon containing gas phase species, i.e. silane, silylene and disilane, was investigated by means of a contribution analysis, see Appendix 6B. In the interwafer space at a silane conversion of 53.5%, silane consumption occurs for only 2% through homogeneous dissociation, see reaction (1) in Table 6.3, and for 98% via heterogeneous decomposition according to reaction (5), followed by instantaneous decomposition of the surface trihydride species into solid silicon and hydrogen adatoms. Production of silane occurs for 2% via homogeneous decomposition of disilane, see reaction (-2), and for 98% via heterogeneous decomposition of disilane according to reaction (7), followed by instantaneous decomposition of the surface dihydride species via reactions (11) and (12). Insertion of silylene into molecular hydrogen, see reaction (-1), has practically no contribution to the total production of silane. Formation of silylene is determined for 99% by homogeneous decomposition of silane and for 1% by homogeneous decomposition of disilane according to reactions (1) and (-2), respectively. Silylene consumption takes place for 10% via insertion into silane, see reaction (2), and for 90% via heterogeneous decomposition according to reaction (6), followed by instantaneous decomposition of the so formed surface dihydride species into solid silicon and hydrogen adatoms. Disappearance of silylene through insertion into molecular hydrogen, reaction (-1), is not significant. Disilane consumption is for 2% accounted for by homogeneous decomposition into silane and silylene, see reaction (-2), and for 98% by heterogeneous decomposition, reaction (7) followed by the instantaneous reactions (11) and (12). Finally, insertion of silylene into silane accounts for 100% to the disilane production. The above mentioned figures clearly illustrate the inferior role of the gas phase reactions with respect to the consumption of the silicon containing gas phase species. Consumption of these species proceeds mainly via the reactions taking place on the surface of the wafer. The predominance of the surface reactions over the gas phase reactions even increases along the length of the wafer section, i.e. with increasing silane conversion. This is in agreement with the result presented in Table 5.10, showing the effect of conversion on the relative importance of gas phase and surface reactions inside the laboratory reactor.

The radial growth rate non-uniformity is more critical than the axial one, provided the latter can be eliminated through injecting silane at different axial positions along the wafer load and/or profiling the temperature. As mentioned before, the radial non-uniformity of the growth rate is completely determined by the radial non-uniformities in the growth rates from silylene and disilane, and hence by the shapes of the radial concentration profiles of these species. To gain more insight in the effects of mass transport and chemical reaction kinetics on the shapes of the concentration profiles of silylene and disilane in an interwafer space, approximate analytical expressions for the latter were derived at a given silane conversion.

The above contribution analysis revealed that silylene production occurs almost completely through homogeneous dissociation of silane, reaction (1), whereas consumption of silylene takes place for 10% through insertion into silane to form disilane, reaction (2), and for 90% via heterogenous decomposition, reaction (6). Formation of disilane is fully accounted for by silylene insertion into silane, reaction (2), whereas consumption of disilane takes place by heterogeneous decomposition according to reaction (7). Figure 6.15 shows the most important reaction paths to and from silylene and disilane.

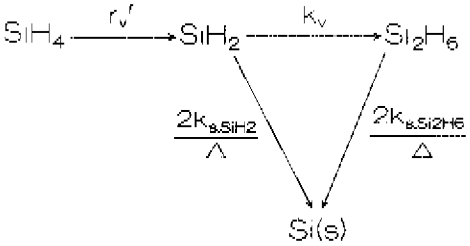

Figure 6.15: *Most important reaction paths to and from silylene and disilane.*

Silylene production is assumed to proceed at a uniform rate r_v^f (mol m^{-3} s^{-1}), equal to the product of the unimolecular reaction rate coefficient k_1 (s^{-1}) of Table 6.3 and the silane concentration, C_{SiH_4} (mol m^{-3}), the latter being uniform in each interwafer space. The insertion reaction of silylene into silane, which contributes to both the disappearance of silylene and the production of disilane, is characterized by a pseudo-first order reaction rate coefficient k_v (s^{-1}), equal to the product of the bimolecular rate coefficient k_2 (m^3 mol^{-1} s^{-1}) of Table 6.3 and again the uniform concentration of silane. Consumption of silylene and disilane at the surface is characterized by the surface reaction rate coefficients k_{s,SiH_2} and k_{s,Si_2H_6} (m s^{-1}), being the products of the rate coefficients k_6 and k_7 (m^3 mol^{-1} s^{-1}) of Table 6.3 and the concentration of vacant surface sites, L. (mol m^{-2}). The latter is practically uniform in each interwafer space, because it is predominantly determined by the heterogeneous decomposition of silane and the desorption of hydrogen.

On the basis of the foregoing considerations and neglecting possible axial concentration gradients the continuity equations for silylene and disilane in an interwafer space become:

$$-\frac{D_{SiH_2,m}}{r}\frac{d}{dr}\left(r\frac{dC_{SiH_2}}{dr}\right) = r_v^f - k_v C_{SiH_2} - \frac{2}{\Delta} k_{s,SiH_2} C_{SiH_2} \qquad (6.44)$$

$$-\frac{D_{Si_2H_6,m}}{r}\frac{d}{dr}\left(r\frac{dC_{Si_2H_6}}{dr}\right) = k_v C_{SiH_2} - \frac{2}{\Delta}k_{s,Si_2H_6}C_{Si_2H_6} \tag{6.45}$$

with $D_{i,m}$ denoting the effective molecular diffusion coeffcient of species i in a multicomponent mixture as postulated by Wilke (Bird *et al.*, 1960). It has to be noted that the factor 2/Δ represents the surface-to-volume ratio in each interwafer space. The appropriate boundary conditions are similar to those expressed by equations (6.2) and (6.3):

$$r = 0 \qquad \frac{dC_i}{dr} = 0 \tag{6.46}$$

$$r = R_w \qquad C_i = C_i^a \tag{6.47}$$

with the superscript a denoting the annular zone.

The second order differential equation for silylene, equation (6.44), is linear in C_{SiH_2} and features constant coefficients at a given silane conversion, i.e. at a given axial position in the annular zone. Integration of this equation with the corresponding boundary conditions leads to the following expression for the silylene concentration as a function of the radial coordinate in an interwafer space, see Appendix 6C:

$$C_{SiH_2} = \frac{r_v'}{k_v + \frac{2}{\Delta}k_{s,SiH_2}} + \left(C^a_{SiH_2} - \frac{r_v'}{k_v + \frac{2}{\Delta}k_{s,SiH_2}}\right)\frac{I_0\left(\phi_{SiH_2}\frac{r}{R_w}\right)}{I_0(\phi_{SiH_2})} \tag{6.48}$$

with I_0 a modified Bessel function of the first kind and order zero and ϕ_{SiH_2} a modified Thiele modulus defined as:

$$\phi_{SiH_2} = R_w\sqrt{\frac{k_v + \frac{2}{\Delta}k_{s,SiH_2}}{D_{SiH_2,m}}} \tag{6.49}$$

and corresponding to the ratio of the time scale of diffusional mass transport to the time scale of disappearance via gas phase as well as surface reactions. The first term on the right-hand side of equation (6.48) denotes the concentration of silylene obtained by applying the steady state approximation to this species:

$$C_{SiH_2}^{SSA} = \frac{r_v'}{k_v + \frac{2}{\Delta} k_{s,SiH_2}} \tag{6.50}$$

The first term inside the brackets of equation (6.48), $C^a_{SiH_2}$, denotes the steady state concentration of silylene in the annular zone corresponding to the locally prevailing concentration of silane. Substitution of equation (6.48) into the second order differential equation for disilane, equation (6.45), and integration of the latter with the corresponding boundary conditions leads to the following expression for the disilane concentration as a function of the radial coordinate in an interwafer space, see Appendix 6C:

$$\begin{aligned} C_{Si_2H_6} = {} & \frac{k_v C_{SiH_2}^{SSA} \Delta}{2 k_{s,Si_2H_6}} + \left(\frac{\frac{k_v}{D_{Si_2H_6,m}} (C^a_{SiH_2} - C^{SSA}_{SiH_2}) R_w^2}{\phi^2_{Si_2H_6} - \phi^2_{SiH_2}} \right) \frac{I_0(\phi_{SiH_2} \frac{r}{R_w})}{I_0(\phi_{SiH_2})} \\ & + \left(C^a_{Si_2H_6} - \frac{k_v C_{SiH_2}^{SSA} \Delta}{2 k_{s,Si_2H_6}} - \frac{\frac{k_v}{D_{Si_2H_6,m}} (C^a_{SiH_2} - C^{SSA}_{SiH_2}) R_w^2}{\phi^2_{Si_2H_6} - \phi^2_{SiH_2}} \right) \frac{I_0(\phi_{Si_2H_6} \frac{r}{R_w})}{I_0(\phi_{Si_2H_6})} \end{aligned} \tag{6.51}$$

with $\phi_{Si_2H_6}$ the Thiele modulus defined as:

$$\phi_{Si_2H_6} = R_w \sqrt{\frac{2 k_{s,Si_2H_6}}{\Delta D_{Si_2H_6,m}}} \tag{6.52}$$

The first term on the right-hand side of equation (6.51) represents the disilane concentration obtained by applying the steady state approximation to this species:

$$C_{Si_2H_6}^{SSA} = \frac{k_v C_{SiH_2}^{SSA}}{\frac{2}{\Delta} k_{s,Si_2H_6}} \tag{6.53}$$

As shown in Figure 6.16, the analytical expressions given by equations (6.48) and (6.51) adequately describe the numerically obtained concentration profiles of silylene and disilane. The full lines represent the concentration profiles as calculated with the one-dimensional two-zone model, whereas the dashed lines show the same profiles obtained using the analytical expressions and the values listed in Table 6.6. The effective molecular diffusion coefficients are based on radially averaged molar fractions obtained with the quadrature formula.

Table 6.6: *Values of kinetic and transport parameters. Conditions:* Q_{SiH_4}= *400 Nml min*$^{-1}$*, 100%* SiH_4*,* p_t= *25 Pa, T= 900 K,* X_{SiH_4}= *53.5%,* $C^a_{SiH_2}$= *3.406 10*$^{-8}$ *mol m*$^{-3}$ *and* $C^a_{Si_2H_6}$= *1.978 10*$^{-7}$ *mol m*$^{-3}$*.*

r_v^f	9.32 10^{-5} mol m^{-3} s^{-1}
k_v	1302.2 s^{-1}
k_{s,SiH_2}	29.175 m s^{-1}
k_{s,Si_2H_6}	2.029 m s^{-1}
$D_{SiH_2,m}$	0.688 m^2 s^{-1}
$D_{Si_2H_6,m}$	0.431 m^2 s^{-1}

The values for the kinetic and transport parameters listed in Table 6.6 lead after substitution into (6.49) and (6.52) to ϕ_{SiH_2}= 13.7 and $\phi_{Si_2H_6}$= 4.3. Due to the large value of ϕ_{SiH_2} the second term on the right-hand side of equation (6.48) is small compared to the first term for small values of the radial coordinate. Hence, the silylene concentration in the centre of the interwafer space equals $C_{SiH_2}^{SSA}$ and mass transport effects are absent. Important to note is that the steady state concentration of silylene is determined solely by the uniform concentration of silane. The shape of the silylene concentration profile is determined by the values of ϕ_{SiH_2} and $C_{SiH_2}^{SSA}$ and hence by the time scale of silylene consumption through surface as well as gas phase reactions provided the effective molecular diffusion coefficient, $D_{SiH_2,m}$, and the silylene production rate, r_v^f, remain the same. Two extreme situations can now be distinguished. In the absence of silylene consumption, i.e. in case ϕ_{SiH_2}= 0, silylene is uniformly distributed throughout the interwafer space and a flat concentration profile results at the level prevailing in the annular zone, $C^a_{SiH_2}$. In case silylene consumption proceeds extremely fast, i.e. in the limit of $\phi_{SiH_2} \rightarrow \infty$, the diffusion cannot keep up with the reactions and a pronounced concentration gradient exists over an infinitesimally small distance from the wafer edge while the concentration in the centre of the interwafer space approaches zero. At intermediate values of ϕ_{SiH_2}, a decrease in the time scale of silylene consumption is accompanied with a decrease in both the concentration in the centre of the interwafer space and the thickness of the layer over which the concentration gradient takes place. It has to be noted that in case ϕ_{SiH_2} is not large enough to completely eliminate mass transport effects in the centre of the interwafer space the concentration in that region does not equal the steady state concentration as given by equation (6.50).

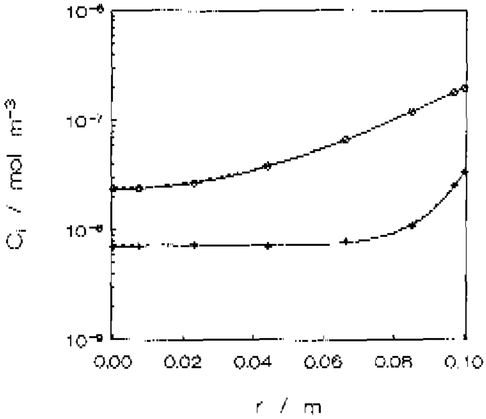

Figure 6.16: Concentration of silylene (+) and disilane (o) versus the radial coordinate in an interwafer space. Full lines: calculated with one-dimensional two-zone model. Dashed lines: calculated with equations (6.48) and (6.51). Conditions: Q_{SiH_4}= 400 Nml min^{-1}, 100% SiH$_4$, p_t= 25 Pa, T= 900 K, X_{SiH_4}= 53.5%.

An analysis of the disilane concentration profile shown in Figure 6.16 on the basis of equation (6.51) is less straightforward. The shape of the disilane concentration profile is effected by that of silylene as well, since formation of disilane is completely accounted for by insertion of silylene into silane. The disilane concentration in the centre of the interwafer space is, contrary to the silylene case, not solely determined by chemical kinetics but effected by mass transport as well. As a result of the relatively small value of $\phi_{Si_2H_6}$ the value of the third term on the right-hand side of equation (6.51) is comparable to the value of the first term. Moreover, the third term can be equated with $C^s_{Si_2H_6}/I_0(\phi_{Si_2H_6})$, since the other terms inside the brackets are in absolute sense much smaller than $C^s_{Si_2H_6}$. The expression for the disilane concentration at r= 0 thus becomes:

$$C_{Si_2H_6}\big|_{r=0} = C^{SSA}_{Si_2H_6} + \frac{C^{s}_{Si_2H_6}}{I_0(\phi_{Si_2H_6})} \tag{6.54}$$

with the first term on the right-hand side merely reflecting chemical kinetics and the second term accounting for diffusional mass transport.

A quantity that will be used in the following sections is the ratio between the concentrations of silylene and disilane prevailing in the centre of an interwafer space, i.e. at r= 0. Based on the foregoing considerations the following expression holds:

$$\left(\frac{C_{SiH_2}}{C_{Si_2H_6}}\right)_{r=0} = \frac{C^{SSA}_{SiH_2}}{C^{SSA}_{Si_2H_6} + \dfrac{C^{s}_{Si_2H_6}}{I_0(\phi_{Si_2H_6})}} \tag{6.55}$$

with the steady state concentrations of silylene and disilane given by equations (6.50) and (6.53), and the Thiele modulus for disilane defined by equation (6.52).

Effect of interwafer spacing

Conform the analytical expressions given by equations (6.48) and (6.51) the surface-to-volume ratio of the interwafer space, 2/Δ, effects the shapes of the concentration profiles of silylene and disilane. Both the steady state concentrations given by equations (6.50) and (6.53) and the Thiele moduli defined by equations (6.49) and (6.52) are functions of the surface-to-volume ratio and hence of the interwafer spacing. Because the analytical expression for silylene, equation (6.48), is more transparent than that obtained for disilane, equation (6.51), the effect of interwafer spacing will be explained in terms of silylene. A similar argumentation, however, holds for disilane.

Figure 6.17 shows the effect of interwafer spacing on the shape of the silylene concentration profile in the interwafer zone for the conditions as listed in Table 6.5. It has to be noted that the interwafer spacing has been altered by changing the total number of wafers positioned in the wafer load, NRWF, while keeping the length of the wafer section fixed at 0.75 m. In order to investigate the effect of interwafer spacing without interference of gas phase composition effects, the silylene concentration profiles shown in Figure 6.17 apply to interwafer spaces at a similar silane conversion, namely 53%. In this way the effects of changing gas phase composition on the effective molecular diffusion coefficient $D_{SiH_2,m}$ and the rate coefficients k_1 and k_2 are eliminated.

It is clear that with decreasing interwafer spacing, i.e. with increasing surface-to-volume ratio, both the concentration of silylene in the centre of the interwafer space and the thickness of the layer over which the concentration gradient takes place decrease. These effects have to be attributed to a decreasing steady state concentration given by equation (6.50) and an increasing Thiele modulus as given by equation (6.49). A smaller value for the interwafer spacing results in a smaller time scale of silylene consumption relative to that of diffusional mass transport. Hence, the consumption of silylene molecules entering the interwafer space takes place over a shorter distance from the wafer edge, thereby reducing the layer over which the concentration gradient occurs.

In order to analyse the effect of interwafer spacing on the relative contribution of gas phase reactions to the total consumption of silylene within an interwafer space, disappearance contribution percentages were calculated for this species for the interwafer spacings of 0.00431 m and 0.00843 m, corresponding to surface-to-volume ratios of 464.0 m^{-1} and 237.2 m^{-1}, see Table 6.7. Formation contribution percentages are not relevant, since production of the gas phase intermediates is a matter of gas phase kinetics only. Clearly, with increasing interwafer spacing the contribution to the total consumption of silylene of gas phase reactions, or more specifically of reaction (2) in Table 6.3, increases. As a matter of course, the contribution of surface reactions, or more specifically of reaction (6) in Table 6.3, decreases. The same table shows similar changes in the contribution of gas phase reactions to the total consumption of silane and disilane. Moreover, the listed percentages reveal the predominance of the surface reactions over the gas phase reactions.

Table 6.7: *Contribution analysis of the disappearance of silane, silylene and disilane for interwafer spacings of 0.00431 m (2/Δ= 464.0 m^{-1}) and 0.00843 m (2/Δ= 237.2 m^{-1}), calculated as described in Appendix 6B after solving the complete set of equations of the one-dimensional two-zone model. Conditions:* Q_{SiH_4}= *400 Nml* min^{-1}*, 100%* SiH_4*,* p_t= *25 Pa, T= 900 K,* X_{SiH_4}= *53%.*

Δ / m	0.00431		0.00843	
	surface / %	gas phase / %	surface / %	gas phase / %
SiH_4	98.4	1.6	96.8	3.2
SiH_2	91.0	9.0	83.8	16.2
Si_2H_6	98.4	1.6	96.9	3.1

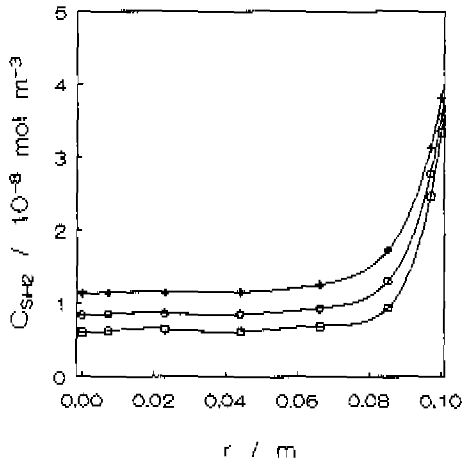

Figure 6.17: Silylene concentration versus the radial coordinate of the interwafer zone. Calculated using the one-dimensional two-zone model. Conditions: Q_{SiH_4}= 400 Nml min^{-1}, 100% SiH_4, p_t= 25 Pa, T= 900 K, X_{SiH_4}= 53%. + Δ= 0.00843 m, o Δ= 0.00605 m, □= 0.00431 m.

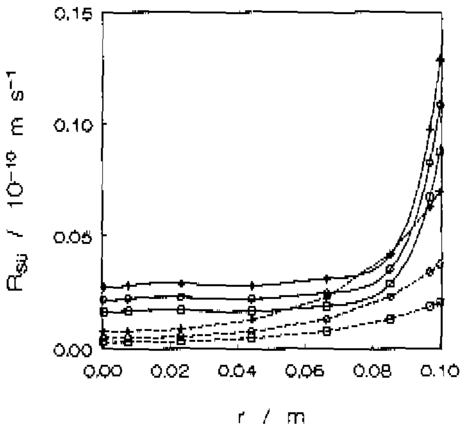

Figure 6.18: Silicon growth rate from silylene (——) and disilane (-------) versus the radial coordinate of the interwafer zone. Calculated using the one-dimensional two-zone model. Conditions: Q_{SiH_4}= 400 Nml min^{-1}, 100% SiH_4, p_t= 25 Pa, T= 900 K, X_{SiH_4}= 53%. + Δ= 0.00843 m, o Δ= 0.00605 m, □= 0.00431 m.

In Figure 6.18 silicon growth rate profiles from silylene and disilane are shown versus the radial coordinate of the interwafer zone for different interwafer spacings. With decreasing interwafer spacing the ratio between the growth rates from silylene and disilane, $R_{SiH_2}/R_{Si_2H_6}$, in the central part of the interwafer space increases. With decreasing interwafer spacing the growth rate from disilane decreases more strongly than that from silylene. This effect has to be explained in terms of the ratio between the gas phase concentrations of silylene and disilane, see equation (6.55). The steady state concentration of silylene and the Thiele modulus of disilane, see equations (6.50) and (6.52), change as a result of changing interwafer spacing only. The steady state concentration of disilane on the other hand, equation (6.53), changes not only as a result of changing interwafer spacing but also as a result of a varying steady state concentration of silylene. Due to the stronger decrease in $C_{Si_2H_6}^{SSA}$ than in $C_{SiH_2}^{SSA}$ with decreasing Δ and due to the exponential character of the modified Bessel function I_0 incorporating the disilane Thiele modulus, the denominator of equation (6.55) more strongly decreases upon decreasing Δ than does the numerator. In this way it is shown that with decreasing interwafer spacing the ratio of silylene concentration to disilane concentration at r= 0 increases and hence the relative contribution of silylene to the silicon growth rate.

As mentioned earlier, the radial variations in the growth rates from silylene and disilane completely determine the radial non-uniformity in the total growth rate across a wafer. Upon increasing the interwafer spacing from 0.00431 m to 0.00843 m the variations in the growth rates from these species significantly decrease. In case Δ= 0.00431 m the growth rate from silylene at the edge of the wafer is 5.5 times that in the centre of the wafer. In case Δ= 0.00843 m this factor amounts to 3.3. With respect to disilane factors of 11.1 and 4.0 are obtained, respectively. Hence, with increasing interwafer spacing, the concentration profile of disilane is smoothened more than that of silylene. This is consistent with the above noted effect of the interwafer spacing on the ratio of the steady state concentrations of silylene and disilane.

Although the radial variations in the growth rates from silylene and disilane significantly reduce at larger interwafer spacings, the net effect on the growth rate profile is quite small. Due to the relatively small contribution of silylene and especially of disilane to the silicon growth rate, the decrease in the radial growth rate non-uniformity is almost negligible. The latter is calculated from the silicon growth rates in the centre and at the edge of the interwafer space according to:

$$\textit{radial non-uniformity} = \frac{R_{Si}|_{r=R_w} - R_{Si}|_{r=0}}{R_{Si}|_{r=0}} \tag{6.56}$$

It decreases only slightly from 6.6% in case Δ= 0.00431 m to 6.3% in case Δ= 0.00843 m. A further increase in interwafer spacing certainly leads to more uniform growth rates along the radial coordinate. It should be noted, however, that an improvement in radial uniformity by an increase in interwafer spacing goes at the cost of the wafer packing density. An increase in interwafer spacing from 0.00431 m to 0.00843 m means already a reduction in the total number of silicon wafers from 175 to 90. The smaller surface-to-volume ratio on the other hand lowers the silane conversion and hence increases the average growth rate in the wafer section, see Table 6.8. The higher average silicon growth rate is attended with a smaller axial growth rate non-uniformity as defined by equation (6.42).

Effect of reactor tube radius

Figure 6.19 shows the effect of reactor tube radius on the axial silicon growth rate profile for the conditions listed in Table 6.5. Since the silane volumetric flow rate, Q_{SiH_4}, was kept constant during the simulations, the superficial gas velocity in the annulus decreases with increasing tube radius thereby increasing the mean residence time of the gas mixture in the wafer section. Consequently, the average silane conversion increases, see Table 6.9, and the average silicon growth rate thus decreases. Moreover, the decrease in superficial gas velocity increases the relative importance of molecular diffusion in respect of convection, leading to a smaller value of the mass Peclet number, Pe= uL/D. In this way axial variations in the silane concentration are reduced more effectively and a more uniform silicon growth rate is obtained along the length of the wafer section. This is also reflected by the values of the axial non-uniformity calculated using equation (6.42), see Table 6.9.

Table 6.8: *Silane conversion and radially averaged silicon growth rate both at the entrance and exit of the wafer section and the axial growth rate non-uniformity versus interwafer spacing. Calculated using the one-dimensional two-zone model. Conditions:* Q_{SiH_4}= *400 Nml min*$^{-1}$, *100%* SiH_4, p_t= *25 Pa, T= 900 K.*

Δ / m	X_{SiH_4} /	%	R_{Si} / 10^{-10}	m s^{-1}	axial non-
	entrance	exit	entrance	exit	uniformity / %
0.00431	50.4	69.6	1.92	1.27	41
0.00605	44.7	62.4	2.11	1.54	31
0.00843	39.4	55.2	2.29	1.79	25

Table 6.9: *Silane conversion and radially averaged silicon growth rate both at the entrance and exit of the wafer section and the axial growth rate non-uniformity versus reactor tube radius. Calculated using the one-dimensional two-zone model. Conditions:* Q_{SiH_4}= *400 Nml min*$^{-1}$, *100%* SiH_4, p_t= *25 Pa, T= 900 K.*

R_t / m	X_{SiH_4} /	%	R_{Si} / 10^{-10}	m s^{-1}	axial non-
	entrance	exit	entrance	exit	uniformity / %
0.14	41.2	67.1	2.18	1.36	46
0.16	47.8	66.3	2.00	1.40	35
0.18	51.9	66.0	1.89	1.42	28

The contribution of the gas phase intermediates to the growth rate is quite small and practically insensitive to a change in tube radius. It decreases from 5% at the entrance to 3% at the exit for a tube radius of 0.18 m and from 4 to 1% in case the tube radius amounts to 0.14 m. The more pronounced decrease at the smaller tube radius is related to the more pronounced decrease in silane concentration for the same radius, see Table 6.9. The above percentages correspond to the lumped growth rate contributions from silylene and disilane. The lumped contribution from the Si_2H_4 isomers to the total growth rate due to gas phase intermediates is typically less than 1%. Figure 6.20 shows the total silicon growth rate due to gas phase intermediates and the individual growth rates from silylene and disilane versus the axial coordinate for the reactor tube radii of 0.14 and 0.18 m. The plotted growth rates concern radially averaged values. Clearly, the growth rates from silylene and disilane increase with increasing radius, which seems to be in contradiction with the corresponding increasing silane conversion, see Table 6.9. However, the occurrence of higher concentrations of silylene and disilane despite the lower concentration of silane is explainable on the basis of a smaller surface-to-volume ratio, $2R_t/(R_t^2-R_w^2)$, of the annular zone.

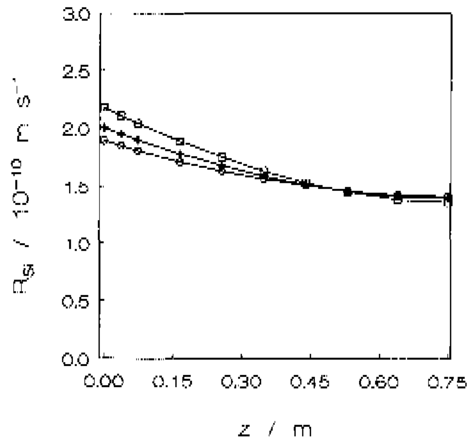

Figure 6.19: *Radially averaged silicon growth rate versus the axial reactor coordinate of the wafer section. Calculated using the one-dimensional two-zone model. Conditions:* Q_{SiH_4}= *400 Nml min*$^{-1}$, *100%* SiH_4, p_t= *25 Pa, T= 900 K.* □ R_t= *0.14 m,* + R_t= *0.16 m,* o R_t= *0.18 m.*

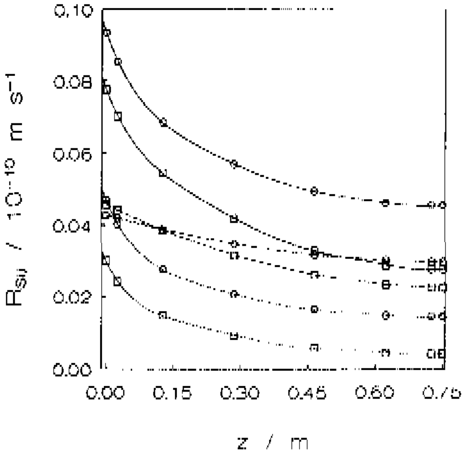

Figure 6.20: *Radially averaged silicon growth rate due to gas phase intermediates (   ) and individual contributions from silylene (-----) and disilane (······) versus the axial reactor coordinate of the wafer section. Calculated using the one-dimensional two-zone model. Conditions:* Q_{SiH_4}= *400 Nml min*$^{-1}$, *100%* SiH_4, p_t= *25 Pa, T= 900 K.* □ R_t=*0.14 m,* o R_t= *0.18 m.*

To analyse the effect of reactor tube radius on the gas phase composition in the annular zone, disappearance contribution percentages were calculated for the most important silicon containing gas phase species and tube radii of 0.14 m and 0.18 m, corresponding to annular surface-to-volume ratios of 29.2 m^{-1} and 16.1 m^{-1}, see Table 6.10. In order to investigate the effect of surface-to-volume ratio without interference of silane conversion effects, the contribution percentages were calculated for the annular space at a silane conversion of 54%. The contribution percentages of Table 6.10 clearly show that with increasing tube radius, i.e. with smaller annular surface-to-volume ratio, the relative importance of the gas phase reactions increases. The production of gas phase intermediates, taking place through gas phase reactions only, starts to overcome the consumption of these species through surface reactions. As a consequence, the gas phase intermediates are present in higher concentrations.

Table 6.10: *Contribution analysis of the disappearance of silane, silylene and disilane for reactor tube radii of 0.14 m ($2R_t/(R_t^2-R_w^2)= 29.2\ m^{-1}$) and 0.18 m ($2R_t/(R_t^2-R_w^2)= 16.1\ m^{-1}$), calculated as described in Appendix 6B after solving the complete set of equations of the one-dimensional two-zone model. Conditions: $Q_{SiH_4}= 400$ Nml min^{-1}, 100% SiH_4, $p_t= 25$ Pa, $T= 900$ K, $X_{SiH_4}= 54\%$.*

R_t / m	0.14		0.18	
	surface / %	gas phase / %	surface / %	gas phase / %
SiH_4	76.8	23.2	61.2	38.8
SiH_2	39.2	60.8	26.1	73.9
Si_2H_6	79.3	20.7	67.6	32.4

Figures 6.21 and 6.22 show the effect of the reactor tube radius on the shapes of the silylene and disilane concentration profiles in the interwafer zone. In order to eliminate gas phase composition effects, all profiles apply to interwafer spaces having a similar silane conversion, namely 54%. Even though the concentration of silylene in the annular space increases from 2.7 10^{-8} mol m^{-3} in case R_t= 0.14 m to 4.0 10^{-8} mol m^{-3} in case R_t= 0.18 m, its value remains unchanged in the centre of the interwafer space. For the conditions considered, the silylene concentration in the centre of the interwafer space equals the steady state concentration of silylene, see equation (6.50). Clearly, this concentration is merely a function of gas phase composition and interwafer spacing. The latter was not changed during the simulations. Since the plotted

concentration profiles all apply to the same concentration of silane and hence to a similar gas phase composition, the concentration of silylene in the centre of the interwafer space, $C_{SiH_2}^{SSA}$, remains constant. It indeed has no dependence on the radius of the reactor tube. Based on the expression for the steady state concentration of disilane, equation (6.53), a constant value for the disilane concentration in the centre of the interwafer space would then be expected as well. However, it has been shown that the Thiele modulus of disilane, see equation (6.52), is too small to completely eliminate mass transport effects in the centre of the interwafer space and hence justify the application of the steady state approximation to this species at this position. Since the steady state concentration and Thiele modulus of disilane remain unchanged, the concentration of disilane in the centre, see equation (6.54), changes merely as a result of changing disilane concentration in the annular space, $C^{a}_{Si_2H_6}$. It thus increases with increasing reactor tube radius.

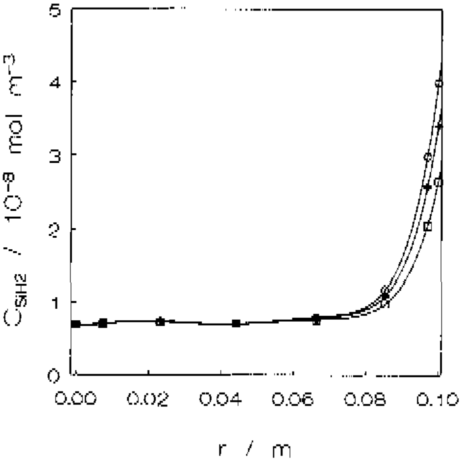

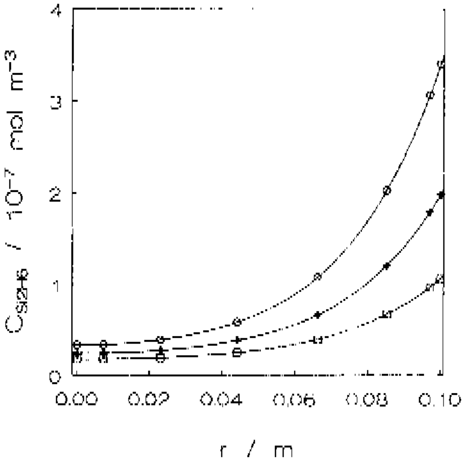

Figure 6.21: *Silylene concentration versus the radial coordinate of the interwafer zone. Calculated with one-dimensional two-zone model. Conditions:* Q_{SiH_4}*= 400 Nml min*$^{-1}$*, 100%* SiH_4*,* p_t*= 25 Pa, T= 900 K,* X_{SiH_4}*= 54%. □* R_t*= 0.14 m, +* R_t*= 0.16 m, o* R_t*= 0.18 m.*

Figure 6.22: *Disilane concentration versus the radial coordinate of the interwafer zone. Calculated with one-dimensional two-zone model. Conditions:* Q_{SiH_4}*= 400 Nml min*$^{-1}$*, 100%* SiH_4*,* p_t*= 25 Pa, T= 900 K,* X_{SiH_4}*= 54%. □* R_t*= 0.14 m, +* R_t*= 0.16 m, o* R_t*= 0.18 m.*

Based on the foregoing considerations it follows that the ratio between the concentrations of silylene and disilane in the centre of the interwafer space decreases with increasing tube radius, i.e. with decreasing annular surface-to-volume ratio. As a consequence, the ratio between the growth rates from silylene and disilane reduces as well, see Figure 6.23. Moreover, the radial growth rate non-uniformity, being completely determined by the radial variations in the growth rates from silylene and disilane, changes with changing reactor tube radius. It almost doubles from 4.4% in case R_t= 0.14 m to 8.6% in case R_t= 0.18 m due to the higher concentrations of silylene and disilane in case of the latter radius. A smaller reactor tube radius promotes radial uniformity of the growth rate in the interwafer zone, but worsens the uniformity of the growth rate along the length of the wafer section, see Table 6.9.

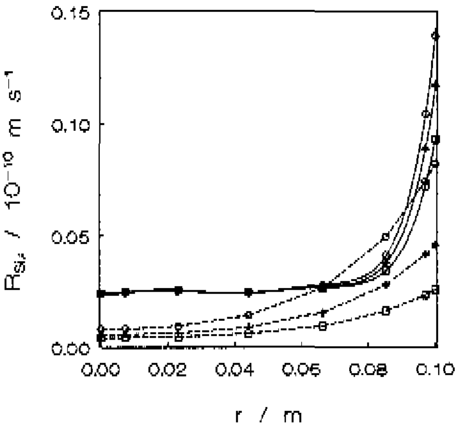

Figure 6.23: Silicon growth rate profiles from silylene (———) and disilane (-------) versus the radial coordinate of the interwafer zone. Calculated using the one-dimensional two-zone model. Conditions: Q_{SiH_4}= 400 Nml min^{-1}, 100% SiH_4, p_t= 25 Pa, T= 900 K, X_{SiH_4}= 54%. □ R_t= 0.14 m, + R_t= 0.16 m, o R_t= 0.18 m.

6.7 Conclusions

The kinetic model based upon experiments in a laboratory microbalance reactor, see Chapter 5, allows to simulate silicon growth rates obtained in a commercial LPCVD reactor without adjustment of any kinetic parameter. As long as heterogeneous silane decomposition predominantly determines the silicon growth a one-dimensional two-zone reactor model is sufficient to adequately describe these data. Due to the small contribution of homogeneously formed reactive gas phase intermediates, growth rates calculated using this strongly simplified reactor model do not essentially differ from those calculated on the basis of a fully two-dimensional model.

Simulations of the performance of an industrial-scale LPCVD reactor showed that the radial growth rate non-uniformity across a wafer is completely determined by the radial variations in the growth rates from silylene and disilane. The latter are the most important gas phase intermediates, with a contribution to the silicon growth rate of typically 1 to 5% at the operating conditions considered. Silylene is formed through homogeneous decomposition of silane and is consumed mainly by heterogeneous decomposition into solid silicon and molecular hydrogen. Consumption of silylene via insertion into silane is of minor importance. This reaction, however, fully accounts for the formation of disilane. Consumption of disilane on the other hand is almost completely accounted for by heterogeneous decomposition into solid silicon, molecular hydrogen and silane. Only a small fraction of the disilane is converted to silane and silylene, and an almost negligible fraction reaches silylsilylene. Due to the high reactivity of silylene and disilane on the surface and/or in the gas phase significant concentration gradients for these species develop in the radial direction between successive wafers. The shape of these concentration profiles can be described in terms of a (modified) Thiele modulus, based on the kinetics of the most important formation and disappearance reactions of the species under consideration.

With increasing reactor tube radius, i.e. with decreasing surface-to-volume ratio of the annular zone, the radial growth rate non-uniformity increases significantly due to the higher concentrations of silylene and disilane formed in this zone. The effect of interwafer spacing on radial growth rate non-uniformity is less pronounced.

References

Abramowitz, M., Stegun, I.A., 1970, Handbook of Mathematical Functions, Dover Publications Inc., New York.

Azzaro, C., Duverneuil, P., Couderc, J.-P., 1992, *J. Electrochem. Soc.*, **139**(1), 305.

Azzaro, C., Duverneuil, P., Couderc, J.-P., 1994, *Int. Chem. Eng.*, **34**(1), 59.

Badgwell, T.A., Edgar, T.F., Trachtenberg, I., 1992a, *J. Electrochem. Soc.*, **139**(2), 524.

Badgwell, T.A., Edgar, T.F., Trachtenberg, I., 1992b, *AIChE Journal*, **38**(6), 926.

Bird, R.B., Stewart, W.E., Lightfoot, E.N., 1960, Transport Phenomena, Wiley, New York.

Coronell, D.G., Jensen, K.F., 1992, *J. Electrochem. Soc.*, **139**(8), 2264.

Danckwerts, P.V., 1953, *Chem. Eng. Sci.*, **2**, 1.

Duverneuil, P., Couderc, J.-P., 1992, *J. Electrochem. Soc.,* **139**(1), 296.

Finlayson, B.A., 1972, The Method of Weighted Residuals and Variational Principles, Academic Press, New York.

Hirschfelder, J.O., Curtiss, C.F., Bird, R.B., 1967, Kinetic Theory of Gases and Liquids, Wiley, New York.

Hitchman, M.L., Jensen, K.F., 1993, Chemical Vapor Deposition, Academic Press, London.

Hopfmann, Ch., Werner, Ch., Ulacia F., J.I., 1991, *Appl. Surf. Sci.,* **52**, 169.

Jensen, K.F., Graves, D.B., 1983, *J. Electrochem. Soc.,* **130**(9), 1950.

Joshi, M.G., 1987, *J. Electrochem. Soc.,* **134**(12), 3118.

Kleijn, C.R., 1991, Transport Phenomena in Chemical Vapor Deposition Reactors, Ph.D. Thesis TUD, Delft.

Middleman, S., Yeckel, A., 1986, *J. Electrochem. Soc.,* **133**(9), 1951.

NAG, Fortran Library Manual, 1991, Mark 15, NAG Ltd, Wilkinson House, Oxford.

Patankar, S.V., 1980, Numerical Heat Transfer and Fluid Flow, Hemisphere Publishing, New York.

Reid, R.C., Prausnitz, J.M., Poling, B.E., 1987, The Properties of Gases and Liquids, 4*th* edition, McGraw-Hill, New York.

Roenigk, K.F., 1987, Analysis of Low Pressure Chemical Vapor Deposition Processes, Ph.D. Thesis University of Minnesota, Minnesota.

Roenigk, K.F., Jensen, K.F., 1985, *J. Electrochem. Soc.,* **132**(2), 448.

Roenigk, K.F., Jensen, K.F., 1987, *J. Electrochem. Soc.,* **134**(7), 1777.

Rosler, R.S., 1977, *Solid State Technol.,* **20**, 63.

Vinante, C., Duverneuil, P., Couderc, J.P., in *Proceedings of the 7th European Conference on CVD, 1989*, edited by M. Ducarroir, C. Bernard and L. Vandenbulcke, p. C5-35.

Wilke, T.E., Turner, K.A., Takoudis, C.G., 1986, *Chem. Eng. Sci,* **41**(4), 643.

Yeckel, A., Middleman, S., 1987, *J. Electrochem. Soc.,* **134**(5), 1275.

Yeckel, A., Middleman, S., Hochberg, A.K., 1989, *J. Electrochem. Soc.,* **136**(7), 2038.

Appendix 6A Solution procedure for one-dimensional model equations

The method of orthogonal collocation is outlined for the first-order ordinary differential equations with corresponding boundary conditions, given by equations (6.1) to (6.4), (6.6), (6.8), (6.10) and (6.11). These are rewritten by replacing r by ξR_w and z by ζL:

Interwafer zone

$$\frac{1}{\xi}\frac{d}{d\xi}(\xi N_i^w) = R_w\left(\frac{2}{\Delta}\sum_{m=1}^{ns}\nu_{m,i}r_{a,m} + \sum_{k=1}^{ng}\nu_{k,i}r_{v,k}\right) \tag{6A.1}$$

$$\frac{dy_i^w}{d\xi} = R_w\sum_{j\neq i}\frac{y_i^w N_j^w - y_j^w N_i^w}{C D_{i,j}} \tag{6A.2}$$

$$\xi = 0 \qquad N_i^w = 0 \tag{6A.3}$$

$$\xi = 1 \qquad y_i^w = y_i^a \tag{6A.4}$$

Annular zone

$$\frac{dN_i^a}{d\zeta} = L\left(\frac{2}{R_t^2 - R_w^2}\left(R_t(1+\alpha)\sum_{m=1}^{ns}\nu_{m,i}r_{a,m} + R_w N_i^w|_{\xi=1}\right) + \sum_{k=1}^{ng}\nu_{k,i}r_{v,k}\right) \tag{6A.5}$$

$$\frac{dy_i^a}{d\zeta} = L\sum_{j\neq i}\frac{y_i^a N_j^a - y_j^a N_i^a}{C D_{i,j}} \tag{6A.6}$$

$$\zeta = 0 \qquad N_i^a = u_0 C y_{i,0}^a \tag{6A.7}$$

$$\zeta = 1 \qquad \frac{dy_i^a}{d\zeta} = 0 \tag{6A.8}$$

For both the interwafer zone and the annular zone a polynomial is defined as a linear combination of both even and odd powers of the corresponding dimensionless coordinate with the highest power being m:

$$P_m^w(\xi) = \sum_{c=0}^{m} c_c^w \xi^c \qquad P_m^a(\zeta) = \sum_{c=0}^{m} c_c^a \zeta^c \tag{6A.9}$$

The coefficients c_c^w and c_c^a are defined in such a way that, in the respective integration intervals $0 \le \xi \le 1$ and $0 \le \zeta \le 1$, the successive polynomials are orthogonal to all polynomials of order less than m, with weighting functions equal to one. The roots of the polynomials $P_m^w(\xi)$ and $P_m^a(\zeta)$ are chosen as interior collocation points for the interwafer and annular zone, respectively. A choice is made for 6*th* order orthogonal collocation (m=6) in both the ξ-direction of the interwafer zone and the ζ-direction of the annular zone. The calculated interior collocation points for both zones are listed in Tables 6A.1 and 6A.2. It has to be noted that cylindrical geometry applies to the interwafer zone, whereas planar geometry applies to the annular zone.

Table 6A.1: *Roots of 6th order orthogonal polynomial for interwafer zone with weighting function equal to one and range from 0 to 1.0.*

$\xi_2 = 0.073054329$

$\xi_3 = 0.230766138$

$\xi_4 = 0.441328481$

$\xi_5 = 0.663015310$

$\xi_6 = 0.851921400$

$\xi_7 = 0.970683573$

Table 6A.2: *Roots of 6th order orthogonal polynomial for annular zone with weighting function equal to one and range from 0 to 1.0.*

$\zeta_2 = 0.033765243$

$\zeta_3 = 0.169395307$

$\zeta_4 = 0.380690407$

$\zeta_5 = 0.619309593$

$\zeta_6 = 0.830604693$

$\zeta_7 = 0.966234757$

Based on the above polynomials for the interwafer and annular zone, equation (6A.9), the following trial functions are defined as approximation for the solution of the molar flux and the molar fraction in both zones:

$$N^w(\xi) = b^{w,n} + d^{w,n}\xi + \xi(1-\xi)\sum_{cc=1}^{M} a_{cc}^{w,n} P_{cc-1}^{w}(\xi) \tag{6A.10}$$

$$y^w(\xi) = b^{w,y} + d^{w,y}\xi + \xi(1-\xi)\sum_{cc=1}^{M} a_{cc}^{w,y} P_{cc-1}^{w}(\xi) \tag{6A.11}$$

$$N^a(\zeta) = b^{a,n} + d^{a,n}\zeta + \zeta(1-\zeta)\sum_{cc=1}^{N} a_{cc}^{a,n} P_{cc-1}^{a}(\zeta) \tag{6A.12}$$

$$y^a(\zeta) = b^{a,y} + d^{a,y}\zeta + \zeta(1-\zeta)\sum_{cc=1}^{N} a_{cc}^{a,y} P_{cc-1}^{a}(\zeta) \tag{6A.13}$$

The trial functions for the interwafer zone feature (M+2) coefficients, resulting from (M+2) conditions. In case of the molar flux M conditions are provided by the residuals evaluated at the M interior collocation points, one by the residual evaluated at the extra collocation point defined at the boundary $\xi = 1$, and one by the boundary condition at $\xi = 0$. In case of the molar fraction M conditions are provided by the residuals evaluated at the M interior collocation points, one by the residual evaluated at the extra collocation point defined at the boundary $\xi = 0$, and one by the boundary condition at $\xi = 1$. The trial functions for the annular zone feature (N+2) coefficients, resulting from (N+2) conditions. In case of the molar flux N conditions are provided by the residuals evaluated at the N interior collocation points, one by the residual evaluated at the extra collocation point defined at the boundary $\zeta = 1$, and one by the boundary condition at $\zeta = 0$. In case of the molar fraction N conditions are again provided by the residuals evaluated at the N interior collocation points, one by the residual evaluated at the extra collocation point defined at the boundary $\zeta = 0$, and one by the boundary condition at $\zeta = 1$. The trial functions are polynomials of degree (M+1) in ξ or (N+1) in ζ. These are rewritten as:

$$N^w(\xi) = \sum_{cc=1}^{M+2} d_{cc}^{w,n}\,\xi^{cc-1} \tag{6A.14}$$

$$y^w(\xi) = \sum_{cc=1}^{M+2} d_{cc}^{w,y}\,\xi^{cc-1} \tag{6A.15}$$

$$N^a(\zeta) = \sum_{cc=1}^{N+2} d_{cc}^{a,n}\,\zeta^{cc-1} \tag{6A.16}$$

$$y^a(\zeta) = \sum_{cc=1}^{N+2} d_{cc}^{a,y}\,\zeta^{cc-1} \tag{6A.17}$$

or in matrix notation as:

$$N^w = Q^w d^{w,n} \qquad y^w = Q^w d^{w,y} \tag{6A.18}$$

$$N^a = Q^a d^{a,n} \qquad y^a = Q^a d^{a,y} \tag{6A.19}$$

with N^w, y^w, $d^{w,n}$ and $d^{w,y}$ vectors of length (M+2), N^a, y^a, $d^{a,n}$ and $d^{a,y}$ vectors of length (N+2), Q^w an (M+2)x(M+2) and Q^a an (N+2)x(N+2) matrix. The operators for the molar flux and molar fraction in equations (6A.1), (6A.2), (6A.5) and (6A.6) are replaced by the matrix operations:

$$\frac{1}{\xi}\frac{d}{d\xi}(\xi N^w) = D^w (Q^w)^{-1} N^w = B^w N^w \tag{6A.20}$$

$$\frac{dy^w}{d\xi} = C^w (Q^w)^{-1} y^w = A^w y^w \tag{6A.21}$$

$$\frac{dN^a}{d\zeta} = C^a (Q^a)^{-1} N^a = A^a N^a \tag{6A.22}$$

$$\frac{dy^a}{d\zeta} = C^a (Q^a)^{-1} y^a = A^a y^a \tag{6A.23}$$

with the elements of the (M+2)x(M+2) and (N+2)x(N+2) square matrices defined as:

$$Q^w_{c,cc} = \xi_c^{cc-1} \qquad C^w_{c,cc} = (cc-1)\,\xi_c^{cc-2} \qquad D^w_{c,cc} = cc\,\xi_c^{cc-2} \tag{6A.24}$$

$$Q^a_{c,cc} = \zeta_c^{cc-1} \qquad C^a_{c,cc} = (cc-1)\,\zeta_c^{cc-2} \tag{6A.25}$$

For both the interwafer and the annular zone, the derivatives are now expressed as a linear combination of the values of the solution of the molar flux or molar fraction at the collocation points. Substitution into equations (6A.1) to (6A.8) yields the following set of collocation equations:

Interwafer zone

$$\sum_{cc=1}^{M+2} B^w_{c,cc} N^w_{i,cc} = R_w \left(\frac{2}{\Delta} \sum_{m=1}^{ns} \nu_{m,i} r_{a,m} + \sum_{k=1}^{ng} \nu_{k,i} r_{v,k} \right) \qquad c = 2 \ldots M+2 \tag{6A.26}$$

$$\sum_{cc=1}^{M+2} A^w_{c,cc} y^w_{i,cc} = R_w \sum_{j \neq i} \frac{y_i^w N_j^w - y_j^w N_i^w}{C D_{i,j}} \qquad c = 1 \ldots M+1 \tag{6A.27}$$

$$N_i^w = 0 \qquad c = 1 \tag{6A.28}$$

$$y_i^w = y_i^a \qquad c = M+2 \tag{6A.29}$$

Annular zone

$$\sum_{cc=1}^{N+2} A^a_{c,cc} N^a_{i,cc} = L\left(\frac{2}{R_l^2 - R_w^2}\left(R_l(1+\alpha)\sum_{m=1}^{ns} \nu_{m,i} r_{a,m} + R_w N_i^w\big|_{\xi=1}\right)\right.$$
$$\left. + \sum_{k=1}^{ng} \nu_{k,i} r_{v,k}\right) \qquad c = 2\ldots N+2 \tag{6A.30}$$

$$\sum_{cc=1}^{N+2} A^a_{c,cc} y^a_{i,cc} = L \sum_{j\neq i} \frac{y_i^a N_j^a - y_j^a N_i^a}{C D_{ij}} \qquad c = 1\ldots N+1 \tag{6A.31}$$

$$N_i^a = u_0 C y_{i,0}^a \qquad c = 1 \tag{6A.32}$$

$$\frac{dy_i^a}{d\zeta} = 0 \qquad c = N+2 \tag{6A.33}$$

In this way a set of (2NG-1)(M+2)+(2NG-1)(N+2)= (2NG-1)(M+N+4) independent algebraic equations results with, at each collocation point, (NG-1) molar fractions and NG molar fluxes as unknowns.

The molar flux to/from the interwafer zone, $N_i^w|_{\xi=1}$, is determined from equation (6.7) in dimensionless form:

$$N_i^w\big|_{\xi=1} = R_w \int_0^1 \left(\frac{2}{\Lambda}\sum_{m=1}^{ns} \nu_{m,i} r_{a,m} + \sum_{k=1}^{ng} \nu_{k,i} r_{v,k}\right)\xi \, d\xi \tag{6A.34}$$

by means of the quadrature formula:

$$\int_0^1 f(\xi)\,\xi\, d\xi \approx \sum_{cc=1}^{M+2} w^w_{cc} f(\xi) \tag{6A.35}$$

with w_{cc}^{w} denoting the weigthing factors for the interwafer zone. The final expression for the molar flux to/from the interwafer zone is then given by:

$$N_i^w|_{\xi-1} = R_w \sum_{cc=1}^{M+2} w_{cc}^w \left(\frac{2}{\Delta} \sum_{m=1}^{ns} \nu_{m,i} r_{s,m}(\xi_{cc}) + \sum_{k=1}^{ng} \nu_{k,i} r_{v,k}(\xi_{cc}) \right) \tag{6A.36}$$

In order to determine the weighting factors the integral in equation (6A.35) needs to be evaluated for $f(\xi) = \xi^{cc-1}$:

$$\sum_{cc=1}^{M+2} w_{cc}^w f(\xi) = \frac{1}{cc+1} \xi^{cc+1} \Big|_0^1 = f_{cc}^w \tag{6A.37}$$

and the resulting f vector, consisting of (M+2) elements f_{cc}, is multiplied with the inverse of the (M+2)x(M+2) Q^w matrix (Finlayson, 1972):

$$(w^w)^T = (f^w)^T (Q^w)^{-1} \tag{6A.38}$$

The resulting weighting factors are listed in Table 6A.3.

Table 6A.3: *Weighting factors for the quadrature formula in the interwafer zone, equation (6A.35).*

$w_1^w = 0$

$w_2^w = 0.00875332$

$w_3^w = 0.04393585$

$w_4^w = 0.09868385$

$w_5^w = 0.14076636$

$w_6^w = 0.13557414$

$w_7^w = 0.07226409$

$w_8^w = 0$

Finally, the radially averaged silicon growth rate, $\bar{R}_{Si}$, is determined from equation (6.13) in dimensionless form:

$$\overline{R_{Si}} = 2\int_0^1 R_{Si}(\xi)\,\xi\,d\xi \tag{6A.39}$$

using the quadrature formula given by equation (6A.35). The final expression for the radially averaged silicon growth rate then becomes:

$$\overline{R_{Si}} = 2\sum_{cc=1}^{M+2} w_{cc}^{w}\,R_{Si}(\xi_{cc}) \tag{6A.40}$$

with the weighting factors w_{cc}^{w} as listed in Table 6A.3.

Appendix 6B Contribution analyses with respect to interwafer and annular space

The contribution analysis determines the relative importance of an elementary step with respect to the total formation or disappearance rate of a species. In general, the disappearance contribution factor of step k towards the disappearance of component i can be calculated as the ratio of the rate of disappearance of i resulting from step k, r_{ki}^{d}, to the total rate of disappearance of i:

$$\Phi_{ki}^{d} = \frac{r_{ki}^{d}}{\sum_{k} r_{ki}^{d}} \tag{6B.1}$$

Here, r_{ki}^{d}, is equal to $\alpha_{ki}\overrightarrow{r}_{k}$ when i appears on the left side of a reaction and to $\alpha_{-ki}\overleftarrow{r}_{k}$ when i appears on the right. In a similar way, the formation contribution factor can be calculated by using the rates of steps in which component i is formed:

$$\Phi_{ki}^{f} = \frac{r_{ki}^{f}}{\sum_{k} r_{ki}^{f}} \tag{6B.2}$$

with r_{ki}^{f} is equal to $\alpha_{-ki}\overrightarrow{r}_{k}$ when i appears on the right side of a reaction and to $\alpha_{ki}\overleftarrow{r}_{k}$ when i appears on the left.

The disappearance and formation contribution factors are considered with respect to all steps of the complete reaction network. The summations in equations (6B.1) and (6B.2) therefore run over all gas phase and surface steps. The reaction rates of the contributing steps, r_{ki} in mol s^{-1}, are calculated after solving the complete set of equations of the one dimensional two-zone model, see paragraph 6.3.1.2.

Interwafer space

In case of a gas phase step, the corresponding volumetric reaction rate, $r_{v,ki}$ in mol m^{-3} s^{-1}, is integrated over the gas phase reaction volume between two adjacent wafers by means of the quadrature formula given by equation (6A.35):

$$r_{ki} = \iiint_{V_g} r_{v,ki}\, dV = 2\pi R_{w}^{2} \Delta \sum_{cc=1}^{M+2} w_{cc}^{w}\, r_{v,ki}(\xi_{cc}) \tag{6B.3}$$

with w_{cc}^{w} denoting the weighting factors for the interwafer zone, see Table 6A.3. In case of a surface step, the areal reaction rate, $r_{a,ki}$ in mol m^{-2} s^{-1}, is integrated over the total deposition surface area enclosing the above gas phase reaction volume according to:

$$r_{ki} = \iint_{A_d} r_{a,ki} \, dA = 4\pi R_w^2 \sum_{cc=1}^{M+2} w_{cc}^{w} \, r_{a,ki}(\xi_{cc}) \qquad (6B.4)$$

Annular space

In case of a gas phase step, the corresponding volumetric reaction rate, $r_{v,ki}$ in mol m^{-3} s^{-1}, is multiplied by the gas phase reaction volume between the wafer edges and the reactor wall:

$$r_{ki} = \iiint_{V_g} r_{v,ki} \, dV = \pi \left(R_t^2 - R_w^2\right) \Delta \, r_{v,ki} \qquad (6B.5)$$

In case of a surface step, the areal reaction rate, $r_{a,ki}$ in mol m^{-2} s^{-1}, is multiplied by the total deposition surface area enclosing the above gas phase reaction volume:

$$r_{ki} = \iint_{A_d} r_{a,ki} \, dA = 2\pi R_t \, \Delta \, r_{a,ki} \qquad (6B.6)$$

It should be noted that due to the occurrence of both surface and gas phase reactions, the contribution analyses as described above inevitably enclose the ratio of deposition surface area to gas phase reaction volume, A_d/V_g.

Appendix 6C Analytical expressions for silylene and disilane concentration profiles in interwafer zone

Concentration profile of silylene

The continuity equation for silylene is given by:

$$-\frac{D_{SiH_2,m}}{r}\frac{d}{dr}\left(r\frac{dC_{SiH_2}}{dr}\right) = r_v^f - k_v C_{SiH_2} - \frac{2}{\Delta}k_{s,SiH_2}C_{SiH_2} \tag{6C.1}$$

with the boundary conditions:

$$r = 0 \qquad \frac{dC_{SiH_2}}{dr} = 0 \tag{6C.2}$$

$$r = R_w \qquad C_{SiH_2} = C^a_{SiH_2} \tag{6C.3}$$

In order to integrate the second order differential equation with corresponding boundary conditions, the silylene concentration is rewritten as:

$$C_{SiH_2} = \frac{r_v^f}{k_v + \frac{2}{\Delta}k_{s,SiH_2}} + f \tag{6C.4}$$

Substitution into equation (6C.1) results in:

$$\frac{1}{r}\frac{d}{dr}\left(r\frac{df}{dr}\right) = \frac{k_v + \frac{2}{\Delta}k_{s,SiH_2}}{D_{SiH_2,m}}f \tag{6C.5}$$

Rearranging gives:

$$r^2\frac{d^2f}{dr^2} + r\frac{df}{dr} - \frac{k_v + \frac{2}{\Delta}k_{s,SiH_2}}{D_{SiH_2,m}}r^2 f = 0 \tag{6C.6}$$

Substitution of the modified Thiele modulus:

$$\phi_{SiH_2} = R_w \sqrt{\frac{k_v + \frac{2}{\Delta} k_{s,SiH_2}}{D_{SiH_2,m}}} \tag{6C.7}$$

results in:

$$r^2 \frac{d^2 f}{dr^2} + r \frac{df}{dr} - \phi^2_{SiH_2} \frac{r^2}{R_w^2} f = 0 \tag{6C.8}$$

The solution to this equation reads (Abramowitz and Stegun, 1970):

$$f = \alpha\, I_0(\phi_{SiH_2} \frac{r}{R_w}) + \beta\, K_0(\phi_{SiH_2} \frac{r}{R_w}) \tag{6C.9}$$

with I_0 a modified Bessel function of the first kind and order zero and K_0 a modified Bessel function of the second kind and order zero. The silylene concentration can now be written as:

$$C_{SiH_2} = \frac{r_v^f}{k_v + \frac{2}{\Delta} k_{s,SiH_2}} + \alpha\, I_0(\phi_{SiH_2} \frac{r}{R_w}) + \beta\, K_0(\phi_{SiH_2} \frac{r}{R_w}) \tag{6C.10}$$

The boundary condition at r= 0, given by equation (6C.2), leads to a value of zero for β since the derivative of $K_0(\phi_{SiH_2} r/R_w)$ approaches infinity when r approaches zero. Equation (6C.10) now reduces to:

$$C_{SiH_2} = \frac{r_v^f}{k_v + \frac{2}{\Delta} k_{s,SiH_2}} + \alpha\, I_0(\phi_{SiH_2} \frac{r}{R_w}) \tag{6C.11}$$

Applying the boundary condition at r= R_w, given by equation (6C.3), results in the following expression for α:

$$\alpha = \frac{1}{I_0(\phi_{SiH_2})} \left(C^s_{SiH_2} - \frac{r_v^f}{k_v + \frac{2}{\Delta} k_{s,SiH_2}} \right) \tag{6C.12}$$

Substitution of α into equation (6C.11) gives:

$$C_{SiH_2} = \frac{r_v^f}{k_v + \frac{2}{\Delta} k_{s,SiH_2}} + \left(C_{SiH_2}^a - \frac{r_v^f}{k_v + \frac{2}{\Delta} k_{s,SiH_2}} \right) \frac{I_0(\phi_{SiH_2} \frac{r}{R_w})}{I_0(\phi_{SiH_2})} \tag{6C.13}$$

By defining:

$$C_{SiH_2}^{SSA} = \frac{r_v^f}{k_v + \frac{2}{\Delta} k_{s,SiH_2}} \tag{6C.14}$$

the expression for the silylene concentration finally becomes:

$$C_{SiH_2} = C_{SiH_2}^{SSA} + \left(C_{SiH_2}^a - C_{SiH_2}^{SSA} \right) \frac{I_0(\phi_{SiH_2} \frac{r}{R_w})}{I_0(\phi_{SiH_2})} \tag{6C.15}$$

Concentration profile of disilane

The continuity equation for disilane is given by:

$$- \frac{D_{Si_2H_6,m}}{r} \frac{d}{dr} \left(r \frac{dC_{Si_2H_6}}{dr} \right) = k_v C_{SiH_2} - \frac{2}{\Delta} k_{s,Si_2H_6} C_{Si_2H_6} \tag{6C.16}$$

with the boundary conditions:

$$r = 0 \qquad \frac{dC_{Si_2H_6}}{dr} = 0 \tag{6C.17}$$

$$r = R_w \qquad C_{Si_2H_6} = C_{Si_2H_6}^a \tag{6C.18}$$

Substitution of equation (6C.15) gives:

$$-\frac{D_{Si_2H_6,m}}{r}\frac{d}{dr}\left(r\frac{dC_{Si_2H_6}}{dr}\right)=k_v\left(C_{SiH_2}^{SSA}+(C_{SiH_2}^{a}-C_{SiH_2}^{SSA})\frac{I_0(\phi_{SiH_2}\frac{r}{R_w})}{I_0(\phi_{SiH_2})}\right) \tag{6C.19}$$

$$-\frac{2}{\Delta}k_{s,Si_2H_6}C_{Si_2H_6}$$

In order to integrate the second order differential equation with corresponding boundary conditions, the disilane concentration is rewritten as:

$$C_{Si_2H_6} = \beta\ I_0(\phi_{SiH_2}\frac{r}{R_w}) + f \tag{6C.20}$$

Substitution into equation (6C.19) results in:

$$-\frac{D_{Si_2H_6,m}}{r}\frac{d}{dr}\left(r\frac{d(\beta\ I_0(\phi_{SiH_2}\frac{r}{R_w})+f)}{dr}\right)=k_v\left(C_{SiH_2}^{SSA}+(C_{SiH_2}^{a}-C_{SiH_2}^{SSA})\frac{I_0(\phi_{SiH_2}\frac{r}{R_w})}{I_0(\phi_{SiH_2})}\right) \tag{6C.21}$$

$$-\frac{2}{\Delta}k_{s,Si_2H_6}\beta\ I_0(\phi_{SiH_2}\frac{r}{R_w})-\frac{2}{\Delta}k_{s,Si_2H_6}f$$

Rearranging gives:

$$-\frac{D_{Si_2H_6,m}}{r}\frac{d}{dr}\left(r\frac{df}{dr}\right) - \frac{D_{Si_2H_6,m}}{R_w^2}\beta\ \phi_{SiH_2}^2\ I_0(\phi_{SiH_2}\frac{r}{R_w}) = k_v\ C_{SiH_2}^{SSA} +$$

$$k_v\ (C_{SiH_2}^{a} - C_{SiH_2}^{SSA})\ \frac{I_0(\phi_{SiH_2}\frac{r}{R_w})}{I_0(\phi_{SiH_2})} - \frac{2}{\Delta}\ k_{s,Si_2H_6}\ \beta\ I_0(\phi_{SiH_2}\frac{r}{R_w}) - \frac{2}{\Delta}\ k_{s,Si_2H_6}\ f \tag{6C.22}$$

By defining:

$$\beta = \frac{\dfrac{k_v}{D_{Si_2H_6,m}}\ (C_{SiH_2}^{a} - C_{SiH_2}^{SSA})\ \dfrac{R_w^2}{I_0(\phi_{SiH_2})}}{\dfrac{2\ k_{SiH_2}\ R_w^2}{\Delta\ D_{Si_2H_6,m}} - \phi_{SiH_2}^2} \tag{6C.23}$$

equation (6C.22) reduces to:

$$-\frac{D_{Si_2H_6,m}}{r}\frac{d}{dr}\left(r\frac{df}{dr}\right) = k_v\,C^{SSA}_{SiH_2} - \frac{2}{\Delta}\,k_{s,Si_2H_6}\,f \tag{6C.24}$$

By considering that:

$$f = g + \frac{k_v\,C^{SSA}_{SiH_2}\,\Delta}{2\,k_{s,Si_2H_6}} \tag{6C.25}$$

equation (6C.24) changes in:

$$\frac{1}{r}\frac{d}{dr}\left(r\frac{dg}{dr}\right) = \frac{2\,k_{s,Si_2H_6}}{\Delta\,D_{Si_2H_6,m}}\,g \tag{6C.26}$$

Rearranging and substituting the Thiele modulus:

$$\phi_{Si_2H_6} = R_w\sqrt{\frac{2\,k_{s,Si_2H_6}}{\Delta\,D_{Si_2H_6,m}}} \tag{6C.27}$$

results in:

$$r^2\frac{d^2g}{dr^2} + r\frac{dg}{dr} - \frac{\phi^2_{Si_2H_6}}{R^2_w}\,r^2\,g = 0 \tag{6C.28}$$

The solution to this equation reads (Abramowitz and Stegun, 1970):

$$g = \eta\;I_0(\phi_{Si_2H_6}\frac{r}{R_w}) + \theta\;K_0(\phi_{Si_2H_6}\frac{r}{R_w}) \tag{6C.29}$$

The boundary condition at r= 0, given by equation (6C.17), leads to a value of zero for θ since the derivative of $K_0(\phi_{Si_2H_6}r/R_w)$ approaches infinity when r approaches zero. The expression for the disilane concentration now reduces to:

$$C_{Si_2H_6} = \frac{k_v\,C^{SSA}_{SiH_2}\,\Delta}{2\,k_{s,Si_2H_6}} + \left(\frac{\frac{k_v}{D_{Si_2H_6,m}}\,(C^{s}_{SiH_2} - C^{SSA}_{SiH_2})\,R^2_w}{\phi^2_{Si_2H_6} - \phi^2_{SiH_2}}\right)\frac{I_0(\phi_{SiH_2}\frac{r}{R_w})}{I_0(\phi_{SiH_2})} \tag{6C.30}$$

$$+\;\eta\;I_0(\phi_{Si_2H_6}\frac{r}{R_w})$$

Applying the boundary condition at r= R_w, given by equation (6C.18), results in the following expression for η:

$$\eta = \frac{1}{I_0(\phi_{Si_2H_6})}\left(C^{a}_{Si_2H_6} - \frac{k_v C^{SSA}_{SiH_2}\Delta}{2\,k_{s,Si_2H_6}} - \frac{\dfrac{k_v}{D_{Si_2H_6,m}}\left(C^{a}_{SiH_2} - C^{SSA}_{SiH_2}\right) R_w^2}{\phi^2_{Si_2H_6} - \phi^2_{SiH_2}} \right) \tag{6C.31}$$

Substitution of η into equation (6C.30) finally results in:

$$\begin{aligned} C_{Si_2H_6} = {} & \frac{k_v C^{SSA}_{SiH_2}\Delta}{2\,k_{s,Si_2H_6}} + \left(\frac{\dfrac{k_v}{D_{Si_2H_6,m}}\left(C^{a}_{SiH_2} - C^{SSA}_{SiH_2}\right) R_w^2}{\phi^2_{Si_2H_6} - \phi^2_{SiH_2}} \right) \frac{I_0(\phi_{SiH_2}\frac{r}{R_w})}{I_0(\phi_{SiH_2})} \\ & + \left(C^{a}_{Si_2H_6} - \frac{k_v C^{SSA}_{SiH_2}\Delta}{2\,k_{s,Si_2H_6}} - \frac{\dfrac{k_v}{D_{Si_2H_6,m}}\left(C^{a}_{SiH_2} - C^{SSA}_{SiH_2}\right) R_w^2}{\phi^2_{Si_2H_6} - \phi^2_{SiH_2}} \right) \frac{I_0(\phi_{Si_2H_6}\frac{r}{R_w})}{I_0(\phi_{Si_2H_6})} \end{aligned} \tag{6C.32}$$

7

ADSORPTION OF SILANE, DISILANE AND TRISILANE ON POLYCRYSTALLINE SILICON: A TRANSIENT KINETIC STUDY

7.1. Introduction

In the recent past the adsorption and concomitant surface reaction pathways of the silanes SiH_4, Si_2H_6 and Si_3H_8 have been investigated using techniques such as temperature programmed desorption (TPD) coupled to static secondary ion mass spectrometry (SSIMS) (Gates *et al.*, 1990; Kulkarni *et al.*, 1990a), laser induced thermal desorption (LITD) (Sinniah *et al.*, 1989; Wise *et al.*, 1991), modulated molecular beam scattering (MMBS) (Farnaam and Olander, 1984; Kulkarni *et al.*, 1990b) and reflection high energy electron diffraction (RHEED) (Werner *et al.*, 1994). These studies all have been performed under UHV conditions on well-defined single-crystalline surfaces.

Direct information about adsorption and subsequent surface reactions of silanes on less well-defined silicon surfaces such as amorphous and polycrystalline silicon is scarce. Indirect information mostly is based on LPCVD growth data. Buss *et al.* (1988) studied the adsorption of silane and disilane on polycrystalline silicon using molecular beam scattering (MBS) in the temperature range from 900 K to 1350 K. In order to explain their experimental observations a simple mechanism was proposed, comprising dissociative adsorption of silane and disilane forming surface dihydride species, competing associative desorption of silane and further dehydrogenation of the silicon dihydride species to solid silicon and molecular hydrogen. In this way a reasonable agreement between model and experiment was obtained.

In the present study an alternative method is chosen to investigate adsorption and surface reactions of silanes on polycrystalline silicon. The Temporal Analysis of Products (TAP) technique (Gleaves *et al.*, 1988) is used to provide direct information about the kinetics and the mechanism of the surface steps. Substrate growth rates are not measured; the primary goal is the elucidation of the kinetics of the reactions that produce solid layers from SiH_4, Si_2H_6 and Si_3H_8 on polysilicon substrates. Only one similar TAP study on CVD precursors is reported on in the literature (Svoboda *et al.*, 1992). In the latter the pyrolysis of trimethylantimony and tetramethyltin was investigated. However, in contrast to the present work, no real planar substrates were used for the deposition in the reactor, but supposedly inert quartz granules, implying that the pyrolysis was assumed to occur by gas phase decomposition. In the present study gas phase reactions are excluded as far as possible in order to focus on surface reactions only.

The relatively high reactivity of the used silanes towards adsorption on polysilicon, and even on fully hydrogenated polysilicon, permits a very large temperature regime from room temperature up to about 1000 K to be studied. During the experiments the responses of the silanes are followed. This implies that the quality of the data becomes less reliable in the high temperature regime due to the large consumption of the silanes. Above about 900 K the conversion of the silanes in the reactor approaches 100%. Therefore, the quality of the data at these temperatures becomes dubious, which is in strong contrast with the MMBS measurements of Farnaam and Olander (1984) and Kulkarni *et al.* (1990b). In principle both TAP and MMBS can provide the same information about adsorption and surface reactions. However, in the above mentioned MMBS studies also the product H_2 was followed in time, leading to a higher reliability of the data at higher temperatures as more hydrogen is formed during the period of measurement. At low temperatures, however, very few hydrogen is formed making the interpretation of the experimental results less obvious. This makes the present TAP and the above mentioned MMBS studies complementary.

7.2. Experimental

7.2.1 Apparatus

All experiments were conducted using a Temporal Analysis of Products (TAP) setup which has been described in detail elsewhere (Gleaves *et al.*, 1988). Only the key features relevant to the present work are given here. The principle components of the TAP setup include (i) a gas feed system that supplies reactants to two high-speed pulse valves and a continuous flow valve, (ii) a microreactor, (iii) three interconnected vacuum chambers that house the microreactor valve assembly and the UTI 100C quadrupole mass spectrometer (QMS) detector, and (iv) a Hewlett-Packard Series 360 computer workstation. Mass spectrometry is used to follow outlet responses towards pulses of reactants admitted at the inlet with a submillisecond time resolution. A schematic diagram of the TAP setup is given in Figure 7.1.

The microreactor, valves for introduction of the gas pulses, and a solenoid valve for introduction of a continuous flow of reactant gas are located in the reactor vacuum chamber with vacuum being supplied from a Varian VHS10 oil diffusion pump and a Varian SD700 mechanical pump. Typical background pressures in this chamber are in the range from 10^{-5} to 10^{-4} Pa. The differential chamber is located between the reactor vacuum chamber and the analytical chamber. Vacuum in the differential chamber is provided by a Varian VHS6 oil diffusion pump with a liquid nitrogen trap, with secondary vacuum being supplied from a Varian SD700 mechanical pump. Vacuum in the analytical chamber, containing the ionisation head of the UTI 100C quadrupole mass spectrometer, is provided by a Balzers TPU450H turbomolecular pump together with a Balzers MD4TC diaphragm pump. The pressures in the differential and analytical chambers are usually 10^{-6} and 10^{-7} Pa respectively.

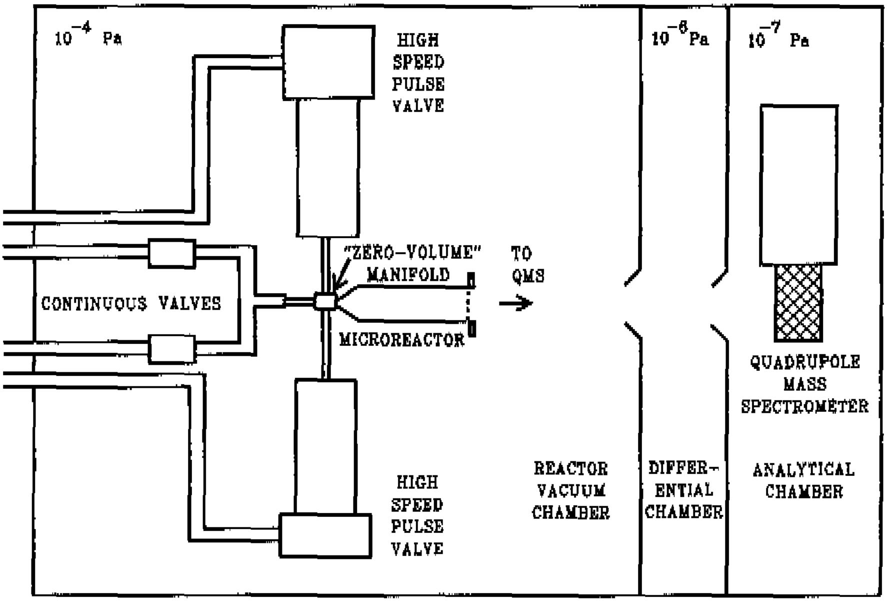

Figure 7.1: Schematic representation of TAP setup.

7.2.2 Microreactor

The microreactor developed for the present work is shown in Figure 7.2. It can be considered as a batchwise operated reactor. Indeed, the reactants are admitted in typically 200 μs which can be considered instantaneously compared to a typical residence time of 20 ms. The square inconel microreactor with an inside diameter of 4.34 mm and an overall length of 47.2 mm is charged with seven Si(100) wafers, placed at equal distances of 278 μm from each other. In this way Knudsen diffusion is ensured for gas pulse intensities up to 3 10^{15} molecules per pulse. The microreactor parameters are given in Table 7.1. The reactor temperature is monitored using a K-type thermocouple located half-way the wafers. For PID temperature control a second K-type thermocouple is positioned in the reactor wall.

As a consequence of the low pressure inside the reactor vacuum chamber significant axial temperature gradients exist over the wafers, see Figure 7.3. Moreover, pulse injection results in total pressure non-uniformity in axial direction. Figure 7.4 illustrates the evolution of a typical pressure profile following upon pulse injection. At any time the pressure is the highest at the entrance of the microreactor and decreases to zero at the outlet of the microreactor where vacuum conditions prevail. Except at the entrance of the microreactor, where the pressure decreases monotonically with time, a maximum in pressure arises as a function of time at each axial position.

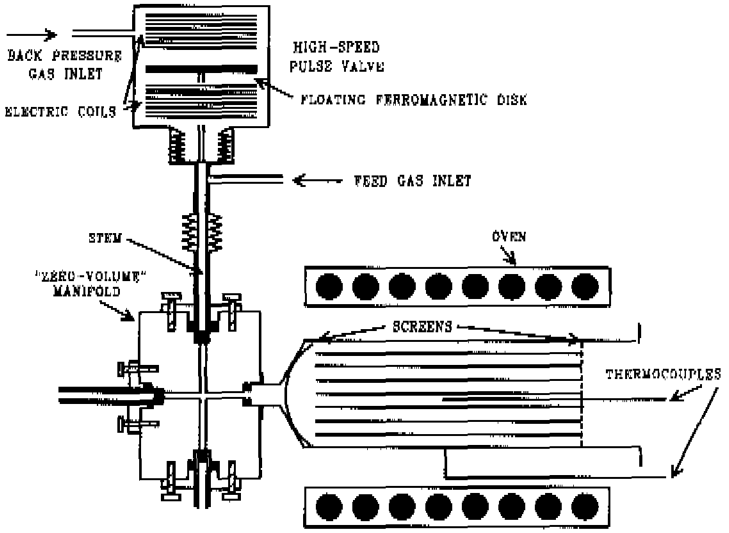

Figure 7.2: Schematic representation showing TAP microreactor, furnace, manifold and one high-speed pulse valve.

Table 7.1: *Values of the microreactor parameters*

stack porosity	ε	$0.513\ m_g^3\ m_r^{-3}$
specific surface area of stack	a_v	$3.994\ 10^3\ m_s^2\ m_r^{-3}$
stack length	L	$3.0\ 10^{-2}\ m_r$
distance between wafers in stack	h	$278\ 10^{-6}\ m_r^2\ m_g^{-1}$
cross sectional area of stack	A_s	$1.88\ 10^{-5}\ m_r^2$
adsorption site density	L_t	$1.13\ 10^{-5}\ mol\ m_s^{-2}$

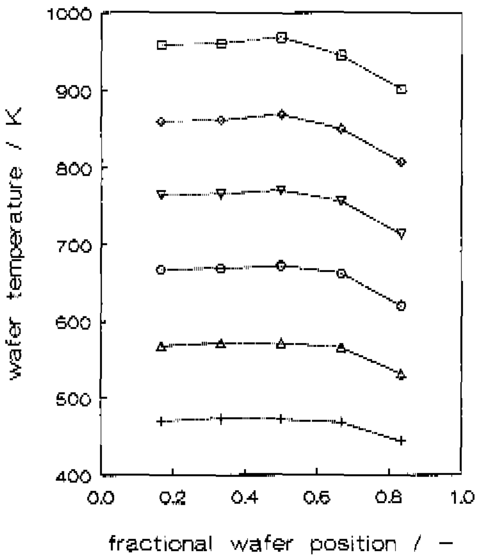

Figure 7.3: *Measured temperature profile in microreactor versus the fractional wafer position at the reactor wall temperatures: □ T= 973 K, ◊ T= 873 K, ▿ T= 773 K, o T= 673 K, ▵ T= 573 K, + T= 473 K.*

7.2.3 Materials

Argon (99.999%, Hoekloos), a mixture of helium, neon, argon, krypton and xenon (20% each, Air Products), silane (99.999%, Air Products), disilane (99.99%, Air Products), trisilane (99.28%, Solkatronic), hydrogen (99.999%, Hoekloos), and deuterium (99.8%, Hoekloos) are used. Pure trisilane and binary gas mixtures of silane/disilane and argon are used as feed gases for the transient experiments. Argon serves as reference component for determination of the pulse size and calculation of the effective Knudsen diffusion coefficient of the other reactant gas. Deuterium is admitted to monitor deuterated desorption products from the surface. Hydrogen is used for pretreatment of the deposition surface.

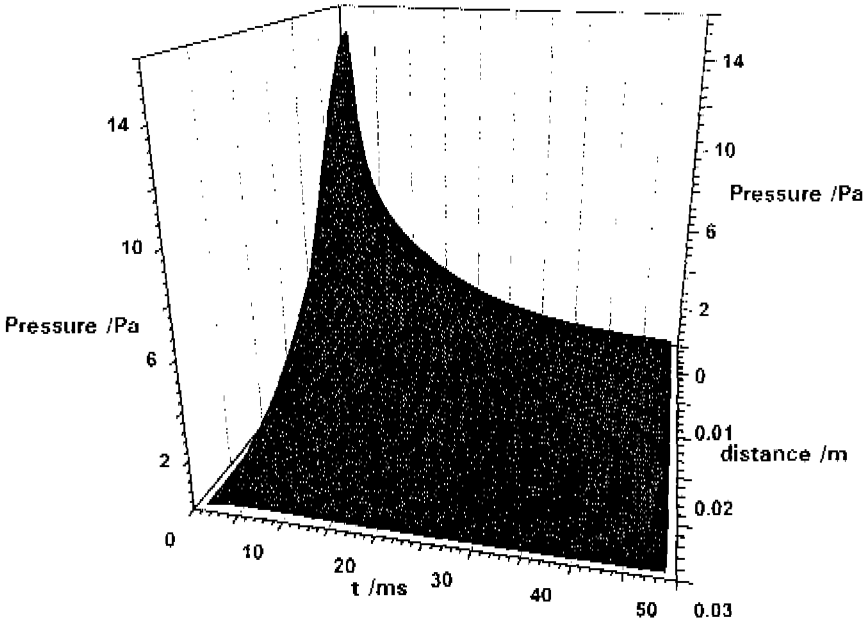

Figure 7.4: Calculated pressure profile in microreactor as a function of time and axial coordinate after the introduction of an argon pulse of 2 10^{14} molecules at $t = 0$ s at the entrance of the wafer stack of length 30 mm with a distance between the wafers of 278 μm at 462 K.

Double-side polished (100) n-type silicon wafers with a resistivity of ~ 0.015 Ω cm and an average thickness of 302 μm are cleaved into small rectangular slices with dimensions 4 and 30 mm and placed inside the microreactor. Prior to each series of experiments the slices and reactor walls are purged with hydrogen at 1100 K and coated with approximately 1000 monolayers of undoped polycrystalline silicon at 900 K. Possible effects of a thin native oxide layer, present in spite of the hydrogen pretreatment, are eliminated during the initial stages of this deposition run.

The adsorption capacity, i.e. the maximum number of molecules that can adsorb on the wafers and reactor walls, equals about 1.5 10^{16}.

7.2.4 Procedures

Types of experiments

Experiments are conducted using both the scan and pulsed modes of operation, reported in detail elsewhere (Gleaves *et al.*, 1988; Huinink, 1995).

In a typical scan experiment a continuous flow of a reactant gas or mixture is introduced to the microreactor, and a user-specified mass spectrum is scanned. Scan experiments are used for determination of the fragmentation patterns of the pure reactant gases as well as for tracing and identification of important reaction products formed in the microreactor.

In a typical pulsed mode experiment the pulse valve driver and reactant pressure are adjusted to produce the desired gas pulse intensity. The QMS is then set to an appropriate amplifier range and mass center for the AMU value to be monitored. Pulse, multipulse and alternating pulse experiments can be distinguished.

During a pulse experiment the raw output signal from the QMS is sampled at a minimum time increment of 10 µs over a minimum sampling period of 0.1 s to produce a maximum of 10000 points per pulse. Provided the pulse shape does not change from pulse to pulse, subsequent pulses, admitted to the microreactor at a user-specified time interval called the repetition time, are signal averaged to improve the signal-to-noise ratio. In most cases, at least ten pulses are needed to obtain a stable response signal as required for the pulse averaging.

During a multipulse experiment a specified number of pulses is given during a specified time interval. No signal averaging is applied in order to visualize the intensity change during the experiment, for instance because of a changing condition of the surface.

During an alternating pulse experiment reactants are introduced in an alternating sequence using the two high-speed pulse valves at a specified time-interval. The data collection window for the QMS is set in a way that both pulses are recorded in the same output response. The sequence is repeated to improve the signal-to-noise ratio.

Silane, disilane and trisilane have key fragments at AMU 30, AMU 60 and AMU 85. The main peak of silane occurs at AMU 30, while those of disilane and trisilane coincide at AMU 60. During the pulsed mode experiments, silane is monitored at AMU 30, disilane at AMU 30 and AMU 60, and trisilane at AMU 30, AMU 60 and AMU 85, whereas molecular hydrogen and argon are followed at AMU 2 and AMU 40, respectively. Due to the low pumping efficiency for hydrogen, quantitative analysis of this surface generated product is not considered accurate enough.

Calibration factor determination

For a quantitative interpretation of the pulse responses, calibration is required with respect to the number of molecules in a pulse. An absolute calibration factor relates the peak surface area to the amount of molecules leaving the reactor per pulse. Determination of the calibration factor for argon is carried out by allowing a continuous flow of argon from a vessel with known volume, V, through the microreactor during a specific time, Δt, while monitoring the constant QMS signal, I_{QMS}. The molar flow rate of argon is calculated from the pressure decrease of argon in the vessel, Δp_{Ar}, the vessel volume and the release time. Applying the ideal gas law, the absolute calibration factor for argon, C_{Ar}, can be calculated according to:

$$C_{Ar} = \frac{\Delta p_{Ar} V}{R T \Delta t I_{QMS}} \tag{7.1}$$

with C_{Ar} in mol C^{-1} and I_{QMS} in C s^{-1}. The absolute calibration factors for silane and disilane are obtained from silane/argon and disilane/argon mixtures of known composition. With these factors it now is possible to convert the QMS signals into flow rates in moles per second.

Regression analysis

TAP responses can be calculated by integrating the appropriate continuity equations analytically or numerically (vide infra). In this work the numerical integration is used during the estimation of parameters with a single-response regression routine (Marquardt, 1963), see also paragraph 4.3.3. The regression consists in obtaining maximum likelihood estimates of the parameters such as effective Knudsen diffusion coefficients and reaction rate coefficients by application of the least square criterion to the observed and calculated molar flow rates at the outlet of the microreactor. The used objective function is based upon the assumption that experimental errors are normally distributed with zero mean. The significance of the global regression is expressed by means of the so-called F-ratio which is based on the ratio of the mean regression sum of squares to the mean residual sum of squares (Draper and Smith, 1966). The significance of the parameter estimates is tested by means of their approximate t-values. These approximate t-values are used to determine the 95%-confidence intervals reported in this work.

For trisilane no good calibration of the pulse intensity could be obtained as pure trisilane was used. So in this case the total amount of sample gas, N_p, is treated as an extra parameter and estimated with the above parameter estimation method. It should be noted that, at least for linear processes, the pulse intensity is not important in the kinetic parameter estimation. The highest binary correlation coefficient between estimated pulse size and other parameters used in the modelling of the trisilane responses amounts to 0.91.

In addition, it is necessary to estimate a delay time t_0 for all experiments, corresponding to the time interval between the triggering of the valve actuator and the opening of the pulse valve. Included in it is the mean time delay needed for the molecules to travel from the reactor outlet to the quadrupole mass spectrometer. For all experiments a delay time of about 1.2 ms is found, which is in agreement with the values observed experimentally.

7.3. Qualitative results

7.3.1 Adsorption of silane

Pulse experiments with a gas mixture of 20% argon and 80% silane were performed in the temperature range from 300 to 1000 K with pulse intensities between $1\ 10^{15}$ and $1\ 10^{16}$ molecules per pulse, i.e. with pulse sizes up to roughly the adsorption capacity of the microreactor.

In the temperature region up to 820 K a rather low and steady conversion of silane of about 16% is observed. Above this temperature the conversion rises sharply indicating a shift in activation energy and/or adsorption mechanism.

Analogue scan experiments show no evidence for gaseous products formed during the chemisorption except for hydrogen. In addition, alternating pulse experiments in which the surface is pretreated with deuterium prior to the admittance of silane do not show formation of deuterated silanes. This demonstrates that silane adsorption is irreversible and that silicon hydride intermediates formed at the surface in the subsequent decomposition reactions do not desorb either.

Multipulse experiments in the temperature region below 820 K show non-changing response shapes for over 200 silane pulses, which is indicative for an unaltered adsorption surface during the experiment. In the high temperature region multipulse experiments are rather difficult to reproduce, whereas signal heights are increasing steadily during the multipulse sequence. Up to 60 pulses are needed to obtain a steady signal of the silane response. The conversion of silane increases considerably as well in this temperature region. A more quantitative discussion of silane adsorption at high temperatures will be given in paragraph 7.4.4.

7.3.2 Adsorption of higher silanes

Trisilane

Pulse experiments with pure trisilane in the temperature region up to 710 K show a rather low conversion of trisilane, increasing from about 18% at 300 K to almost 35% at 710 K, which is indicative for a slightly activated chemisorption reaction of trisilane in this region. Figure 7.5 shows the normalized responses of AMU 30, AMU 60 and AMU 85 measured during a pulse experiment performed at 648 K. The fact that all responses coincide points out that formation of silane and disilane does not occur. Multipulse experiments with pure trisilane performed in the same temperature region reveal equal response shapes over more than 100 pulses, indicative for a non-changing adsorption surface. Moreover, deuterium/trisilane alternating pulse experiments in which the surface is pretreated with deuterium prior to the admittance of trisilane show no formation of deuterated trisilane or of deuterated silicon containing products. This indicates that trisilane adsorption is irreversible and that possible silicon hydride species formed at the surface in subsequent decomposition reactions do not desorb either.

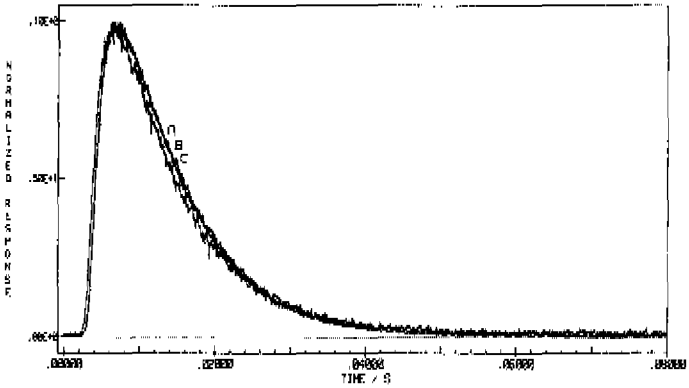

Figure 7.5: Normalized responses of AMU 85 (A), AMU 60 (B) and AMU 30 (C) during a pulse experiment with pure trisilane at 648 K.

Above 710 K a second chemisorption reaction of trisilane is observed, leading to considerably higher conversions of trisilane. Figure 7.6 again shows the normalized responses of AMU 30, AMU 60 and AMU 85, but now for a pulse experiment with pure trisilane performed at 846 K. The abundance of the AMU 30 response compared to the coinciding AMU 60 and AMU 85 responses provides direct evidence for the presence of silane formation and the absence of disilane formation. The maximum of the silane outlet molar flow rate occurs at approximately 1 10^{-2} s and the maximum of the trisilane outlet molar flow rate at 5 10^{-3} s. The question now arises if silane is formed through heterogeneous or through homogeneous decomposition of trisilane. Homogeneous decomposition of trisilane into silane and silylsilylene is possible on the time scale of a typical pulse experiment, 10^{-2} s, as may be calculated using the Rice-Ramsperger-Kassel-Marcus (RRKM) theory, see paragraph 5.3. The corresponding unimolecular reaction rate coefficient, calculated from the values listed in Table 5.4, amounts to 55.5 s^{-1} at 850 K and 100 Pa, giving rise to a characteristic reaction time of 1.8 10^{-2} s, which indeed is comparable to the time scale of a pulse experiment.

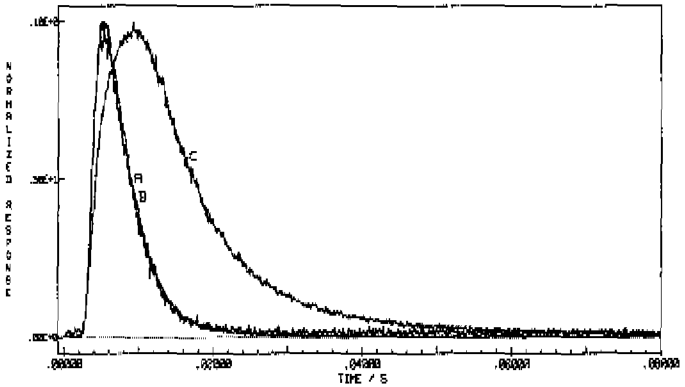

Figure 7.6: *Normalized responses of AMU 85 (A), AMU 60 (B) and AMU 30 (C) during a pulse experiment with pure trisilane at 846 K.*

Evidence for the heterogeneous decomposition of trisilane into silane, however, is obtained from Figure 7.7 showing the overall AMU 30 response, originating from both trisilane and formed silane, as a function of pulse intensity at 797 K. The responses A to D clearly consist of two peaks, one positioned at roughly 4 10^{-3} s and corresponding to the response of trisilane, and another located around 1.3 10^{-2} s reflecting the response of the formed silane. With decreasing pulse intensity going from response A to D and, hence, with decreasing total pressure the relative importance of the silane response increases. This effect is opposite to that expected on the basis of the RRKM theory, meaning that the silane leaving the microreactor is formed at the surface during the chemisorption of trisilane.

Figure 7.7 in addition shows that the amount of formed silane, reflected by the surface area of the corresponding response, is independent of trisilane pulse intensity for responses A to D. This implies that the number of sites available for trisilane adsorption is independent of the number of admitted trisilane molecules. The response denoted by E clearly behaves different. Here, the number of admitted trisilane molecules probably is smaller than the number of available adsorption sites. During this pulse practically all admitted trisilane is converted, as indicated by the indistinguishability of the corresponding AMU 60 and AMU 85 responses from the noise signal. The overall AMU 30 response denoted by E therefore mainly originates from silane.

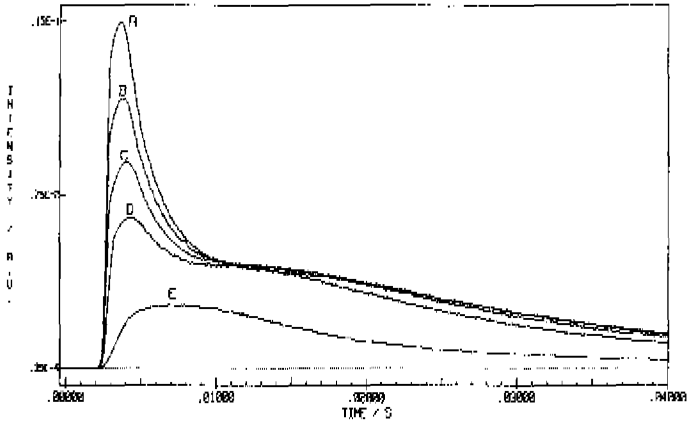

Figure 7.7: *AMU 30 response, originating from both trisilane and formed silane, as a function of pulse intensity during pulse experiments with pure trisilane at 797 K. Pulse intensity decreases from A to E.*

Figures 7.8 and 7.9 show the trisilane AMU 60 and the overall AMU 30 responses as a function of the temperature. The trisilane AMU 60 response decreases with increasing temperature from 772 K (A) to 869 K (D). At 944 K all trisilane is converted. The corresponding response, not shown, completely coincides with the time axis. The faster the adsorption with increasing temperature, the shorter the mean residence time of the trisilane molecules. This is caused by the greater adsorption probability of the trisilane molecules with a larger residence time, leading to less tailing. At 772 K normalization of the trisilane AMU 60 and the overall AMU 30 responses, similar to the case depicted in Figure 7.6, demonstrates the presence of a small amount of formed silane. An increase in temperature from 772 K to 819 K shows a decrease in the trisilane AMU 60 response with a concomitant increase in the overall AMU 30 response, indicative for more silane formation at higher temperature. By increasing the temperature from 819 K to 846 K more silane is formed. Then going from 846 K to 944 K the overall AMU 30 response considerably reduces in height and exhibits a strong narrowing. This points to adsorption of the silane formed upon the adsorption of trisilane. At 944 K the overall AMU 30 response fully originates from silane as all trisilane has been converted at this temperature.

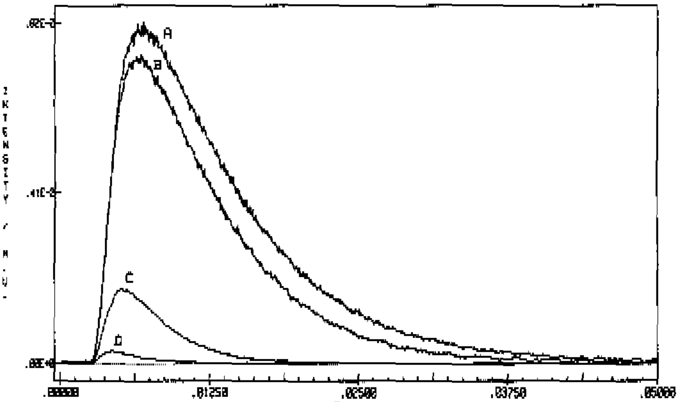

Figure 7.8: *Trisilane AMU 60 response as a function of temperature during pulse experiments with pure trisilane at fixed pulse intensity. (A) T= 772 K, (B) T= 819 K, (C) T= 846 K, (D) T= 869 K.*

In the literature it is generally agreed that the adsorption processes of silane and trisilane are not or only slightly activated. Reported activation energies for silane adsorption range between 0 and 17 kJ mol^{-1} (Gates *et al.*, 1989; Gates and Kulkarni, 1991; Buss *et al.*, 1988), whereas Gates (1988) obtained a negative activation energy for trisilane adsorption of -21 kJ mol^{-1}. The strong effect of temperature on the trisilane and formed silane responses, outlined above, most probably can be attributed to a strongly activated surface process responsible for the partial regeneration of the hydrogenated silicon surface in the time intervals between subsequent pulses. An increase in temperature from 772 K to 819 K consequently results in an increase in the number of vacant surface sites at the beginning of the pulses and hence in an increase in the number of converted trisilane and formed silane molecules. At these temperatures the number of vacant surface sites probably is too small to additionally permit adsorption of the formed silane. Around 846 K the onset of silane adsorption can be detected, considering the narrowing of the overall AMU 30 response denoted by (C). A further increase in temperature towards 944 K results in an even faster regeneration of vacant surface sites in the time intervals between the pulses, leading to an enhanced adsorption of silane and hence to a decrease in the number of silane molecules reaching the outlet of the microreactor. Note that almost all of the admitted trisilane molecules are converted at these high temperatures.

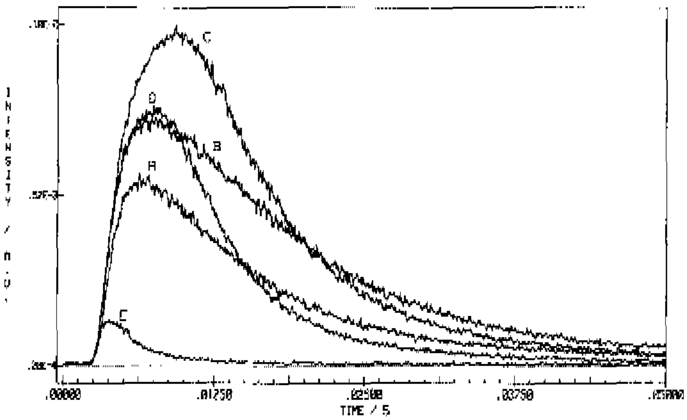

Figure 7.9: AMU 30 response, originating from both trisilane and formed silane, as a function of temperature during pulse experiments with pure trisilane at fixed pulse intensity. (A) T= 772 K, (B) T= 819 K, (C) T= 846 K, (D) T= 869 K, (E) T= 944 K.

Disilane

Pulse experiments with a gas mixture of 20% argon and 80% disilane in the temperature range between 300 K and 900 K using pulse intensities from 1 10^{15} to 1 10^{16} molecules per pulse revealed similar results to those reported for trisilane in the previous section.

In the temperature region up to 640 K a rather constant disilane conversion of roughly 25% can be derived from an overall silicon balance, indicating that the chemisorption of disilane is only slightly activated. As in the case of trisilane, no silane formation is observed in this low temperature region. Deuterium/disilane alternating pulse experiments in which the surface is pretreated with deuterium prior to the admittance of disilane do not show any significant responses of deuterated silicon hydride species, implying irreversible adsorption of disilane and the absence of desorbing silicon hydride intermediates formed at the surface in subsequent decomposition reactions. Moreover, multipulse experiments reveal equal response shapes over more than 100 pulses in the same temperature region, indicative for a non-changing adsorption surface.

Above 640 K another chemisorption reaction of disilane is observed, producing silane in the gas phase. The considerably higher disilane conversion in this temperature region points to a shift in activation energy to much higher values. The question again arises if silane is formed through heterogeneous or through homogeneous decomposition of disilane. With the RRKM values listed in Table 5.4 a unimolecular reaction rate coefficient equal to 13.4 s^{-1} can be calculated for gas phase decomposition of disilane into silane and silylene at 100 Pa and 850 K. Comparison of the resulting characteristic reaction time, 7.5 10^{-2} s, with the time scale of a pulse experiment, 10^{-2} s, does not allow to exclude homogeneous silane formation. However, evidence for the heterogeneous formation of silane is obtained from Figure 7.10, showing the overall AMU 30 response, originating from both disilane and formed silane, as a function of pulse intensity at 821 K. With decreasing pulse intensity going from response A to E the maximum of the peak shifts to larger time values. This indicates that the overall AMU 30 response is mainly caused by the desorption of silane and not by the fragmentation of disilane in the quadrupole mass spectrometer. In the latter case the peak maximum of the presented AMU 30 response would shift in the opposite direction, in exactly the same way as the response completely representative of the non-converted disilane. The formation of larger amounts of silane at lower pulse intensities, i.e. at lower total pressures, eliminates the possibility of homogeneous silane formation, since gas phase decomposition of disilane will be faster at higher pressures, see paragraph 5.3.

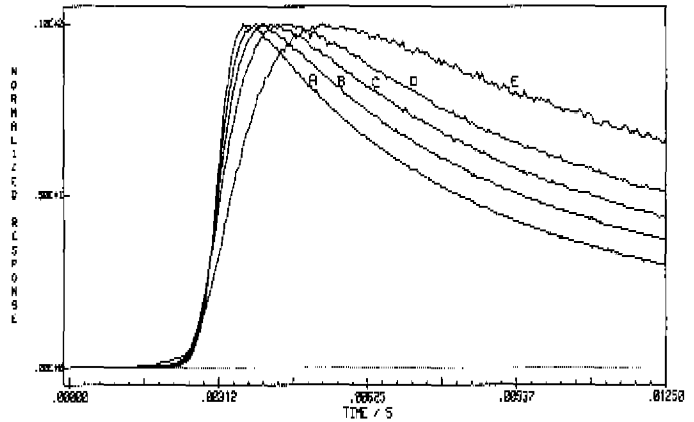

__Figure 7.10:__ Normalized AMU 30 response, originating from both disilane and formed silane, as a function of pulse intensity during pulse experiments with a mixture of 20% Ar and 80% disilane at 821 K. Pulse intensity decreases from A to E.

Similar temperature effects as those shown in Figures 7.8 and 7.9 on the responses representative of trisilane and formed silane are observed in the disilane/argon pulse experiments performed at various temperatures above 640 K. Upon increasing the temperature the response representative of formed silane first increases, then reaches its maximum value at about 650 K, and finally decreases.

7.4. Quantitative results and discussion

7.4.1 Experiments with inert gas

An inert isothermal gas mixture can be transported through the microreactor by various mechanisms such as viscous flow, molecular diffusion and Knudsen diffusion. At high pressures, i.e. at pulse intensities above 2 10^{17} molecules per pulse, viscous flow will dominate, whereas at low pressures, i.e. at pulse intensities below 5 10^{15} molecules per pulse, diffusional transport will be predominant (Huinink, 1995). Molecular diffusion in gas mixtures can be neglected as at low pressures molecular diffusion coefficients are much larger than Knudsen diffusion coefficients. Note that both types of diffusional resistance must be added (Mason and Malinauskas, 1983). A pulsed mode experiment involves total pressures of many orders of magnitude: relatively high pressures at the reactor inlet in the beginning of the pulse and low pressures at the reactor outlet, see Figure 7.4. To ensure that the gas transport is fully determined by Knudsen diffusion, the effective diffusion coefficient has to be determined as a function of pulse intensity. In case of Knudsen diffusion, this coefficient has to be a constant for constant temperature, showing a square root dependence on temperature and an inverse square root dependence on the molar mass of the molecule under consideration.

In case diffusion is the controlling mechanism of gas transport and no reaction occurs, the continuity equation under isothermal conditions for a gas phase component A in the microreactor is given by:

$$\varepsilon \frac{\partial C_A}{\partial t} = D_{eff,A} \frac{\partial^2 C_A}{\partial x^2} \tag{7.2}$$

where C_A is the gas phase concentration of component A (mol m_g^{-3}); ε the porosity of the stack in the microreactor ($m_g^3\ m_r^{-3}$); $D_{eff,A}$ the effective diffusion coefficient of A ($m_g^3\ m_r^{-1}\ s^{-1}$); x the axial coordinate in the microreactor (m_r). Equation (7.2) has to be solved using the following initial and boundary conditions (Huinink, 1995):

$$t = t_0 \ \wedge \ 0 \le x \le L \qquad C_A = \delta_x \frac{N_{p,A}}{\varepsilon A_s} \tag{7.3}$$

$$t \ge t_0 \ \wedge \ x = 0 \qquad \frac{\partial C_A}{\partial x} = 0 \tag{7.4}$$

$$t \ge t_0 \ \wedge \ x = L \qquad C_A = 0 \tag{7.5}$$

Here, $N_{p,A}$ is the inlet pulse size of component A (mol); A_s the cross sectional area of the microreactor (m_r^2); L the stack length (m_r). The initial condition, given by equation (7.3), specifies that the initial gas phase concentration profile in the microreactor is a delta-function, which is a good approximation as long as the time scale on which the inlet pulse is admitted is much smaller than the time scale of the experiment. Other initial conditions, however, are conceivable (Zou *et al.*, 1994), but the above initial condition is the easiest to implement both in the analytical and in the numerical solution of the continuity equation. Moreover, calculations of molar flow rates using various initial conditions reveal only minor differences between them, mostly within experimental error. The first boundary condition, given by equation (7.4), implies the absence of flux at the reactor inlet when the pulse valve is closed. The second boundary condition, given by equation (7.5), specifies that the reactor outlet is kept at vacuum conditions. The molar flow rate of component A, F_A, at the outlet of the microreactor (mol s^{-1}), i.e. at x = L, is given by:

$$F_A \big|_{x=L} = -D_{eff,A} \, A_s \, \frac{\partial C_A}{\partial x} \big|_{x=L} \tag{7.6}$$

The set of equations given by (7.2) to (7.6) can be integrated analytically leading to a series expansion of the molar flow rate of A at the reactor outlet as a function of time (Huinink, 1995), see Appendix 7A. Alternatively it can be solved numerically using the NAG Fortran Library routine D03PGF (NAG, 1991). This routine integrates a set of nonlinear parabolic differential equations in one space variable by the method of lines and Gear's method. The partial differential equations are approximated by a set of ordinary differential equations obtained by replacing the space derivatives by finite differences. This set is then integrated forwards in time using the method of Gear. The approximation applies a uniform user-specified grid in the space direction, whereas the time intervals are chosen by the routine. The routine does not allow a delta-function for the initial gas phase concentration profile such as given in equation (7.3). Therefore, the initial gas phase concentrations at the first and second discretized space points are set to the value C_A^0, given by:

$$C_A^0 = \frac{2\, N_{p,A}}{3\, \varepsilon\, A_s\, \Delta x} \tag{7.7}$$

with Δx denoting the distance between two successive grid points (m_r). In this way the boundary condition, given by equation (7.4), is satisfied at $t = t_0$. The gas phase concentrations at the third and following grid points are taken zero. A comparison between analytically and numerically calculated molar flow rates for various sets of parameters showed that at least 100 spacial grid points need to be applied to obtain an agreement within 0.25% between them.

Pulse experiments with an inert gas mixture of helium, neon, argon, krypton and xenon were performed using total pulse intensities from 5 10^{14} up to 1 10^{16} molecules per pulse. Knudsen type diffusion was experimentally confirmed by reducing the inlet gas pulse intensity until for each component the normalized output response remains the same. This was found to occur at an intensity of approximately 3 10^{15} molecules per pulse. The numerical model was used for the estimation of effective diffusion coefficients as discussed in paragraph 7.2.4. An initial guess of the parameter is given by $W_{1/2}$, the width of the response curve at half-height (s), which can be deduced from the analytical solution, see Appendix 7A:

$$W_{1/2} = 0.4227\, \frac{\varepsilon\, L^2}{D_{eff,A}} \tag{7.8}$$

Figure 7.11 presents the results from the experiments in which the five inert inlet gases are pulsed through the wafer-stacked microreactor at a total pulse intensity of about 10^{15} molecules per pulse and 312 K. The estimated effective diffusion coefficients are shown versus the inverse square root of the molar mass. A linear dependence as expected for Knudsen diffusion is observed. Similar experiments in which argon is pulsed while the reactor temperature is varied between 313 K and 841 K show the expected square root dependence of the effective diffusion coefficient on the temperature, see Figure 7.12. Figure 7.13 shows a typical experimental argon response as compared to one calculated with model equations (7.2) to (7.6) for pulse sizes below 3 10^{15} molecules. An almost perfect agreement is obtained between experimental and calculated curve using only two parameters, i.e. the effective diffusion coefficient and the delay time, t_0. For all experiments a delay time of about 1.2 ms is found.

The above results indicate that at sufficiently low pulse intensities, thus at pulse sizes below 3 10^{15} molecules, Knudsen diffusion is the dominant mechanism of gas transport in the microreactor. In principle the effective Knudsen diffusion coefficient can be calculated from:

$$D^{K}_{eff,A} = \frac{\varepsilon}{\tau_s} D^{K}_{A} \tag{7.9}$$

with ε and τ_s the porosity and tortuosity of the wafer packed microreactor, and D^K_A the Knudsen diffusion coefficient given by:

$$D^{K}_{A} = \frac{2}{3} h \sqrt{\frac{8RT}{\pi M_A}} \, f_1(w/h) \, f_2(h/L) \tag{7.10}$$

Here, h is the distance between two successive wafers in the stack; w the width of the wafers; L the length of the wafers. R, T and M_A have their usual meaning. The function $f_1(w/h)$ corrects for the effect of noncircular cross section as given by Eldridge and Brown (1976). The function $f_2(h/L)$ corrects for the finite length of the microreactor as discussed by Clausing (1929).

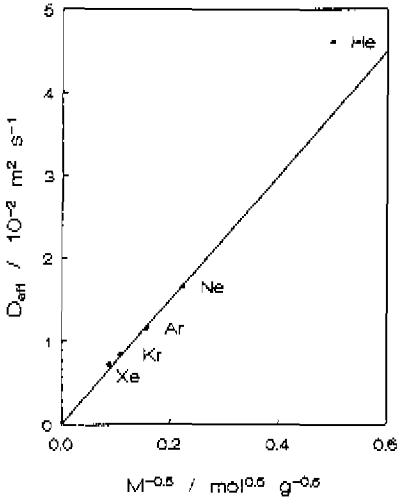

Figure 7.11: Estimated effective diffusion coefficients of He, Ne, Ar, Kr and Xe versus the inverse square root of their molar mass at 312 K.

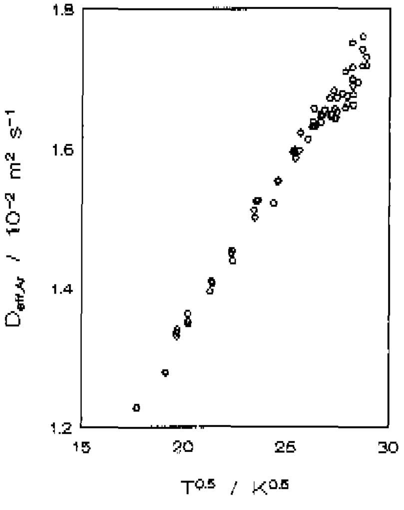

Figure 7.12: Estimated effective diffusion coefficient of Ar versus the square root of the reactor temperature.

Introduction of both corrections leads to calculated values of the effective Knudsen diffusion coefficient for argon which only are equal to the measured values if τ_s is set at about 4. Thus the calculated values of the effective Knudsen diffusion coefficient are much larger than those deduced from the responses as for the wafer-packed microreactor a tortuosity τ_s equal to 1 is expected. Coronell and Jensen (1992) simulated transition regime flow in a horizontal LPCVD reactor by means of a Monte Carlo method and obtained Knudsen diffusion coefficients a factor of 9 lower than expected from equation (7.10) without the correction function $f_2(h/L)$. It was argued that the notion of a Knudsen diffusion coefficient in the interwafer geometry is ill-defined since the diffusing molecules are not completely confined by the wafers as is the case for the situation of axial diffusion through an infinite tube. Clausing stated that the function f_2, deduced for a finite cylindrical tube only, is a very crude approximation. A better understanding of Knudsen flow in finite length, non cylindrical tubes should be a subject of further study. For the present purposes, however, it is sufficient to have shown the linear relation between the effective diffusion coefficients in the CVD microreactor and the inverse square root of the molar mass of the used gases and the square root of the temperature. In this way it is possible to calculate effective Knudsen diffusion coefficients for all gases in a mixture at an arbitrary temperature knowing only one at a given temperature.

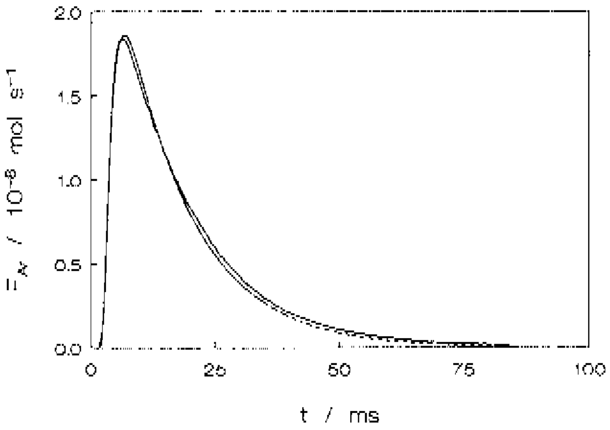

Figure 7.13: *Argon molar flow rate at outlet of micro-reactor versus the time at 462 K. Full line: experimental. Dashed line: calculated using equations (7.2) to (7.6) and the estimated values* $D_{eff,Ar} = 1.37\ 10^{-2}\ m_g^3\ m_r^{-1}\ s^{-1}$ *and* $t_0 = 1.07\ 10^{-3}$ *s.* $N_{p,Ar} = 3.41\ 10^{-10}$ *mol.*

7.4.2 Accessible (pseudo-)first order kinetic parameters

In this paragraph the window of (pseudo-)first order kinetic parameters will be discussed that is accessible with the setup used in the present study. Reaction rate coefficients measurable with TAP have a lower and a higher bound. These bounds arise because the measured outlet signal has to show a significant deviation from both the noise signal and from the outlet signal in case no reaction occurs. Consider a (pseudo-)first order reaction:

$$A \xrightarrow{k} Products \tag{7.11}$$

which could be an chemisorption reaction where the fraction of vacant sites for adsorption is assumed to be constant, or a gas phase reaction. The corresponding continuity equation for reactant A, taking Knudsen diffusion as the predominant mode of transport, is given by:

$$\varepsilon \frac{\partial C_A}{\partial t} = D^K_{eff,A} \frac{\partial^2 C_A}{\partial x^2} - r_A \tag{7.12}$$

with:

$$r_A = a_v L_l k_a C_A \tag{7.13}$$

in case of an adsorption reaction, or:

$$r_A = \varepsilon k_g C_A \tag{7.14}$$

in case of a gas phase reaction. Here, k_a (m_g^3 mol^{-1} s^{-1}) and k_g (s^{-1}) are the (pseudo-) first order reaction rate coefficients for adsorption and gas phase reaction, respectively. The corresponding initial and boundary conditions are again given by equations (7.3) to (7.5). In dimensionless form equation (7.12) reads:

$$\frac{\partial C_A}{\partial \tau} = \frac{\partial^2 C_A}{\partial z^2} - Da_l C_A \tag{7.15}$$

where the dimensionless time τ and the dimensionless place coordinate z are given by:

$$\tau = \frac{D^K_{eff,A} t}{\varepsilon L^2} \tag{7.16}$$

$$z = \frac{x}{L} \tag{7.17}$$

and the Damköhler-I number is defined as:

$$Da_I = \frac{r_A L^2}{D^K_{eff,A} C_A} \tag{7.18}$$

corresponding to the ratio of the time scale of transport through the microreactor to the time scale of reaction. Equation (7.15) can be solved analytically using the Laplace Transform method (Huinink, 1995). It is easily verified, see Appendix 7A, that the ratio of the signal surface areas with and without reaction, Q, is given by:

$$Q = \frac{1}{\cosh\sqrt{Da_I}} \tag{7.19}$$

The conversion in the reactor obviously is equal to 1-Q. Assuming that a response surface area of approximately 1% of the inlet surface area is significantly above the noise level and therefore readily detectable, substitution of 1% in equation (7.19) and solving for Da_I yields a value of 28 for the upper bound of the Damköhler-I number. Under the assumption that a deviation of 5% of the width at half height of the response signal $W_{1/2}$ is significant, a Damköhler-I number of 0.19 is obtained for the lower bound. See Appendix 7A for further details. Both criteria can be cast into:

$$28 \geq Da_I \geq 0.19 \tag{7.20}$$

This equation states that the time scale of adsorption here defined by:

$$\tau_{ads} \quad \frac{\varepsilon}{a_v \, L_I \, k_a} \tag{7.21}$$

or the time scale of gas phase reaction:

$$\tau_{gas} = \frac{1}{k_g} \tag{7.22}$$

should be comparable to the time scale of transport through the microreactor within a factor of about 10 to both sides. This statement not only is true for chemisorption or gas phase reaction, but in fact for every reaction in the wafer-packed microreactor that has some influence on the measured responses. A reaction with a characteristic reaction time beyond the range defined by equation (7.20) will either have no significant effect on the response shape, or will be instantaneous on the time scale of the experiment.

In terms of the mean residence time of an inert in the microreactor, τ_{res}, and the time scale of a (pseudo-)first order reaction, τ_{reac}, the criterion given by equation (7.20) can be restated as:

$$10.5\ \tau_{res} \geq \tau_{reac} \geq 0.07\ \tau_{res} \tag{7.23}$$

as shown in Appendix 7A. Defining next to τ_{ads} characteristic times for (pseudo-)first order desorption, τ_{des} (s), and surface reaction, τ_{sur} (s), as:

$$\tau_{des} = \frac{1}{k_d} \tag{7.24}$$

and:

$$\tau_{sur} = \frac{1}{k_r} \tag{7.25}$$

with k_d and k_r denoting the (pseudo-)first order reaction rate coefficients for desorption and surface reaction respectively, an estimate can be made of the lower and upper bounds of the chemical time scales accessible by TAP experiments using the CVD microreactor with a typical residence time of 20 ms. A range from about 100 up to 10000 m_g^3 mol^{-1} s^{-1} is obtained for the (pseudo-)first order adsorption rate coefficient. For the desorption and surface reaction rate coefficients a range from 10 to 1000 s^{-1} is calculated. Hence, the wafer-packed microreactor allows to obtain information about elementary reactions occurring on a millisecond time scale.

7.4.3 Adsorption of silanes at low temperatures

The qualitative experiments outlined in paragraph 7.3 revealed a weak temperature dependence for all three silanes in the low temperature region, which may be attributed to adsorption kinetics (Buss *et al.*, 1988; Gates, 1988). Moreover, in the same region the surface was found to have a constant composition even after 100 to 200 pulses, that is after the adsorption of at least several monolayers. For example, 200 pulses of silane at a conversion of 16% correspond to the adsorption of 10 monolayers considering a mean pulse size of 5 10^{15} molecules per pulse and the adsorption capacity of the microreactor equal to 1.5 10^{16} molecules. This is not much of a problem as long as the reactions after the adsorption step are so fast that in the time interval between two pulses, which is mainly of the order of a second, the free surface can be regenerated. It is known, however, that hydrogen desorption, whether first order as on Si(001) (Sinniah *et al.*, 1989, D'Evelyn *et al.*, 1992, Wise *et al.*, 1991) or second order as on Si(111) (Wise *et al.*, 1991), is a slow process with a characteristic time of about 1 s even at 850 K. This is consistent with the results obtained by Holleman and Verweij (1993) and those presented in Chapters 4 and 5 of this thesis. These kinetic modelling studies showed that the desorption of molecular hydrogen from the hydrogenated polysilicon surface occurs with a similar characteristic time.

From the above considerations it can be inferred that the silicon surface used in the low temperature TAP experiments is almost completely saturated with hydrogen. Adsorption processes therefore can not take place at vacant surface sites but have to occur at hydrogen covered sites. This implies that adsorption most likely occurs via an insertion reaction, e.g. for silane:

$$\mathrm{Si(s)\text{-}H} + \mathrm{SiH_4} \rightarrow \mathrm{Si(s)\text{-}SiH_3} + \mathrm{H_2} \tag{7.26}$$

Since in the low temperature region the reactivity towards adsorption is about equal for all three silanes, as can be deduced from the experimental conversions, similar reactions are postulated for the higher silanes:

$$\mathrm{Si(s)\text{-}H} + \mathrm{Si_2H_6} \rightarrow \mathrm{Si(s)\text{-}Si_2H_5} + \mathrm{H_2} \tag{7.27}$$

$$\mathrm{Si(s)\text{-}H} + \mathrm{Si_3H_8} \rightarrow \mathrm{Si(s)\text{-}Si_3H_7} + \mathrm{H_2} \tag{7.28}$$

With Knudsen diffusion as the predominant mode of gas transport the mass balance for all three silanes becomes:

$$\varepsilon \frac{\partial C_i}{\partial t} = D^K_{eff,i} \frac{\partial^2 C_i}{\partial x^2} - a_v L_t k_{ins} C_i \tag{7.29}$$

which is subjected to the initial and boundary conditions given by equations (7.3) to (7.5). Here, k_{ins} denotes the adsorption/insertion rate coefficient. The disappearance term on the right-hand side of this equation features no dependency of the coverage of hydrogen covered sites. It implies a constant and uniform adsorption surface during the pulse experiment. Complete desorption of hydrogen from the formed, presumably very instable, compounds up to monohydride species will indeed result in a surface with the same amount of active Si-H sites for all three silanes at the beginning of each pulse. However, this needs not necessarily be true as can be inferred from literature on plasma-free CVD growth of hydrogenated amorphous silicon layers (Kanoh *et al.*, 1993). These layers were grown in the same temperature region in which the TAP experiments have been performed. The data support a hydrogen content in the bulk of the layer of seven atomic percent for trisilane and of about five atomic percent for disilane, both at 673 K, implying that probably not all secondary hydrogen atoms desorb during the growth process. The figures may suggest small changes in the available amount of adsorption sites, i.e. of Si-H sites at or near the surface, for the various silanes. However, it is questionable whether secondary hydrogen atoms on adsorbed higher silanes are sterically available as adsorption sites. Static SIMS measurements on Si(111) (7x7) show that adsorbed SiH-species are the primary stable species after exposure of the silicon surface to disilane in the temperature region of interest (Kulkarni *et al.*, 1990a). From time-of-flight direct reactivity measurements of the surface hydrogen coverage on Si(100) during Chemical Beam Epitaxy (CBE) growth of silicon from SiH_4 and Si_2H_6 (Gates and Kulkarni, 1992) about constant surface hydrogen/silicon atom ratio's were obtained at low temperatures, although for Si_2H_6 the ratio proved not to be 1.0 but 1.5. These measurements give evidence for a constant amount of adsorption sites as requested by the above stated model.

Pulse experiments with a binary gas mixture of 20% argon and 80% silane performed in the temperature range from 462 to 850 K were modelled using the above mentioned equations. The effective Knudsen diffusion coefficient of silane was obtained from that of argon by correcting the latter by the appropriate square-root inverse ratio of the corresponding molar masses. This approach reduces the total number of unknown parameters to be estimated. The parameter estimation was performed as outlined in paragraph 7.2.4.

Figure 7.14 shows a typical comparison between an experimental and a calculated silane response. The experimental response applies to a pulse experiment performed at 811 K. Table 7.2 lists the corresponding parameter estimates with their 95%-confidence intervals. Clearly, an excellent agreement between experiment and model is observed. Moreover, the parameter estimates are not strongly correlated, the highest binary correlation coefficient amounting to 0.85.

Simulation of the same silane response with these parameter estimates yields a silane conversion equal to 18.6%, corresponding to a Da_I-number of 0.44. In case the consumption of silane would be entirely determined by homogeneous decomposition, the corresponding unimolecular reaction rate coefficient, k_g, would amount to 17 s^{-1} as calculated from:

$$Da_I = k_g \frac{\varepsilon L^2}{D^K_{eff,SiH_4}} \qquad (7.30)$$

Comparison with the value of 4 10^{-4} s^{-1} obtained from RRKM theory for silane decomposition into silylene and molecular hydrogen at 100 Pa and 811 K, see paragraph 5.3, justifies the assumption of neglecting gas phase pyrolysis.

Table 7.2: *Parameter estimates with their approximate individual 95%-confidence intervals obtained by regression of a silane response at 811 K using* D^K_{eff,SiH_4} = 1.80 10^{-2} m_g^3 m_r^{-1} s^{-1}, N_{p,SiH_4} = 7.97 10^{-10} mol.

Parameter	Estimate
k_{ins} \ 10^2 m_g^3 mol^{-1} s^{-1}	1.98 ± 0.06
t_0 \ 10^{-3} s	1.15 ± 0.01

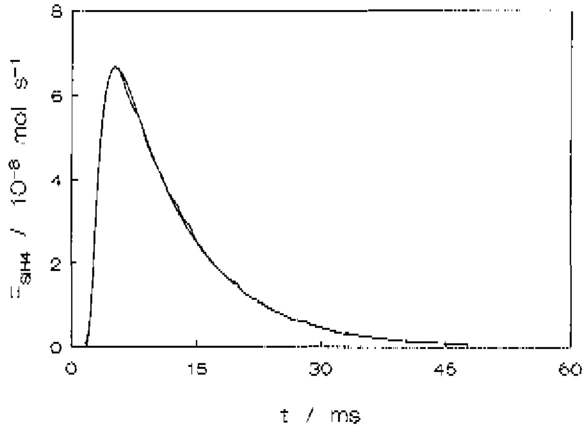

Figure 7.14: *Silane molar flow rate at outlet of reactor versus the time at 811 K. Full line: experimental. Dashed line: calculated using equations (7.29) and (7.3) to (7.5) and the estimated parameters listed in Table 7.2.* N_{p,SiH_4} = 7.97 10^{-10} mol, D^K_{eff,SiH_4} = 1.80 10^{-2} m_g^3 m_r^{-1} s^{-1}.

Figure 7.15a shows an Arrhenius diagram of the adsorption/insertion rate coefficient k_{ins} obtained by regression of silane response data in the temperature range between 462 K and 850 K. Clearly, two regimes can be distinguished with a transition occurring at a temperature of about 820 K.

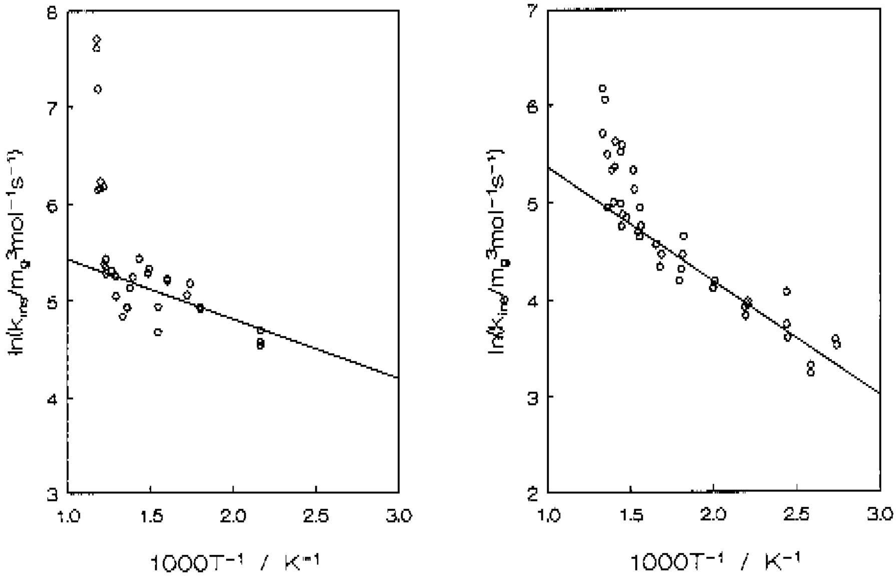

a)

b)

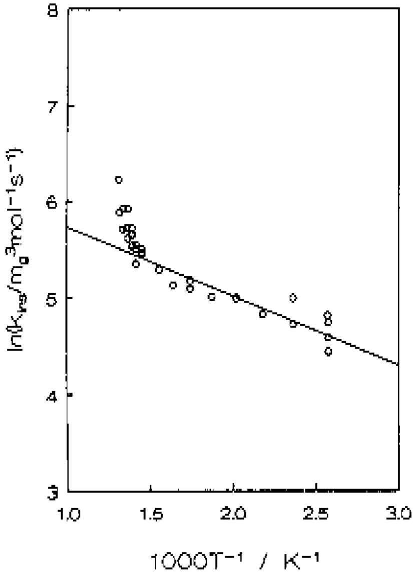

c)

Figure 7.15: *Arrhenius diagram of the adsorption/insertion rate coefficient of SiH_4 (a), Si_2H_6 (b) and Si_3H_8 (c) applying to the low temperature regions.*

Pulse experiments with binary gas mixtures of 80% disilane and 20% argon and with pure trisilane performed in the temperature range from 365 to 755 K and from 388 up to 762 K respectively were also modelled. The effective Knudsen diffusion coefficients of disilane were obtained from the corresponding argon responses as outlined earlier. The effective Knudsen diffusion coefficients of trisilane on the other hand were calculated by interpolation of the effective Knudsen diffusion coefficients of argon obtained from the silane and disilane experiments using the square root dependence on temperature.

Figures 7.15b and 7.15c show the Arrhenius diagrams of the adsorption/insertion rate coefficients for disilane and trisilane as obtained by regression of the above mentioned responses. In both cases two temperature regimes can be distinguished with a transition for disilane at 650 K and for trisilane at 710 K.

For all three silanes the significance of the global regression of the responses in the high temperature regions is smaller than in the low temperature regions as expressed by means of the F-ratio. This also points to a change in mechanism.

Table 7.3 lists the Arrhenius parameters with approximate individual 95%-confidence intervals obtained by regression of the adsorption/insertion rate coefficients of silane, disilane and trisilane in the low temperature regions.

Table 7.3: *Estimates with approximate individual 95%-confidence intervals of the Arrhenius parameters associated with the adsorption/insertion reactions of SiH_4, Si_2H_6 and Si_3H_8 on polycrystalline silicon at low temperatures.*

Species	A / m_g^3 mol^{-1} s^{-1}	E_a / kJ mol^{-1}
SiH_4	424±188	5.14±2.52
Si_2H_6	693±274	9.77±1.84
Si_3H_8	627±141	5.92±1.08

Similar to the insertion reaction of silane given in equation (7.26) a gas phase reaction between silane and silylene giving silylsilylene and hydrogen is described by Ho *et al.* (1994) with a slightly larger activation energy of 24.2 kJ mol^{-1} as compared to 5.1 kJ mol^{-1} estimated here. Indeed, even at temperatures as low as 462 K small amounts of hydrogen were detected in the present work during the adsorption of silane.

As mentioned in the experimental section, considerable temperature gradients exist in the axial direction of the microreactor. The model equations given above do not provide in such gradients. Nevertheless, the assumption concerning isothermicity is quite plausible as the adsorption processes of all three silanes prove to be only slightly activated as shown in Table 7.3.

Transition state theory yields the following expression for the adsorption/insertion rate coefficient k_{ins} in units $atm^{-1}\ s^{-1}$:

$$k_{ins} = \frac{kT}{h} \exp\left(\frac{\Delta^{\ddagger}S^{\circ}}{R} - \frac{\Delta^{\ddagger}H^{\circ}}{RT}\right) \qquad (7.31)$$

with $\Delta^{\ddagger}S^0$ and $\Delta^{\ddagger}H^0$ denoting the standard activation entropy and enthalpy. Table 7.4 lists the standard activation entropies with approximate individual 95%-confidence intervals obtained by regression of the adsorption/insertion rate coefficients of silane, disilane and trisilane in the low temperature regions.

Table 7.4: *Estimates with approximate individual 95%-confidence intervals of the standard activation entropies associated with the insertion reactions of SiH_4, Si_2H_6 and Si_3H_8 into surface hydrogen bonds. Standard state: 1 atm, $\theta^{*} = 0.5$.*

Species	$\Delta^{\ddagger}S^0$ / $J\ mol^{-1}\ K^{-1}$
SiH_4	-192±4
Si_2H_6	-186±4
Si_3H_8	-187±2

No literature data on standard activation entropies for the adsorption of silanes exist. Upon adsorption, however, the silanes will lose their translational and at least a part of their external rotational entropy. By means of statistical thermodynamics it can be calculated that at the mean temperature of the experiments the values for the standard translational entropy amount to 168 $J\ mol^{-1}\ K^{-1}$ for silane, 171 $J\ mol^{-1}\ K^{-1}$ for disilane and 178 $J\ mol^{-1}\ K^{-1}$ for trisilane. For the external rotational entropy values of 59 $J\ mol^{-1}\ K^{-1}$ for silane, 89 $J\ mol^{-1}\ K^{-1}$ for disilane and 121 $J\ mol^{-1}\ K^{-1}$ for trisilane can be calculated. The standard activation entropies listed in Table 7.4 and obtained by regression of the experimental data agree reasonably well with the theoretical expectations since on adsorption the translational entropy as well as a part of the rotational entropy of the adsorbing species will be lost.

7.4.4 Adsorption of silane at temperatures higher than 820 K

In the previous paragraph the slow adsorption of silane via insertion at low temperatures was discussed. At 820 K distinct changes are observed in the silane conversion and the activation energy of the reaction. This seems to correspond to a change in mechanism as from this temperature on regression results using the model equations for the low temperature region are rather poor.

In order to describe the experimental observations at temperatures higher than 820 K, the six-step reaction mechanism proposed in Chapter 4 is used. This mechanism, shown in Table 7.5, was derived by quantitative modelling of steady state kinetic experiments performed at operating conditions where gas phase reactions can be omitted and, hence, silicon deposition is predominantly determined by the heterogeneous decomposition of silane.

Table 7.5: *Elementary reactions considered on the silicon surface (1-6) and global reactions (α,β).*

	σ_α	σ_β	
$SiH_4 + 2^* \rightarrow SiH_3^* + H^*$	1		(1)
$SiH_3^* + {}^* \rightarrow SiH_2^* + H^*$	1		(2)
$SiH_2^* + {}^* \rightarrow SiH^* + H^*$	1		(3)
$SiH^* \rightarrow Si(s) + H^*$	1		(4)
+ ----------------------------------			
$SiH_4 + 4^* \rightarrow Si(s) + 4H^*$		1	(α)
$H^* \rightleftharpoons H^\theta + {}^*$		2	(5)
$H^* + H^\theta \rightleftharpoons H_2 + {}^*$		2	(6)
+ ----------------------------------			
$SiH_4 \rightarrow Si(s) + 2H_2$			(β)

The global reaction (α), built up from elementary steps and symbolized by the column with stoichiometric numbers σ_α, describes the decomposition of silane into solid silicon and hydrogen adatoms. The decomposition reactions of the surface trihydride, dihydride and monohydride species, see reactions (2) to (4), are considered to proceed fast compared to the silane adsorption reaction, reaction (1). The rate of global reaction (α) is consequently given by the rate of adsorption, as follows from the stoichiometric numbers. Together with the elementary reactions (5) and (6), reflecting the desorption of molecular hydrogen, global reaction (α) takes part in global deposition path (β), symbolized by the column with stoichiometric numbers σ_β. In this sequence, global reaction (α) is now considered to be fast compared to the desorption of hydrogen or more specifically to the excitation of a covalently bound hydrogen adatom given by reaction (5).

Evidence for the irreversible adsorption of silane is provided by the alternating pulse experiments with silane and deuterium presented in paragraph 7.3.1, revealing no desorption of deuterated silicon containg gas phase species. The elementary reactions reflecting hydrogen desorption, reactions (5) and (6), are considered to proceed irreversibly as well. According to Sinniah *et al.* (1989) the formation of a localized hydrogen adatom via interaction of a delocalized hydrogen atom with a vacant surface site indeed is slow. For any appreciable coverage of localized hydrogen adatoms the diffusion length of an excited hydrogen atom necessary to find such localized adatom is not very large making recombination with a localized hydrogen adatom, reaction (6), much more likely to occur than interaction with a vacant surface site, the reverse of reaction (5). Adsorption of molecular hydrogen, the reverse of reaction (6), is not considered either, because only small amounts of hydrogen are produced during the pulse experiments.

The reaction sequence of Table 7.5 consists of only two kinetically significant reactions, i.e. the adsorption of silane, reaction (1), with rate coefficient k_a, and the thermal excitation of hydrogen adatoms, reaction (5), with rate coefficient k_e. Consequently, localized hydrogen adatoms, H*, are the only kinetically significant surface species.

With Knudsen diffusion as the predominant mode of gas transport the following mass balances for silane and vacant surface sites apply:

$$\varepsilon \frac{\partial C_{SiH_4}}{\partial t} = D^{K}_{eff.SiH_4} \frac{\partial^2 C_{SiH_4}}{\partial x^2} - a_v L_t k_a \theta_*^2 C_{SiH_4} \tag{7.32}$$

$$\frac{\partial \theta_*}{\partial t} = -4 k_a \theta_*^2 C_{SiH_4} + 2 k_e (1 - \theta_*) \tag{7.33}$$

subjected to the following initial and boundary conditions:

$$t = t_0 \ \wedge \ 0 \le x \le L \qquad C_{SiH_4} = \frac{N_{p.SiH_4}}{\varepsilon A_s} \delta_x \tag{7.34}$$

$$t = t_0 \;\wedge\; 0 \le x \le L \qquad \theta_* = 1 - \theta^0_{H*} \tag{7.35}$$

$$t \ge t_0 \;\wedge\; x = 0 \qquad \frac{\partial C_{SiH_4}}{\partial x} = 0 \tag{7.36}$$

$$t \ge t_0 \;\wedge\; x = L \qquad C_{SiH_4} = 0 \tag{7.37}$$

Note that contrary to the mass balance given by equation (7.29), the production term in equation (7.32) explicitly shows a dependency on the fraction of vacant surface sites. Corresponding with this there is a continuity equation for the vacant sites as well, see equation (7.33). At temperatures above 820 K it is assumed that the adsorption takes place on vacant surface sites. The fraction of these sites will be significantly larger than zero at the used temperatures but certainly not amount to one. Therefore, the amount of adsorption sites in the microreactor will be of the same order of magnitude as the pulse size and changes in it can not be neglected. The initial condition for the fraction of vacant surface sites, given by equation (7.35), is determined by the fractional surface coverage of hydrogen adatoms, θ^0_{H*}, at the beginning of each pulse. Note that the slow adsorption process via insertion which is dominating at the low temperatures and can be written in the terminology of Table 7.5 as:

$$*H + SiH_4 \rightarrow Si(s){-}H + 2H_2 \tag{7.38}$$

has not been accounted for in the mass balances. At the relatively high temperatures considered here, this insertion process has only a minor contribution to the overall adsorption process.

Parameter estimates for pulse experiments with a binary gas mixture of 20% argon and 80% silane at 844 K and 849 K were obtained using the above continuity equations. The value of the rate coefficient for thermal excitation of hydrogen adatoms, k_e, could not be estimated significantly, indicating that the characteristic time for hydrogen desorption, even at these temperatures, is too large to be within the window of measurable time scales in TAP, see paragraph 7.4.2. Therefore, the term corresponding to hydrogen desorption was omitted from equation (7.33). It thus is assumed that hydrogen, adsorbed on the surface at $t = t_0$, stays there during the experiment. This implies that a part of the surface is unavailable for adsorption during the experiment, as it is already covered with hydrogen. The fraction of vacant sites at the beginning of the experiment, i.e. the part of the surface available for adsorption, then equals $(1-\theta^0_{H*})$ with θ^0_{H*} denoting the fractional coverage of hydrogen at $t = t_0$.

Obviously, the mass balances for silane and vacant surface sites now can be rewritten as:

$$\varepsilon \frac{\partial C_{SiH_4}}{\partial t} = D^{K}_{eff,SiH_4} \frac{\partial^2 C_{SiH_4}}{\partial x^2} - a_v L_t (1 - \theta^0_{H\cdot})^2 k_a \hat{\theta}^2 C_{SiH_4} \tag{7.39}$$

$$\frac{\partial \hat{\theta}}{\partial t} = -4 k_a (1 - \theta^0_{H\cdot}) \hat{\theta}^2 C_{SiH_4} \tag{7.40}$$

with initial and boundary conditions:

$$t = t_0 \wedge 0 \leq x \leq L \qquad C_{SiH_4} = \frac{N_{p,SiH_4}}{\varepsilon A_s} \delta_x \tag{7.41}$$

$$t = t_0 \wedge 0 \leq x \leq L \qquad \hat{\theta} = 1 \tag{7.42}$$

$$t \geq t_0 \wedge x = 0 \qquad \frac{\partial C_{SiH_4}}{\partial x} = 0 \tag{7.43}$$

$$t \geq t_0 \wedge x = L \qquad C_{SiH_4} = 0 \tag{7.44}$$

Here, $\hat{\theta}$ is the fraction of vacant sites on the available part of the surface at t= t_0. The same pulse experiments performed at 844 K and 849 K were then regressed with equations (7.39) to (7.44). The adsorption rate coefficient k_a, the initial fraction of vacant surface ($1-\theta^0_{H\cdot}$), and the zero time t_0 were estimated using the parameter estimation method discussed in paragraph 7.2.4. Very good agreement between experiment and model is observed for both experiments. However, as expected, the estimates for k_a and ($1-\theta^0_{H\cdot}$) are strongly correlated with a binary correlation coefficient up to 0.994, implying that the significance of the values obtained for k_a and ($1-\theta^0_{H\cdot}$) is rather low. Hence, an independent estimate of one of these parameters is required in order to obtain a significant estimate of the other.

The kinetic modelling study described in Chapter 4 resulted in a value of 2.3 10^{-3} for the sticking probability of silane on an empty surface. Substitution of this value into equation (4.24) yields values for the adsorption rate coefficient k_a, in this equation denoted by k_1, equal to 37665 m_g^3 mol^{-1} s^{-1} for 844 K and to 37776 m_g^3 mol^{-1} s^{-1} for 849 K. Applying these values of k_a in the modelling, excellent agreement between the experimental responses and the responses calculated using equations (7.39) to (7.44) is obtained, as can be seen in Figure 7.16 for 849 K. For both experiments the zero time t_0 found by regression equals about 1.2 ms, the same value as found for the experiments discussed in the previous paragraphs. The initial vacant fraction of the surface, $(1-\theta^0_{H^*})$, equals 0.236 ± 0.002 at 844 K and 0.316 ± 0.001 at 849 K.

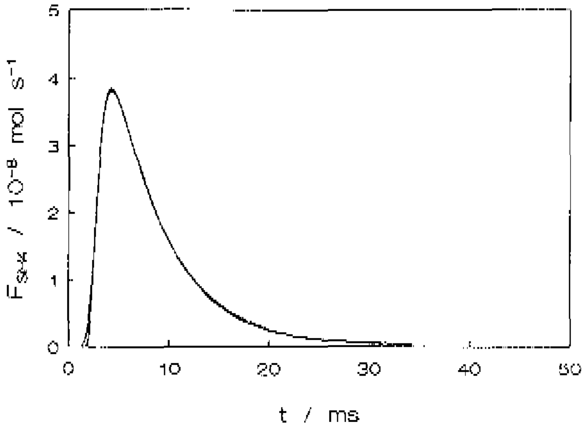

Figure 7.16: *Silane molar flow rate at outlet of reactor versus the time at 849 K. Full line: experimental. Dashed line: calculated using equations (7.39) to (7.44) and the estimated values* $(1-\theta^0_{H^*}) = 0.316$ *and* $t_0 = 1.20\ 10^{-3}$ *s.* $N_{p,SiH_4} = 1.12\ 10^{-9}$ *mol,* $D^K_{eff,SiH_4} = 1.90\ 10^{-2}\ m_g^3\ m_r^{-1}\ s^{-1}$, $k_a = 37776\ m_g^3\ mol^{-1}\ s^{-1}$.

Reconsidering the qualitative results given in paragraph 7.3.1, it now is clear why the multipulse experiments in the high temperature region are hardly reproducible and why the conversion of silane is increasing strongly from about 820 K on. Obviously, the conversion of silane is a strong function of the initial state of the surface and a small change in initial hydrogen coverage, $\theta^0_{H^*}$, will lead to a large change in silane conversion. As all pulse experiments have been performed using signal averaging after the admittance of a number of pulses needed to obtain a stable response signal, it is difficult to tell the exact amount of vacant sites at the beginning of the pulse sequence. However, the values for the initial fraction of vacant surface, $(1-\theta^0_{H^*})$, found from the regression analysis of the experimental data, seem quite reasonable taking into account a characteristic time for hydrogen desorption of about 1 s and a time between pulses in the signal averaging mode also of 1 s, see Appendix 7B.

7.5 Conclusions

The adsorption of silanes on polycrystalline silicon was studied by means of Temporal Analysis of Products in the temperature range between 300 K and 1000 K. Qualitative experiments with silane, disilane and trisilane revealed that at low temperatures slow adsorption processes are operative. The reactivity for the three silanes towards adsorption on polysilicon is about equal, whereas the apparant activation energies are quite low and more or less equal to each other. However, at 820 K for silane, 600 K for disilane and 710 K for trisilane a transition is observed towards a faster mode of adsorption. The adsorption of the higher silanes above the respective transition temperatures is accompanied by silane formation. For all three silanes the apparant activation energy for adsorption has strongly increased in this temperature region.

Quantitative experiments with inert gases showed that the gas transport through the microreactor can be described by Knudsen diffusion. The same transport mode is used for the quantitative modelling of the responses of silane, disilane and trisilane. An adequate description of the adsorption of the silanes in the temperature regions below the respective transition temperatures is provided by an insertion reaction of SiH_4, Si_2H_6 or Si_3H_8 into surface hydrogen bonds followed by fast decomposition of the formed species into Si-H moieties, which can act as new adsorption sites.

Silane adsorption above the transition temperature of 820 K can be described very well with a mechanism consisting of dual-site dissociative adsorption of silane onto vacant surface sites, subsequent fast decomposition of the formed surface hydride species, and desorption of hydrogen. This mechanism is similar to that deduced in Chapter 4 and indeed gives strong evidence for the correctness of the latter.

References

Buss, R.J., Ho, P., Breiland, W.G., Coltrin, M.E., 1988, *J. Appl. Phys.*, **63**(8), 2808.

Clausing, P., 1929, *Physica*, **9**, 65.

Coronell, D.G., Jensen, K.F., 1992, *J. Electrochem. Soc.*, **139**(8), 2264.

Croon, M.H.J.M. de, 1995, personal communication, Eindhoven University of Technology.

D'Evelyn, M.P., Yang, Y.L., Sutcu, L.F., 1992, *J. Chem. Phys.*, **96**(1), 852.

Draper, N.R., Smith, H., 1966, Applied Regression Analysis, Wiley, New York.

Eldridge, B.D., Brown, L.F., 1976, *AIChE J.*, **22**(5), 942.

Farnaam, M.K., Olander, D.R., 1984, *Surf. Sci.*, **145**, 390.

Gates, S.M., 1988, *Surf. Sci.*, **195**, 307.

Gates, S.M., Greenlief, C.M., Beach, D.B., Kunz, R.R., 1989, *Chem. Phys. Lett.*, **154**, 505.

Gates, S.M., Greenlief, C.M., Beach, D.B., 1990, *J. Chem. Phys.*, **93**(10), 7493.

Gates, S.M., Kulkarni, S.K., 1991, *Appl. Phys. Lett.*, **58**(25), 2963.

Gates, S.M., Kulkarni, S.K., 1992, *Appl. Phys. Lett.*, **60**(1), 53.

Gleaves, J.T., Ebner, J.R., Kuechler, T.C., 1988, *Catal. Rev - Sci. Eng.*, **30**(1), 49.

Ho, P., Coltrin, M.E., Breiland, W.G., 1994, *J. Phys. Chem.*, **98**(40), 10138.

Holleman, J., Verweij, J.F., 1993, *J. Electrochem. Soc.*, **140**(7), 2089.

Huinink, J.P., 1995, A Quantitative Analysis of Transient Kinetic Experiments: The Oxidation of CO by O_2/NO on Pt, Ph.D. Thesis TUE, Eindhoven.

Kanoh, H., Sugiura, O., Matsumura, M., 1993, *Jpn. J. Appl. Phys.*, **32**, 2613.

Kulkarni, S.K., Gates, S.M., Greenlief, C.M., Sawin, H.H., 1990a, *Surf. Sci.*, **239**, 26.

Kulkarni, S.K., Gates, S.M., Scott, B.A., Sawin, H.H., 1990b, *Surf. Sci.*, **239**, 13.

Marquardt, D.W., 1963, *J. Soc. Indust. Appl. Math.*, **11**, 431.

Mason, E.A., Malinauskas, A.P., 1983, Gas Transport in Porous Media: The Dusty-Gas Model, in Chemical Engineering Monographs 17, Elsevier, Amsterdam.

NAG, Fortran Library Manual, 1991, Mark 15, NAG Ltd, Wilkinson House, Oxford.

Sinniah, K., Sherman, M.G., Lewis, L.B., Weinberg, W.H., Yates, J.T., Janda, K.C., 1989, *Phys. Rev. Lett.*, **62**(5), 567.

Svoboda, G.D., Gleaves, J.T., Mills, P.L., 1992, *Ind. Eng. Chem. Res.*, **31**(1), 19.

Werner, K., Butzke, S., Radelaar, S., Balk, P., 1994, *J. Cryst. Growth*, **136**, 322.

Wise, M.L., Koehler, B.G., Gupta, P., Coon, P.A., George, S.M., 1991, *Surf. Sci.*, **258**, 166.

Zou, B.S., Dudukovic, M.P., Mills, P.L., 1994, *J. Catal.*, **145**, 683.

Appendix 7A Window of measurable Damköhler-I numbers

In case of a first order reaction the continuity equation for reactant A can be written as (Huinink, 1995):

$$\frac{\partial C_A}{\partial \tau} = \frac{\partial^2 C_A}{\partial z^2} - Da_I C_A \tag{7A.1}$$

with the dimensionless time τ and the dimensionless place coordinate z given by:

$$\tau = \frac{D^K_{eff,A}\, t}{\varepsilon L^2} \tag{7A.2}$$

$$z = \frac{x}{L} \tag{7A.3}$$

and the Damköhler-I number defined as:

$$Da_I = \frac{\varepsilon k L^2}{D^K_{eff,A}} \tag{7A.4}$$

with k denoting the first order rate coefficient (s^{-1}). Solving equation (7A.1) with initial and boundary conditions:

$$C(z,o) = \delta_z \frac{N_{p,A}}{\varepsilon A_s L} \tag{7A.5}$$

$$\frac{\partial C}{\partial z}\Big|_{z=0} = 0 \tag{7A.6}$$

$$C(1,\tau) = 0 \tag{7A.7}$$

gives for the Laplace transform of the molar flow rate at the outlet of the microreactor (de Croon, 1995):

$$\mathcal{F}_A = \frac{D^K_{eff,A} N_{p,A}}{\varepsilon L^2} \frac{1}{\cosh \sqrt{s + Da_I}} \tag{7A.8}$$

Consider first the situation that $Da_I = 0$, i.e. no reaction occurs in the microreactor.

Then:

$$\mathcal{F}_{A,Da_l=0} = \frac{D^K_{eff,A}\, N_{p,A}}{\varepsilon\, L^2} \cdot \frac{1}{\cosh \sqrt{s}} \tag{7A.9}$$

which can be shown to be equivalent to:

$$\mathcal{F}_{A,Da_l=0} = 2\,\frac{D^K_{eff,A}\, N_{p,A}}{\varepsilon\, L^2} \sum_{n=0}^{\infty} (-1)^n \exp[-(2n+1)\sqrt{s}] \tag{7A.10}$$

The inverse Laplace transform of equation (7A.10) leads to an expression for the molar flow rate $F_{A,Da_l=0}$ in case $Da_l = 0$:

$$F_{A,Da_l=0} = \frac{D^K_{eff,A}\, N_{p,A}}{\sqrt{\pi}\, \varepsilon\, L^2}\; \frac{\exp\left(-\frac{1}{4\tau}\right)}{\tau^{3/2}} \sum_{n=0}^{\infty} (-1)^n\, (2n+1)\, \exp\left(-\frac{n(n+1)}{\tau}\right) \tag{7A.11}$$

Inspecting equation (7A.8) it will be clear that the expression for F_{A,Da_l} for an arbitrary value of Da_l is:

$$F_{A,Da_l} = \frac{D^K_{eff,A}\, N_{p,A}}{\sqrt{\pi}\, \varepsilon\, L^2}\; \frac{\exp\left(-\left(Da_l \tau + \frac{1}{4\tau}\right)\right)}{\tau^{3/2}} \sum_{n=0}^{\infty} (-1)^n (2n+1)\, \exp\left(-\frac{n(n+1)}{\tau}\right) \tag{7A.12}$$

The maximum in the curve of F_{A,Da_l} can be calculated from:

$$\frac{dF_{A,Da_l}}{dt} = 0 \tag{7A.13}$$

Considering only the first term in the series expansion of F_{A,Da_l}, the following expression is obtained for the position of the maximum:

$$\tau_{max,1} = \frac{3}{4\, Da_l} \left(\sqrt{1 + \frac{4}{9}\, Da_l} - 1 \right) \tag{7A.14}$$

whereas in case both the first and second term in the series expansion are considered, the position of the maximum $\tau_{max,2}$ can be obtained from the implicit equation:

$$\exp\left(-\frac{2}{\tau}\right) = \frac{\dfrac{1}{4\tau} - Da_I\tau - 3/2}{\dfrac{27}{4\tau} - 3\,Da_I\tau - 9/2} \tag{7A.15}$$

For all practical purposes, equation (7A.14) is sufficiently accurate to calculate τ_{max} for an arbitrary value of Da_I. It now is possible to calculate $F_{A,Da_I,max}$, the value of F_{A,Da_I} at τ_{max}:

$$F_{A,Da_I,max} = \frac{D^K_{eff,A}\,N_{p,A}}{\sqrt{\pi}\,\varepsilon\,L^2}\;\frac{\exp\left(-3/2\sqrt{1+\dfrac{4}{9}\,Da_I}\right)}{\left[\dfrac{3}{4\,Da_I}\left(\sqrt{1+\dfrac{4}{9}\,Da_I}-1\right)\right]^{3/2}}\;\cdot$$

$$\left(1-3\exp\left(-6\left(\sqrt{1+4/9\,Da_I}+1\right)\right)+\ldots\right) \tag{7A.16}$$

For $Da_I = 0$ the following expression is obtained:

$$F_{A,Da_I=0,max} = \frac{D^K_{eff,A}\,N_{p,A}}{\sqrt{\pi}\,\varepsilon\,L^2}\;6^{3/2}\exp(-3/2)\;(1-3\exp(-12)+\ldots) \tag{7A.17}$$

The second and higher terms inside the brackets in this equation are smaller than 2 10^{-5} and can therefore be omitted. Dividing equation (7A.12) by equation (7A.16) leads to the following expression for the relative molar flow rate for an arbitrary value Da_I:

$$\frac{F_{A,Da_I}}{F_{A,Da_I,max}} = \frac{\exp\left(-\left(Da_I\tau+\dfrac{1}{4\tau}-3/2\sqrt{1+4/9\,Da_I}\right)\right)}{\left(3\tau\left(\sqrt{1+4/9\,Da_I}+1\right)\right)^{3/2}}\;\cdot$$

$$\left(\sum_{n=0}^{\infty}(-1)^n\,(2n+1)\,\exp\left(-\frac{n(n+1)}{\tau}\right)\right) \tag{7A.18}$$

For $Da_I = 0$ division of equation (7A.11) by equation (7A.17) leads to:

$$\frac{F_{A,Da_I=0}}{F_{A,Da_I=0,\max}} = \frac{\exp\left(-\dfrac{1}{4\tau}\right)\exp(3/2)}{(6\tau)^{3/2}} \sum_{n=0}^{\infty} (-1)^n (2n+1) \exp\left(-\frac{n(n+1)}{\tau}\right) \qquad (7A.19)$$

The half height of the TAP response curve is defined by:

$$\frac{F_{A,Da_I}}{F_{A,Da_I,\max}} = 1/2 \qquad (7A.20)$$

Equation (7A.20) has two solutions: τ_1 and τ_2, with $\tau_2 > \tau_1$. The width of the response curve at half height, $W_{1/2}$, is defined as:

$$W_{1/2} \doteq \tau_2 - \tau_1 \qquad (7A.21)$$

Up to second order in the series expansion of equation (7A.19) yields for $Da_I = 0$:

$$W_{1/2,Da_I=0} = 0.4227 \qquad (7A.22)$$

in units of τ. Assuming that a deviation of about 5% in $W_{1/2}$ is readily observable, the matching Damköhler-I number can be calculated from equations (7A.20) to (7A.22). Using:

$$\Delta W_{1/2} = 0.05\, W_{1/2,Da_I=0} \qquad (7A.23)$$

implies that:

$$W_{1/2,Da_I} = 0.4015 \qquad (7A.24)$$

Up to second order in the series expansion of equation (7A.18) gives for the corresponding Damköhler-I number:

$$Da_{I,low} \doteq 0.19 \qquad (7A.25)$$

This is the lower bound of measurable Damköhler-I numbers in TAP. The upper bound can be found by assuming that a response area of 1% of the inlet signal area is significantly above the noise level. The corresponding Damköhler-I number is readily obtained from equation (7A.8). The surface area of the response signal, F_A, is given by:

$$\int_0^\infty F_A \, dt = \lim_{s \to 0} \mathcal{F}_A = \frac{D^K_{eff,A} N_{p,A}}{\varepsilon L^2} \frac{1}{\cosh\sqrt{Da_I}} \tag{7A.26}$$

The surface area of the inlet signal, $F_{A,in}$, is given by:

$$\int_0^\infty F_{A,in} \, dt = \frac{D^K_{eff,A} N_{p,A}}{\varepsilon L^2} \tag{7A.27}$$

Therefore:

$$\frac{\int_0^\infty F_A \, dt}{\int_0^\infty F_{A,in} \, dt} = \frac{1}{\cosh\sqrt{Da_I}} = 0.01 \tag{7A.28}$$

leading to the upper bound of measurable Damköhler-I numbers:

$$Da_{I,up} = 28.07 \tag{7A.29}$$

From equations (7A.25) and (7A.29) it is obtained that:

$$0.19 < Da_I < 28 \tag{7A.30}$$

or:

$$0.19 < \frac{\varepsilon k L^2}{D^K_{eff,A}} < 28 \tag{7A.31}$$

$W_{1/2,Da_I=0}$, now in units of t (s), follows from equation (7A.2):

$$W_{1/2,Da_I=0} = 0.4227 \frac{\varepsilon L^2}{D^K_{eff,A}} \tag{7A.32}$$

Equation (7A.31) can now be restated as:

$$12.45 \, W_{1/2,Da_I=0} > 1/k > 0.0845 \, W_{1/2,Da_I=0} \tag{7A.33}$$

Approximating this inequality in powers of ten results in:

$$10\, W_{1/2,Da_l=0} > \frac{1}{k} > 0.1\; W_{1/2,Da_l=0} \qquad (7A.34)$$

Alternatively, the inequality given by equation (7A.33) can be stated in terms of τ_{res} being the mean residence time of component A in the microreactor without reaction and defined as:

$$\tau_{res} = \frac{\varepsilon L^2}{D^K_{eff,A}} \; \frac{\int\limits_0^\infty \tau\, F_{A,Da_l=0}(\tau)\, d\tau}{\int\limits_0^\infty F_{A,Da_l=0}(\tau)\, d\tau} \qquad (7A.35)$$

Using the Laplace transform of $F_{A,Da_l=0}$, equation (7A.9), it is obtained that:

$$\tau_{res} = \frac{\varepsilon L^2}{D^K_{eff,A}} \; \frac{\lim\limits_{s\to 0}\left(-\dfrac{d\bar{F}_{A,Da_l=0}}{ds}\right)}{\lim\limits_{s\to 0} \bar{F}_{A,Da_l=0}} = \frac{\varepsilon L^2}{D^K_{eff,A}} \; \frac{\lim\limits_{s\to 0} \dfrac{\sinh\sqrt{s}}{\sqrt{s}\,(\cosh\sqrt{s})^2}}{\lim\limits_{s\to 0} \dfrac{1}{\cosh\sqrt{s}}} = \frac{\varepsilon L^2}{2\, D^K_{eff,A}} \qquad (7A.36)$$

Equation (7A.33) in terms of τ_{res} in stead of $W_{1/2,Da_l=0}$ now becomes:

$$10.5\; \tau_{res} > \frac{1}{k} > 0.07\; \tau_{res} \qquad (7A.37)$$

Appendix 7B Estimation of the thermal excitation rate coefficient from silane responses at temperatures higher than 820 K

Stable response signals are obtained by applying at least ten pulses before pulse averaging, with a repetition time equal to 1 s. To describe the sequence of stable response signals, the concentration profile in time in the reactor is approximated by a square wave. For the nth pulse it follows that:

$$C = C_0 \qquad t \in (n\tau_r\,,\ n\tau_r+\tau_1) \tag{7B.1}$$

and:

$$C = 0 \qquad t \in (n\tau_r+\tau_1\,,\ (n+1)\tau_r) \tag{7B.2}$$

with τ_1 denoting the pulse width and τ_r the repetition time. Thus, during the pulse the concentration is taken constant, whereas between pulses the concentration in the gas phase is set to zero. According to the reaction mechanism shown in Table 7.5, the following mass balances for the vacant surface sites in the reactor apply. For $\tau \in (n\tau_r, n\tau_r+\tau_1)$:

$$\frac{d\theta_*}{dt} = -4\,k_a\,C_0\,\theta_*^2 + 2\,k_e\,(1-\theta_*) \tag{7B.3}$$

with:

$$\theta_*\big|_{t=n\tau_r} = \theta_*^0 \tag{7B.4}$$

where θ_*^0 is the fraction of vacant surface sites at the beginning of the pulse in the stable response regime. For $\tau \in (n\tau_r+\tau_1,(n+1)\tau_r)$:

$$\frac{d\theta_*}{dt} = 2\,k_e\,(1-\theta_*) \tag{7B.5}$$

At $t= n\tau_r+\tau_1$ the solutions of equations (7B.3) and (7B.5) must be equal. These equations can be integrated easily. For $\tau \in (n\tau_r,n\tau_r+\tau_1)$ the solution is:

$$\theta_* = -\alpha/2 + \beta\,\frac{1 + \dfrac{\theta_*^0 + \alpha/2 - \beta}{\theta_*^0 + \alpha/2 + \beta}\exp\left[-8\,k_a\,C_0\,\beta\,(t - n\,\tau_r)\right]}{1 - \dfrac{\theta_*^0 + \alpha/2 - \beta}{\theta_*^0 + \alpha/2 + \beta}\exp\left[-8\,k_a\,C_0\,\beta\,(t - n\,\tau_r)\right]} \tag{7B.6}$$

with:

$$\alpha = \frac{k_e}{2\,k_a\,C_0} \qquad (7B.7)$$

and:

$$\beta = \frac{\alpha}{2}\sqrt{1+\frac{4}{\alpha}} \qquad (7B.8)$$

For $\tau \in (n\tau_r+\tau_1,(n+1)\tau_r)$ the solution is:

$$\theta_* = 1 - \left(1-\theta_*\big|_{n\tau_r+\tau_1}\right)\exp\left[-2\,k_e\,(t-n\tau_r-\tau_1)\right] \qquad (7B.9)$$

Now a stable response indicates that:

$$\theta_*\big|_{n\tau_r} = \theta_*\big|_{(n+1)\tau_r} = \theta_*^0 \qquad (7B.10)$$

as in the stable regime the surface has to be equal at the beginning of every pulse. Substitution of $\theta_*\big|_{n\tau_r+\tau_1}$ from equation (7B.6) at $t = n\tau_r+\tau_1$ into equation (7B.9) and evaluation of θ_* from this equation at $t = (n+1)\tau_r$, results in:

$$\theta_*^0 = 1 - \left[1+\alpha/2-\beta\,\frac{1+\dfrac{\theta_*^0+\alpha/2-\beta}{\theta_*^0+\alpha/2+\beta}\exp\left[-8\,k_a\,C_0\,\beta\,\tau_1\right]}{1-\dfrac{\theta_*^0+\alpha/2-\beta}{\theta_*^0+\alpha/2+\beta}\exp\left[-8\,k_a\,C_0\,\beta\,\tau_1\right]}\right] \qquad (7B.11)$$

$$\cdot\exp\left[-2\,k_e\,(\tau_r-\tau_1)\right]$$

In equation (7B.11) all parameters are known except k_e. Taking θ_*^0 equal to 0.316, k_a to 37776 m_g^3 mol^{-1} s^{-1}, τ_r to 1 s, τ_1 to about 20 ms and C_0 to about 5 10^{-3} mol m_g^{-3}, a value of 0.164 s^{-1} is calculated for k_e at 849 K. This value should be compared to the value for k_e calculated from the Arrhenius parameters given in Table 5.6 of Chapter 5. The calculated value amounts to 1.15 s^{-1}, which is equal to the one obtained here within one order of magnitude.

8

CONCLUSIONS

The work presented in this thesis focused on the development of a kinetic model which allows an adequate description of the experimental observations during the low pressure CVD of polycrystalline silicon from silane at industrially relevant operating conditions. This model could be reached using quantitative modelling of well-defined steady state kinetic experiments performed in a microbalance laboratory reactor, both in the absence and in the presence of gas phase reactions. First, a six-step elementary reaction mechanism was developed describing the growth rate data in the range of operating conditions where silicon deposition is predominantly determined by the heterogeneous decomposition of silane. This mechanism was then used as basis for a more comprehensive one, consisting of four elementary gas phase reactions and ten elementary surface reactions, to describe the silicon deposition process in the presence of gas phase reactions. The quantitative analysis of the microbalance data required the development of a reactor model explicitly taking into account the irreducible concentration gradients of the gas phase intermediates formed during the pyrolysis of silane. These gradients develop due to the high surface consumption rates of these species as compared to their transport rate by molecular diffusion.

Heterogeneous decomposition of silane occurs via dual-site dissociative adsorption forming a surface trihydride species and a hydrogen adatom, followed by potentially fast decomposition of this trihydride species through dihydride and monohydride species towards solid silicon and hydrogen adatoms. Regeneration of the partially hydrogenated silicon surface occurs by first order recombinative desorption of molecular hydrogen through excitation of a covalently bound hydrogen adatom from a localized surface Si-H bond to a two-dimensional delocalized state followed by recombination of this excited delocalized hydrogen atom with a second localized hydrogen adatom.

The relative importance of gas phase reactions for the silicon deposition process increases with increasing total pressure and is independent of temperature. Furthermore, it increases with decreasing surface-to-volume ratio. Under all circumstances silylene and disilane are the most important gas phase intermediates, with a contribution to the silicon growth rate between 1 and 44% depending on the operating conditions and the reactor geometry. Silylene is almost predominantly formed by gas phase decomposition of silane. Formation of silylene through gas phase decomposition of disilane is less important. Consumption of silylene takes place through surface decomposition into solid silicon and molecular hydrogen, and via insertion into silane forming disilane. The latter reaction fully accounts for the production of disilane. Consumption of disilane on the other hand occurs via surface decomposition into solid silicon, silane and hydrogen, via gas phase decomposition into silane and silylene, and to a much lesser extent via gas phase decomposition into silylsilylene and hydrogen.

For an adequate simulation of silicon growth rate data obtained in a conventional hot-wall multiwafer LPCVD reactor, a one-dimensional two-zone reactor model is sufficient, at least as long as the heterogeneous decomposition of silane dominates the silicon growth. The latter is the case at typical industrial conditions. Due to the relatively small contribution of the homogeneously formed reactive intermediates, growth rates calculated using this strongly simplified reactor model do not essentially differ from those calculated on the basis of a fully two-dimensional reactor model. Simulations of an industrial-scale LPCVD reactor showed that the radial growth rate non-uniformity across a wafer is completely determined by the radial variations in the growth rates from silylene and disilane, contributing to the silicon growth rate for 1 to 5% at industrially relevant operating conditions.

Additional evidence for the correctness of the six-step mechanism postulated for the deposition of polysilicon in the absence of gas phase reactions was obtained by quantitative modelling of transient kinetic experiments performed using the Temporal Analysis of Products (TAP) technique. This technique provides an alternative approach for studying CVD reaction kinetics. However, in order to take complete advantage of its strength in elucidating the kinetics of individual elementary steps, techniques like temperature programmed desorption (TPD) and static secondary ion mass spectrometry (SSIMS) are additionally needed for in-situ determination of the exact condition of the surface.

DANKWOORD

In tegenstelling tot hetgeen de omslag doet vermoeden is dit proefschrift allerminst het werk van één persoon. Ik wil dan ook iedereen die heeft bijgedragen aan de totstandkoming van dit proefschrift, zonder hen expliciet bij naam te noemen, van harte bedanken.

CURRICULUM VITAE

De schrijfster van dit proefschrift werd geboren op 12 februari 1965 te Maastricht. Na het behalen van het gymnasium-β diploma aan het Van Maerlantlyceum te Eindhoven begon zij in september 1984 met de studie Scheikundige Technologie aan de Technische Universiteit Eindhoven. In juni 1989 studeerde zij af bij prof. dr. R. Metselaar bij de vakgroep Vastestofchemie en Materialen. De titel van het afstudeeronderzoek was: " Diffusiebarrières tussen silicium carbide en nikkel of ijzer". In juli 1989 begon zij bij de vakgroep Chemische Proceskunde met haar promotieonderzoek dat leidde tot dit proefschrift. Vanaf 6 februari 1995 is zij werkzaam bij het Centre for Manufacturing Technology (CFT) van Philips op het gebied van het afzetten van dunne lagen via Low Pressure Chemical Vapour Deposition (LPCVD).